



ulm university universität
uulm

UNIVERSITÄT ULM
INSTITUT FÜR THEORETISCHE PHYSIK

COLORED NOISE IN OPEN QUANTUM SYSTEMS:
NOISY FREQUENCY ESTIMATION AND QUANTUM
CONTROL METHODS

Dissertation zur Erlangung des Doktorgrades Dr. rer. nat.
der Fakultät für Naturwissenschaften der Universität Ulm

vorgelegt von
Jan Friedrich Haase
aus Ulm

Ulm, August 2018

Dissertation

Titel Colored Noise in Open Quantum Systems:
 Noisy Frequency Estimation and Quantum Control Methods

Tag der Prüfung 20. November 2018

 This thesis was jointly supervised by
Prof. Dr. Susana F. Huelga and **Prof. Dr. Martin B. Plenio**.

Dekan der Fakultät: Prof. Dr. Peter Dürre

Erstgutachter: Prof. Dr. Susana F. Huelga

Zweitgutachter: Prof. Dr. Martin B. Plenio

Drittgutachter: Prof. Dr. Mauro Paternostro

Abstract

The dynamics of any quantum device is altered by its interaction with the surrounding environment. This thesis discusses the impact of noise in a scenario of quantum frequency estimation and techniques to control the dynamics between interacting quantum systems, as well as a method to tailor memory effects in the dynamics of an experimentally relevant system.

The first part of the thesis focuses on how to achieve the best possible frequency estimation in the presence of noise. In particular, we exploit a quantum metrology setting where N two level systems are employed as probes to estimate the amplitude of a field which alters their level splitting in a linear fashion. Thereby, we invoke a microscopic derivation of the spin-boson model to describe the appearing noise effects. We distinguish two main situations, the phase-covariant one, ensuring that the action of the noise commutes with the encoding of the parameter, and the non-phase-covariant one breaking this symmetry. We clarify the origin of this commutativity, that is ensured by the secular approximation. Subsequently, we perform a sensitivity analysis on the level of a single probe. Here, it turns out not only that the inclusion of non-phase-covariant terms may increase the achievable precision, but importantly, also that the noise terms themselves are able to contain relevant information on the frequency, a fact that is commonly neglected in the current literature. Moreover, as our microscopic approach covers all classes of dissipative dynamics, it provides an exhaustive picture in which all the different asymptotic scalings of precision naturally emerge when the probes are used in parallel. In particular, as soon as the noise terms exhibit temporal correlations, we observe the Zeno limit $1/N^{3/2}$ for any dynamics except the case where the noise is completely transversal to the encoding of the frequency. In the latter case, we demonstrate that a novel scaling of $1/N^{7/4}$ arises.

The second part of the thesis is instead dedicated to the development of techniques for quantum sensing and control.

Single probe quantum systems have also become a promising candidate as nanoscale spectrometers. Here, we present a method which enables effortless detection of spurious signals generated by finite-width pulses in quantum sensing experiments and apply it to recently proposed dynamical decoupling sequences for accurate spectral interpretation. We first study the origin of these fake resonances and quantify their behavior in a situation that involves the measurement of a classical magnetic field. In particular, we show that a change of the initial phase of the sensor or, equivalently, of the decoupling pulses, leads to oscillations in the spurious signal intensity while the real resonances remain intact. Finally, we extend our results to the quantum regime for the unambiguous detection of remote nuclear spins by utilization of a nitrogen-vacancy center in diamond.

In the process of constructing robust multi-qubit quantum registers, the pairwise coupling of individual systems is a challenging task, further complicated by noise originating from other qubits in the register. We propose to solve this issue with an adiabatic on and off switching of the coupling Hamiltonian. If this is performed according to a Gaussian shape, the coupling between off resonant systems falls off exponentially with their frequency detuning. The idea is motivated via a derivation utilizing first order average Hamiltonian theory and extended to higher orders by employing the adiabatic theorem. We demonstrate that this modulation yields a highly improved rotating wave approximation, that is even valid in a regime where coupling and transition frequency are on the same order. Conversely, this accelerated averaging is accompanied with a speedup in the performance of quantum gates. In order to be able to implement this adiabatic modulation physically, we present a dynamical decoupling sequence that assembles an effective Hamiltonian that mimics the adiabatic modulation. Numerical simulations confirm the validity of that approach and demonstrate high selective addressing and high fidelity quantum gates in the vicinity of a second frequency and furthermore the removal of side oscillations in sensing spectra.

Memory effects in the evolution of an open quantum system represent a long term topic of interest. Here, we investigate, theoretically and experimentally, the nitrogen-vacancy center in diamond as a flexible platform for a systematic exploration of the regime of non-Markovian dynamics. More specifically, we show that the degree of non-Markovianity of the electron spin in the nitrogen-vacancy center can be tuned continuously, where the inherent nitrogen spin serves as a regulator of the imposed dynamics. Our analysis of the collected experimental data is performed employing Bayesian inference methods, allowing to draw conclusions from a minimal data set, while predicting the ability to tune the non-Markovianity continuously.

Publications

Large parts of this thesis are based or taken from different publications. These publications, along with the parts of the thesis where those are contained are listed in the following.

[H1] J. Casanova, Z.-Y. Wang, J. F. Haase and M. B. Plenio.

Robust dynamical decoupling sequences for individual-nuclear-spin addressing.

Phys. Rev. A **92**, 042304 (2015), Preprint: [arXiv:1506.03766](https://arxiv.org/abs/1506.03766)

Copyright (2015) by the American Physical Society

Section 3.3.2

[H2] J. F. Haase, Z.-Y. Wang, J. Casanova and M. B. Plenio.

Pulse-phase control for spectral disambiguation in quantum sensing protocols.

Phys. Rev. A **94**, 032322 (2016), Preprint: [arXiv:1608.00418](https://arxiv.org/abs/1608.00418)

Copyright (2016) by the American Physical Society

Chapter 7, Appendix B.2

[H3] J. F. Haase, A. Smirne, J. Kołodyński, R. Demkowicz-Dobrzański and S. F. Huelga.

Fundamental limits to frequency estimation: a comprehensive microscopic perspective.

New J. Phys. **20**, 053009 (2018), Preprint: [arXiv:1710.04673](https://arxiv.org/abs/1710.04673)

Copyright (2018) by the authors.

Published by IOP Publishing Ltd on behalf of Deutsche Physikalische Gesellschaft

(Published under a Creative Commons Attribution 3.0 License¹: CC BY 3.0)

Sections 1.3 and 1.5, Chapter 5, Appendix A.2

[H4] J. F. Haase, Z.-Y. Wang, J. Casanova and M. B. Plenio.

Soft Quantum Control for Highly Selective Interactions among Joint Quantum Systems.

Phys. Rev. Lett. **121**, 050402 (2018), Preprint: [arXiv:1708.09611](https://arxiv.org/abs/1708.09611)

Copyright (2018) by the American Physical Society

Chapter 8 and Appendix B.3

[H5] J. F. Haase, P. J. Vetter, T. Uden, A. Smirne, J. Rosskopf, B. Naydenov, A. Stacey, F. Jelezko, M. B. Plenio and S. F. Huelga.

Controllable Non-Markovianity for a Spin Qubit in Diamond.

Phys. Rev. Lett. **121**, 060401 (2018), Preprint: [arXiv:1802.00819](https://arxiv.org/abs/1802.00819)

Copyright (2018) by the American Physical Society

Chapter 9

¹<https://creativecommons.org/licenses/by/3.0/>

- [H6] J. F. Haase, A. Smirne, J. Kołodyński, R. Demkowicz-Dobrzański and S. F. Huelga.
Precision Limits in Quantum Metrology with Open Quantum Systems.
[Quantum Measurements and Quantum Metrology](#) **5**, 13 (2018),
Preprint: [arXiv:1807.11882](#)
Copyright (2018) by the authors. Published by De Gruyter. (Published under a Creative Commons Attribution-NonCommercial-NoDerivatives 4.0 License²: CC BY-NC-ND 4.0)
Chapter 4, Section 5.4.1

The following publication is not a direct part of the thesis:

- [H7] Z.-Y. Wang, J. F. Haase, J. Casanova and M. B. Plenio.
Positioning nuclear spins in interacting clusters for quantum technologies and bioimaging.
[Phys. Rev. B](#) **93**, 174104 (2016), Preprint: [arXiv:1510.02811](#)

²<https://creativecommons.org/licenses/by-nc-nd/4.0/>

Acknowledgments

The author list of a PhD thesis is naturally quite minimal, consisting only of a single name. Nevertheless, such a thesis is the product of the interaction with others, fruitful collaborations and enlightening discussions. Certainly, the thesis at hand represents no exception and would never exist in the present form, if it would not have been for the numerous people to whom I devote the following paragraphs.

First of all, I thank **Prof. Dr. Susana F. Huelga** and **Prof. Dr. Martin B. Plenio** for the supervision of this thesis and crucially, allowing me to be part of their group since I started my masters, which is now almost five years ago. Their constant support and advice are of great value for this thesis but go well beyond that. Moreover, their always open doors, encouragements and patience is something that I wish every PhD student could experience. I am highly grateful for the opportunity to attend conferences, workshops and summer schools which allowed me to make new contacts and find friendships all over the world. However, most importantly, I do owe them special thanks for creating this working environment where I could follow my own interests and curiosity, work on fascinating projects and explore captivating new things about physics.

Furthermore, I am grateful for all the effort that **Dr. Jorge Casanova**, **Dr. Andrea Smirne** and **Dr. Zhenyu Wang** have put into assisting me during the developments of this thesis.

Andrea's encyclopedic knowledge of open quantum systems saved me more than once from mispending time in further pursuing erroneous calculations. He always invested a lot of time in answering my, probably often absolutely basic questions. His answers are always detailed and on point, such that one barely has to consider any additional literature; and if so, he already knows the correct reference. I also gladly remember the various discussions on fundamentals and topics apart from the current projects we were working on. In the end, that is what makes physics enjoyable: the discussion of ideas, interpretations and approaches to different topics.

I am also highly thankful to Jorge and Zhenyu. Initially, they invited me to simulate the NV center's dynamics for one of their common works. In the end, the projects which followed are now an integral part of this thesis. Their patience with me, Jorge's fastidious manner to go through my drafts and Zhenyu's inexorable urge to formulate things more general and add further details, in the end also made me rethink my own standards. Their relaxed approach to unforeseen challenges in our work made our collaboration highly enjoyable.

Sometimes, details that seem small at first, turn out to have a great impact on the final product or even change the total course of the work. Here, I want to thank **Dr. Jan Kołodyński**

and **Prof. Dr. Rafał Demkowicz-Dobrzański** for helping with the semidefinite programming and answering questions concerning the general theory of parameter estimation. More than once, they exposed details that I would have otherwise overseen. Furthermore, I thank **Joachim Roskopf** for the fast introduction to the PyMC3 library. Also I am grateful to **Prof. Dr. Fedor Jelezko, Thomas Unden, Philipp J. Vetter** and everybody who contributed to the NV center FID and non-Markovianity measurements.

The thesis itself is a lengthy project and there are numerous eyes that corrected endless typos and grammar issues, but also give helpful input and suggestions on how to improve the manuscript further. Consequently, I want to thank **Alexander Nüßeler, Julen S. Pedernales, Martin Pietsch, Andrea Smirne, Thomas Theurer** and **Zhenyu Wang** for proofreading my drafts. Their careful study greatly improved the quality of the following pages.

Needless to say, the atmosphere at the office is greatly influenced by the people at the Institute of Theoretical Physics. I want to thank all of them, regardless of whether they are still a member of the group or already left to pursue their interests in different groups or industry, for distracting and interesting discussions during lunch and coffee breaks, also on topics apart from physics. Especially, I want to mention **Pelayo Fernández-Acebal**, with whom I had the pleasure to share the office since we both started our stay at the institute. Furthermore, I want to thank my fellow students many of whom I know since I started studying physics in 2009. Some of them also took the route of a PhD and I hope they all soon accomplish their thesis, too. Our Wednesday lunch breaks were always a highlight during the week.

Finally, I want to acknowledge my parents, **Heike** and **Christian**. There is no doubt, I would not have made it to this point or anywhere else, without their constant support, motivation and advice. I know, you always say you won't understand anything that comes beyond this page. However, that is completely irrelevant. Neither did I a few years ago and I still wouldn't if it wasn't for you. That is what counts. Thank you so much for everything.

Jan Friedrich Haase

Contents

Introduction and Overview	1
I. Preliminaries	7
1. A Primer on Open Quantum Systems	9
1.1. Closed versus Open Quantum Systems	9
1.2. Master Equations	12
1.2.1. Time-Convolutionless - Master Equation	14
1.3. Matrix Representation of linear Qubit Maps	16
1.4. Non-Markovianity of Quantum Evolutions	17
1.4.1. A Measure of non-Markovianity	21
1.5. Phase-Covariant versus non-Phase-Covariant Dynamics	23
2. The Nitrogen-Vacancy Center in Diamond	25
2.1. The Level Structure and its Consequences	25
2.1.1. Ground State Spin Dynamics	28
2.1.2. Peculiarities of the Electron Spin Readout	30
2.2. Hamiltonian of the NV Center	31
2.2.1. The NV Center as a Qubit	33
2.2.2. Coherent Quantum Control	34
3. Basic Principles of Dynamical Decoupling	37
3.1. The Filter Function Approach	41
3.2. Effective Hamiltonian Picture	45
3.3. Pulse Sequences	48
3.3.1. CPMG and the XY-Family	50

3.3.2. Adaptive-XY Sequences	52
--	----

II. Noisy Frequency Estimation in the Framework of Quantum Metrology 55

4. Noisy Quantum Metrology:	
Frequency Estimation	57
4.1. Motivation	58
4.2. The Frequency Estimation Protocol - Analyzing a Specific Measurement Procedure	61
4.2.1. The Cramér-Rao Bound	61
4.2.2. Noiseless Estimation with Entangled States - Obtaining Heisenberg Limited Precision	66
4.2.3. The Impact of Noise: Lindbladian Dephasing	67
4.3. Ultimate Precision Limits - Analyzing Arbitrary Quantum Channels, Initial States and Measurements	69
4.3.1. Quantum Fisher Information and Quantum-CRB	70
4.3.2. Achieving Maximal Precision - Bounding the QFI	72
4.3.3. Saturation of the (Quantum-)CRB	75
4.4. Realistic Bounds on the Precision	78
4.4.1. The Zeno-Limit under Phase-Covariant Noise	79
4.4.2. Transversal Noise	81
4.4.3. Arbitrary, non-Phase-Covariant Noise	82
4.4.4. Motivating Toy Model	82
4.5. Remarks	84
4.5.1. The Role of non-Markovianity	84
4.5.2. Precision, Accuracy and Sensitivity	85
4.5.3. Ultimate Precision without Entanglement	88
4.5.4. Geometrical Distance of Quantum States	88
4.6. Beyond the Independent Noise Model: Correlations and Control	90
4.6.1. Correlated Noise and Interacting Probes	90
4.6.2. External Control	92
4.7. Time Dependent Encoding	94

5. Realistic Bounds on the Precision:	
An Analysis Involving a Microscopic Noise Model	97
5.1. Spin-Boson Model: Weak-Coupling Master Equation and Secular Approximation	98
5.1.1. Second-Order TCL-Master Equation	99
5.1.2. Secular Approximation	102
5.2. Solutions in the High-Temperature Regime	104
5.2.1. The Short-Time Evolution	106
5.2.2. Finite-Time Evolution for an Ohmic Spectral Density	107
5.3. Single-Qubit Quantum Fisher Information	110
5.3.1. Short-Time Limit	110
5.3.2. Finite-Time Analysis for the Ohmic Spectral Density	116
5.4. N -Probe Quantum Fisher Information and Achievable Metrological Limits .	118
5.4.1. Asymptotic Scaling of the Ultimate Estimation Precision	119
5.4.2. Finite- N Behavior	122
5.5. Conclusions	124
6. Open Questions in Quantum Metrology	127
 III. Quantum Control	 131
7. Field Detection with Real Pulses	133
7.1. Detection of a Classical AC-Signal	134
7.2. Identifying Spurious Responses	137
7.2.1. A Criteria to Detect Spurious Resonances	141
7.2.2. Effects of Pulse Errors.	141
7.2.3. Remark on Pulse Phases	142
7.3. Detection of a Quantum Signal	142
7.4. Spurious Resonances of Quantized Signal Sources	144
7.4.1. A Scheme for Quantum Emitters	144
7.4.2. Numerical Results in NV-based Schemes	145
7.4.3. Distinguishing Close Peaks	147
7.5. Conclusion	148

8. Soft Control of Quantum Interactions	149
8.1. Generic Model for Temporal Control of Quantum Interactions	151
8.1.1. Leading-Order Effects and Soft Quantum Control	152
8.1.2. Higher-Order Effects and Adiabatic Average Hamiltonian	154
8.2. An Implementation using Dynamical Decoupling	156
8.3. Applications	158
8.3.1. Improving the Rotating Wave Approximation	158
8.3.2. Sensing and Quantum Gates	161
8.4. Conclusions	164
9. Controllable Non-Markovianity for an Electron Spin in Diamond	167
9.1. Introduction to Bayesian Inference	169
9.2. Modeling and Measuring the Sample Dynamics	171
9.2.1. The Role of Correlations and a non-Markovian Evolution	175
9.3. Measuring the Free Induction Decay	177
9.3.1. Bayesian Modeling of Free Induction Decay	179
9.4. Tuning the Non-Markovianity	180
9.4.1. Bayesian Inference Model for Tuneable non-Markovianity	184
9.4.2. Details of the Obtained Posterior Distribution	187
9.5. Conclusions	188
Concluding Remarks - Outlook	191
Bibliography	195
Appendix	227
A. Metrology	229
A.1. Derivation of CRB and FI	229
A.2. Microscopic Model	230
A.2.1. Equivalence with an Engineered Coupling Hamiltonian	230
A.2.2. Derivation of the TCL Master Equation	231
A.2.3. Solutions of the Master Equation in the High Temperature Limit	234
A.2.4. Differential Equations for the Density Matrix Elements in the case of Ohmic Spectral Densities	235
A.2.5. Semigroup Limit of the Ohmic Spectral Density	236

A.2.6. A General Formula for the Single Probe QFI of PC Dynamics	237
A.2.7. Expectation Value of the Parity Operator using GHZ-States	237
B. Quantum Control	239
B.1. Calculation of the Overlap Integral	239
B.2. Signal for an XY-8 Sequence Employing Realistic Pulses	240
B.2.1. Ideal Signal after a single XY-8 Sequence	240
B.2.2. Impact of the Second Order	241
B.3. High Selective Coupling using Soft Quantum Control	242
B.3.1. Adiabatic evolution	242
B.3.2. Calculation of Energy Shifts using the Adiabatic Theory	243
B.3.3. Improved RWA: Two Qubits	244
B.3.4. Continuous Dynamical Decoupling and Hartmann-Hahn Resonance .	245
B.3.5. Variation of the Fourier Coefficients in the Simulations of the Soft Quantum Control	247

Introduction and Overview

Noise, either quantum or classical [1–4], is certainly an ubiquitous and inevitable feature any quantum device striving for technological applications has to deal with [5–9]. It poses additional challenges on our abilities to make accurate statements about parameters we measure [6, 10–13] and decreases the fidelity of operations we perform to manipulate quantum systems [8, 14–16]. On the other hand, the description of quantum noise alone introduced a completely new and exciting field in the study of quantum theory. While noise represents a restrictive factor in many situations encountered experimentally and theoretically, it is nevertheless one of the reasons for the great variety of attempts tackling these restrictions, whether it is to understand fundamental limitations or to push these boundaries via the aid of sophisticated control strategies.

Generally, the action of noise is by no means a vacuous process but possesses distinctive features [2–4]. For instance, it may exhibit temporal correlations and, in fact, all results in this thesis are in one way or the other connected to this key characteristic. In frequency space, temporally uncorrelated noise yields a flat spectrum [17], while temporal correlations yield a variety of pronounced spectral features. Therefore widely denoted as *colored noise*, the occurrence of temporal correlations allows the derivation and development of various fascinating results which have often proven to be advantageous when compared to uncorrelated *white noise*.

A paradigmatic situation is encountered in the field of quantum metrology. Here, colored noise is observed to be less harmful when compared to white noise [18, 19]. On the other hand, the motivation to develop physical architectures for widespread applications relies on the distinct spectral features colored noise provides. Crucially, the recognition of special patterns in the noise spectrum allows the accurate discrimination of individual constituents assembling the environment as it is done in sensing applications [9, 13]. At the same time, it offers the possibility to employ the environmental subsystems responsible for those features in quantum information [14, 20], computation [21, 22] and simulation tasks [23, 24].

In this thesis, we address the analysis of fundamental restrictions in quantum metrology

(Chapters 4 and 5), but also provide instruments to detect (Chapter 7), circumvent, employ (Chapter 8) and explore (Chapter 9) the impact of noise in different scenarios.

The field of metrology discusses the achievable precision of protocols aimed to estimate the value of a chosen parameter [18, 19, 25, 26]. Any protocol operating at the quantum level evermore suffers from the fact that quantum mechanics is a probabilistic theory, which naturally sets a lower bound on the achievable precision [27–30]. Importantly, this limit is less restrictive when quantum resources, such as entanglement, are included into the protocol [31–33]. On the other hand, this quantum improvement is extremely fragile under the impact of noise and easily lost [34, 35]. Nevertheless, it is known that colored noise is able to maintain at least part of the advantage that quantum features provide over classical strategies [36–39]. Here, we approach the scenario of frequency estimation, where one considers qubit-like probes in a Ramsey-type protocol to sense an external field that affects their energy splitting in a linear fashion. To obtain a maximized precision, one optimizes the three stages of the protocol, preparation of the initial state, encoding time and employed measurement [40–43]. We present an in-depth study of the ultimate attainable precision under the impact of noise that is acting during the encoding stage and originating from uncoupled harmonic oscillators, i.e., we employ the spin-boson model [44]. Previous studies in this field have shown that the achievable precision is highly sensitive to the chosen noise regime [34, 37, 39, 45, 46]. We distinguish two main situations, the one being called *non-phase-covariant noise*, which conversely describes all regimes which do not fulfill the condition of *phase-covariance* [47–49]. The latter is characterized by the commutativity of the frequency encoding and the noise, that is, all terms describing the dynamics due to the noise commute with the encoding Hamiltonian. Crucially, as we are going to clarify, such a regime is always guaranteed by the secular approximation [50]. Using a single probe, we show that the inclusion of non-phase-covariant terms can significantly increase the precision, while being detrimental in other situations. Moreover, we point out that the frequency dependence of the noise terms, i.e., the rates appearing in a quantum master equation, generally contains relevant information improving the precision. Nevertheless, this assertion does not hold for all spectral densities used to describe the spin-bath coupling. In particular, a so called *Ohmic* spectral density does not imply these dependencies. However, usually the dependencies of the rates are either neglected or unclear due to the lack of a microscopic model. The master equations are then postulated, together with their phenomenological rates, whose purpose is to mimic the (experimentally) observed dynamics in a small range of parameters.

We further perform an analysis of the scaling of the precision, when N probes are used in parallel. Here, the ultimate limit is given by the so called *Heisenberg Limit*, $1/N^2$, which is substantially more favorable but under the impact of noise immediately decays to the standard

quantum limit, $1/N$ [19]. That is particularly unfortunate, since the latter is achievable by classical strategies as well. A recent work however showed that, as long as the noise is colored and phase-covariant, the precision is asymptotically bounded by the Zeno-Limit $1/N^{3/2}$ [39]. We study an analogous situation employing the microscopic spin-boson model characterized by an Ohmic spectral density. Including non-phase-covariant terms, we demonstrate numerically that this limit is universal for any dynamics altered by colored noise, except the situation where the action of the noise is completely transversal to the encoding of the parameter. The latter is a special case, where we observe the emergence of a novel scaling of $1/N^{7/4}$, which is the greatest scaling observed so far under noisy conditions. Furthermore, applying the right approximations and choosing appropriate model parameters, we reproduce all the so far disconnected situations encountered in the literature, providing a thorough and comprehensive study of the ultimate achievable precision from a vivid microscopic perspective.

The devices one aims to implement for quantum technologies pose very specific requirements on the physical quantum system itself. In many cases, the total system is in fact a conglomerate of many constituents, while one specific part represents a "hub" which is utilized to selectively interact with a chosen constituent of the remaining "resource" system. Transferring this abstract concept to sensing applications, the hub assembles the quantum sensor which interacts, for example with a molecule from whom one aims to determine its chemical composition and spacial structure [5, 9, 13, 51–53]. On the other hand, when constructing a quantum register, the hub serves as a control unit that one desires to interact selectively with individual building blocks of the register, to either utilize them as a memory [54, 55] or for quantum simulation, communication and information tasks [23, 56–58]. Importantly, it is necessary that gates applied to manipulate one of the target systems do not alter the state of other constituents [22, 59].

Crucially, both applications are very well connected in the sense that they require the individual and high selective addressing of single frequencies in the colored spectrum assembled by the resource system. In the first case, the desired information about the molecule is encoded into the different features of the spectrum, while in the second case distinct peaks indicate the target frequencies of transitions where information can be stored in the register. The ability to sense and control different constituents in an interacting cluster of quantum systems is hence an inevitable prerequisite in a manifold of technological applications.

Nevertheless, whether proposed methods are indeed functional is an obvious question one has to address. In this thesis, we choose the nitrogen-vacancy center in diamond [60, 61] as the working platform for the control methods we are describing. Due to its excellent properties concerning experimental effort necessary for preparation, readout and manipulation, its long

coherence and relaxation times, this atom-like defect has qualified itself as one of the most promising candidates to assemble a robust qubit required for the applications mentioned above. It furthermore assembles the hub to access the even more robust nuclear spin qubits which naturally appear in diamond [16, 62, 63, H7].

A standard technique providing individual addressing is dynamical decoupling [64–66], the working horse of current quantum sensing experiments and well suited for the isolation of a sought-after signal out of the noisy fog [67–70, H1, H7]. Naturally, realistic implementations of pulsed dynamical decoupling sequences suffer under drawbacks induced by experimental limitations. In order to reduce these limitations, imperfections in the control pulses such as amplitude and detuning errors, are counteracted by a sophisticated design of the employed pulse sequence where the pulse phases follow an ingenious pattern [71–73]. These try to refocus appearing pulse errors, such that they average out periodically when a specific number of pulses is applied. Here, we approach the issue that these pulse sequences can lead to spurious responses [74] when the controlled system is employed as a spectrometer.³ More specifically, we first study the detection of a classical oscillating field and show that these spurious responses appear at even integer multiples of the true responses. Thereby we make the crucial observation that a spurious response is easily identified by modulating the phase of the sensor’s initial state, or equivalently, the phase of the applied pulse sequence. We prove analytically that the amplitude of a spurious response is highly sensitive to changes in these phases, while real resonances are basically unaffected. Hence we provide an effortless and quick criterion to expel doubtful parts of a recorded spectral response. The validity of the analytic calculations is then finally verified and illustrated with numerical simulations of the employed sensing protocols in realistic situations where we employ the nitrogen-vacancy center as a quantum sensor.

Indeed, the task of generating a selective coupling between two quantum systems of choice is generally a challenge, even for advanced dynamical decoupling sequences. The crucial

³ At this point one should mention the impressive success story of *nuclear magnetic resonance* (NMR), since many of the concepts enabling recent results on spectroscopy of, e.g., single molecules [51–53] are derived from this essential discovery. In 1938, Rabi et. al. laid the fundamentals to the field with “*A new method of measuring nuclear magnetic moment*” [75]. Shortly after, Purcell observed “*Resonance Absorption by Nuclear Magnetic Moments in a Solid*” (which was paraffin) in 1946 [76]. The same year, Bloch published “*The Nuclear Induction Experiment*” [77], where he describes his experimental arrangement to measure “the signals from protons contained in a variety of substances”. Rabi was awarded the Physics Nobel Prize in 1944, Purcell and Bloch shared the prize in 1952. Since then, the field evolved fruitfully, yielding magnetic resonance of molecules and electrons [78] (Ramsey, Physics Nobel Prize 1989), methods to resolve the three-dimensional structure of proteins (Wüthrich, Chemistry Nobel Prize 2002) and finally magnetic resonance imaging, where the 2003 Medicine Nobel Prize was awarded to Lauterbur and Mansfield.

bottleneck is determined by the frequency detuning of the transitions one aims to couple selectively. For all standard techniques, the coupling between these transitions exhibits a power-law dependence, i.e., it decreases slowly since the coupling strength is inversely proportional to the detuning. Hence, in a system where the transition frequencies are densely distributed, individual addressing is strongly aggravated.

We put forward the idea of *soft quantum control* and propose to solve this issue with an adiabatic on and off switching of the coupling Hamiltonian. If this is performed according to a Gaussian shape, the coupling between off resonant systems falls off exponentially with their detuning. We motivate this idea via a derivation utilizing first order average Hamiltonian theory [79] and explicitly show the exponential improvement in the individual addressing. Furthermore, by employing the adiabatic theorem [80], we develop a theory which also includes higher order corrections and we subsequently present two applications. The first one is a highly improved rotating wave approximation that is even valid in the strong coupling regime where coupling and transition frequency are of the same order of magnitude. This enables the execution of gates with a much improved fidelity. Conversely, the accelerated averaging is accompanied with a decrease of the required time in case the coupling is weaker. In order to be able to implement this adiabatic modulation physically, we present a modified dynamical decoupling sequence that assembles an effective Hamiltonian mimicking the desired evolution. Numerical simulations confirm the validity of that approach and demonstrate high selective addressing of spins whose resonance frequencies are separated by only 4.4 kHz. Additionally, the demonstrated capability of individual addressing is also shown to enable high fidelity quantum gates. An interesting and important aspect is furthermore the removal of side oscillations in sensing spectra, where the usual sinc-form [81] of a peak is replaced by a Gaussian shape. This aspect contributes to an unambiguous identification of peaks, especially if the obtained spectra are dense.

This thesis closes with the experimental and theoretical investigation of a convenient system allowing to tailor memory effects in the noise itself. The appearance of these memory effects is associated with a dynamics that is non-Markovian [82–84]. This class of dynamics is generating broad interest, especially since it has been shown that a system’s memory of the past is advantageous in a manifold of applications [85–91]. Furthermore, it is important to understand the impact of different characteristics of noise when exploiting nanoscale systems for quantum technologies, since they always alter the dynamics and hence suitable countermeasures need to be designed [92]. Platforms that provide non-Markovian dynamics for a detailed investigation of the associated effects in the desired applications are rarely available. Besides allowing memory effects, such a platform should also provide the possibility to remove the latter to enable comparable studies. The controlled creation of non-Markovian dynamics has been

accomplished in optical systems [93–99] and ion traps [100]. Here, we present the electron spin of a nitrogen-vacancy center as a solid state system with tuneable non-Markovianity. The inherent nitrogen spin of the color center naturally interacts with the electron spin [101] and can hence serve as an intrinsic regulator of the degree of non-Markovianity [102, 103]. In fact, the degree is fully controllable, from completely Markovian up to some maximum value of the chosen non-Markovianity measure. Crucially, our system does not require intervening during the evolution, since the non-Markovianity is only defined by the initial preparation of the nitrogen nuclear spin. Hence, the evolution is completely determined by the quantum nature of the two subsystems, including back action. Furthermore, since no control during the evolution is required, this time can be employed completely for the study of non-Markovian effects, e.g., in a simulator, under the effect of pulse sequences or in a sensor. The conducted experiment is divided into two parts. In the first part, we characterize the environment around the nitrogen-vacancy center to exclude any uncontrollable non-Markovian effects. In the second step, we show that the degree of non-Markovianity is fully controllable. To analyze the data, we employ a method based on Bayesian inference [104–106]. To do so, we develop a cohesive model, that takes not only the theoretical details, but also the experimental peculiarities into account, such as the different read-out contrast that is determined by the nuclear spin state of the nitrogen.

The thesis at hand is divided into three main parts. In Part I, we introduce auxiliary preliminaries from the theory of open quantum systems (Chapter 1), the nitrogen-vacancy center in diamond (Chapter 2) and give a short introduction to dynamical decoupling (Chapter 3). Following is Part II which starts with an overview of recent results derived in the context of quantum frequency estimation in Chapter 4. Subsequently, we introduce the microscopic model in Chapter 5 and analyze the restrictions it imposes on the estimation precision. All results concerned with quantum control are contained in Part III. Here, we propose an easy criterion to detect spurious resonances in sensing spectra in Chapter 7, introduce the soft quantum control method for high fidelity quantum gates in Chapter 8 and lastly, present the nitrogen-vacancy center as a flexible platform to explore non-Markovian effects in Chapter 9.

Part I.

Preliminaries

CHAPTER 1

A Primer on Open Quantum Systems

The theory of open quantum systems is an essential field in quantum mechanics. The secure and well behaved world of closed quantum systems¹ is always obliterated when the system is taken from the paper and transferred into the lab. Not only do we have to adapt results derived for closed systems due to the interaction with the surrounding environment, but the whole theory necessary to describe the different types of dynamics observed becomes richer, e.g., modifications of the fundamental Schrödinger equation to include environmental effects is already a complex field on its own.

This section aims to address the concepts, tools and characterizations required for the work at hand. For detailed in-depth study of the topic, the reader is referred to the books and reviews at the references [1–4, 14, 82, 83].

1.1. Closed versus Open Quantum Systems

The initial state of a closed system $\rho_S(t_0) \equiv \rho_0$ evolves according to the unitary operator U governed by the associated Hermitian Hamiltonian H_S in the Hilbert space \mathcal{H}_S of the closed system. For the sake of simplicity, the Hamiltonian is considered time independent during this section. The solution of the Schrödinger equation of motion is then immediately given by (from now on we set $\hbar = 1$)

$$\rho(t) = U(t - t_0) \rho_0 U^\dagger(t - t_0) = e^{-i(t-t_0)H_S} \rho_0 e^{i(t-t_0)H_S}. \quad (1.1)$$

¹Whether one might speak of "well behaved" when having quantum theory in mind is already a philosophical question itself, going well beyond the scope of this work. However, it is just that dissent from our everyday experiences in the "classical" world which renders the properties of quantum mechanics fascinating.

Crucially, due to the cyclic properties of the trace, this structure preserves the purity of the system [14], i.e. $\text{tr} [\rho(t)^2]$ is conserved and furthermore equal to one for pure states².

However, in realistic scenarios, the system of interest is in contact with an environment, which unavoidably alters the evolution of the system. Usually this leads to decoherence and relaxation processes, i.e. a decay of coherences and populations respectively³. In such a case, the system is referred to as an *open (quantum) system*. To obtain a description of the open system, one modifies the Hamiltonian in a way such that it contains the free Hamiltonian of the environment H_E (often also called *bath*) and a Hamiltonian H_{int} introducing the coupling terms, leading to

$$H = H_S \otimes \mathbb{1}_E + \mathbb{1}_S \otimes H_E + H_{\text{int}}, \quad (1.2)$$

where $\mathbb{1}_S$ and $\mathbb{1}_E$ are identity operators on the specific spaces to lift the operators of different subspaces into the extended Hilbert space $\mathcal{H}_{S+E} = \mathcal{H}_S \otimes \mathcal{H}_E$. From now on, we will implicitly assume the tensor product with the identity and neglect it for brevity.

The open system and the environment form a closed system whose dynamics is governed by the unitary operator corresponding to the Hamiltonian H , starting from the total initial state $\rho_{SE}(0)$. The state of the open system is obtained via the partial trace over the environmental degrees of freedom [2, 4], i.e.

$$\rho(t) = \text{tr}_E \left[U_{SE}(t - t_0) \rho_{SE}(t_0) U_{SE}^\dagger(t - t_0) \right] = \text{tr}_E \left[e^{-i(t-t_0)H_{SE}} \rho_{SE}(t_0) e^{i(t-t_0)H_{SE}} \right]. \quad (1.3)$$

Usually the explicit form of the unitary operators $U_{SE}(t - t_0)$ escapes our access due to the sheer size of the environment, or technical restrictions which forbid its observation during an experiment. From a different point of view, the structure of the specific environment and therefore the Hamiltonians H_E and H_{int} are often not known exactly. In such cases, one introduces a model which mimics the dynamics observed in experiments, e.g. the spin-boson model [44] as we will do later in this work. A further hurdle is the choice of an initial state for the combined system. Specifically, the state of the environment $\rho_E(t_0) = \text{tr}_S [\rho_{SE}(t_0)]$ is not known in general, while in an even more complex case $\rho_{SE}(t_0)$ can carry correlations between the open system and the environment.

The disregarding of the latter case, i.e. assuming the initial state to be a product such that $\rho_{SE}(t_0) = \rho_0 \otimes \rho_E(t_0)$, allows for the derivation of powerful equations of motion for the state

²Pure states are the states fully described by a vector $|\psi\rangle$ in the corresponding Hilbert space, while an arbitrary state is represented by a convex mixture of those, i.e. $\rho = \sum_i p_i |\psi_i\rangle\langle\psi_i|$ with $\sum_i p_i = 1$ and all $p_i \geq 0$.

³Here we consider finite dimensional open systems, where the coherence elements are given by the off-diagonal elements of $\rho(t)$, while the populations are fixed by the diagonal elements. Also note that coherence is a basis dependent property, e.g. no coherence is present in the basis diagonalizing $\rho(t)$ [107].

of the open system and it is realistic for several settings. These equations are so called quantum master equations, and we will review them in Section 1.2.1. Furthermore, uncorrelated initial states enable us to identify an analogous relation to Eq. (1.1),

$$\rho(t) = \Lambda_{t \leftarrow t_0} [\rho_0] = \sum_{r=1}^R K_r(t, t_0) \rho_0 K_r^\dagger(t, t_0). \quad (1.4)$$

Here $\Lambda_{t \leftarrow t_0}$ is a so called *dynamical map* [4] or *quantum channel* [14] evolving the state of the open system from time t_0 to t . We already stress that the notion of the two time points, t_0 and t , is important as the successive application of the same dynamical map is not correct in general (see also Section 1.4). For the second equality we used the *Kraus-representation* of $\Lambda_{t \leftarrow t_0}$, invoking the Kraus operators $K_r(t, t_0)$ fulfilling $\sum_{r=1}^R K_r^\dagger(t, t_0) K_r(t, t_0) = \mathbb{1}$ which guarantees the preservation of the trace of ρ_0 . Here, $R \leq (\dim \rho)^2$ is the so called *rank* of the evolution. It is important to stress that this representation exists iff the dynamical map $\Lambda_{t \leftarrow t_0}$ is *completely positive* (CP) [14, 108, 109]. That is, for $\Lambda_{t \leftarrow t_0}$ acting on a space of dimension d it has to hold that

$$(\Lambda_{t \leftarrow t_0} \otimes \mathbb{I}_D) [\Pi] \geq 0 \quad \text{for any } \Pi \geq 0, \quad (1.5)$$

where \mathbb{I}_D is the identity map on an extending Hilbert space of dimension $d \geq D$ and Π is an arbitrary, positive-semidefinite operator on the extended space [82]. A weaker criteria is the *positivity* (P) of the map, i.e. the criteria in Eq. (1.5) has to hold only for $D = 1$. However, this is often considered as insufficient since a positive map does not necessarily preserve the positivity of an extended system. Such situation naturally appears when the open system is entangled with another quantum system. Furthermore, any dynamical map is required to preserve hermiticity, i.e. $\Lambda_{t \leftarrow t_0}[\rho]^\dagger = \Lambda_{t \leftarrow t_0}[\rho^\dagger]$ and the trace, i.e. $\text{tr} [\Lambda_{t \leftarrow t_0}[\rho]] = \text{tr} [\rho]$. A map following all of these requirements for $D = 1$ is called *positive and trace preserving* (PTP). Such a map actually represents a physical evolution, i.e. it maps density operators to density operators. However, as mentioned, one conveniently demands the stronger characterization and requires the map to be *completely positive and trace preserving* (CPTP) as this allows the arbitrary extension of the Hilbert space⁴, e.g. by additional ancillas. Nevertheless, is worth mentioning that the characterization of CPTP maps is less involved than the one of PTP maps. For CPTP maps, CP is directly certified via the positivity of the Choi matrix or rather the Choi-Jamiołkowski-isomorphism [108, 109].

⁴Note that these requirements are trivially fulfilled for the dynamical map generating a unitary evolution, i.e. $\Lambda_{t \leftarrow t_0}[\rho_0] = \Lambda_{t-t_0}[\rho_0] = U(t-t_0) \rho(t_0) U^\dagger(t-t_0)$.

1.2. Master Equations

A quantum *master equation* (ME) is a differential equation dictating the evolution of an open quantum system. The key result leading to the commonly known structure of a time-local⁵ ME is the famous theorem by Gorini, Kossakowski, Sudarshan [110] and independently proven by Lindblad [111]. The theorem tells the following:

For any evolution that can be described via a family of Kraus operators

$$\rho(t) = \Lambda_{t \leftarrow t_1} [\rho(t_1)] = \sum_{r=1}^R K_r(t, t_1) \rho_1 K_r^\dagger(t, t_1), \quad (1.6)$$

valid for any couple of times t and t_1 with $t \geq t_1 \geq t_0$, the time-local generator $\mathcal{L}(t)[\bullet]$ of the corresponding ME is of the form

$$\begin{aligned} \frac{d}{dt} \rho(t) &= \mathcal{L}(t) [\rho(t)] \\ &= -i [H(t), \rho(t)] + \sum_{r=1}^{d^2-1} \gamma_r(t) \left[V_r(t) \rho(t) V_r(t)^\dagger - \frac{1}{2} \{V_r(t)^\dagger V_r(t), \rho(t)\} \right]. \end{aligned} \quad (1.7)$$

Here, $d = \dim[\rho(t)]$, $\gamma_r(t)$ are possibly time dependent but positive *decay rates*, and we have possibly time dependent operators $V_r(t)$ and $H(t)$ where the latter is furthermore self-adjoint.⁶ Additionally we have the anti-commutator $\{A, B\} = AB + BA$.

In contrast to Eq. (1.4), the family of Kraus operators characterized here holds for any combination of $t \geq t_1 \geq t_0$ and is not restricted to a fixed combination t_0 and $t \geq t_0$. Consequently, all of those maps fulfill the *composition law*

$$\Lambda_{t_3 \leftarrow t_1} = \Lambda_{t_3 \leftarrow t_2} \circ \Lambda_{t_2 \leftarrow t_1} \quad \forall t_3 \geq t_2 \geq t_1 \geq t_0. \quad (1.8)$$

Importantly, each of these maps Λ is CP. This composition manifests an crucial property of the evolution which is called *CP-divisibility* [82]. In Section 1.4 we will see that, in general, CP-divisibility cannot be taken for granted in the evolution of open quantum systems. Note, also if CP-divisibility does not hold, one will be able to write the ME in the form of Eq. (1.7) but, in this case, the coefficients $\gamma_r(t)$ may take also negative values.

⁵The evolution of $\rho(t)$ only depends on the state of the system at the current time point specified by t and is independent of the previous history. Crucially, this is not equivalent to the definition of quantum Markovianity which will be defined in Section 1.4.

⁶Note that the original works considered only time independent generators, a proof for time dependent generators can be found in [4]

A special case of the composition law is encountered when the generator $\mathcal{L}(t) \equiv \mathcal{L}$ is time independent. The ME in (1.7) is then usually called *Lindblad equation* and its solution is then formally given by

$$\rho(t) = e^{(t-t_1)\mathcal{L}}\rho(t_1), \quad \forall t \geq t_1 \geq t_0, \quad (1.9)$$

where the corresponding maps hence form a so called *semigroup*. Crucially, the maps belonging to that semigroup only depend on the length of the evolved time interval, $\Lambda_{t_2 \leftarrow t_1} = \Lambda_{t_2-t_1}$, and the composition law 1.8 is reduced to [4, 82]

$$\Lambda_{t_2+t_1} = \Lambda_{t_2} \circ \Lambda_{t_1} \quad \forall t_1, t_2 \geq 0, \quad (1.10)$$

which is the *semigroup composition law*. We remark that $\Lambda_0 = \mathbb{I}$ represents the identity map. Commonly a master equation is divided into two parts: first a unitary evolution governed by the commutator of the state and the Hamiltonian $H(t)$, and second a part which is called the dissipator $\mathcal{D}(t)$. The latter captures the non-unitary influence of the environment onto the open system and one writes

$$\frac{d}{dt}\rho(t) = \mathcal{L}(t) [\rho(t)] = -i[H(t), \rho(t)] + \mathcal{D}(t) [\rho(t)]. \quad (1.11)$$

Formally, any time-local generator is related to the corresponding dynamical map by the *Dyson expansion*,

$$\Lambda_{t \leftarrow t_0} = T_{\leftarrow} e^{\int_{t_0}^t d\tau \mathcal{L}(\tau)} = \sum_{k=0}^{\infty} \int_{t_0}^t dt_1 \int_{t_0}^{t_1} dt_2 \dots \int_{t_0}^{t_{k-1}} dt_k \mathcal{L}(t_1) \dots \mathcal{L}(t_k), \quad (1.12)$$

where T_{\leftarrow} is the chronological time-ordering operator. The dynamical map obtained by solving the master equation is by no means guaranteed to be positive or even completely positive when the Dyson expansion is used and only the first $K \geq 0$ terms of the series are considered. Then one has to pay particular care, e.g., P or CP may then be violated at longer evolution times.

This is a rather axiomatic approach to the evolution of open quantum systems, which is very useful to characterize the properties of the dynamics. In particular all conditions for CP, trace and hermiticity preservation are sufficiently fulfilled when the ME is of the form given in Eq. (1.7), while the latter two even hold if the rates $\gamma_r(t)$ are not positive for all times [4]. These characterizations come in handy when one derives the dynamics of an open system from a microscopic model, as we are in Chapter 5. Hence, in the next section we will approach further peculiarities one has to take into account.

1.2.1. Time-Convolutionless - Master Equation

To derive a closed form of the master equation ruling the evolution of an open system subject to the noise fixed by the Hamiltonian in Eq. (1.2), we may exploit a perturbative approach, assuming that the system is weakly coupled to the environment. In particular, this approach yields the *time-convolutionless* (TCL) master equation [2, 112], which has the form of an infinite series ordered by powers of an overall coupling constant. Including terms up to the second order, its general form in the interaction picture is given by (denoting as $\tilde{\rho}(t)$ the open system state in the interaction picture with respect to $H_S + H_E$)

$$\frac{d\tilde{\rho}(t)}{dt} = - \int_{t_0}^t d\tau \operatorname{tr}_E [[H_{\text{int}}(t), [H_{\text{int}}(\tau), \tilde{\rho}(t) \otimes \rho_E]]], \quad (1.13)$$

where $H_{\text{int}}(t)$ is the interaction Hamiltonian H_{int} in the interaction picture. We stress that during the derivation of this equation, no approximations other than the weak coupling assumption have to be employed. The separable form of the total quantum state $\rho(t) \otimes \rho_E$ is a direct consequence when employing the Nakajima-Zwanzig projection operator technique [113, 114], while the equation is local in time due to the expansion of the integral kernel in the time-convolutionless approach. Let us remark that, usually, the separable system-bath state is artificially introduced by performing the Born approximation [2]. It is assumed that the bath is much larger than the system (i.e. the absolute number of states is larger) and hence the total bath state is not changed. Time-locality is introduced by artificially changing the time argument in the system state⁷ to t . One should note that there is no physical reason why this replacement would be justified separately from the *Markov approximation* that is invoked subsequently. Under the premise that all functions corresponding to the evolution of the environment⁸ in Eq. (1.13) decay on a much faster timescale than the one relevant for a change in $\tilde{\rho}(t)$, one extends the upper bound of the integral to infinity. In other words, one assumes that the integrand is effectively zero for all times but the current one. This introduces an effectively "coarse-grained" timescale [2] where all the dynamics of the environment is expiring during short intervals we are not able to resolve. Importantly, one has to keep in mind that the ME is an effective description of the open system dynamics, and $\rho(t) \otimes \rho_E$ should not be confused with the true physical state of the total system [115].

The interaction Hamiltonian can always be brought into the form of a sum of product operators,

⁷Note that in Eq. (1.13) the time argument of $\tilde{\rho}$ would be τ if the derivation would not have been carried out using the TCL approach, see e.g. [2].

⁸These are the correlation functions of the environment. One assumes that these are essentially delta peaked, i.e. the environment carries no memory. Hence the name *Markov approximation*. However, the latter is not necessary to obtain a Markovian evolution of a quantum system as we discuss in Section 1.4.

$H_{\text{int}} = \sum_{\alpha} S_{\alpha} \otimes E_{\alpha}$ with S_{α} (E_{α}) being operators acting on the open system (environment). Using the weak coupling assumption [i.e. the time-convolutionless expansion to the second order given in Eq. (1.13)] the master equation can be brought into the practical form of Eq. (1.7). We now specify it in the Schrödinger picture, where it reads

$$\frac{d}{dt}\rho(t) = -i [H'_S(t), \rho(t)] + \sum_{r=1}^{d^2-1} \gamma_r(t) \left[V_r(t) \rho(t) V_r(t)^{\dagger} - \frac{1}{2} \{V_r(t)^{\dagger} V_r(t), \rho(t)\} \right]. \quad (1.14)$$

The Hamiltonian $H'_S(t)$ is the sum of the open system's free Hamiltonian and an additional Lamb shift contribution which can depend on time, $H'_S(t) = H_S + H_{LS}(t)$. We stress that the decay rates $\gamma_r(t)$ are now not guaranteed to be positive, i.e. they may take negative values for limited time intervals or even for the complete evolution. As mentioned above, $\gamma_r(t) \geq 0 \forall t, r$ iff the evolution is CP-divisible [82] and consequently the dynamical maps possesses a representation via Kraus operators, Eq. (1.6). For rates $\gamma_r(t) < 0$ at some arbitrary time, the CP-divisibility is broken and even the CP of the map $\Lambda_{t \leftarrow t_0}$ is not necessarily warranted, therefore one has to resort to the Choi-Jamiołkowski-isomorphism to verify CP.

Nevertheless, the just mentioned Markov approximation in combination with the *secular approximation* ensure that the resulting ME induces a CP dynamics. The secular approximation neglects terms in the ME which oscillate sufficiently fast such that they are averaged out during the timescale on which the open system decays (see Section 5.1.2 for an example). More specifically, these approximation induce the semigroup dynamics, i.e. we have the Lindblad ME

$$\frac{d}{dt}\rho(t) = -i [H'_S, \rho(t)] + \sum_{r=1}^{d^2-1} \gamma_r \left[V_r \rho(t) V_r^{\dagger} - \frac{1}{2} \{V_r^{\dagger} V_r, \rho(t)\} \right], \quad (1.15)$$

where the solutions are given by Eq. (1.9). To that end, note that the secular approximation is not a necessary but (along with the Markov approximation) a sufficient condition to obtain a semigroup dynamics, see for example the derivation of a semigroup limit in Appendix A.2.6 for the microscopic model in Section 5.2.2.

1.3. Matrix Representation of linear Qubit Maps

This section has been first published in [H3] and, in large parts, has been taken from there.

The transformations introduced by some dynamical maps can appear to be quite complex and unintuitive. Moreover, as we will see later, different types of transformations can substantially alter the results obtained in frequency estimation tasks. Here we provide a geometric representation of the dynamical map which will allow us to build some intuition on the dynamics introduced. Note that due to the dimension of systems with more than two levels, the illustrative representation we are going to discuss here and in Section 1.5 only exists for qubits, however the technical aspect of the result can be generalized easily.

We use a representation of qubit quantum channels, which relies on the Hilbert-Schmidt scalar product on the Hilbert space of the linear operators on finite-dimensional Hilbert spaces, and which is directly linked to the action of the channels on the Bloch sphere. For further details the reader is referred to [116–122].

Recall that the Hilbert-Schmidt scalar product among two linear operators ξ and χ is defined as

$$\langle \xi, \chi \rangle = \text{tr} [\xi^\dagger \chi]. \quad (1.16)$$

Hence, given the orthonormal basis of operators $\{\tau_\alpha\}_{\alpha=0,\dots,3} = \{\mathbb{1}/\sqrt{2}, \sigma^j/\sqrt{2}\}_{j=x,y,z}$ acting on \mathbb{C}^2 , with σ^j the Pauli matrices, any qubit state ρ can be represented as

$$\rho = \sum_{\alpha=0}^3 \langle \tau_\alpha, \rho \rangle \tau_\alpha = \frac{1}{2} (\mathbb{1} + \vec{r} \cdot \vec{\sigma}). \quad (1.17)$$

Here, $\vec{\sigma}$ is the vector of Pauli matrices and \vec{r} is the Bloch vector associated with the state ρ , which has components $r_j = \text{tr} [\sigma^j \rho]$ for $j = x, y, z$ and must fulfill $|\vec{r}| \leq 1$ to guarantee positivity. As well-known, any qubit state is in one-to-one correspondence with a vector inside of a unit sphere centered at the origin, i.e., the *Bloch sphere*.

In the same way, any linear map Ξ acting on the qubit operators can be represented as a 4×4 matrix by means of the relation

$$\Xi[\rho] = \sum_{\alpha\beta=0}^3 D_{\alpha\beta}^\Xi \langle \tau_\beta, \rho \rangle \tau_\alpha \quad D_{\alpha\beta}^\Xi = \langle \tau_\alpha, \Xi[\tau_\beta] \rangle. \quad (1.18)$$

Thus, given the CPTP dynamical map Λ , the most general form of the matrix D^Λ associated with it reads

$$D^\Lambda = \begin{pmatrix} 1 & \vec{0}^T \\ \vec{v} & V \end{pmatrix}, \quad (1.19)$$

where \vec{v} is a real 3 dimensional column-vector, $\vec{0}^T$ is a 3 dimensional row-vector of zeros and V a real 3-by-3 matrix. The first row guarantees the preservation of the trace, the real coefficients guarantee the Hermiticity preservation, while the general conditions for the CP can be found in reference [116]. Using Eqns. (1.17-1.19), one can easily see that the action of the dynamical map Λ on a state ρ associated with a Bloch vector \vec{r} simply corresponds to the affine transformation

$$\vec{r} \longrightarrow \vec{v} + V\vec{r}, \quad (1.20)$$

where \vec{v} describes translations of the Bloch sphere, while V describes rotations, reflections and contractions. The latter point can be shown via the singular value decomposition, which allows us to write the 3×3 real matrix V as [116]

$$V = R_{n_1}^{\varphi_1} D R_{n_2}^{\varphi_2}, \quad (1.21)$$

where $R_{n_1}^{\varphi_1}$ and $R_{n_2}^{\varphi_2}$ are two rotation matrices, about the axis \hat{n}_k by the angle φ_k for $k = 1, 2$, while D is a diagonal matrix $D = \text{diag}\{d_x, d_y, d_z\}$. Then $|d_j|$ describes the contraction along the j -axis ($|d_j| \leq 1$ to guarantee the positivity of the dynamics), and $d_j < 0$ implies a reflection with respect to the plane perpendicular to the j -axis.

1.4. Non-Markovianity of Quantum Evolutions

To date, even the fundamentals of non-Markovianity in quantum evolutions are still a frequently addressed problem, lacking a unified and commonly accepted definition [84]. This surely originates in the fact that a straightforward definition in analogy to the conditional probabilities of a classical stochastic process is not possible [82].

Consider a stochastic process fixed by a random variable $X(t)$ at time t . For the sake of simplicity, we assume $X(t)$ to be discrete, i.e. at each time t_n it takes a value x_n which is chosen from a discrete set $\{x_n^{(m)}\}_{m \in \mathbb{N}}$. The stochastic process is a *Markov process* if the probability for $X(t)$ to take the value x_n at t_n conditioned on the previous history is only determined by

the value x_{n-1} at t_{n-1} , i.e. earlier values at $t < t_{n-1}$ have no influence. Mathematically, we formulate this in terms of conditional probabilities,

$$\begin{aligned} P(x_n, t_n | x_{n-1}, t_{n-1}; x_{n-2}, t_{n-2}; \dots; x_0, t_0) &= P(x_n, t_n | x_{n-1}, t_{n-1}) \\ \text{for all } t_n \geq t_{n-1} \geq t_{n-2} \geq \dots \geq t_0 \quad &\text{and} \\ \text{for all } x_0, x_1, x_2, \dots, x_n. \end{aligned} \quad (1.22)$$

The reduction to conditional probabilities only depending on the previous value (x_{n-1}) is obviously in harmony with the notion that a Markovian process possesses no memory of earlier times.

The fundamental problem of transferring this definition to the quantum regime is the following. In case the stochastic process is referred to a classical system, sampling of the probabilities at times t_i is feasible. Contrary, in a quantum mechanical setup each measurement would disturb the system and hence alter the statistics of the process at later times. Moreover, quantum mechanics allows a variety of different measurements, consequently a possible detection of non-Markovianity would require an assignment to the measurement chosen. However, we ultimately desire a criteria characterizing the dynamics of the system rather than the outcomes of a particular measurement.

Consequently, finding an ansatz for a universal definition of non-Markovianity is a fiddly task. On the one hand, it is desired to follow the classical case as close as possible, on the other hand, verification of (non-) Markovianity should be experimentally feasible. From the numerous definitions that have been put forward [4, 83, 84], we present the sole two which are important for the discussions in the later parts of this work.

CP - Divisibility

Put forward by Rivas, Huelga and Plenio (hence also called RHP-criteria), this definition characterizes non-Markovianity via the divisibility of a dynamical map [103]. This characterization of a Markovian process is motivated by the *divisibility* of a classical Markovian process. In particular, for a classical stochastic process the probabilities of the random variables $X(t_{n-1})$ and $X(t_n)$ can be connected via a transition matrix $T(x_n, t_n | x_{n-1}, t_{n-1})$ according to the relation

$$P(x_n, t_n) = \sum_{x_{n-1}} T(x_n, t_n | x_{n-1}, t_{n-1}) P(x_{n-1}, t_{n-1}), \quad (1.23)$$

where the sum runs over all possible values of x_{n-1} . A stochastic process, whose transition

matrices for $t_3 \geq t_2 \geq t_1 \geq t_0$ satisfy

$$\sum_{x_2} T(x_2, t_2 | x_1, t_1) = 1, \quad (1.24)$$

$$T(x_2, t_2 | x_1, t_1) \geq 0, \quad (1.25)$$

$$T(x_3, t_3 | x_1, t_1) = \sum_{x_2} T(x_3, t_3 | x_2, t_2) T(x_2, t_2 | x_1, t_1), \quad (1.26)$$

is called divisible. Crucially, for a Markovian process $T(x_2, t_2 | x_1, t_1) = P(x_2, t_2 | x_1, t_1)$ and on the level of one point probabilities divisibility coincides with Markovianity⁹ [82]. This property is suitable for the definition of a quantum Markovian process. By relating the dynamical maps $\Lambda_{t_2 \leftarrow t_1}$ to the transition matrices $T(x_2, t_2 | x_1, t_1)$, we replace Eq. (1.24) with the preservation of the trace and Eq. (1.25) with complete positivity. Remaining is the composition law, Eq. (1.26), which we like to convert for a quantum evolution into the one stated in Eq. (1.8), however we introduce a slight modification, i.e. we have

$$\Lambda_{t_3 \leftarrow t_1} = \Phi_{t_3 \leftarrow t_2} \circ \Lambda_{t_2 \leftarrow t_1} \quad \forall t_3 \geq t_2 \geq t_1 \equiv t_0. \quad (1.27)$$

In contrast to 1.8, the time t_1 is fixed to the initial time t_0 . By $\Phi_{t_3 \leftarrow t_2}$ we denote the *propagator* from time t_2 to t_3 and importantly, this propagator does not have to be a CPTP map. Finally, we define any quantum evolution, whose family of dynamical maps can be decomposed according to the modified composition law in Eq. (1.27) where indeed $\Phi_{t_3 \leftarrow t_2}$ is a CPTP map, as a quantum Markovian evolution. Therefore, any CP-divisible dynamics is Markovian. In particular, note that Eqs. (1.8) and (1.27) coincide here. Conversely, any evolution that cannot be decomposed as such, that is when the propagator $\Phi_{t_3 \leftarrow t_2}$ is not a CPTP map, represents a quantum non-Markovian evolution.

Trace Distance

The definition via the trace distance has been proposed by Breuer, Laine and Piilo (BLP-criteria) [102]. It is stated, that iff the evolution is Markovian, the trace distance for any two states ρ and σ is either decreasing or constant in time, i.e.

$$\|\rho(t_2) - \sigma(t_2)\|_1 \leq \|\rho(t_1) - \sigma(t_1)\|_1 \quad \forall t_2 \geq t_1, \quad (1.28)$$

where $\|A\|_1 = \text{tr} [\sqrt{AA^\dagger}]$ is the trace norm. The motivation behind this definition is the memory

⁹Note that there are classical non-Markovian processes which are divisible [82].

property of non-Markovian processes: Note that the trace distance

$$D[\rho(t_1), \sigma(t_1)] = \frac{1}{2} \|\rho(t_1) - \sigma(t_1)\|_1 \quad (1.29)$$

describes the distinguishability of the two states [123]. Therefore, one considers loss of distinguishability as a flow of information from the system to the environment, and vice versa, an increase of the distinguishability as a backflow of information. The loss of distinguishability is generally associated with Markovian processes.

Let us make a few remarks concerning the implication and history of the above definitions. The RHP-criteria and the BLP-criteria are not equivalent. It can be shown that every CP-divisible dynamics fulfills the contractive property of the trace distance in Eq. (1.28), while the converse is not true [82]. However, note that in the case of a pure dephasing dynamics, all common definitions of non-Markovianity coincide [124]. Hence the RHP-criteria is in closer relation to the classical notion of a Markovian process to be without memory, since according to the BLP-criteria there exist processes which are not CP-divisible and at the same time do not decrease the trace distance. On the other hand, since the CP-divisibility is based on the dynamical maps, it requires process tomography [125, 126] to be fully characterized experimentally. At the same time, only two states with an increasing trace distance are required to identify a dynamics as non-Markovian (note however that in general the estimation of the state also requires state-tomography [127]). In an optimal case, these states are orthogonal and lay on the boundary of the set of physical states [128]. Hence, the trace distance also serves as a useful witness.

An evolution according to a semigroup ("semigroup evolution") was historically defined to be the criteria for a Markovian evolution, as it corresponds to an evolution governed by the Lindblad equation (1.15). Due to its positive and constant rates in the dissipator it is also referred to as *time-homogeneous Markovian* [82]. As mentioned in Section 1.2.1, the constant rates are achieved by the Markov approximation in the derivation of this master equation [2]. Thereby it is assumed that the environmental correlations are essentially delta peaked and the corresponding frequency spectrum approaches the flat distribution of *white noise* [17]. In the same way, these delta correlations are associated with a memoryless environment and on this account with the resulting Markovian dynamics of the open system. Therefore, one might refer to a semigroup evolution as an open system undergoing *quantum white noise*.

Furthermore, note that positive, but time dependent rates $\gamma_r(t)$ in the Lindblad-form of Eq. (1.7) guarantee a Markovian evolution by both the RHP- and BLP-criteria and the dynamics are

referred to as *time-inhomogeneous Markovian* [82]. On the other hand, rates which are negative at some times $t \geq 0$ result in non-Markovian dynamics according to the RHP-criteria, however, one may construct examples where the trace distance according to the BLP-criteria is non-decreasing [129].

Finally, we want to mention that the specific definition of non-Markovianity, apart from the semigroup composition law, does not play any role for the interpretation of the results presented in this work.

1.4.1. A Measure of non-Markovianity

The question, whether a given dynamics is non-Markovian, possesses a binary answer, at least if the definition of non-Markovianity is fixed. Nevertheless, one may desire to refine this answer by quantifying, "how non-Markovian" a given dynamics actually is. This refinement is provided by a proper measure assigning the degree of non-Markovianity to the dynamics. Due to the deviant definitions, it is a natural consequence that also different measures have been proposed [82, 83, 102, 103, 130–132].

Since we will require a measure of non-Markovianity in Chapter 9 to quantify a pure dephasing dynamics, we will dedicate this section to the introduction of a measure based on the trace distance definition of non-Markovianity [102]. We stress again that the measure according to any other definition would yield a quantitatively equal result (all detections of non-Markovianity would coincide, but the measures would have different values) [124].

Recalling the trace distance in the previous section, we define the rate of change of the latter as

$$\mathcal{R}(t, \rho, \sigma) = \frac{d}{dt} D[\rho(t), \sigma(t)] = \frac{1}{2} \frac{d}{dt} \|\Lambda_{t \leftarrow t_0} [\rho(t_0)] - \Lambda_{t \leftarrow t_0} [\sigma(t_0)]\|_1. \quad (1.30)$$

There is a backflow of information and hence non-Markovianity if $\mathcal{R}(t, \rho, \sigma) > 0$, i.e. Eq. (1.28) is violated. Hence, a natural way to quantify the degree of non-Markovianity is to measure that backflow by integration over these times, i.e. we have the measure

$$\mathcal{N}(\Lambda_{t \leftarrow t_0}) = \max_{\rho(t_0), \sigma(t_0)} \int_{t_0}^t d\tau \mathcal{R}(\tau, \rho, \sigma) \text{Ind}[\mathcal{R}(\tau, \rho, \sigma) > 0], \quad (1.31)$$

where $\text{Ind}[\bullet]$ is an indicator function taking the value 1 for a true statement and zero otherwise. Obviously, the measure is zero for all dynamics where the trace distance is non-increasing. The maximization over possible initial states is a consequence of our demand that the measure should quantify the non-Markovianity degree of the map inducing the dynamics and not a particular realization of latter. A convenient expression of the integral can be found in terms of

a sum, i.e. we write

$$\mathcal{N}(\Lambda_{t \leftarrow t_0}) = \max_{\rho(t_0), \sigma(t_0)} \sum_m D(\tau'_m, \rho, \sigma) - D(\tau_m, \rho, \sigma), \quad (1.32)$$

where m labels all intervals (τ_m, τ'_m) with $D(\tau'_m, \rho, \sigma) - D(\tau_m, \rho, \sigma) > 0$.

Let us discuss an essential example. Consider a qubit undergoing a pure dephasing dynamics. In the basis that diagonalizes its free Hamiltonian, the corresponding state at any time t can always be written as

$$\rho(t) = \begin{pmatrix} p & \sqrt{p(1-p)}e^{-\Gamma(t)+i\varphi(t)} \\ \sqrt{p(1-p)}e^{-\Gamma(t)-i\varphi(t)} & (1-p) \end{pmatrix} \quad (1.33)$$

where $\varphi(t)$ denotes a possibly time dependent phase and $\Gamma(t)$ is the *decoherence function* [2], while p parametrizes the population of the basis states. The initial state is given for $t = t_0$. For any given p , the state $\sigma(t)$ maximizing the trace distance¹⁰ $D[\rho(t_0), \sigma(t_0)]$ can be obtained via $\rho(t)$ employing the transformations $\phi(t) \mapsto \phi(t) + \pi$ and $p \mapsto 1 - p$.

Calculation of the trace distance yields

$$D(t, \rho, \sigma) = e^{-\Gamma(t)} \sqrt{e^{2\Gamma(t)}(1-2p)^2 - 4(p-1)p}. \quad (1.34)$$

Crucially, this expression is exactly equivalent to the length of the Bloch vector $\vec{r}(t)$ of the state $\rho(t)$ (see Section 1.3 above). By virtue of Eq. (1.32) we hence arrive at the measure of non-Markovianity for a qubit undergoing pure dephasing dynamics

$$\mathcal{N} = \sum_m r(\tau'_m) - r(\tau_m), \quad (1.35)$$

where m labels all intervals (τ_m, τ'_m) where $r(\tau'_m) > r(\tau_m)$. We add the following remark. The coherence of a qubit state can be quantified by the length of projection of its Bloch vector into the xy plane of the Bloch sphere [107]. Since p is constant for a pure dephasing dynamics, it is absolutely enough to observe the evolution of the qubit's coherence to quantify the degree of non-Markovianity in its dynamics.

¹⁰These states directly oppose each other on the Bloch sphere [a concept we are introducing in Section 1.3], i.e. their Bloch vectors only differ in a global sign. Moreover, note that this observation holds for any time t , not just for $t = t_0$.

1.5. Phase-Covariant versus non-Phase-Covariant Dynamics

This section has been first published in [H3] and, in large parts, has been taken from there.

The nature of the noise strongly influences the metrological bounds on the achievable precision in frequency estimation we are going to explore in Chapters 4 and 5. Thereby, a crucial role is played by the *phase-covariance* (PC) [47–50] of the noise. Whether the noise is PC or *non-phase-covariant* (NPC) can have a heavy impact on the achievable precision, hence, it is worth presenting explicitly an intuitive way to differentiate between the two kinds of dynamics, which we will intensively exploit in Chapter 5.

Phase-covariance is straightforwardly characterized by a commutation relation on the level of dynamical maps. The requirement is defined through the condition that the channel generating the evolution commutes with any rotation $R_z[\bullet] = \exp(-i\phi\sigma^z) \bullet \exp(i\phi\sigma^z)$ of the qubit's state around the z axis, i.e.

$$[\Lambda_{t_2 \leftarrow t_1}, R_z] = \Lambda_{t_2 \leftarrow t_1} \circ R_z - R_z \circ \Lambda_{t_2 \leftarrow t_1} = 0 \quad (1.36)$$

for any arbitrary angle ϕ . For the case that the free evolution is also in the z direction, a colloquial formulation would be that the free evolution and the action of the noise commute. Phase-covariance results in a particular geometry of the available transformations made through the channel, where it is now convenient to employ the matrix form of linear maps introduced in the last Section 1.3. Such a representation of the dynamical maps allows us to easily detect PC dynamical maps out of all the possible transformations of the Bloch sphere: for any fixed time, a dynamical map satisfies Equation (1.36) if and only if its matrix representation reads

$$D_{\text{PC}}^\Lambda = \begin{pmatrix} 1 & 0 & 0 & 0 \\ 0 & d \cos \xi & -d \sin \xi & 0 \\ 0 & d \sin \xi & d \cos \xi & 0 \\ v_z & 0 & 0 & d_z \end{pmatrix}. \quad (1.37)$$

With reference to the general form of a qubit dynamical map in Equation (1.19) and the decomposition in Equation (1.21), we see that PC maps are identified by: equal contractions along the \hat{x} and \hat{y} axes ($D = \text{diag}\{d, d, d_z\}$), a translation only along the \hat{z} -axis ($\vec{v} = \{0, 0, v_z\}$) and a rotation only about the z -axis, which we get by setting $\hat{n}_1 = \hat{z}$ and $\varphi_1 = \xi$, while $R_{n_2}^{\varphi_2} = \mathbb{1}$ (other completely equivalent choices can be made, since D commutes with the rotations about

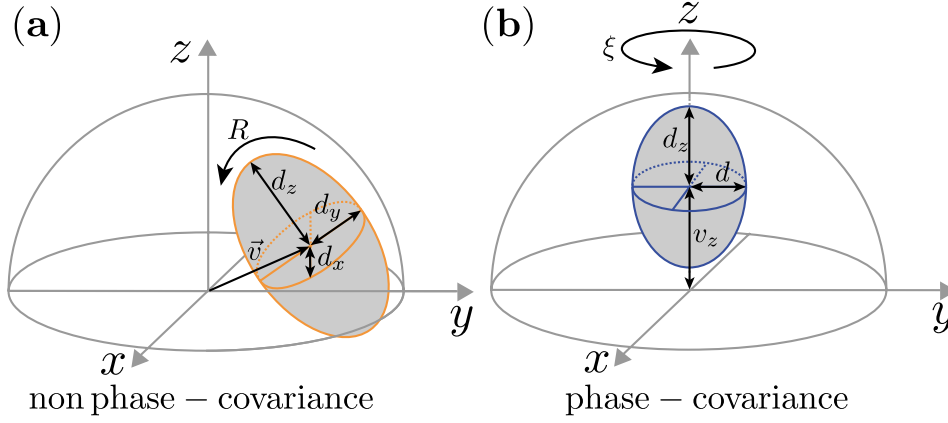


Figure 1.1.: **Transformations of NPC and PC dynamics on the Bloch sphere.** (a): The NPC dynamics can be viewed as a general affine transformation Eq. (1.20) of the Bloch sphere (see Section 1.3) contracting it to an ellipsoid that is parametrized by (in order): a rotation $R_{n_1}^{\varphi_1}$, contractions d_x, d_y, d_z , along the three axes, a reflection, a second rotation $R_{n_2}^{\varphi_2}$ and a translation by a vector \vec{v} (for simplicity, we denote the two rotations by a single R above). (b): PC dynamics is then obtained by a restriction to transformations that forces the *cylindrical symmetry* (indicated by a circular arrow) of the ellipsoid around the \hat{z} axis to be conserved. (Figure first published in [H6])

the \hat{z} axis). Of course, PC maps include only the affine transformations of the Bloch sphere commuting with the rotation about the \hat{z} axis, while NPC maps include also rotations about any axis different from the \hat{z} -axis, translations with non-zero components along the \hat{x} and \hat{y} axes and unequal contractions along the \hat{x} and \hat{y} axes, see Figure 1.1.

Finally and crucially for our purposes, let us recall that given a PC dynamics, the functional form of the corresponding master equation can be univocally characterized and it reads [39]

$$\begin{aligned} \frac{d\rho(t)}{dt} = & -i [(\omega_0 + h(t))\sigma^z, \rho(t)] + \gamma_+(t) \left(\sigma^+ \rho(t) \sigma^- - \frac{1}{2} \{ \sigma^- \sigma^+, \rho(t) \} \right) \\ & + \gamma_-(t) \left(\sigma^- \rho(t) \sigma^+ - \frac{1}{2} \{ \sigma^+ \sigma^-, \rho(t) \} \right) + \gamma_z(t) (\sigma^z \rho(t) \sigma^z - \rho(t)), \end{aligned} \quad (1.38)$$

for some, possibly time dependent, real coefficients $h(t), \gamma_+(t), \gamma_-(t), \gamma_z(t)$. Equivalently, in the other direction, any master equation of the form as in Equation (1.38) will give rise to a PC dynamics. In particular, one can show that starting from the ME Eq. (1.38) the affine representation of the map must take form Eq. (1.37) [39]. From a physical point of view, the ME in Eq. (1.38) includes the common noise processes of dephasing $[\gamma_z(t)]$, emission $[\gamma_-(t)]$ and absorption $[\gamma_+(t)]$.

CHAPTER 2

The Nitrogen-Vacancy Center in Diamond

The *nitrogen-vacancy center* (NV) is a color¹ defect in diamond. First discovered in the seventies [134, 135], in recent years it has enjoyed lots of attention and has become a widely used experimental platform in quantum sensing, quantum computation, quantum simulation, quantum metrology and quantum information [5, 8, 9, 21]. Its increasing usage in these fields surely has to be ascribed to reasonable experimental effort, as many of its advantages still persist at room temperature, such as long coherence times [136, 137], optical readout and initialization [138]. Advanced manufacturing processes of diamond crystals, like chemical vapor deposition [139, 140] or high-temperature-high-pressure methods [141] pave the way for the controlled creation of nearly impurity-free samples of the host material, avoiding otherwise persistent noise sources. The NV centers themselves are generated by ion beam implementation [142, 143] and delta-doping [144–146]. However, a deterministic creation, especially at specifically picked locations, is still an unsolved task [142].

In the following, we illustrate the basic properties of the NV center which will become important in the course of Part III of this work. There, the NV center serves as an experimental platform for illustration purposes. For an in depth description of the NV center and its properties we refer to the review by Doherty et al. [61].

2.1. The Level Structure and its Consequences

The NV is a point defect in the diamond lattice [Figure 2.1 (a)], where it replaces two adjacent carbon atoms. It consists of a nitrogen at the first lattice site, while the other one remains

¹These defects "colorize" the otherwise translucent diamond. NV centers give a diamond a pink tint [133].

vacant. The diamond lattice belongs to the face-centered cubic point group with a two atomic basis, which results in four possible spatial orientations of the defect [147]. The C_{3v} symmetry of the defect [134], together with its charge state completely determine the level structure [135, 148–155]. Importantly, the rotational symmetry axis connects the vacancy and the nitrogen spin and defines the quantization (\hat{z}) axis.² The three dangling carbon bonds donate three electrons to the NV, while the nitrogen atom possesses two free electrons. Together with an additional electron of an external donor, the NV center can form a negatively charged state³, which has an electronic spin of $S = 1$ [151, 156, 157]. In the electronic ground state, this forms a spin triplet 3A with a zero field splitting of $\Delta = 2\pi \cdot 2.87$ GHz [135, 158, 159] between the $|m_s = 0\rangle$ and $|m_s = \pm 1\rangle$ states [153, 160, 161]. Interaction with the inherent nitrogen nuclear spin results in further hyperfine splitting of the $|m_s = \pm 1\rangle$ states, depending on the nitrogen isotope, e.g., $A_{||} = 2\pi \cdot 2.14$ MHz for the ^{14}N isotope [101, 162] with $I = 1$. This isotope further possesses a quadrupole splitting $Q = 2\pi \cdot 5.01$ MHz. This splitting is sketched in Figure 2.1 (b) to (e).

While the manipulation of the electronic spin states was found achievable via a microwave drive [163], the preparation and readout of the electron spin is performed by optical excitation of the 3A state into the electronic 3E excited state. This transition is spin preserving, i.e. the population distribution in the $|m_s\rangle$ levels is not touched. The decay back to the 3A state, however, is strongly spin selective. The excited $|m_s = 0\rangle$ state radiatively decays into its ground state, while the excited $|m_s = \pm 1\rangle$ mainly passes through a non-radiative inter-system crossing to a metastable singlet state between the excited and the ground state [159].⁴ The latter also decays preferentially into the $|m_s = 0\rangle$ ground state, i.e. this total transition is not spin preserving [166, 167]. Firstly, this results in a higher intensity if the initial state is $|m_s = 0\rangle$ compared to $|m_s = \pm 1\rangle$ and hence this difference in luminescence is used to determine the electron spin state. Secondly, optical pumping for sufficiently long time polarizes the electron spin into the $|m_s = 0\rangle$ ground state. Conveniently, these mechanisms can be observed at room temperature, too [138].

The spin states are sensitive to the to magnetic fields. Often, an externally applied field along the symmetry axis of the NV center is employed to lift the degeneracy between the $|m_s = \pm 1\rangle$ states due to the Zeeman effect.⁵ In this work, we employ the $|m_s = 0\rangle$ and

²Note that this also sets a preferred coordinate system when the NV center is employed for sensing applications.

³The neutrally charged state of the NV is not considered in this work.

⁴The exact path of the decay is yet to be sorted out completely, as there is also evidence of two singlet states separated by a radiative 1042 nm infrared transition [156, 164, 165]. However, the detailed level structure is not important for this thesis, hence we will work with one single singlet.

⁵Also other directions are possible, however this may lead to a tilted quantization axis and therefore new eigenstates which are mixtures of the free $|m_s\rangle$ states.

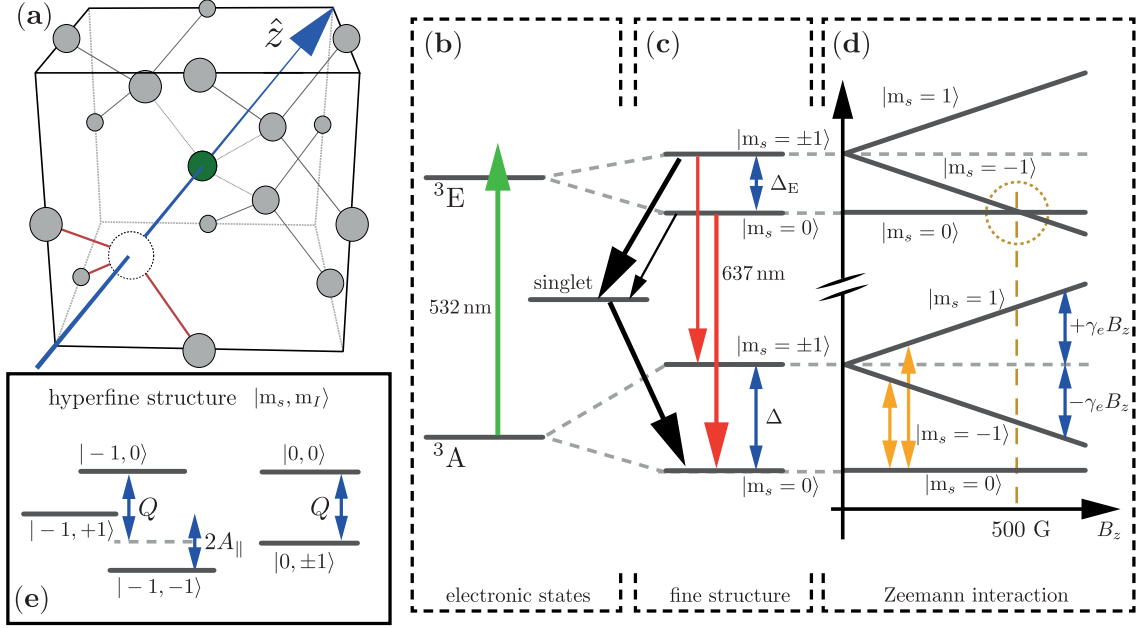


Figure 2.1.: Properties of the nitrogen-vacancy center. Panel (a) illustrates the geometry of the NV center. It exhibits a symmetry for rotations of $2\pi/3$ around the axis (blue) connecting the nitrogen atom (green) and the vacancy (white circle), which is furthermore chosen as the \hat{z} axis. The other three possible orientations of the NV are marked in red. The corresponding simplified energy-level scheme is shown in panels (b)-(e). The orbital 3A electronic spin ground state is excited by a green laser (532 nm, green arrow) into the 3E excited state [panel (b)]. The fine structure illustrated in (c) shows the zero field splittings of the ground state spin triplet and the excited state respectively (blue arrows). Subsequently to optical excitation, the state decays according to the electronic spin state. Spin preserving radiative decay into the 3A state is indicated by the red arrows (600 to 800 nm, the noted 637 nm correspond to the zero-phonon line [60]). The excited $|m_s = \pm 1\rangle$ states preferentially decay by a non-radiative path (black arrows) through the intermediate singlet to the $|m_s = 0\rangle$ ground state. Note that the excited $|m_s = 0\rangle$ also possesses a finite probability to pass through the singlet. This induces a difference in photoluminescence for the different excited states and enables polarization into $|m_s = 0\rangle$. An external magnetic field along the \hat{z} axis of magnitude B_z lifts the degeneracy of the $|m_s = \pm 1\rangle$ states, see panel (d). The yellow arrows mark the artificial qubits chosen in this work and therefore also the transitions driven by microwaves. Around 500 G the $|m_s = 0\rangle$ and $|m_s = -1\rangle$ states cross, which together with the hyperfine splitting in (e) caused by a ^{14}N spin result in either crossing or repelling states. Since the ^{14}N nuclear spin represents a spin-1 system, it possesses a quadrupole splitting Q , additionally to the hyperfine constant $A_{||}$. The hyperfine structure for $|m_s = 1\rangle$ is not shown here.

one of the $|m_s = \pm 1\rangle$ states as our working transition for the artificial qubit. Furthermore, the application of the external magnetic field close to 500 G sets the steady state for optical pumping to $|m_s = 0, m_I = +1\rangle$ [168]. This is due to a spin level anticrossing in the 3E state which allows energy conserving spin flip-flop processes between the electron and nitrogen spin.

2.1.1. Ground State Spin Dynamics

The NV center's electron spin interacts with multiple quantum systems naturally occurring inside of the surrounding diamond. Depending on the type of the diamond [133, 141, 169], different elements besides carbon can occur. In NV related experiments, this is mainly nitrogen which appears naturally or as a residue from nitrogen implementation. As a consequence, also other types of defects occur [158], e.g., nitrogen P_1 centers (which carry an electron spin), or vacancies that haven't been converted to NV centers during the manufacturing process [142, 146]. Further noise originates from the diamond surface because of the dangling bonds of the most upper carbon layer [170–173]. However, for NV centers located deep (few μm) in a diamond of low nitrogen content⁶, the dominant coupling antagonists are ^{13}C nuclear spins-1/2. ^{13}C is a stable and naturally occurring isotope of carbon, appearing with a natural abundance of 1.1%, on the other hand, the most abundant ^{12}C isotope (98.9%) carries no spin.

The detrimental consequences of the interaction with these impurities are decoherence effects (dephasing), i.e., relaxation of the transversal spin components. At the most basic level, the coupling to the impurities can be understood as a fluctuating magnetic field introducing random phase shifts on the electron spin [174, 175]. The longitudinal decay driving the population distribution into an equilibrium state originates from transitions induced between the different magnetic sublevels of the NV electron spin. This decay is mainly governed by phonons in the diamond lattice and hence a great temperature dependence is expected.

To characterize the effects of these processes, we distinguish three timescales (or rates, which are given by the inverse of these times).

- The *homogeneous dephasing time* or *coherence time* T_2 . This time is usually measured via a Hahn echo [176] or extended via multipulse dynamical decoupling sequences, see Section 3. Spin-spin interactions of the NV center and other impurities result in correlation processes decreasing the purity of the reduced NV spin state. The T_2 time increases with higher magnetic field amplitudes but saturates in the strong field regime

⁶This is a so called type-IIa diamond, where the nitrogen content is basically undetectable (<1 ppm) [61, 169]. Diamond containing single substitutional nitrogen impurities is usually categorized as type-Ib.

beyond 300 G [175, 177, 178]. Contributions originating from other electronic spins freeze out below 20 Kelvin [179]. Naturally, another crucial factor is given by the impurity concentration. In a ^{13}C depleted diamond, $T_2 \sim 1.8$ ms was measured [136] (at room temperature), while using multipulse sequences showed $T_2 \sim 3.3$ ms (at room temperature) and $T_2 = 580$ ms (at liquid-nitrogen temperature of 77 K) [137]. In diamond with natural ^{13}C abundance, T_2 has been pushed to about a second, employing a cryogenic temperature of 3.7 K [180].

- The *inhomogeneous dephasing time* T_2^* characterizes the so called *free induction decay* (FID) recorded by a Ramsey measurement [78]. Inhomogeneous dephasing is an effect that appears when measurements of ensembles are considered. There, one may speak of a simultaneous measurement of multiple systems or repeated measurements of a single system. In this context it is caused by slight inhomogenities in the applied fields or due to slow fluctuations of other impurities in the diamond lattice, that vary locally from system to system or between separate measurement cycles. Since echo techniques refocus these slow fluctuations during each single run, for non-echo techniques like the Ramsey measurement one has $T_2^* \leq T_2$ [61]. The FID decay is therefore also strongly dependent on the magnetic field and the temperature [175, 181] and usually happens on the order of a few μs . In Chapter 9, we measure $T_2^* \approx 22.26 \mu\text{s}$ for an ultra pure diamond (^{13}C abundance 0.01%), while for natural abundance it is predicted to be around $4 \mu\text{s}$ [175, 181].
- The *spin relaxation time* T_1 , sometimes also called *spin-lattice relaxation time*. This time scale is rather independent from the magnetic field (besides an anomaly at around 600 G which appears in nitrogen rich samples), but highly temperature dependent as it is mainly caused by phonon induced transitions between the magnetic sublevels. [61, 179]. These phonons freeze out with decreasing temperature. A relaxation time of $T_1 \sim 508$ ms has been observed at 77 K [137], while at 3.7 K, a relaxation time of greater than one hour has been reported [180]. Even at room temperature one usually finds that $T_1 \sim 6$ ms [137, 179], which is far longer than any dynamics we examine in the work present at hand. Hence for all calculations in this work we follow the usual practice and neglect these relaxation processes.

We stress that these timescales are not as disconnected as they appear. The relation between T_2 and T_2^* has already been mentioned. However, another crucial relation is set by $T_1 \geq T_2/2$, which is a necessary condition for the evolution to be physically well defined, in particular

CP⁷ [50]. However, in [137] it is argued that before reaching that limit, spin-phonon coupling, which may only be removed at very low temperatures, contributes to the T_2 process.

2.1.2. Peculiarities of the Electron Spin Readout

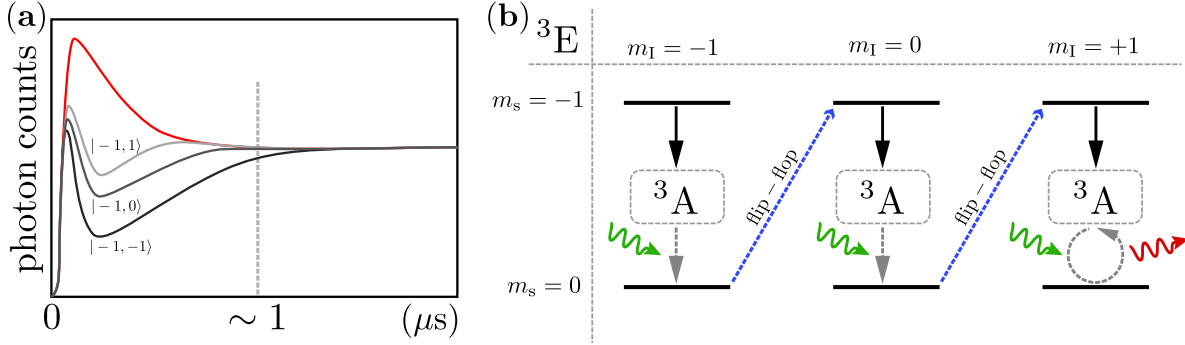


Figure 2.2.: **Readout of NV centers.** The photon counts during optical cycles driven by laser illumination are shown in (a). The red curve displays the curves for a spin state in $|m_s = 0\rangle$, while the grey curves show lower rates due to the non-radiative pathway illustrated in Figure 2.1. Depending on the spin state of the ^{14}N spin, these darker count rates differ. The responsible mechanism is shown in (b). The diagram shows the sequence of events happening in the 3E state. The non-radiative decay is marked with black arrows. The state yielding the least photons is $|m_s = -1, m_I = -1\rangle$ in the top left. After passing through the ground state and subsequent excitation (grey dotted arrows), the $|m_s = 0, m_I = -1\rangle$ state may undergo a total spin conserving flip flop dynamics (blue arrow) to $|m_s = -1, m_I = 0\rangle$ and hence pass again through the singlet state. This can be repeated analogously, until $|m_s = 0, m_I = 1\rangle$ is reached. This is the steady state where most cycles include the radiative pathway. Note that this scheme allows polarization of the ^{14}N state into $|m_I = 1\rangle$.

As mentioned before, the readout of the electron spin state is performed by optical excitation and collection of the resulting fluorescence. Nevertheless, there is a particularity of this process that will become relevant in Section 9.4.1. During illumination, the system undergoes optical cycles between the 3A and 3E states, increasing the collected number of photons [166]. Especially, this is the case for the $|m_s = 0\rangle$ state resulting in the high photon counting rate shown in Figure 2.2 (a). On the other hand, starting from the $|m_s = \pm 1\rangle$ states the system gets trapped in the singlet state, which has a lifetime of $\approx 150 - 450$ ns [153, 164], see Figure 2.1. Hence, no optical cycles are performed during this time and the initial fluorescence drops [166, 167],

⁷Strictly speaking, this relation is only true for systems with a single transition, i.e. qubits. For multiple levels, the harmonic mean of all coherence times approaches the harmonic mean of all relaxation times from above [50].

resulting in the lower fluorescence curves in Figure 2.2 (a). However, the preferential decay of the singlet state into $|m_s = 0\rangle$ leads to the convergence of the counting rate onto a stable value. This value is lower compared to the initial counting rate recorded for $|m_s = 0\rangle$, since this state also possesses a final probability to pass through the singlet state [182].

For a critical magnetic field strength of about 500 G, important details are added to the procedure. Here, the $|m_s = 0\rangle$ and $|m_s = -1\rangle$ states of the 3E state become degenerate, and together with the nitrogen spin some of the $|m_s, m_I\rangle$ states exhibit a level-anticrossing due to the interaction of electron and nitrogen spin. The strong orthogonal hyperfine interaction of around 40 MHz (for ${}^{14}\text{N}$) allows for flip-flop⁸ interactions in the 3E level [182, 183]. Depending on the state of the nitrogen spin at the start of the readout, the system passes up to three times through the singlet before finally being polarized into $|m_s = 0, m_I = +1\rangle$ [182], see the scheme in Figure 2.2. Naively speaking, the polarization inversion of the ${}^{14}\text{N}$ from $|m_I = -1\rangle \rightarrow |m_I = 0\rangle \rightarrow |m_I = 1\rangle$ can be "consumed as a fuel" to increase the number of dark optical cycles. On the one hand, this provides a method to increase the contrast⁹ between the $|m_s = 0\rangle$ and $|m_s = \pm 1\rangle$ state up to three times [182], on the other hand this effect has to be kept in mind when the electron spin state is read out and the nitrogen spin is a crucial part of the dynamics, as we will encounter in Chapter 9.

2.2. Hamiltonian of the NV Center

In the course of this work, we exclusively consider dynamics taking place in the orbital ground state manifold of the NV center. The corresponding free Hamiltonian contains the zero field splitting and a term for the Zeeman interaction [61, 157, 184]. It reads

$$H_0 = \Delta S_z^2 + \gamma_e \vec{B} \cdot \vec{S}, \quad (2.1)$$

where $\vec{S} = \hat{x}S_x + \hat{y}S_y + \hat{z}S_z$ is a "vector" containing the spin-1 operators $S_{x,y,z}$, $\gamma_e \approx -2\pi \cdot 2.8 \text{ MHz/G}$ is the gyromagnetic ratio of the electron and $\vec{B} = \hat{x}B_x + \hat{y}B_y + \hat{z}B_z$ a magnetic field applied externally¹⁰. Usually, one chooses \vec{B} along the symmetry axis of the NV center, i.e. $B_x = B_y = 0$, to lift the degeneracy between the $|m_s = \pm 1\rangle$ spin states.

As discussed in Section 2.1.1, the electron spin couples to several other systems present in the

⁸The formulation "flip-flop" characterizes an interaction between two spins that conserves the total spin of the system. For example in Figure 2.2 (b), all flip-flop interactions conserve the the sum $m_s + m_I$. Conversely, a "flip-flip" interaction does not conserve the total spin.

⁹By contrast we mean the area between the different photon count curves shown in Figure 2.2 (a).

¹⁰Note that, \vec{S} is not a vector in \mathbb{R}^3 , likewise $\vec{B} \cdot \vec{S}$ is not a scalar product. It rather is a sloppy notation for $\sum_{j=1}^3 (\vec{S})_j (\vec{B})_j = \sum_{j=x,y,z} B_j S_j$.

diamond host. The free Hamiltonian of those impurities and their coupling to the NV center can be written as

$$H_E = - \sum_{j=1}^N \gamma_j B_z I_j^z + \sum_{j<l}^N \vec{I}_j \mathbb{C}_{jl} \vec{I}_l \quad \text{and} \quad H_{NV-E} = \sum_{j=1}^N \vec{S} \mathbb{A}_j \vec{I}_j \quad (2.2)$$

respectively, where \mathbb{A}_j (\mathbb{C}_{jl}) is the hyperfine tensor between the electron spin and nuclear spin j (nuclear spins j and l). The impurities interact as well with the magnetic field, hence γ_j is their gyromagnetic ratio leading to a Larmor frequency of $|\gamma_j B_z|$. For ^{13}C one has $\gamma_C = 2\pi \cdot 1.07 \cdot 10^{-3} \text{ MHz/G}$. The hyperfine tensor

$$\mathbb{A}_j = A_j^{\text{iso}} \mathbb{1} + \mathbb{A}_j^{\text{dip}}, \quad (2.3)$$

is composed of two contributions, namely the isotropic Fermi contact interaction A_j^{iso} and an anisotropic dipolar interaction $\mathbb{A}_j^{\text{dip}}$ [155, 185]. The contact interaction is proportional to the electron spin density at the location of the defect. This density is highly localized at the position of the vacancy and vanishes practically at distances larger than $\approx 0.75 \text{ nm}$. Hence the coupling to distant spins is mainly dipolar. For the inherent nitrogen spin, \mathbb{A}_j is diagonal [101, 157, 162]. The coupling tensor \mathbb{C}_{jl} between constituents of the bath is usually purely dipolar. Hence the tensors conveniently realize the forms

$$\vec{S} \mathbb{A}_j^{\text{dip}} \vec{I}_j = \frac{\mu_0 \gamma_e \gamma_j}{4\pi r_j^3} \left[\vec{S} \cdot \vec{I}_j - \frac{3(\vec{S} \cdot \vec{r}_j)(\vec{r}_j \cdot \vec{I}_j)}{r_j^2} \right] \quad (\text{dipolar}), \quad (2.4)$$

$$\vec{S} \mathbb{A}_j^{\text{iso}} \vec{I}_j = \frac{8}{3\pi} \frac{\mu_0}{4\pi} \gamma_e \gamma_j \rho_s(\vec{r}_j) (S_x I_x^j + S_y I_y^j + S_z I_z^j) \quad (\text{Fermi contact}), \quad (2.5)$$

$$\vec{I}_j \mathbb{C}_{jl} \vec{I}_l = \frac{\mu_0 \gamma_j \gamma_l}{4\pi r_{jl}^3} \left[\vec{I}_j \cdot \vec{I}_l - \frac{3(\vec{I}_j \cdot \vec{r}_{jl})(\vec{r}_{jl} \cdot \vec{I}_l)}{r_{jl}^2} \right] \quad (\text{dipolar}), \quad (2.6)$$

where \vec{r}_j ($\vec{r}_{jl} = \vec{r}_j - \vec{r}_l$) is the vector connecting the NV and the j -th impurity (bath spin j and l), $r_j = |\vec{r}_j|$ ($r_{jl} = |\vec{r}_{jl}|$) and μ_0 is the vacuum permeability. The electron spin density $\rho_s(\vec{r}_j)$ has to be determined from ab initio calculations using density functional theory [155, 157, 185].

The large zero field splitting Δ of the NV center prohibits dynamics which flip the electron spin, hence we neglect these terms by virtue of the secular approximation¹¹ [181, 188]. This

¹¹Note that we are using the term secular approximation following the convention of the community working on NMR, which is however different from that mentioned earlier exploited in the community of open quantum systems, where it is applied during the microscopic derivation of a ME. The approximation used here would be

can be motivated in a frame rotating with respect to ΔS_z^2 , where all terms proportional to S_x and S_y will oscillate with an angular frequency $\Delta = 2\pi \cdot 2.87 \text{ GHz}$. The strength of the dipolar coupling \mathbb{A}^{dip} decreases with r^{-3} , in particular for ^{13}C spins it is on the order of $\sim 2\pi \cdot 20 \text{ kHz}(\text{nm}/r)^3$. ^{13}C spins located at the nearest neighbor positions possess coupling constants of about $\approx 2\pi \cdot 100 \text{ MHz}$, which are still one order of magnitude below Δ . Therefore, all oscillating terms are efficiently suppressed. Consequently, the tensor \mathbb{A}_j can be effectively reduced to a vector $(\vec{A}_j)_k = (\mathbb{A}_j)_{z,k}$, $k = x, y, z$. Then, the total Hamiltonian of the NV and the bath after the secular approximation reads

$$H = \Delta S_z^2 + \gamma_e B_z S_z - \sum_{j=1}^N \gamma_j B_z I_j^z + S_z \sum_{j=1}^N \vec{A}_j \vec{I}_j + \sum_{j < l}^N \vec{I}_j \mathbb{C}_{jl} \vec{I}_l. \quad (2.7)$$

However, the validity of approximation has to be examined carefully. When the externally applied magnetic field is different from zero, one has to ensure that the spin transitions of the NV center are farther off-resonant with the transitions of impurities in the bath. In particular, at 514 G the $|m_s = 0\rangle \leftrightarrow |m_s = -1\rangle$ transition is on resonance with the splitting of P_1 centers [189]. Moreover, at 1030 G the $|m_s = 0\rangle$ and $|m_s = -1\rangle$ states experience a level anticrossing, hence the transition frequency and the coupling strength become comparable. Therefore, energy-exchanging process cannot be neglected.

For brevity and simplicity, we neglect the interactions between different bath spins in the following, nevertheless include them in performed simulations. Importantly, note that the secular approximation induces a pure dephasing dynamics of the NV center, as the free Hamiltonian now commutes with the terms describing the interaction. From now on we assume that all conditions for the secular approximation to hold are valid and we remove the free terms of the NV center, i.e., the first two in Eq. (2.7), by moving to a rotating frame.

2.2.1. The NV Center as a Qubit

Most protocols in quantum sensing, algorithms in quantum simulation and computation are designed to employ qubits for their specific tasks. The NV center represents a system suitable for the creation of an artificial qubit. From the three electron spin levels, one may choose the subspace of $|m_s = 0\rangle$ and one of the $|m_s = \pm 1\rangle$ states to assemble the qubit. Due to the large zero field splitting, populations in this subspace are relatively protected against losses into the remaining space. With $S_z = \sum_{m_s=0,\pm 1} m_s |m_s\rangle \langle m_s|$, the Pauli operator $\sigma_z = |m_s\rangle \langle m_s| - |0\rangle \langle 0|$

referred to as a rotating wave approximation, as it is performed on the global Hamiltonian. It can be shown that these approximations are generally not equivalent [186, 187]. In the context of NMR, the term rotating wave approximation is popular for situations where classical fields act on a quantum object.

and the identity $\mathbb{1} = |m_s\rangle\langle m_s| + |0\rangle\langle 0|$ of the chosen subspace, we obtain

$$H_{\text{TLS}} = \frac{m_s}{2} \sigma^z \sum_{j=1}^N \vec{A}_j \vec{I}_j - \sum_{j=1}^N \left(\gamma_j B_z \hat{z} - \frac{m_s}{2} \vec{A}_j \right) \vec{I}_j, \quad (2.8)$$

by invoking the identity $m_s |m_s\rangle\langle m_s| = m_s(\sigma^z + \mathbb{1})/2$. We emphasize that this picture already gives a direct insight into why individual addressing of nuclear spins in the diamond lattice is possible to achieve. In particular, this is true even for spins of the same species, i.e. if $\gamma_j = \gamma_k$ for $j \neq k$. The Larmor frequency of each nuclear spin, $\gamma_j B_z \hat{z} - \frac{m_s}{2} \vec{A}_j$, is determined by its hyperfine coupling to the NV electron spin. The latter strongly depends on the specific position of the nuclear spin with respect to the NV center, see Eq. (2.4), therefore each Larmor frequency is unique. Hence, the absolute value ω_j of the Larmor frequency of the j -th spin and its quantization axis $\hat{\omega}_j$ are given as

$$\omega_j = \left| \gamma_j B_z \hat{z} - \frac{m_s}{2} \vec{A}_j \right| = \sqrt{\left(\gamma_j B_z - \frac{m_s}{2} A_j^z \right)^2 + \frac{m_s^2}{4} \left[(A_j^x)^2 + (A_j^y)^2 \right]}, \quad (2.9)$$

$$\hat{\omega}_j = \frac{\gamma_j B_z \hat{z} - \frac{m_s}{2} \vec{A}_j}{\left| \gamma_j B_z \hat{z} - \frac{m_s}{2} \vec{A}_j \right|} = \frac{\vec{\omega}_j}{\omega_j}. \quad (2.10)$$

This unique shift in the Larmor frequency of each spin enables individual addressing as we show in Section 3. Without this feature, one would have to rely on artificial methods to shift the frequencies locally, e.g., a gradient in the strength of the magnetic field applied externally.

2.2.2. Coherent Quantum Control

The ability to perform coherent manipulations of the NV center is an absolute necessity for all applications exploiting its quantum features. More explicitly, we desire the possibility to perform rotations on its electron spin state. This coherent control is a crucial ingredient that allows the implementation of dynamical decoupling sequences which we will discuss in Chapter 3. On a more fundamental level, this control is required for preparation and readout of states that are not eigenstates of the free Hamiltonian in Eq. (2.7).

As mentioned in Section 2.1, we can drive transitions of the NV center electron spin via a microwave drive [163]. Employing a semiclassical description, we add the microwave drive to the free Hamiltonian in Eq. (2.1) and choose already $\vec{B} = B_z \hat{z}$, thus

$$H(t) = H_0 + H_{\text{MW}}(t) = \Delta S_z^2 + \gamma_e B_z S_z + \sqrt{2} \Omega \cos(\omega_{\text{MW}} t + \varphi) S_x, \quad (2.11)$$

where ω_{MW} and φ are the microwave-frequency and phase of the applied field, while Ω is the associated Rabi-frequency. This Hamiltonian is only capable of driving transitions between $|0\rangle \leftrightarrow |\pm 1\rangle$, while the so called double quantum transitions $|1\rangle \leftrightarrow |-1\rangle$ are forbidden. In order to address only the single transition $|0\rangle \leftrightarrow |m'_s\rangle$, we choose $\omega_{\text{MW}} = \Delta + m'_s \gamma_e B_z + \delta$. Here, δ is a possible detuning of the driving frequency which we assume to be small compared to $\gamma_e B_z$ and Δ . In a rotating frame with respect to the free part, we write the Hamiltonian as

$$H'_{\text{MW}}(t) = \frac{\Omega}{2} \sum_{m_s = \pm 1} \left[\left(e^{i\varphi} e^{it[2\Delta + (m_s + m'_s)\gamma_e B_z + \delta]} + e^{-i\varphi} e^{it[(m_s - m'_s)\gamma_e B_z - \delta]} \right) |m_s\rangle \langle 0| + \text{H.c.} \right]. \quad (2.12)$$

At first, we neglect all the contributions whose oscillation frequency is dominated by 2Δ by virtue of the *rotating wave approximation* (RWA) [190]. Surely, this is only justified provided that $|\Omega| \ll |2\Delta + (m_s + m'_s)\gamma_e B_z + \delta|$. In typical NV experiments, high Rabi frequencies reach $\Omega \sim 2\pi \times 30$ MHz, hence Δ is larger by three orders of magnitude ensuring this condition to be satisfied. When a similar condition also holds for the second frequency, where $|m_s - m'_s| = 1$, i.e. $|\Omega| \ll |2\gamma_e B_z - \delta|$, we can further approximate the Hamiltonian to

$$H'_{\text{MW}}(t) \approx \frac{1}{2} \Omega \left(e^{-i(\delta t + \varphi)} \sigma^+ + e^{i(\delta t + \varphi)} \sigma^- \right), \quad (2.13)$$

where the rising and lowering operators are given as $\sigma^+ = |m'_s\rangle \langle 0|$ and $\sigma^- = |0\rangle \langle m'_s|$ respectively. The third level, $m_s \neq m'_s$ and $m_s \neq 0$, is completely eliminated from the dynamics. The remaining time dependence of this Hamiltonian can be removed conveniently by noting that it is the interaction picture Hamiltonian of

$$H''_{\text{MW}} = -\frac{\delta}{2} \sigma^z + \frac{1}{2} \Omega [\cos(\varphi) \sigma^x + \sin(\varphi) \sigma^y], \quad (2.14)$$

with respect to $-\frac{\delta}{2} \sigma^z$. The abbreviations $\sigma^x = |0\rangle \langle m'_s| + |m'_s\rangle \langle 0|$ and $\sigma^y = i |0\rangle \langle m'_s| - i |m'_s\rangle \langle 0|$ are just the Pauli operators in the subspace spanned by $\{|0\rangle, |m'_s\rangle\}$, as employed already in Section 2.2.1.

Often, the coherent control is implemented as a *pulse* performing the desired operation (or a sequence of pulses as we will investigate in Chapter 3). During the course of this thesis, we employ box pulses. This means that the Rabi frequency is constant and the action of the pulse is generated by the Hamiltonian in Eq. (2.14). The phase φ represents the so called *phase of the pulse* and fixes the axis around which the state's Bloch vector is rotated. The phase of the pulse determines the angle between the rotation axis and the \hat{x} axis of the Bloch sphere. Crucially,

the detuning of the drive now assembles a free Hamiltonian tilting the rotation axis out of the xy plane.

Let us finally exemplify the control with two essential pulses. For the sake of simplicity, we assume a perfectly resonant drive and thus choose $\delta = 0$ in the following. The evolution operator corresponding to the Hamiltonian in Eq. (2.14) is given by

$$U(t, \varphi) = \cos\left(\frac{\Omega t}{2}\right) \mathbb{1} - i \sin\left(\frac{\Omega t}{2}\right) [\cos(\varphi)\sigma^x + \sin(\varphi)\sigma^y], \quad (2.15)$$

and we can identify two important evolution times defining:

1. the $\pi/2$ -pulse. For $\Omega t = \pi/2$ one has

$$U_{\pi/2}(\varphi) = \frac{\mathbb{1} - i [\cos(\varphi)\sigma^x + \sin(\varphi)\sigma^y]}{\sqrt{2}}, \quad (2.16)$$

which mixes populations and coherences, e.g., one has $|0\rangle \rightarrow (|0\rangle - ie^{-i\varphi}|m'_s\rangle)/\sqrt{2}$. This pulse is crucial for the transformation of the NV spin state to perform initialization and readout of states that are sensitive to fields parallel to the quantization (z)-axis, which we will employ in Section 4.2. Thereby recall that only population differences of the σ^z eigenstates can be read out experimentally, see Section 2.1.2. For example, eigenstates of σ^x are orthogonal to the ones of σ^z and thus one would always obtain $\langle\sigma^z\rangle = 0$.

2. the π -pulse. For $\Omega t = \pi$ one obtains instead

$$U_{\pi}(\varphi) = -i [\cos(\varphi)\sigma^x + \sin(\varphi)\sigma^y], \quad (2.17)$$

which implements the transformation $|0\rangle \leftrightarrow |m'_s\rangle$ up to a global phase. Hence, this pulse inverts the populations of σ^z eigenstates. These pulses are the essential building blocks for dynamical decoupling sequences as they allow to refocus undesired phase evolutions (see Chapter 3).

CHAPTER 3

Basic Principles of Dynamical Decoupling

Dynamical decoupling (DD) is a strategy to perform modulations on the system of interest, such that unintended effects induced by an environment are averaged out at a specifically chosen time of evolution. The approach proposed by Viola et al. [191, 192] is based on the idea that the noise acting on the system ultimately possesses a temporal correlation, i.e. its action during a short time interval may be regarded as constant¹. Naively speaking, when the system suffers under this effect, one performs a transformation on the system after half of that interval such that during the second half the environment reverses the effect by itself.

To illustrate this idea, let us describe a Hahn echo sequence [176] where a qubit experiences dephasing noise. For that, we assume a model of random unitary evolutions. Consider a set of static Hamiltonians with random but constant amplitudes, $\{H_j = \gamma B_j \sigma^z / 2\}$, $j \in \mathbb{N}$. The corresponding evolution reads

$$\rho(t) = \sum_j p(B_j) e^{-i \frac{\gamma B_j}{2} \sigma^z} \rho_0 e^{i \frac{\gamma B_j}{2} \sigma^z}, \quad (3.1)$$

where $p(B_j)$ is the probability for the amplitude B_j to appear. The state $\rho(t)$ hence represents an ensemble average of all the trajectories j and a measurement of the state constitutes then as a selection of one of those trajectories. Let us examine the effect of DD on one of those trajectories. The chosen initial state illustrated in Figure 3.1 (a) is given by an equally weighted superposition of the eigenstates, $|0\rangle$ and $|1\rangle$. During the free evolution of length $\tau/2$, Figure 3.1 (b), this state rotates around the \hat{z} axis changing the phase relation between $|0\rangle$ and $|1\rangle$. Now, a π -pulse is

¹This assertion may be assumed incorrect for the case of a semigroup dynamics, i.e. white noise. However and importantly, noise is regarded as delta correlated if the decay of the correlation functions appears on a practically non-accessible timescale [2]. Hence, under white noise, DD is impossible.

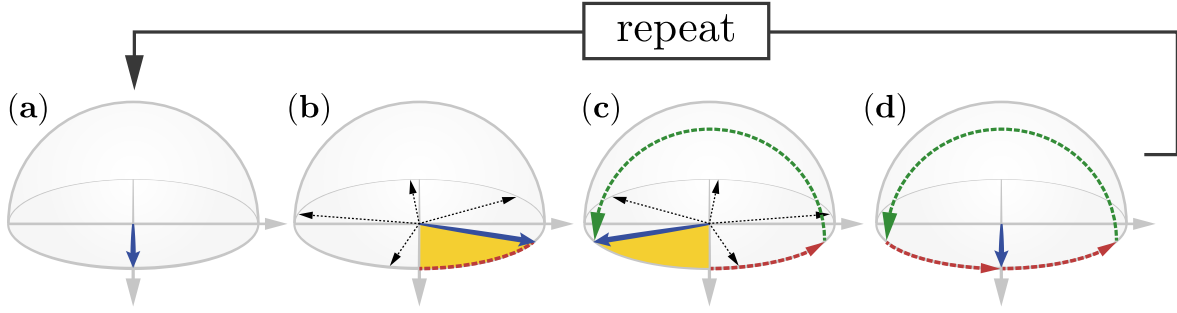


Figure 3.1.: **Hahn Echo on the Bloch Sphere.** The initial spin state is represented by the blue arrow in panel (a). During a free evolution, the state rotates around the \hat{z} -axis with a constant angular velocity and hence collects a phase illustrated by the yellow surface in (b). Other possible trajectories are indicated with black dotted arrows. A π -Pulse around the axis defined by the initial state flips the phase of the state. The path of the state during rotation is marked by the green path in panel (c), where it is assumed that rotation around \hat{z} is frozen, i.e. much slower than the pulse. Subsequently, after the same evolution time as from (a) to (b), the state in (d) coincides with the initial one in (a). The total path of the state is shown as the sequence of red and green arrows. This scheme may be repeated, decoupling the state stroboscopically at each instance it arrives in panel (d).

applied, corresponding to a rotation around the \hat{x} axis by an angle π , see Figure 3.1 (c). For the sake of simplicity, we assume this pulse to be instantaneous, or equivalently that the free dynamics is frozen during the pulse application. The subsequent evolution, again of length $\tau/2$ cancels the previous phase evolution [Figure 3.1 (d)] and we arrive at the initial state²

$$\frac{|0\rangle + |1\rangle}{\sqrt{2}} \xrightarrow{\tau/2} \frac{e^{i\gamma B_j \tau/4} |0\rangle + e^{-i\gamma B_j \tau/4} |1\rangle}{\sqrt{2}} \xrightarrow{\pi} \frac{e^{i\gamma B_j \tau/4} |1\rangle + e^{-i\gamma B_j \tau/4} |0\rangle}{\sqrt{2}} \xrightarrow{\tau/2} \frac{|1\rangle + |0\rangle}{\sqrt{2}}. \quad (3.2)$$

The total evolution for the ensemble average can be written accordingly. Note that a π -pulse inverting the populations of the given initial state can be modeled by $R_\pi = \exp\{-i\pi\sigma^x/2\}$, therefore we have

$$\begin{aligned} \rho(t) &= \sum_j p(B_j) e^{-i\frac{\gamma B_j}{4}\sigma^z} R_\pi e^{-i\frac{\gamma B_j}{4}\sigma^z} \rho_0 e^{i\frac{\gamma B_j}{4}\sigma^z} R_\pi^\dagger e^{i\frac{\gamma B_j}{4}\sigma^z} \\ &= \sum_j p(B_j) \sigma^x \rho_0 \sigma^x \\ &= \sigma^x \rho_0 \sigma^x = \rho_0. \end{aligned} \quad (3.3)$$

²Note that we suppress possible global phases.

Here, the last equality is true since ρ_0 constitutes an eigenstate of σ^x as it was chosen above. Nevertheless, if we allow ρ_0 to present an arbitrary, even unknown state, the application of a further pulse around the \hat{x} axis would bring the state back to the initial one. Clearly, each of those trajectories refocuses itself during the time τ which is illustrated by the black arrows in Figure 3.1. At this point it is intuitive that one may perform multiple of these cycles of length τ which stroboscopically return the quantum state to the initial one.

The original proposal in 1998 [191] indeed only covered decoherence affecting a qubit undergoing pure dephasing dynamics, but was quickly generalized to any unknown couplings between an arbitrary system and the environment [192–194]. Since then, many theoretical [64, 195–198] and experimental [68, 199–205] works followed³, demonstrating the power of the approach. On the other hand, one should recall that these approaches are based on ideas stemming from *nuclear magnetic resonance* (NMR) spectroscopy [56] developed by Rabi in 1938 [75] and, in particular the *Spin (Hahn) Echo* published by Hahn in 1950 [176], which is a refocusing technique as exemplified above. Nevertheless, one should remark that the precise type of DD employed here is termed *pulsed dynamical decoupling*, since there exist also approaches employing continuous driving fields [207, 208].

DD is used as a tool for the spectral decomposition of signal fields [64, 68, 70, 199, 209], which is best described by the filter formalism presented in Section 3.1. Likewise, it represents a neat method to create two-qubit-gates [56, 203, 204] where one is modulated by DD control. The best illustration of the gate’s dynamics is the calculation of effective Hamiltonians presented in Section 3.2, but before moving to these approaches we introduce some common notations and particularities.

Assume that a sequence of N instantaneous π -pulses which are applied at times t_j with $j = 1, 2, 3 \dots, N$. In the course of this thesis, we stick to pure dephasing dynamics which is sufficient to describe the dynamics of the NV center required here (see Section 2.2.1). We farther focus on a single trajectory. This represents exactly the case covered in the effective Hamiltonian approach, while the ensemble average, as done in the filter formalism can be performed afterwards (as also done above). We assume a single field $B(t)$ along the \hat{z} axis, which is now allowed to be time dependent. In principle we may imagine that as a collection of not necessarily in-phase fields where each is oscillating with a different frequency, or a randomly fluctuating field.

The unitary operator $U_j = \exp\{-i\kappa_{\text{free},j}\sigma^z/2\}$ dictating the free evolution after the j -th pulse is

³The references given here are only exemplary and much more can be found throughout this work. However, comprehensive reviews are found in [13, 16, 56, 92, 206].

completely determined by the collected phase

$$\kappa_{\text{free},j} = \int_{t_j}^{t_{j+1}} d\tau \gamma B(\tau). \quad (3.4)$$

An instantaneous π -pulse is farther written as⁴ $R_\pi = \exp\{-i\pi\sigma^x/2\}$. At this point, it is convenient to note that (up to a global phase)

$$R_\pi U_j R_\pi = R_\pi e^{-i\kappa_{\text{free},j}\sigma^z/2} R_\pi \propto e^{i\kappa_{\text{free},j}\sigma^z/2}, \quad (3.5)$$

and thus a π -Pulse has the effect $\sigma^z \mapsto -\sigma^z$. Therefore, we write the total evolution operator as

$$U = U_N \dots R_\pi U_3 R_\pi U_2 R_\pi U_1 R_\pi U_0 = \begin{cases} e^{-\frac{i}{2}\mathbb{K}_{\text{free}}(t,N)\sigma^z}, & N \text{ even} \\ R_\pi^\dagger e^{-\frac{i}{2}\mathbb{K}_{\text{free}}(t,N)\sigma^z}, & N \text{ odd.} \end{cases} \quad (3.6)$$

Here, the total phase collected over the whole time of the sequence $\mathbb{K}_{\text{free}}(t, N)$ is given by [64, 191]

$$\mathbb{K}_{\text{free}}(t, N) = \sum_{j=0}^N (-1)^j \kappa_{\text{free},j} = \int_{t_0}^{t_{N+1}} d\tau F(\tau) \gamma B(\tau), \quad (3.7)$$

where t_0 is the initial time and $t_{N+1} = t$ the end of the evolution. The effect of the π -pulses is accounted by the prefactor $(-1)^j$ which takes care of the fact that the effective phase evolution changes the sign after a pulse. The change of the sign may also be conveniently written as a modulation function $F(t)$ which takes the values ± 1 depending on the number of pulses already applied. Obviously, for $\mathbb{K}_{\text{free}}(t, N) = 0$ we achieve $U = \mathbb{1}$ and the system is completely decoupled⁵.

To gain further insight we revisit the Hahn echo but consider an oscillating field $B(t) = B \sin \omega t$ instead of the static one. There is only one pulse to be applied, hence $N = 1$. Choosing additionally $t_0 = 0$, $t_1 = \tau/2$ and $t_2 = \tau$ results in the same pulse spacing as above. One straightforwardly derives

$$\mathbb{K}_{\text{free}}(\tau, 1) = \frac{2\gamma}{\omega} \sin^2\left(\frac{\omega\tau}{4}\right) \cos\left(\frac{\omega\tau}{2}\right). \quad (3.8)$$

For this phase to vanish, we have different choices for τ :

⁴Note that we chose σ^x here which corresponds to a rotation around the \hat{x} axis. We will mention more advanced choices which introduce an alternation in the pulse phase later 3.3.

⁵In the case that N is odd, we apply another pulse R_π at the end of the evolution to achieve the identity operator.

- $\tau = l \frac{4\pi}{\omega}$, $l \in \mathbb{N}^+$: This corresponds to a natural averaging of the phase due to the oscillatory nature of the signal. Indeed, here we have $\kappa_{\text{free},j} \equiv 0 \forall j$ and the pulses are placed at the nodes of the sinusoidal field.
- $\tau = (2l - 1) \frac{\pi}{\omega}$, $l \in \mathbb{N}^+$: For this choice the averaging is due to the pulses, i.e. they set $\cos(\omega\tau/2) \equiv 0$.

We emphasize that the latter result, despite its simplicity, is quite general, as it basically represents one building block of a DD sequence of equidistant pulses; the Hahn echo is just iterated multiple times. See also Section 3.1 and Chapter 7 for further details. Surely, as soon as more frequencies are present, i.e. the Hamiltonian contains multiple fields of different amplitude and frequency, the problem quickly becomes rather involved, but this case can be treated efficiently via the filter formalism described in Section 3.1. However, one can already build an intuition of how fields with multiple frequencies can be suppressed. Therefore, recall the case of the constant field, where the precise value of τ does not play any role. This observation serves as a motivation for the limiting case: Imagine τ is reduced such that the quickest $B(t)$ is perceived approximately constant by the system. Then the DD refocusing works as described above in case the pulses can still be applied at $\tau/2$ [191], i.e. τ is not too short. Indeed, for that situation to apply, we require $\tau \ll \omega^{-1}$, where ω represents the fastest frequency in the environment. In practice, such an approach is ultimately limited by the available Rabi frequencies Ω for the π -pulses. For these to be still treated as instantaneous, $\pi/\Omega = t_{\text{pulse}} \ll \omega^{-1}$ needs to hold, i.e. even the fastest dynamics can be considered frozen during the pulse (in Chapter 7 this condition is relaxed). Naturally, the Rabi frequency cannot be increased arbitrarily, as it is limited by the maximal available amplitude E of the driving field as $\Omega \sim E$ [190]. Furthermore, high driving amplitudes result in heating processes of the probe (intensity $\sim |E|^2$). For NV centers, this can lead to decoherence and relaxation processes due to the excitation of phonons in the diamond lattice, or in some other cases may also destroy the probe, e.g., when DD protocols are used on biological materials.

Moreover, let us already take a leap ahead of Chapter 7, where we show how the interplay of the time τ with the frequencies appearing in $B(t)$ results in a change of \mathbb{K}_{free} , enabling to employ the same approach for sensing applications, where the aim is to characterize $B(t)$ [13].

3.1. The Filter Function Approach

The filter function approach is an often invoked tool [64, 81, 198, 210–213] as its simplicity and illustrative capabilities stand out when compared to the effective Hamiltonian picture.

In many cases, the environment can be efficiently represented with a classical stochastic process [174,214,215]. Considering the spectrum of the environment then renders it unnecessary to specify the explicit form of the environment Hamiltonian. That said, the filter function approach is widely used in noise spectroscopy as it allows the experimental extraction of the possibly continuous spectral function of the environment [171,209].

For illustrative purposes, let us discuss the simple Hamiltonian

$$H(t) = \frac{b(t)}{2} F(t) \sigma_z, \quad (3.9)$$

where $b(t)$ is the amplitude of a stationary⁶ random process with $\langle b(t) \rangle = 0$ where $\langle \bullet \rangle$ denotes the ensemble average over the possible realizations of $b(t)$. As seen in the previous section, a population-inverting π -pulse effectively results in $\sigma^z \mapsto -\sigma^z$, hence we include the modulation function $F(t)$ of Eq. (3.7) directly into the Hamiltonian and write it as

$$F(t) = \sum_{j=0}^N (-1)^j \Theta(t_{j+1} - t) \Theta(t - t_j), \quad (3.10)$$

where in total N pulses are applied at times t_j , except for $t_0 = 0$ and t_{N+1} , while $t_j \leq t_{j+1}$ and $\Theta(\bullet)$ is the Heaviside step function. In other words, $F(t)$ either takes the value 1 or -1 depending on whether an even or odd number of pulses has been applied prior to time t . Due to the pure dephasing dynamics ensuring $[H(t), H(t')] = 0$, the calculation of the dynamics is straightforward. Since the Hamiltonian is diagonal, it will only act on the phase of an initial state. Hence we can write the state's coherence element as⁷

$$\begin{aligned} \rho_{10}(t) &= \rho_{10}(0) \langle e^{-i\mathbb{K}_{\text{free}}(t)} \rangle \equiv \rho_{10}(0) e^{-\xi(t)} \\ \mathbb{K}_{\text{free}}(t) &= \int_0^t d\tau b(\tau) F(\tau), \end{aligned} \quad (3.11)$$

where we define $\xi(t)$ as the decoherence function. If the stochastic process is Gaussian, i.e. $\mathbb{K}_{\text{free}}(t)$ obeys a Gaussian distribution, one can use Wick's theorem to prove that

⁶By stationary we mean that for all times t , the random values for $b(t)$ are drawn according to the same probability distribution.

⁷Note that contrary to Eq. (3.6) no distinction between even and odd pulse numbers has to be made here. That is, because for equivalent $B(t) = b(t)$, the state-trajectory governed by Eq. (3.6) is fundamentally different than the one induced by the Hamiltonian (3.9). At an arbitrary time during the evolution, they generally do not coincide. However, at the final time they yield the same phase \mathbb{K}_{free} . Their final states are equivalent for even N . These observations are quickly confirmed by comparing the individual trajectories on the Bloch sphere.

$\langle \exp \{-i\mathbb{K}_{\text{free}}(t)\} \rangle = \exp \left\{ -\langle \mathbb{K}_{\text{free}}(t)^2 \rangle / 2 \right\}$ [215], which we use in Appendix B.1 to show that

$$\begin{aligned} \xi(t) &= \frac{1}{2\pi} \int_0^\infty d\omega S(\omega) f_\omega(t), \quad \text{where} \\ f_\omega(t) &= \left| \int_0^t d\tau e^{-i\omega\tau} F(\tau) \right|^2 = \frac{1}{\omega^2} \left| \sum_{j=0}^N (-1)^j (e^{-i\omega t_{j+1}} - e^{-i\omega t_j}) \right|^2 \end{aligned} \quad (3.12)$$

is the filter function given by the absolute value of the Fourier transformed modulation function. The spectrum $S(\omega)$ of the environment is given by the Fourier transform of the two time correlation function $\langle b(0)b(t) \rangle$ and contains information about the spectral components of the environment.

Equation (3.12) is also known as the overlap integral of the spectrum and the filter function. The system only couples to frequencies where $f_\omega(t) \neq 0$, i.e. by tuning the modulation $F(t)$ we are able to precisely control the system-environment coupling. Let us note here, that although we used a classical stochastic process in the Hamiltonian, the overlap integral is also exact for a pure dephasing spin-boson model where the environment is fully quantum. For that model, the result given in [2] reads

$$\xi_{\text{spin-boson}}(t) = \int_0^\infty d\omega J(\omega) \coth\left(\frac{\beta\omega}{2}\right) \frac{1 - \cos \omega t}{\omega^2}. \quad (3.13)$$

Defining $S(\omega) = \pi J(\omega) \coth(\beta\omega/2)$, with $J(\omega)$ the spectral density and β the inverse temperature, we arrive exactly at Eq. (3.13) when we calculate the filter for a free evolution (i.e. no pulses, $F(t) \equiv 1 \forall t$):

$$\begin{aligned} f_\omega(t) &= \int_0^t d\tau_1 \int_0^t d\tau_2 F(\tau_1) F(\tau_2) e^{i\omega(\tau_1 - \tau_2)} = \int_0^t d\tau_1 \int_0^t d\tau_2 e^{i\omega(\tau_1 - \tau_2)} \\ &= 2 \frac{1 - \cos \omega t}{\omega^2} = 4 \frac{\sin^2(\omega t/2)}{\omega^2}. \end{aligned} \quad (3.14)$$

At last, we employ the illustrative strength of the filter formalism to demonstrate the interplay between the number of pulses and the number of periods of a DD sequence. Therefore, let us first set a fixed evolution time T during which we apply N pulses in such a way that they correspond to a concatenation of Hahn echos. This construction is shown in Figure 3.2 (a). Obviously, we have the special cases $N = 0$, corresponding to a free evolution, and $N = 1$ that assembles the standard Hahn echo of length T . In the following we restrict to even $N \geq 2$, where T/N is also given as the spacing between two pulses. Comparing this relation with $\tau = (2l - 1)\frac{\pi}{\omega}$ derived above, we can rearrange it and obtain $\omega = \frac{\pi N}{T}(2l - 1)$. Calculating $f_\omega(t)$

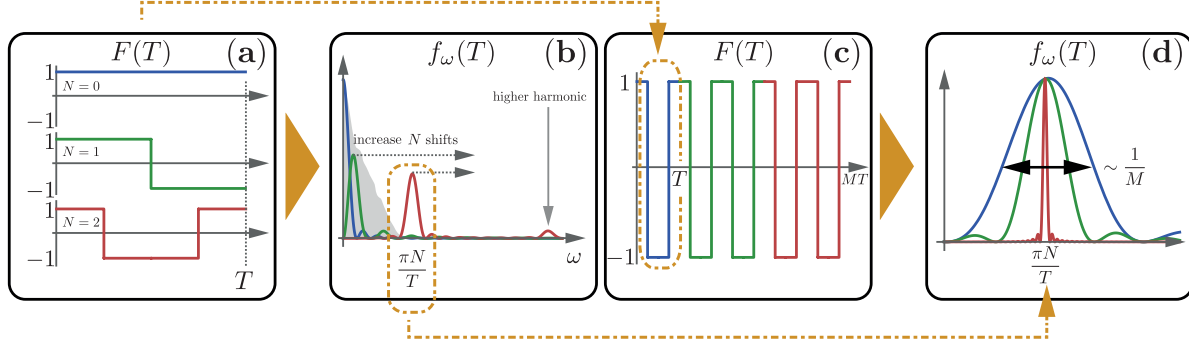


Figure 3.2.: Properties of the filter function. Choosing N pulses during a fixed time T results in a higher switching rate of $F(t)$, panel (a). The corresponding filter function shows a peak (or "window") at $\pi N/T$ and corresponding higher harmonics, see (b). A schematic noise spectrum is illustrated with a grey shading. Crucially, the only sequence showing a non-vanishing filter function at $\omega = 0$ is the free evolution $N = 0$, marked in blue. The succession of M periods of length T [panel (c)] ensures that the width of the peaks decrease. For a large number of successions, this width is approximately proportional to M^{-1} as illustrated in (d). Note that the peaks have been normalized here, the actual height is proportional to M^2 . Therefore one can conclude: For a fixed T , the position of the peaks is determined by N while M controls the height and width.

via the Fourier transform of $F(t)$, we observe that $f_\omega(t)$ shows local maxima at exactly these frequencies, see Figure 3.2 (b) for a sketch. Sometimes, these peaks are also called "windows" since they determine which parts of the spectrum [grey shading in panel (b)] are felt by the system. From here it becomes clear that, to decouple the system, one has to increase N such that the first peak ($l = 1$) has no overlap with the spectrum⁸. In principle, we can repeat this N -pulse sequence M times, i.e. applying $M \cdot N$ pulses during a time $M \cdot T$, as illustrated in Figure 3.2 (c). This does not change the location of the peaks, but changes their width. Figure 3.2 (d) illustrates this effect for an $l = 1$ peak. This is one of the major challenges in the engineering of advanced DD sequences [70, 216, H1], as this determines the *selectivity* of the sequence. The more narrow these peaks are, the more precise the frequency $\omega = \frac{\pi N}{T}(2l - 1)$ is targeted, suppressing dilution through other frequency components.

Obviously there exist different combinations of N , M and T which yield the same sequences. Hence, one usually fixes $N = 2$ as this results in a modulation function of period T employing a minimal number of pulses⁹. We denote the corresponding *DD-frequency* by $\omega_{\text{DD}} = 2\pi/T$ which

⁸Note, that it is just a general recipe. There might exist spectra which possess holes such that it is enough to overlay those with the windows of the filter.

⁹Thereby note that $N = 0$ is not considered (free evolution), while uneven N are periodic in a mathematical

furthermore fixes the position of the first ($l = 1$) peak in $f_\omega(t)$, while the spacing between subsequent pulses is given by π/ω_{DD} . The frequencies $\omega_{\text{DD}}(2l - 1)$ are usually called *higher harmonics* (one usually restricts l to odd integer numbers to write $l\omega_{\text{DD}}$). For a large number of periods, the width of the peaks is approximately $\sim M^{-1}$. Finally, a DD sequence yielding this specific modulation function was first introduced by Carr, Purcell, Meiboom and Gill, hence it is usually termed CPMG-sequence [217, 218].

3.2. Effective Hamiltonian Picture

The effective Hamiltonian picture provides a simple way to illustrate the conditions required for single spin addressing. In particular, using DD one aims to engineer an effective Hamiltonian that only contains a coupling term to the desired target spin. In contrast to the filter function approach, the assumption of a Gaussian random process or a bath that can be mapped to a bosonic bath is not necessary. Let us directly employ the Hamiltonian of a qubit subspace of the NV center already noted in Equation (2.8) where we have J nuclei, not necessarily of the same species. The effect of the pulses has been discussed in the section above, hence we analogously include the modulation into the Hamiltonian and arrive at

$$H(t) = \frac{m_s}{2} \sigma^z F(t) \sum_{j=1}^J \vec{A}_j \vec{I}_j - \sum_{j=1}^J \omega_j \hat{\omega}_j \vec{I}_j. \quad (3.15)$$

In a rotating frame with respect to the free part of the nuclear spins, we arrive at¹⁰

$$H_I(t) = \frac{m_s}{2} \sigma^z F(t) \sum_{j=1}^N \left[\vec{a}_j^x \cos(\omega_j t) + \vec{a}_j^y \sin(\omega_j t) + \vec{a}_j^z \right] \vec{I}_j, \quad (3.16)$$

where

$$\begin{aligned} \vec{a}_j^x &= \vec{A}_j - \hat{\omega}_j (\hat{\omega}_j \cdot \vec{A}_j), \\ \vec{a}_j^y &= \hat{\omega}_j \times \vec{A}_j, \\ \vec{a}_j^z &= \hat{\omega}_j (\hat{\omega}_j \cdot \vec{A}_j). \end{aligned} \quad (3.17)$$

sense but their physical implementation requires then $N + 1$ pulses to decouple the state completely, compare Eq. (3.6).

¹⁰Note that we used the identity

$$e^{i\vec{r}\vec{\omega}\varphi} \vec{I} \vec{a} e^{-i\vec{r}\vec{\omega}\varphi} = \vec{I} \{ [\vec{a} - \vec{r}(\vec{r} \cdot \vec{a})] \cos(\varphi) - (\vec{r} \times \vec{a}) \sin(\varphi) + \vec{r}(\vec{r} \cdot \vec{a}) \}$$

for a vector \vec{r} and a scalar φ .

It is convenient to note that the vectors \vec{a}_j^α ($\alpha = x, y, z$) are pairwise orthogonal, which allows the identification of new spin operators in the rotating frame, $I_j^\alpha \equiv \vec{I}_j \cdot \vec{a}_j^\alpha / |\vec{a}_j^\alpha|$. Furthermore, it is that $|\vec{a}_j^x| = |\vec{a}_j^y| \equiv a_j^\perp$, which we define as the perpendicular coupling constant. Equivalently, we define the parallel coupling component along the quantization axis of the nuclear spin in the rotating frame, i.e. $a_j^\parallel \equiv |\vec{a}_j^z| = \hat{\omega}_j \cdot \vec{A}_j$.

For a moment, let us focus on the modulation function $F(t)$. While in theory this function can represent arbitrary pulse sequences only composed of π -pulses, here we want to further assume that it is an even [i.e. $F(-t) = F(t)$] periodic function. The periodicity is a useful feature when non-instantaneous pulses are considered, as pulse errors can be averaged out by specific pulse phase constructions, as we will mention in Section 3.3. These assumptions allow to cast the modulation as a Fourier series, $F(t) = \sum_{l=1}^{\infty} f_l \cos(l\omega_{\text{DD}}t)$, where ω_{DD} is the DD frequency defining the period by $F(t + 2\pi/\omega_{\text{DD}}) = F(t)$ (compare also the example treated in Section 3.1). Consequently we have the Fourier coefficients $f_l = \int_{-\infty}^{\infty} dt F(t) \cos(l\omega_{\text{DD}}t)$, with $f_l = 0$ for even l as the function is symmetric (also $f_0 = 0$ because of the zero mean). The terms corresponding to different l are called the different harmonics for $F(t)$. For a conventional pulse series, e.g., the CPMG series of Sections 3.1 and 3.3, one finds that $f_l = 4 \sin(\pi l/2)/(\pi l)$, where $l > 0$.

Plugging these definitions into the Hamiltonian yields

$$H_I(t) = \frac{m_s}{2} \sigma^z \sum_{l=1}^{\infty} f_l \cos(l\omega_{\text{DD}}t) \sum_{j=1}^J \left\{ a_j^\perp \left[I_j^x \cos(\omega_j t) + I_j^y \sin(\omega_j t) \right] + a_j^\parallel I_j^z \right\}, \quad (3.18)$$

where it is already justified to neglect terms proportional to I_j^z since $F(t)$ oscillates with zero mean. Let us target nuclear spin n with harmonic l_{DD} , i.e. we require $l_{\text{DD}}\omega_{\text{DD}} = \omega_n$. Moreover, we use that $I_j^\pm = (I_j^x \pm iI_j^y)/2$ and neglect all terms oscillating with the sum of two frequencies by virtue of the RWA. Subsequently we can distinguish different contributions in the Hamiltonian

$$\begin{aligned} H_I(t) = & \frac{m_s}{8} \sigma^z \left[f_{l_{\text{DD}}} a_n^\perp (I_n^+ + I_n^-) \right. \\ & + \sum_{\substack{l=1 \\ l \neq l_{\text{DD}}}}^{\infty} \sum_{j=1}^J f_l a_j^\perp \left(e^{-i(\omega_n/l_{\text{DD}} - \omega_j)t} I_j^+ + e^{i(\omega_n/l_{\text{DD}} - \omega_j)t} I_j^- \right) \\ & \left. + \sum_{\substack{j=1 \\ j \neq n}}^J f_{l_{\text{DD}}} a_j^\perp \left(e^{-i(\omega_n - \omega_j)t} I_j^+ + e^{i(\omega_n - \omega_j)t} I_j^- \right) \right], \end{aligned} \quad (3.19)$$

where most of them are off-resonant but require different conditions under which these can be

suppressed. To neglect the terms in the second and third line, it is required that

$$l_{\text{DD}} |a_j^\perp| \ll |\omega_n l - \omega_j l_{\text{DD}}| \quad (3.20)$$

and

$$f_{l_{\text{DD}}} |a_j^\perp| \ll |\omega_n - \omega_j| \quad (3.21)$$

hold for any $j \neq n$ respectively. Fulfilling these conditions is particularly challenging. For a strong magnetic field, i.e. $|\gamma_j B_z| \gg |\vec{A}_j|$ we have $\omega_j \sim |\gamma_j B_z|$ [see Eq. (2.9)] and the first condition in Eq. (3.20) reduces to

$$l_{\text{DD}} |a_j^\perp| \ll |B_z(\gamma_n l - \gamma_j l_{\text{DD}})|. \quad (3.22)$$

This explains possible overlap of different harmonics between target spins of different species, i.e. there might be a combination of gyromagnetic ratios and harmonics such that $|\gamma_j l - \gamma_n l_{\text{DD}}| \ll 1$. We stress here that the effect is not the one of *spurious harmonics* which we will discuss later in Section 7.2. In the filter function formalism, this condition corresponds to the windows in the filter, which appear periodically at higher frequencies and may lay on a further peak in the spectrum $S(\omega)$ [see the discussion at the end of Section 3.1 and Figure 3.2 (b)]. For identical species with gyromagnetic ratio γ , we obtain

$$l_{\text{DD}} |a_j^\perp| \ll |\gamma B_z| |l - l_{\text{DD}}| \Rightarrow |a_j^\perp| l_{\text{DD}} \ll |\gamma B_z|, \quad (3.23)$$

where we used that $|l - l_{\text{DD}}| \geq 1$. Obviously, we can always fulfill the condition for equal species by increasing the strength of the external field. The second condition, Eq. (3.21), represents the fact that the Larmor frequencies need to possess a finite detuning, otherwise they are indistinguishable. In the filter formalism, this is represented by the finite width of the window. For a high magnetic field, the detuning yields

$$f_{l_{\text{DD}}} |a_j^\perp| \ll |\omega_n - \omega_j| \approx \left| B_z (|\gamma_n| - |\gamma_j|) + \frac{m_s}{2} [\text{sgn}(\gamma_j) A_j^z - \text{sgn}(\gamma_n) A_n^z] \right| = \frac{1}{2} |A_j^z - A_n^z|, \quad (3.24)$$

where the equality on the right is true for targets of the same species, i.e. $\gamma_j = \gamma_n$, and we introduced the sign function $\text{sgn}(\bullet)$. Crucially, increasing the magnetic field might not help in the case at hand, especially for unique species. Then, one can only decrease $f_{l_{\text{DD}}}$ to match the condition. Conventionally, this is done by using a higher harmonic of the DD sequence, i.e. increasing l_{DD} while keeping $\omega_{\text{DD}} l_{\text{DD}} = \omega_n$ constant. This will yield a decreased $f_{l_{\text{DD}}}$, e.g., for

a CPMG sequence we have $f_{l_{\text{DD}}} \sim 1/l_{\text{DD}}$. On the other hand, l_{DD} also appears on the left-hand side of Eq. (3.20), hence increasing the used harmonic is simultaneously increasing the risk of potential influences of other harmonics. Thus, this trade-off has to be well considered. A solution to this dilemma will be presented in Section 3.3.2 where we introduce a pulse sequence that grants control over $f_{l_{\text{DD}}}$ without using higher harmonics.

Nevertheless, assuming that both conditions are satisfied, we arrive at the effective Hamiltonian targeting spin n ,

$$H_{\text{eff},n} = \frac{m_s}{4} f_{l_{\text{DD}}} a_n^\perp \sigma_n^z I_n^x, \quad (3.25)$$

realizing coherent control on the target spin via the NV center. In the case shown here, rotations of the spin around the \hat{x} axis can be performed. If we would have chosen an antisymmetric modulation function $F(t)$, the Fourier expansion would consist of sin functions and the spin would rotate around the \hat{y} axis [22]. Let us further remark that rotations around \hat{z} can not be performed by these methods, since the $\sigma_n^z I_n^z$ terms are always removed due to the averaging. However, a different scheme enabling also such a gate has been proposed [219].

A crucial difference in the description of DD using either the effective Hamiltonian approach or the filter formalism is that the latter only influences the phase of the system qubit, while the former describes the interaction to a nuclear spin. Hence, only the Hamiltonian approach explicitly reveals the backaction of the nuclear spin, which allows the application of gates via the electron spin. In particular, the electron-nuclear spin pair can become entangled. In sensing scenarios, it is exactly this correlating process which ultimately yields a signal, while in the filter formalism this is less clear. In fact, the origin of the coherence modulation described by Eq. (3.12) is disconnected from a microscopic model describing the environment, hence quantum features are excluded.

3.3. Pulse Sequences

Unavoidably, the application of a population inverting pulse is not perfect. In practice, different kinds of errors altering the obtained signals are introduced. Relaxing the assumption of an instantaneous pulse as employed until now, the two main sources of signal distortion are detuning and amplitude errors. For a detuning error to occur, the pulse drive is off-resonant, i.e. $\delta \neq 0$ in Eq. (2.14). Amplitude errors are observed when the rotation angle is not matched, e.g. $\Omega t_{\text{pulse}} \neq \pi$ for a π -pulse. The reasons behind their appearance are manifold. Detunings can originate from the side of the device generating the pulse, e.g., an arbitrary waveform generator which slightly fluctuates in the frequency generated. However, also the system itself might

experience drifts in its resonance frequency originating from thermal fluctuations or interaction with other noise sources nearby. For example, the nitrogen spin in the case of NV centers can induce shifts in the transition frequency of up to 1 MHz due to the hyperfine interaction [74]. Amplitude errors occur when the duration of the application of the field and the corresponding Rabi frequency do not match. This results in a pulse which rotates more or less than the desired angle, caused by either fluctuations in the generated power (Ω fluctuates) or imprecise on/off toggling (t_{pulse} varies). Further errors one might think of are errors in the timing of the precise moment where the pulse is applied or the phase of the applied field determining the phase of the pulse (see Section 2.2.2). However, the latter two are generally under sufficiently good control, at least in setups operating with NV centers which we are primarily discussing here. Therefore, we will neglect those imperfections.

The main approach to overcome these errors is a sophisticated use of the pulse phases introduced in Section 2.2.2. In the context of NMR, a whole forest of sequences has been presented [71–73, 217, 218], whose purpose was to achieve a robust experimental implementation of the refocusing, in order to increase the number of pulses resulting in longer evolution times and increasing the frequency sensitivity (compare Section 3.1). It turned out to be favorable when the rotation axis of the pulses is alternated according to a suitable pattern which results in "destructive interference" of the errors, i.e. they are averaged out. Therefore, a combination of considerably poor quality pulses is still able to assemble a robust sequence [72]. Naturally, these concepts found their way into the field of dynamical decoupling of quantum systems aiming at the realization of the modulation $F(t)$ [65, 66, 220–222, H1]. Importantly, pulse errors are neither included in the filter formalism (Section 3.1) nor the effective Hamiltonian approach (Section 3.2), as both deal with ideal, instantaneous pulses. Nevertheless, if one manages to suppress the mentioned errors, the restriction to instantaneous pulses is not critical. Both approaches will accurately predict the obtained dynamics given the pulses are applied fast enough, i.e. t_{pulse} is the fastest timescale involved in the dynamics. Surely, the regime where this assertion holds has to be defined properly.

Another aspect of engineered pulse sequences are the development of sophisticated modulation functions, which add control of further features of the filter function. A common approach is to deviate from the common π/ω_{DD} pulse spacing by altering the distribution of the pulse locations or add further pulses in between [70, 196, 216, 223, H1]. We will exploit this concept in Chapter 8 to design a sequence which transforms the typical sinc shape [81] of the peaks in the filter function into a Gaussian shape.

However, let us first introduce the sequence patterns we require throughout this work.

3.3.1. CPMG and the XY-Family

Carr-Purcell-Meiboom-Gill (CPMG) sequences [217, 218] and the sequences of the XY-family [71, 73] generate the same modulation function $F(t)$ with equidistant pulses as displayed in Figure 3.3 (a). Hence both sequences yield equivalent filter functions and effective Hamiltonians. However, the CPMG-sequence only invokes one pulse phase for all the pulses. It turns out that this is a good choice for longitudinal states (i.e. their initial phase is equivalent to the pulse phase modulo π). In fact, Figure 3.1 displays exactly this specific case. Contrary, for transversal states, pulse errors quickly accumulate, which introduces additional decoherence effects¹¹ [65]. The XY-family relies on an alternating pulse phase and additional symmetric constructions, which preserves states with an arbitrary initial phase. One denotes an arbitrary but chosen pulse phase φ by X. Consequently the pulse phase denoted by Y is then given by $\varphi + \pi/2$. The two mostly used constructions are given in Table 3.1, where the order of the dimensionless expansion parameter η denotes the order where errors appear. The orders can be straightforwardly calculated employing equally spaced pulses and a pulse operator of the form

$$R_\pi(\varphi) = \exp \left\{ -i \frac{\pi}{\Omega} \left[\tilde{\delta} \eta \sigma^z + (\Omega + \tilde{\epsilon} \eta) (\sigma^x \cos \varphi + \sigma^y \sin \varphi) \right] \right\}, \quad (3.26)$$

where the tilde denotes quantities rescaled in terms of η , while δ, ϵ are small detuning and amplitude errors respectively [indeed, compare Eq. (2.14)].

Table 3.1.: **Pulse phases and error suppression in the XY-family of DD sequences.** The overline denotes an additional phase shift of π .

	phase	order of the errors
XY-4	XYXY	$O(\eta^2)$
XY-8	XYXY YXYX	$O(\eta^3)$
XY-16	XYXY YXYX <u>XYXY YXYX</u>	$O(\eta^4)$

All of these sequences are already remarkably robust. CPMG has been demonstrated to yield good coherence protection with up to 10.000 pulses in NV centers [137] and rare-earth-doped crystals [224] as well as 10.000 pulses according to the XY-8 pattern in NV centers [180]. Furthermore, an XY-16 sequence consisting of over one million pulses was implemented for a phosphorus nuclear spin in silicon [225]. Finally, let us note that for all CPMG and XY

¹¹Note that the CPMG sequence shares this effect with the *Uhrig-DD* sequences, which also apply all pulses around a single axis but vary the spacing between the pulses [196].

sequences, the Fourier series of $F(t)$ is given by

$$F(t) = \sum_{l=1}^{\infty} f_l \cos(l\omega_{\text{DD}}t) \quad \text{where} \quad f_l = \frac{4}{l\pi} \sin\left(\frac{\pi l}{2}\right), \quad (3.27)$$

which restricts the available set of effective Hamiltonians [recall Eq. (3.18)] that is producible, since the only way to change the amplitude $a_n^\perp f_{l_{\text{DD}}}$ is to move to a different harmonic. Moreover, each application of an XY- k sequence requires an integer number M of $k/2$ DD periods, i.e. an XY- k sequence has at last the evolution time $\pi k/\omega_{\text{DD}}$. Therefore, the set of rotation angles $Mk\pi f_{l_{\text{DD}}} a_n^\perp/\omega_{\text{DD}}$ is discontinuous, which finally restricts the assembly of arbitrary gates. On this account, the development of a pulse sequence granting continuous control over $f_{l_{\text{DD}}}$ is motivated, which indeed is the subject of the next section.

3.3.2. Adaptive-XY Sequences

The ideas of this section have been developed in publication [H1].

The key feature of the *adaptive-XY* (AXY) sequences [H1] is the removal of the strict inverse proportionality $f_l \propto l^{-1}$ of the Fourier components for the modulation function of the CPMG and XY sequences [see Eq. (3.27)]. Instead, a more sophisticated method to specify their value is provided. Besides removing the disadvantage of discrete rotation angles as mentioned briefly at the end of Section 3.2, the AXY sequences drastically simplifies the addressing of single targets (i.e. specific frequency components) by decoupling the conditions given in Eqs. (3.20) and (3.21).

The AXY sequences extend the XY-family by adding another layer of complexity. Let us refer to Figure 3.3. As shown in panel (a) and (b), the first step is the consideration of a usual XY-4 (XY-8) sequence as given in Table 3.1. For the new second step, the sequence is modified such that around each π pulse four additional π -pulses are applied. This construction is interpreted as a *composite pulse* now consisting of five consecutive population inverting pulses, see Figure 3.3 (c). The five consecutive pulses possess a non-equal spacing which is characterized by the quantities ξ_1 and ξ_2 . At the same time they are stringently symmetric around the third pulse. The third pulse is located at the instant in time where the conventional sequences introduced above would apply their single pulse. Emerging from the fact that ξ_1 and ξ_2 can be chosen from a certain parameter range to tune different properties in a desired manner, depending on the individual problem at hand, these sequences were given the prefix "adaptive". A seeming drawback in the design of the sequence is the requirement of five times more pulses compared to the conventional XY sequences. Consequently, it has to be designed circumspectly to suppress pulse errors as much as possible. Fortunately, the KDD sequence [221] proposes a ten pulse pattern, where the first five pulses realize the phases $\pi/6 - 0 - \pi/2 - 0 - \pi/6$, while the phases for the next five pulses are shifted by π as shown in Figure 3.3 (c). As a result, these five-pulse building blocks are associated with either an adaptive-X or an adaptive-Y pulse. It turns out that despite the KDD sequence was developed for equally spaced pulses, the symmetric construction of the AXY composite pulses in an AXY-4 (AXY-8) sequence suppresses pulse errors including the first (second) order terms [H1].

The modulation function $F(t)$ describing the effect of the AXY sequence is sketched in Figure 3.3 (d). Calculating the Fourier series of the modulation function leads to the Fourier

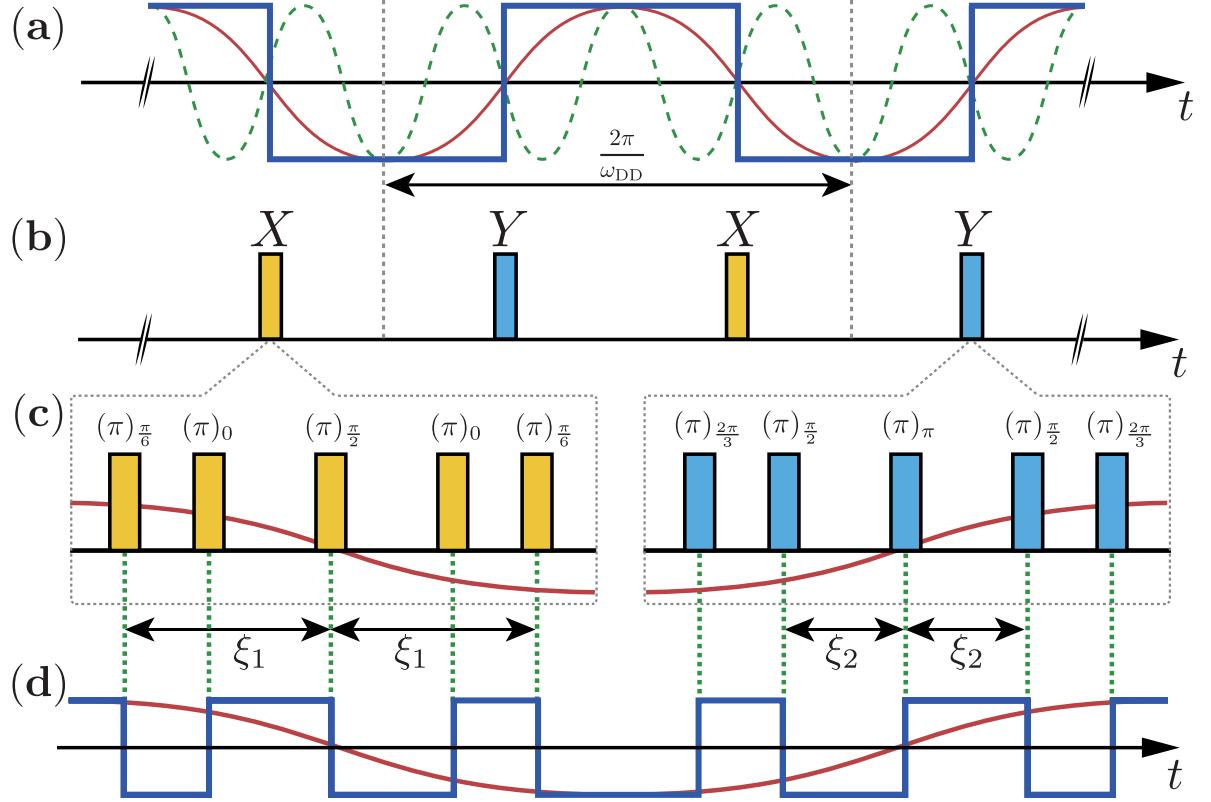


Figure 3.3.: The pulse scheme of the XY and AXY sequences. The AXY sequences are an extension of the XY sequences. A standard modulation function of CPMG or XY- k with four pulses is displayed in (a) via the blue solid curve. The first and third harmonic of the corresponding Fourier series are drawn in red and green (dashed) respectively. The equidistant pulse spacing is fixed by ω_{DD} , where two pulses are applied per period. The pulses toggling the sign of $F(t)$ are shown in (b). Here, an XY-4 sequence has been chosen exemplary. Pulses are applied at the moments where $\cos(\omega_{DD}t) = 0$. For the AXY sequence, around each π -pulse, four additional pulses are applied, building either a composite-X pulse (yellow) or composite-Y pulse (blue), see panel (c). The pulse phases φ_i are specified according to the KDD sequence and noted as $(\pi)_{\varphi_i}$, while the pulse spacing inside the composite pulses is determined by ξ_1 and ξ_2 . We remark that both composite pulses possess the same interpulse-spacing. The red curve marks the first harmonic of $F(t)$. Hence, the central pulse is applied at the same time as it would have been done in a usual XY sequence. This is also illustrated by the modulation of the AXY sequence shown in (d).

coefficients

$$f_l(\xi_1, \xi_2) = \frac{4}{l\pi} \left\{ \sum_{j=1,2} (-1)^j \left[(-1)^k - 1 \right] \sin \left[2\pi l \left(\frac{1}{4} - \xi_j \right) \right] + \sin \left(l \frac{\pi}{2} \right) \right\}, \quad (3.28)$$

where it is evident that the parameters ξ_1, ξ_2 change the coefficients without changing the harmonic l . To close this section, we now present two convenient choices of ξ_1 and ξ_2 that allow to suppress the influence of a neighboring harmonic.

1. Let us choose $l_{\text{DD}}\omega_{\text{DD}} = \omega_{\text{target}}$ with $l_{\text{DD}} = 1$. The flexible pulse spacing allows to fix $f_2 = f_3 = f_4 = 0$, while $f_1 = f_{l_{\text{DD}}}$ can be tuned to any value $|f_1| < 4|1 - 2\cos\frac{\pi}{9}|/\pi$. In particular, this is true for a pulse spacing

$$\xi_{1/2} = \frac{1}{4} - \frac{1}{2\pi} \arctan \frac{\pm(2f_1\pi - 12)w_1 + \sqrt{3}w_2}{\sqrt{6}\sqrt{w_2 - 96f_1w_1\pi \pm w_1^2\sqrt{3}w_2}}, \quad (3.29)$$

where we have the functions $w_1 = 4 - f_1\pi$ and $w_2 = w_1[960 - 144f_1\pi - 12(f_1\pi)^2 + (f_1\pi)^3]$.

2. If one desires to apply less pulses during the same evolution time, one can use the third harmonic $l_{\text{DD}} = 3$ to address the target frequency. Then, one may choose $f_1 = f_2 = f_4 = 0$, while a desired value for f_3 needs to fulfill $|f_3| < \frac{\pi}{4}$. One arrives at

$$\xi_{1/2} = \frac{1}{2\pi} \arctan \sqrt{\left[\frac{4}{\sqrt{5 + \pi f_3} \mp 1} \right]^2 - 1}. \quad (3.30)$$

We remark that these are just two possible examples where the sequence enables control of two Fourier coefficients at the same time. Finding the solutions, requires to solve a system of two equations fixed by Eq. (3.28) (thereby recall that $f_l = 0$ for $l = 0$ and any even l).

Part II.

Noisy Frequency Estimation in the Framework of Quantum Metrology

CHAPTER 4

Noisy Quantum Metrology: Frequency Estimation

Large parts of this chapter are published in [H6].

Parameter estimation within the framework of quantum metrology is a paradigmatic example of the advantage provided by the use of quantum features when compared to a classical setting [18]. Increasing attention to the field has put it into context with quantum technologies striving for commercial applications [6, 7]. At its core lies a framework for the most precise estimation of physical parameters possible [11–13, 226, 227], where specialized measurement protocols can surpass the *Standard Quantum Limit* (SQL) of precision which is governed by classical statistics [29]. The recent progress allows for a wide spectrum of applications in magnetometry [228, 229], the determination of atomic transition frequencies [31, 32], biological imaging [230], the stabilization of atomic clocks [231, 232] or the detection of gravitational waves¹ [235–238].

Besides many other quantum features improving the precision in quantum estimation (or equivalently "sensing") experiments [227], great effort has been dedicated to the examination of multi-probe scenarios whose inter-probe entanglement allows to surpass the SQL [19] by means of a scaling in the number of probes employed. For example, implementation of the

¹Unarguably, one of the most sensational results is the experimental observation of gravitational waves [233]. However, these results have been obtained by pushing conventional laser technology to its edge, accompanied by numerous other noise stabilization mechanisms. Nevertheless, at higher detection frequencies (> 70 Hz) they were operating at the SQL [234].

latter has been demonstrated in NMR experiments [239, 240].

During the course of this chapter, we will give an introduction to the particular case of *frequency estimation*. Thereby it is of greatest importance to discuss the protocol employed for the estimation process of the frequency, where we consider the so called *parallel estimation with an independent noise model*. This discussion, along with an introduction to the mathematical tools and procedures are given in Sections 4.2.1 and 4.3, where we also cover a basic example to derive the ultimate limit which is set by the *Heisenberg Limit*. Nevertheless, this limit only holds for unitary evolutions, hence examinations of the ultimate precision limits under the influence of noise are contained in Section 4.4. After some final remarks in Section 4.5 concerning, e.g. the role of non-Markovianity or terminology appearing in different research areas, we will go beyond the discussed model and have a brief review of correlated noise or time dependent control and encoding methods in Sections 4.6.1 and 4.7.

We already want to stress that basic theory presented in this chapter has its origins in classical estimation theory [29] and is by no means due to a quantum mechanical phenomenon, as the connection to quantum mechanics only arises solely from the statistical nature of quantum measurements. Any theory, may it be quantum or classical, that contains probabilistic outcomes is a suitable candidate for the application of the tools presented here. To give a concrete example, we will start this chapter in Section 4.1 with the analysis of a coin toss.

For further reading we also refer to the reviews on quantum enhanced metrology with atomic ensembles [226], trapped ions and cold atoms [11] or optical interferometry [12].

4.1. Motivation

Let us first present a simple estimation problem, which allows us to illustrate how most basic notions and tools we are going to discuss in the coming sections have their roots in classical statistics and, in particular, in the quantification of measurement errors. We want to exemplify this along the lines of the following example.

Imagine, one has N identical coins, where a flip of an individual coin either gives heads with probability p_h or tails with p_t . We stress that the only necessity to introduce these probabilities is our lack of knowledge of the exact initial conditions of the coin flip. The introduction of these probabilities is a way to describe the experiment statistically, while each flip and the subsequent observation of head or tail is completely deterministic and will depend on certain parameters of the coin which are too complicated to access, hence we resort to the much simpler quantification of the coin via its probabilities for heads and tails. To that end, one way to proceed is to flip each coin ν times to estimate p_h . Then, the probability variable X describing the number of

heads after νN tosses is distributed according to binomial distribution

$$B(X = x|p_h, \nu N) = \binom{\nu N}{x} p_h^x (1 - p_h)^{\nu N - x}, \quad (4.1)$$

with x the number of heads found. Our best guess for p_h is then obviously $\hat{p}_h = x/(\nu N)$: we simply take the ratio between the number of observed heads and the total number of tosses. Indeed, p_h coincides with the expectation value $\langle X/(\nu N) \rangle$. However, due to the finite quantities N and ν , our guess will carry an error. A natural way to quantify this error is the variance

$$\text{var} [\hat{p}_h] = \text{var} \left[\frac{X}{\nu N} \right] = \frac{p_h(1 - p_h)}{\nu N}. \quad (4.2)$$

Note that the variance is never equal to zero, besides the two special cases $p_h = 0, 1$, while the best strategy is to flip as many coins as often as possible. However, it is important to stress that the probabilities used to calculate the variance are not known as they themselves are the parameters to be estimated. As a consequence, the variance will never vanish in practice since the certain determination of the probabilities would require an infinite number of tosses.

To go a step further, we now assume that we are able to determine a parameter which changes the result of a coin toss, let's say its roundness r . Therefore, using the statistical model, it will change the probability of finding head and we assume that we know the deterministic dependence $p_h(r)$. An estimate of r is then immediately given by the inverse function² $r(p_h) = p_h^{-1}(r)$ and we can use error propagation to find the variance on our estimate of r ,

$$\text{var} [\hat{r}] = \frac{\text{var} [\hat{p}_h(r)]}{[dp_h(r)/dr]^2} = \frac{p_h(r)[1 - p_h(r)]}{\nu n} \left[\frac{dp_h(r)}{dr} \right]^{-2}. \quad (4.3)$$

In essence, it will turn out that this equation (or slight variations) is the working horse for estimation tasks we will deal with in the following. While we will perform generalizations to include the particularities of quantum mechanics in our theoretical descriptions, any quantification in sensing experiments can be linked to it [13].

Indeed we may compare the results above with an experiment utilizing quantum coins, i.e. two level systems (qubits). We replace the coins by N qubits, each in the state $|x_+\rangle$, an eigenstate of the Pauli spin matrix σ^x . Instead of a toss, we perform a unitary operation $U = \exp(-i\phi\sigma^z/2)$ and measure the survival probability p_s of the state (note that this is conceptually a Ramsey

²This function is not always guaranteed to exist. However, we may assume here that for all practical situations this is possible at least in a small region around r .

experiment [78]):

$$p_s = |\langle x_+ | U | x_+ \rangle|^2 = \cos^2 \frac{\phi}{2}. \quad (4.4)$$

Following the same ideas as above, we determine p_s by the number of qubits found in $|x_+\rangle$ divided by νN , consequently $\text{var} [\hat{p}_s]$ and $\text{var} [\hat{\phi}]$ are immediately given by Eqs. (4.2) and (4.3) respectively.

We can directly use these relations to derive a well known bound in frequency estimation following [34]. Here the role of ϕ is taken by $\omega_0 t$ where ω_0 is the frequency to estimate (i.e. the role of r) while t represents the time required to perform the unitary transformation. Because this time limits the number of repetitions, we also rephrase $\nu = T/t$ in terms of a total time T that we have at our disposal to perform the measurement. Hence, we use Eq. (4.3) and obtain

$$\text{var} [\hat{\omega}_0] = \frac{1}{n\nu t^2} = \frac{1}{ntT}. \quad (4.5)$$

This equation manifests the so called *Shot Noise Limit* [28] or *Standard Quantum Limit* (SQL). While this term is used in the context of experiments involving quantum mechanics, its true origin lies, as we saw above, in the finite sample size of the underlying probability distribution. In other words, this effect is inevitable when dealing with randomly distributed data. Crucially, in quantum mechanics every experiment includes probability as an inherent feature. Thereby note that quantum mechanics is a probability theory itself, however, it is non-contextual. In other words, there are no deterministic processes which are ignored due to inaccessibility. With the recent developments in quantum technologies, promising sensors exploiting quantum mechanics have been put into the near future, explaining the rising interest in the field of quantum metrology.

4.2. The Frequency Estimation Protocol - Analyzing a Specific Measurement Procedure

In this section, we want to analyze a specific measurement setup, in particular, we will use a Ramsey protocol [78] that we utilize to measure the energy separation in a qubit. Indeed, the Ramsey experiment is nothing else than the quantum coins introduced in the section before.

Imagine we possess N atoms and each can be modeled by two levels with a splitting of ω_0 (we take $\hbar = 1$ throughout the whole work). For any of those atoms, we can assume the Hamiltonian $H_0 = \omega_0 \sigma^z / 2$. Following the Ramsey scheme outlined in Figure 4.1 (a), we initialize each qubit in its ground state $|0\rangle$ and apply a Hadamard gate C_h which brings each of these qubits into an equally weighted superposition $(|0\rangle + |1\rangle) / \sqrt{2}$. Subsequently, these atoms are let to evolve freely for a time t where they will collect a phase $\omega_0 t$ such that the state is given by $(|0\rangle + \exp(-i\omega_0 t) |1\rangle) / \sqrt{2}$. A second Hadamard gate will transfer the phase onto a population difference, which we measure via a suitable detector. The probability to find the qubit in $|0\rangle$ is then

$$p_{\omega_0 t}(|0\rangle) = \left| \langle 0 | C_h e^{-it\omega_0 \sigma^z / 2} C_h | 0 \rangle \right|^2 = \cos^2 \frac{\omega_0 t}{2}. \quad (4.6)$$

Indeed, we have $C_h |0\rangle = |x_+\rangle$ and thus everything is totally equivalent to the quantum coin example made in the introduction. However, the Ramsey experiment clearly illustrates the three stages present in a *quantum frequency estimation protocol* (FEP), see Figure 4.1, which will be the topic in the following. Other configurations are indeed possible [19, 26]. The first step is the *preparation* of an input state for the *probe*. Here, the probes are the qubits and the preparation is represented by the initialization and the application of the first Hadamard gate. It is followed by the *encoding* which lasts for a *time* t . The third step is then the *measurement* of the probe, where we include the second Hadamard gate.

Crucially, any specification of an achievable precision needs to be on a common ground. For that matter, we choose the number of probes N and the total time T as the *resources* we have at our disposal. In particular, we assume the preparation and measurement process not to consume any resources, meaning the time needed for preparation and readout is negligibly small. An analysis relaxing this assumption can be found in [241].

4.2.1. The Cramér-Rao Bound

As for the Ramsey setup, we will restrict to frequencies which are a linear parameter in the Hamiltonian H_0 . Throughout this review, ω_0 always denotes the parameter (or frequency) to be estimated. We already emphasize that in this context a *probe* denotes the reduced quantum

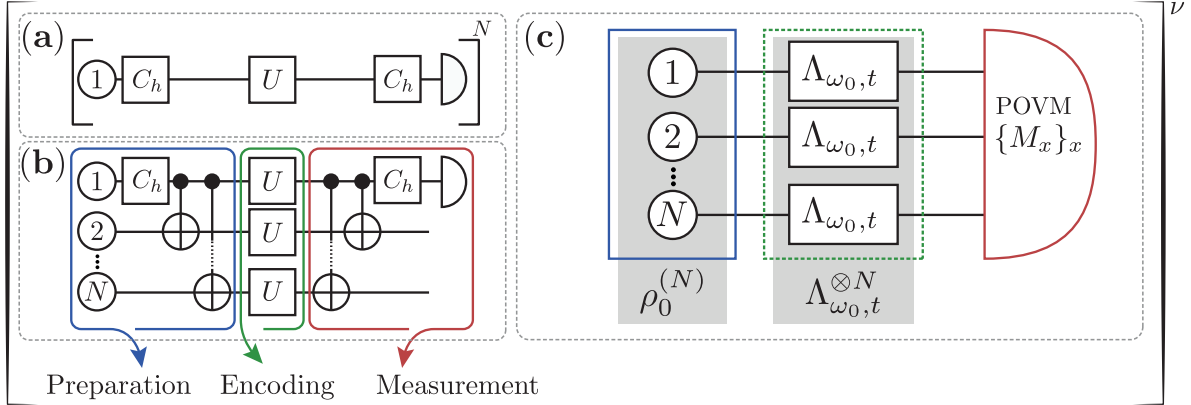


Figure 4.1.: **The frequency estimation protocol.** (a) Shows a single probe Ramsey type protocol for the quantum coins described in the main text. A Hadamard gate C_h creates a state sensitive to the field during the free evolution U . After a second Hadamard gate, the state is measured and the sequence is repeated. In (b), the N probes are prepared in a GHZ state via the Hadamard and CNOT gates. The free evolution acts independent on each probe, which is the main characteristic of the FEP. Subsequently, the state is disentangled which allows to perform a measurement on the first probe only. Note that for other setups than the Ramsey scheme, the building blocks in the FEP may appear substantially different. All elements of (b) are assigned to either the preparation (blue), the encoding (green) or the measurement stage (red). These stages are generalized in the cFEP in panel (c). For the preparation, any state involving all N probes is considered, while the product $\Lambda_{\omega_0,t}^{(N)} = \Lambda_{\omega_0,t}^{\otimes N}$ is allowed to describe any physical transformation, while the POVM invoked to describe the measurement has the only restriction to be independent of ω_0 . (Figure first published in [H6])

system we utilize for the estimation. This will become important later when noise is introduced into the system.

In general, a completed cycle of the FEP can be repeated several times. Obviously, the number of repetitions is fixed by the total time divided by the interrogation time, $\nu = T/t$. After each of these cycles, an outcome is detected. We collect all of these outcomes in the vector \vec{x} . To deduce ω_0 from the outcomes, an *estimator* $\hat{\omega}(\vec{x})$ is constructed. Depending on the measured outcomes, the estimator yields an estimate $\hat{\omega}(\vec{x}) = \tilde{\omega}_0$ of the true value ω_0 . Let's emphasize here that the estimator itself is a random variable, as the input (outcome of the measurement, i.e. the observation) is a random variable itself, i.e. \vec{x} is one specific realization of the random variable \vec{X} . Therefore, it is possible to calculate different moments of the estimator's probability distribution. We stress that the expectation value denoted by $\langle \bullet \rangle_{\vec{x}}$ is taken with respect to the

possible collections of outcomes \vec{x} , i.e.

$$\langle \bullet \rangle_{\vec{x}} = \sum_{\vec{x}} p_{\omega_0}(\vec{x}) \bullet. \quad (4.7)$$

The sum runs over all possible realizations of outcomes with $p_{\omega_0}(\vec{x})$ being the probability that \vec{x} is the realization obtained via the FEP. Note that we focus here and in the following on the case where we have a discrete set of possible outcomes. Indeed, the whole description can be generalized (straightforwardly) to the case of a continuous set of outcomes. For the sake of brevity, we adopt the notation $p_{\omega_0}(\vec{x})$ for the conditional probability $p(\vec{x}|\omega_0)$ to obtain the set \vec{x} given the parameter ω_0 . However, after the data collection, we can think of $p_{\omega_0}(\vec{x})$ as the *likelihood function* for ω_0 because the observations have already been made. Then, $p_{\omega_0}(\vec{x})$ may be interpreted as a function of ω_0 quantifying how well different values would agree with the observed data set.

The explicit form of the estimator is not important for the further calculations, but we will always focus on estimators with the two following properties [29, 30].

- *Unbiasedness*, that is $\langle \hat{\omega}(\vec{x}) \rangle_{\vec{x}} = \omega_0$. A biased estimator would yield $\langle \hat{\omega}(\vec{x}) \rangle_{\vec{x}} = \omega_0 + \beta$ where we have the bias $\beta \neq 0$.
- *Consistency*, that is for all $\nu > \nu'$ there are $\epsilon(\nu'), \delta(\nu') > 0$ such that the probability $P(|\tilde{\omega}_0 - \omega_0| < \epsilon) > 1 - \delta$. Recall that ν describes the number of repetitions. In other words, in the case of an infinitely large sample size, i.e. $\dim(\vec{x}) = \xi \rightarrow \infty$, we have $\lim_{\xi \rightarrow \infty} \hat{\omega}(\vec{x}) = \omega_0$.

Note that consistency implies *asymptotic unbiasedness*, meaning that any bias β vanishes for a large sample size. We stress that the converse is not true, see Fig.4.2 for an illustration.

We define the precision of an estimator in terms of its *mean squared error* $\Delta^2 \hat{\omega}$ (MSE),

$$\Delta^2 \hat{\omega} = \left\langle (\hat{\omega}(\vec{x}) - \omega_0)^2 \right\rangle_{\vec{x}}, \quad (4.8)$$

which is a natural choice as it measures the expected squared distance of the estimate $\tilde{\omega}_0$ from the true value ω_0 . In particular, the MSE coincides with the variance of an unbiased estimator, defined as $\text{var}[\hat{\omega}(\vec{x})] = \left\langle (\hat{\omega}(\vec{x}) - \langle \hat{\omega} \rangle_{\vec{x}})^2 \right\rangle_{\vec{x}}$. While we will focus on unbiased estimators in the following, we will keep the notion of MSE instead of the variance.

For any unbiased estimator, its MSE can be bounded from below by the *Cramér-Rao bound*

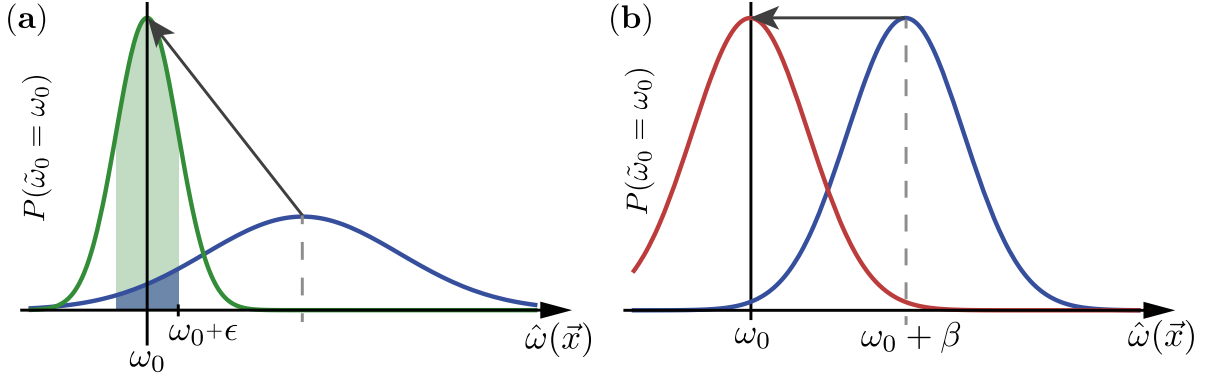


Figure 4.2.: **Properties of the estimator.** Both panels show the probability density (blue) for an arbitrary estimator, for an arbitrary large data set \vec{x} . Likewise, the second curve represents the probability density for an enlarged data set. The estimator in (a) is consistent: further data collection removes any bias, while the probability to find $|\tilde{\omega}_0 - \omega_0| < \epsilon$ increases (shaded regions). Contrary, the estimator in panel (b) is only asymptotically unbiased, as the shape of the probability density does not change. (Figure first published in [H6])

(CRB) [29, 30], which we derive in Appendix A.1. It reads

$$\Delta^2 \hat{\omega} \geq \frac{1}{\nu F_{\text{cl}}[p_{\omega_0}]}, \text{ where } F_{\text{cl}}[p_{\omega_0}] = \sum_{\vec{x}} \frac{[\partial p_{\omega_0}(\vec{x}) / \partial \omega_0]^2}{p_{\omega_0}(\vec{x})} \quad (4.9)$$

is the (*classical*) *Fisher Information* (FI). Here, the sum runs over all possible collections of outcomes \vec{x} and p_{ω_0} is the same distribution as in Eq. (4.7). Any estimator achieving equality in the CRB is termed *efficient*, but it is not a priori given that one can always find an estimator of that kind [29].

The Fisher Information is a non-negative quantity which is additive for uncorrelated events [12], i.e.

$$F_{\text{cl}}[p_{\omega_0}^{(1,2)}] = F_{\text{cl}}[p_{\omega_0}^{(1)}] + F_{\text{cl}}[p_{\omega_0}^{(2)}], \quad (4.10)$$

where $p_{\omega_0}^{(1,2)}(\vec{x}_1, \vec{x}_2) = p_{\omega_0}^{(1)}(\vec{x}_1)p_{\omega_0}^{(2)}(\vec{x}_2)$ is the joint probability distribution for the two events. This is of practical interest, as we will consider subsequent repetitions of the FEP which are uncorrelated by definition. Crucially, it is that additivity which is responsible for the ν in denominator of the CRB in Eq. (4.9). Hence we are also able to give a precise meaning to \vec{x} in the context of the FEP, which now contains the possible single run outcomes. Conversely, schemes employing an adaptive strategy, e.g. successively changing the measurement apparatus according to some prior acquired knowledge about ω_0 , are not subject to the formulation in Eq. (4.9), i.e. for them one cannot employ the sum given by Eq. (4.10). We will briefly discuss

these strategies in Section 4.6.

Furthermore, the FI is a local quantity, as it only depends on the value of probability distribution at the true value of the parameter and the first derivative. We may expand the probability distribution determining the observations,

$$p_{\omega_0+\delta\omega}(\vec{x}) = p_{\omega_0}(\vec{x}) + \frac{\partial p_{\omega_0}(\vec{x})}{\partial \omega_0} \delta\omega + O(\delta\omega^2), \quad (4.11)$$

where all terms fixing the FI are contained. Therefore, all distributions coinciding in zeroth and first order possess the same FI.

To exemplify the formalism now introduced, we directly calculate Eq. (4.3) for the setup considered in the introduction, without passing through the Bernoulli distribution. We assume the FEP to be repeated ν times. After each cycle, the possible outcome of each qubit is either $|0\rangle$ or $|1\rangle$, hence $\vec{x} = (|0\rangle, |1\rangle)$. Thereby keep in mind that each qubit is independent from the other. Using the additivity property, we first obtain $F_{\text{cl}}[\Pi_{n=1}^N p_{\omega_0,t}^n] = N F_{\text{cl}}[p_{\omega_0,t}]$, then we note that $1 - p_{\omega_0,t}(|0\rangle) = p_{\omega_0,t}(|1\rangle)$ which plugged into the CRB directly becomes the Eq. (4.3) with $p_h \mapsto p_{\omega_0,t}(|0\rangle)$. Furthermore, utilization of Eq. (4.6) directly yields the SQL Eq. (4.5).

For a further remark, note that the CRB in Eq. (4.9) is directly connected to the error propagation formula, as the FI is nothing else than the variance of an efficient, unbiased estimator. A more general derivation (see Appendix A.1) of the CRB for the estimator \hat{g}_{ω_0} of a function g_{ω_0} which is dependent on ω_0 yields [30]

$$\Delta^2 \hat{g}_{\omega_0} \geq \frac{1}{F_{\text{cl}}[p_{\omega_0}]} \left(\frac{\partial g_{\omega_0}}{\partial \omega_0} \right)^2, \quad (4.12)$$

but of course it still holds that for a suitable estimator of ω_0 , $\Delta^2 \hat{\omega} \geq (F_{\text{cl}}[p_{\omega_0}])^{-1}$. The combination yields (for efficient estimators)

$$\Delta^2 \hat{g}_{\omega_0} = \Delta^2 \hat{\omega} \left(\frac{\partial g_{\omega_0}}{\partial \omega_0} \right)^2 \Leftrightarrow \Delta^2 \hat{\omega} = \frac{\Delta^2 \hat{g}_{\omega_0}}{(\partial g_{\omega_0} / \partial \omega_0)^2}, \quad (4.13)$$

which is exactly the error propagation formula. Crucially, Eq. (4.9) and (4.13) coincide if $g_{\omega_0} \equiv p_{\omega_0}$ and $\Delta^2 \hat{g}_{\omega_0}$ is the variance of the distribution. Furthermore, for the estimation via any suitable observable O_{ω_0} , which in particular is an observable dependent on ω_0 , we can choose $g_{\omega_0} = \langle O_{\omega_0} \rangle$ and arrive at

$$\Delta^2 \hat{\omega} = \frac{\langle O_{\omega_0}^2 \rangle - \langle O_{\omega_0} \rangle^2}{(\partial \langle O_{\omega_0} \rangle / \partial \omega_0)^2}. \quad (4.14)$$

4.2.2. Noiseless Estimation with Entangled States - Obtaining Heisenberg Limited Precision

In this section, we will show that quantum features can indeed improve the achievable precision below the SQL. Therefore, we use all N probes together in a modified Ramsey setup. We stress again that all N probes are absolutely equal and each local Hamiltonian is of the form given in terms of $\omega_0 \sigma^z/2$. The modified setup, see Figure 4.1 (b), applies the Hadamard gate only on the first qubit, while there are controlled-not gates $C_{\text{not}}^{(1,n)}$ on the n -th qubit, where the first qubit acts as the control. Instead of preparing the equally weighted superposition N times, this arrangement creates an entangled *GHZ*-state [242] using the eigenstates of σ^z ,

$$\prod_{n=2}^N C_{\text{not}}^{(1,n)} C_h^{(1)} \bigotimes_{m=1}^N |0\rangle_m = \frac{|0\rangle^{\otimes N} + |1\rangle^{\otimes N}}{\sqrt{2}} = |\text{GHZ}\rangle. \quad (4.15)$$

After the encoding, the gates are applied in the reverse order and the state of the first qubit is measured. The probability of finding it in $|0\rangle$ is $p_{\omega_0,t}(|0\rangle) = \cos^2(N\omega_0 t/2)$ and a direct combination with the CRB [or Eq. (4.3)] yields (for an efficient estimator)

$$\Delta^2 \hat{\omega}_{\text{HL}} = \frac{1}{\nu t^2 N^2} = \frac{1}{t T N^2}. \quad (4.16)$$

This scheme achieves a lower bound than the SQL, by an astounding factor of $1/N$, although we used the same number N of probes and total time T as before. This limit, scaling with N^{-2} , is named the *Heisenberg Limit* (HL). It was argued to be the best achievable precision [33] and indeed, this bound can be seen as an instance of the Heisenberg uncertainty relation [27, 243]. Later in Section 4.3.1, we will see how this connection can be made.

The role of entanglement in the preparation of the input state to obtain the HL has been extensively studied [18, 244–246]. Indeed, the presence of entanglement is a strict requirement in the context of qubit probes in the FEP as considered here. However, we want to stress that it is *not* true that entanglement is a necessary ingredient to beat the SQL or even achieve the HL in isolated quantum systems, when different estimation schemes are considered. We will comment on the latter in Sec. 4.5.3 and exemplify that a scaling similar to the HL can also be reached using a single probe repetitively.

4.2.3. The Impact of Noise: Lindbladian Dephasing

In a real world experiment, the evolution of the probes is unavoidably affected by noise. To give a flavor of the works presented later in this draft, we calculate an explicit example of an evolution effected by noise. Each probe is then an open quantum system [2, 4], whose evolution is crucially shaped by the environment surrounding the probe. For the illustration of the peculiarities due to the presence of noise during the encoding stage, we restrict to a very specific kind of noise, i.e. we demand the noise to act independently but identically on each probe. Additionally, it has to be Markovian [82]. For simplicity, we restrict to pure dephasing, i.e. the probe's Hamiltonian commutes with the Hamiltonian introducing the noise, or in other words, in the basis which fixes σ_z , pure dephasing only damps the coherence elements of the probe's density matrix. This kind of noise can be seen, e.g., as a random fluctuation of the frequency, i.e., the parameter to be estimated. The evolution is then modeled by a master equation of Lindblad form,

$$\frac{d\rho}{dt} = -i[H_0, \rho] + \gamma (\sigma^z \rho \sigma^z - \rho), \quad (4.17)$$

where γ is a constant describing the decay strength of the noise.

We now repeat the calculations for the Ramsey scheme. For the scheme using N probes in parallel, we mark all quantities with the subscript "sep" (for separable), while the setup entangling the probes gets the subscript "ent". We arrive at the probabilities

$$p_{\omega_0 t}^{\text{sep}}(|0\rangle) = \frac{1 + e^{-\gamma t} \cos \omega_0 t}{2}, \quad (4.18)$$

$$p_{\omega_0 t}^{\text{ent}}(|0\rangle) = \frac{1 + e^{-N\gamma t} \cos N\omega_0 t}{2}, \quad (4.19)$$

respectively, where we recognize the N times higher oscillation frequency for the entangled state, however the exponential decay term stemming from noise obtains the same amplification. A subsequent calculation of the CRB yields

$$\Delta^2 \hat{\omega}^{\text{sep}} \geq \frac{1 - e^{-2\gamma t} \cos^2 \omega_0 t}{N T t e^{-2\gamma t} \sin^2 \omega_0 t}, \quad (4.20)$$

$$\Delta^2 \hat{\omega}^{\text{ent}} \geq \frac{1 - e^{-2N\gamma t} \cos^2 N\omega_0 t}{N^2 T t e^{-2N\gamma t} \sin^2 N\omega_0 t}. \quad (4.21)$$

Indeed, these expressions are much more involved than the corresponding results for the noiseless cases, Eqs. (4.5) and (4.16), and intuitively it is clear that the precision ought to

possess an optimal interrogation time t_{opt} . Note that for t large enough, the derivatives of the probabilities in Eq. (4.21) with respect to ω_0 vanish, which in turn causes the FI to vanish and hence the CRB diverges, see Eq. (4.9). This is also the case for $t = 0$, hence there has to be an optimal time of interrogation. To find this optimal point of operation, we minimize the CRB over the interrogation time, yielding

$$t_{\text{opt}}^{\text{sep}} = \frac{k\pi}{2\omega_0} \stackrel{!}{=} \frac{1}{2\gamma} \Rightarrow \Delta^2\omega_0^{\text{sep}} \geq \frac{2\gamma e}{NT}, \quad (4.22)$$

$$t_{\text{opt}}^{\text{ent}} = \frac{k\pi}{2n\omega_0} \stackrel{!}{=} \frac{1}{2N\gamma} \Rightarrow \Delta^2\omega_0^{\text{ent}} \geq \frac{2\gamma e}{NT}, \quad (4.23)$$

where k is an integer number. The achievable precision is exactly the same for both cases. This leads to the conclusion that product and entangled states (strategies) are metrological equivalent under local dephasing Lindbladian noise. While this is certainly true for the scaling in the number of particles, a constant improvement of a factor $1/e$ can be achieved by using different entangled states (instead of GHZ) and measurement strategies [34, 42, 43].

At this point, let us stress a subtlety related with Eqs. (4.22) and (4.23) which involve a cyclic dependence on ω_0 , γ and the optimal time, while ω_0 is actually unknown. Importantly, these, and the following limits derived on $\Delta^2\hat{\omega}$ are always understood as the best possible precision achievable. One may always interpret these limits as a second step estimation process, where ω_0 is known roughly and the rest of the strategy is adapted according to the current knowledge. This may even be done by the choice of a suitable coordinate frame, see for example Appendix A.2.1. For a more detailed discussion of this issue, see also Section 4.3.3.

Note that the just derived bounds for a single probe ($N = 1$) can be associated with the T_2 limit in quantum sensing [13, 229]. Here it is used that $\gamma = 1/T_2$, which results in an optimal time $t_{\text{opt}} = T_2/2$, and therefore the precision is said to be T_2 limited.

4.3. Ultimate Precision Limits - Analyzing Arbitrary Quantum Channels, Initial States and Measurements

To evaluate the highest achievable precision of a measurement device operating in the quantum regime, it is necessary to specify additional boundary conditions. At first, let us mention the possibility of different initial states which can be prepared. As we have already seen, the employment of entanglement yields a higher scaling of the achievable precision in the number of probes. Second, during the encoding period, the noise affects the system. While this may also be the case for a classical measurement device, here the noise can be purely quantum, e.g. the interaction with a quantized radiation field [1, 2]. And third, one can consider different possible measurement procedures. Realistically however, experimental realizations often limit this pool to a finite set.

Consequently, we consider a framework where these possibilities are taken into account. Therefore we generalize the FEP to the *frequency estimation protocol for arbitrary quantum channels* (cFEP) within the *independent noise model* and arbitrary initial states as well as arbitrary measurements. It is sketched in Figure 4.1 (c). In a first step, the N probes are prepared in an arbitrary but known state. The specific properties of this state, i.e., whether it carries coherence or correlations, are transferred to an optimization involving all possible input states. Subsequently, the probes evolve for the encoding time t . The evolution of each single probe's reduced state is described via a completely positive and trace preserving (CPTP) *dynamical map* [4] or equivalently a CPTP *quantum channel* [14]. We denote this channel by $\Lambda_{\omega_0, t}$ which acts on the total input state $\rho_0^{(N)}$ of all N probes as

$$\rho_{\omega_0, t}^{(N)} = \Lambda_{\omega_0, t}^{\otimes N} [\rho_0^{(N)}]. \quad (4.24)$$

The definition of the total map as the product of each single qubit channel, i.e. $\Lambda_{\omega_0, t}^{\otimes N} = \bigotimes_{n=1}^N \Lambda_{\omega_0, t}^{(n)}$, is a necessity of the independent noise model. It ensures that all probes undergo the same evolution, i.e. the impact of noise on each probe is individual but identical, while it forbids direct and environmentally mediated interactions of the probes during the interrogation time. The index ω_0 reminds that the channel possesses a dependence on the parameter to be estimated.

The last step in the protocol is the measurement. Again, this is kept completely general in terms of the allowed measurements, i.e. they may be local on a single probe or global measurements on an arbitrary number of the probes. Needless to say, the choice of the measurement will

fix the probability distribution of outcomes, which in turn fixes the Fisher Information and therefore the CRB. In this section, we will see how in the quantum framework it is possible to get an explicit form for the best possible precision, maximized over all the measurement procedures.

4.3.1. Quantum Fisher Information and Quantum-CRB

Indeed, a chosen measurement transfers a statistical operator (quantum state) to a (classical) probability distribution. A generic quantum measurement is described by a *positive operator valued measure* (POVM), $\{M_x\}_x$ whose elements are positive-semidefinite operators associated with outcome x for which it holds $\sum_x M_x = \mathbb{1}$. Choosing a POVM fixes the probability distribution $p_{\omega_0,t}^{(N)}$, i.e. the probability to obtain outcome x is $p_{\omega_0,t}^{(N)}(x) = \text{tr} [M_x \rho_{\omega_0,t}^{(N)}]$. Following [27, 41], the maximization of the FI over all POVMs yields the *Quantum-Fisher-Information* (QFI)

$$F_Q [\rho_{\omega_0,t}^{(N)}] := \max_{\{M_x\}_x} F_{\text{cl}}[p_{\omega_0,t}^{(N)}(x)] = \text{tr} [\rho_{\omega_0,t}^{(N)} L_{\omega_0,t}^2]. \quad (4.25)$$

Here, $L_{\omega_0,t}$ is the *symmetric logarithmic derivative* (SLD) of the state $\rho_{\omega_0,t}^{(N)}$, which itself completely determines the QFI. Note that here we restrict to POVMs independent of ω_0 , otherwise additional contributions appear [247]. The SLD is implicitly defined as

$$\frac{\partial \rho_{\omega_0,t}^{(N)}}{\partial \omega_0} = \frac{1}{2} (L_{\omega_0,t} \rho_{\omega_0,t}^{(N)} + \rho_{\omega_0,t}^{(N)} L_{\omega_0,t}), \quad (4.26)$$

which is an instance of the Lyapunov equation [248] and more ore less states one of the core problems in quantum metrology. There exists an explicit solution to this equation, namely in the basis that diagonalizes ρ , $L_{\omega_0,t}$ can be expressed as

$$L_{\omega_0,t} = \sum_{\{j,k|p_{jj}+p_{kk} \neq 0\}} \frac{2}{p_{jj} + p_{kk}} \langle j | \frac{\partial \rho_{\omega_0,t}^{(N)}}{\partial \omega_0} | k \rangle | j \rangle \langle k |, \quad (4.27)$$

where $p_{jk} = \langle j | \rho_{\omega_0,t}^{(N)} | k \rangle$. However, the involved diagonalization renders this problem numerically infeasible for systems of large dimension. If the state $\rho_{\omega_0,t}^{(N)}$ is pure, i.e. $\rho_{\omega_0,t}^{(N)} = |\psi_{\omega_0,t}\rangle \langle \psi_{\omega_0,t}|$ the QFI immediately reduces to (we suppress the index ω_0, t for readability)

$$F_Q [|\psi\rangle] = 4 \left(\langle \partial_{\omega_0} \psi | \partial_{\omega_0} \psi \rangle - |\langle \psi | \partial_{\omega_0} \psi \rangle|^2 \right). \quad (4.28)$$

Using this equation, it is straightforward to calculate the QFI in case of a noiseless, i.e. a unitary evolution. Assuming we can write the encoding Hamiltonian in the form $H = \omega_0 H_{\text{red}}$, with some suitable ω_0 -independent Hermitian operator H_{red} , the quantum channel is directly given by $\Lambda_{\omega_0,t}[\bullet] = U \bullet U^\dagger$ with $U = \exp(-it\omega_0 H_{\text{red}})$ and one arrives at

$$F_Q[U|\psi\rangle] = 4t^2 \Delta^2 H_{\text{red}}|_{|\psi\rangle}. \quad (4.29)$$

Crucially, $\Delta^2 H_{\text{red}}|_{|\psi\rangle}$ is nothing else but the variance of the reduced Hamiltonian³ H_{red} generating the dynamics taken with respect to the initial state $|\psi\rangle$. Note that for $H = \omega_0 H_{\text{red}}$ the QFI is always independent of ω_0 itself [10].

We emphasize that the statistical operator $\rho_{\omega_0,t}^{(N)}$ is the quantum state of all N particles at once and may contain correlations between the different subsystems. This reduces the additivity of the QFI to the case of uncorrelated states, i.e. $F_Q[\rho_{\omega_0,t}^{\otimes N}] = N F_Q[\rho_{\omega_0,t}]$, since this is the only case where the measurements are indeed independent [43]. Analogously to the classical case, this could be thought of as either a parallel measurement on N probes or an N times repetition of the same measurement on a single probe. Furthermore, the QFI is convex under incoherent mixtures of quantum states [249], i.e. for valid states ρ, σ, τ with $\rho = \lambda \sigma + (1 - \lambda) \tau$ and $0 \leq \lambda \leq 1$ we have

$$F_Q[\rho] \leq \lambda F_Q[\sigma] + (1 - \lambda) F_Q[\tau]. \quad (4.30)$$

Hence, any mixing of states cannot increase the QFI.

An equivalent definition of the QFI can be given in terms of a purification $|\Psi_{\omega_0,t}\rangle$ of the state $\rho_{\omega_0,t}^{(N)}$. By lifting the state into an Hilbert space extended by \mathcal{H}_E , the common state can be expressed via a pure state vector $|\Psi_{\omega_0,t}\rangle$, where $\rho_{\omega_0,t}^{(N)} = \text{tr}_E [|\Psi_{\omega_0,t}\rangle \langle \Psi_{\omega_0,t}|]$. Then, the QFI can be expressed as the minimum over these purifications [42, 43, 250]

$$F_Q[\rho_{\omega_0,t}^{(N)}] = 4 \min_{\Psi_{\omega_0,t}} \langle \partial_{\omega_0} \Psi_{\omega_0,t} | \partial_{\omega_0} \Psi_{\omega_0,t} \rangle. \quad (4.31)$$

Indeed, the crucial role of the QFI is due to the fact that it bounds the achievable precision for any possible measurement. Recalling the CRB in Eq. (4.9) and the definition of the QFI in Eq. (4.25), we arrive in fact at the *Quantum Cramér-Rao Bound* (QCRB), stating that the estimation error, minimized over any possible measurement for any initial state $\rho_0^{(N)}$, is lower

³Note that here it is straightforward to derive the connection to the Heisenberg inequality: Instead of estimating ω_0 one directly measures the interrogation time, i.e. all derivatives in Eq. (4.28) are taken with respect to t instead of ω_0 . The result $F_Q = 4\Delta^2 H$ in combination with the QCRB in Eq. (4.32) yields the desired energy-time Heisenberg inequality.

bounded by

$$\Delta^2 \hat{\omega} \geq \min_{t \in [0, T]} \frac{t}{T F_Q \left\{ \Lambda_{\omega_0, t}^{\otimes N} [\rho_0^{(N)}] \right\}}. \quad (4.32)$$

Note that we explicitly mention the minimization to be performed over the interrogation time to obtain the optimal performance for the particular input state $\rho_0^{(N)}$.

To simplify the notation, from now on we will denote a derivation with respect to ω_0 with a simple overdot, i.e. $\partial_{\omega_0} \bullet = \dot{\bullet}$.

4.3.2. Achieving Maximal Precision - Bounding the QFI

For the aim of finding the maximal achievable precision for an arbitrary quantum channel, the maximization of the QFI with respect to the initial state is inevitable. While we already removed the necessity of specifying a measurement (POVM) in Section 4.3.1, here we will explore how the optimization of the QFI with respect to the input state can be performed efficiently. The only "free" parameters left are then the encoding time t and the quantum channel itself. In any case, the result of the input state optimization will indeed depend on the channel, hence it is meaningful to define the *channel – QFI* (cQFI), which for a given channel is the maximum FI at a time t achievable when input state and readout are optimal. We define the cQFI as in [35, 43],

$$\mathcal{F}[\Lambda_{\omega_0, t}^{\otimes N}] = \max_{\rho_0^{(N)}} F_Q \left\{ \Lambda_{\omega_0, t}^{\otimes N} [\rho_0^{(N)}] \right\}. \quad (4.33)$$

The task of maximization quickly becomes involved, although due to the convexity of the QFI, Eq. (4.30), the set of states over which the optimization in Eq. (4.33) has to be performed can be confined to pure states. For an increasing probe number, it is not a priori given that the optimal input state grows trivially with N , e.g. like the GHZ states in Section 4.2.2, but non-trivial correlations may become important for some channels when N is increased. Since the dimension of the state grows exponentially with N , numerical computation becomes infeasible even for small N rendering the cQFI out of reach for examinations of an asymptotic scaling law. However, the cQFI can be bounded in terms of the Kraus operators representing the channel on the single probe level. Therefore, we will give an idea of the procedure in the single probe cQFI and state the result for the arbitrary N case.

To avoid the calculation of the SLD, one utilizes the purification-based definition of the QFI, Eq. (4.31). The channel at any fixed time t , $\Lambda_{\omega_0, t}(t)$, can be regarded as a unitary evolution of the system in an extended Hilbert space, i.e. $\mathcal{H}_{\text{ext}} = \mathcal{H}_S \otimes \mathcal{H}_E$, and subsequent tracing over of

this extension, using the Stinespring dilation theorem [14]. Specifically we have

$$\begin{aligned}\Lambda_{\omega_0,t}[\rho_0] &= \text{tr}_E \left[U_{\omega_0}(t) \rho_0 \otimes \rho_E U_{\omega_0}^\dagger(t) \right] \\ &= \sum_j K_j(t, \omega_0) \rho_0 K_j^\dagger(t, \omega_0)\end{aligned}\tag{4.34}$$

where $K_j(t, \omega_0)$ are the Kraus operators representing $\Lambda_{\omega_0,t}$ and ρ_E is a state of the extending subspace, which can always be assumed to be pure in terms of a purification performed on the extending subspace. Since the convexity of the QFI restricts ρ_0 to be pure, $\rho_0 \otimes \rho_E$ is pure and hence we can invoke Eq. (4.31). All purifications of ρ_0 can then be reached by rotating the fixed ρ_E with a unitary operator acting only on the extending subspace, $V_{\omega_0} \rho_E V_{\omega_0}^\dagger$ [42, 43]. Note that these unitary operators will in general depend on the frequency ω_0 itself. Thanks to the locality of the QFI, we are allowed to write this unitary operators in terms of a Hermitian matrix h independent from ω_0 , $V_{\omega_0} = \exp(-ih\omega_0)$. Note that after performing the partial trace using the rotated environmental state, the whole transformation boils down to a rotation of the channel's Kraus operators, i.e. we have $\tilde{K}_i(\omega_0, t) = \sum_j^R (V_{\omega_0})_{ij} K_j(\omega_0, t)$ with R the rank of the channel (note that this conversely implies that the dimension of \mathcal{H}_E is at least R). Taking the trace yields the cQFI as

$$\mathcal{F}[\Lambda_{\omega_0,t}] = 4 \max_{\rho_0} \min_h \text{tr} \left[\sum_{i=1}^R \dot{\tilde{K}}_i(t, \omega_0) \rho_0 \dot{\tilde{K}}_i^\dagger(t, \omega_0) \right],$$

where

(4.35)

$$\dot{\tilde{K}}_i(t, \omega_0) = \dot{K}_i(t, \omega_0) - i \sum_{j=1}^R h_{ij} K_j(t, \omega_0),$$

while higher order terms in ω_0 in $\dot{\tilde{K}}_i(t, \omega_0)$ do not contribute due to the mentioned locality of the QFI. We want to emphasize that the environment used to employ Stinespring's theorem and, at the same time, the purification to obtain the cQFI is not necessarily a physical environment, but merely a theoretical construct to avoid calculations involving the SLD.

The remaining maximization over (pure) input states ρ_0 is still a tedious task, especially for complicated channels or high dimensional systems. Importantly, the order of min and max cannot be exchanged. Nevertheless, it turned out that an upper bound to the cQFI, based on the representation just calculated, can be efficiently determined, as it allows to exchange the order of the optimizations and hence the maximizations over input states can be performed. This approach has been named *channel extension* and the idea is the following [250]: One extends the channel by an, at least equally large Hilbert space. In particular, one assumes an

arbitrary number of ancilla systems which are not affected by the application of the quantum channel. However, if measurements on the new total space are considered, the information content measured by the cQFI can only grow, i.e. it is $\mathcal{F}[\Lambda_{\omega_0,t}] \leq \mathcal{F}[\Lambda_{\omega_0,t} \otimes \mathbb{I}]$. The total state of the system and the ancillas $|\Psi_{SA}\rangle$ may be entangled, but can be assumed to be pure. After performing the partial trace over the (artificial) ancillas, one obtains [see Eq. (4.31)]

$$\begin{aligned} \mathcal{F}[\Lambda_{\omega_0}(t) \otimes \mathbb{I}] &= 4 \max_{\rho_S} \min_h \text{tr} \left[\rho_S \sum_{i=1}^R \dot{K}_i^\dagger(t, \omega_0) \dot{K}_i(t, \omega_0) \right] \\ &= 4 \min_h \left\| \sum_{i=1}^R \dot{K}_i^\dagger(t, \omega_0) \dot{K}_i(t, \omega_0) \right\| \end{aligned} \quad (4.36)$$

with $\|\bullet\|$ the operator norm.⁴ In the second equality, we used that $\rho_S = \text{tr}_A[|\Psi_{SA}\rangle\langle\Psi_{SA}|]$ is now mixed and thus both optimization domains are convex. Hence we are able to exchange the order of min and max by virtue of the minmax theorem [251] and, subsequently, the maximum over the states can be calculated by means of the Cauchy-Schwarz inequality. In particular, $\max_{\rho_S} \text{tr}[\rho_S A] = \|A\|$ for any operator A since ρ_S is positive with $\text{tr}[\rho_S] = 1$.

In principle, for the case of N probes building up the cFEP the single probe result could be derived directly, however, the problematic exponential increase of Hilbert space's dimension remains. Luckily, one can further bound the channel extended cQFI for N probes in terms of the single channel Kraus operators. When the global channel for the common state of the probes is given by $\Lambda_{\omega_0,t}^{\otimes N}$, it can be shown that [43, 250]

$$\begin{aligned} \mathcal{F}[\Lambda_{\omega_0,t}^{\otimes N}] &\leq \mathcal{F}[(\Lambda_{\omega_0,t} \otimes \mathbb{1})^{\otimes N}] \\ &\leq 4N \min_{h(N)} \left[\|\alpha_{\tilde{K}}\| + (N-1) \|\beta_{\tilde{K}}\|^2 \right] \equiv \mathcal{F}^\uparrow[\Lambda_{\omega_0,t}^{\otimes N}], \end{aligned} \quad (4.37)$$

with

$$\begin{aligned} \alpha_{\tilde{K}} &= \sum_{i=1}^R \dot{K}_i^\dagger(t, \omega_0) \dot{K}_i(t, \omega_0), \\ \beta_{\tilde{K}} &= i \sum_{i=1}^R \dot{K}_i^\dagger(t, \omega_0) \tilde{K}_i(t, \omega_0). \end{aligned}$$

We stress the dependence of the optimal h on the number of probes, i.e. the minimization has to be performed for every N . It has been discussed that indeed, this bound provides useful estimates of the QFI for all N , even in the asymptotic regime $N \rightarrow \infty$ [35, 43] and, in fact, this will be the basis for the results presented in the next sections. Indeed, the extended cQFI in

⁴Note that a norm is naturally induced by the Hilbert-Schmidt scalar product, $\langle A, B \rangle = \text{tr}[A^\dagger B]$.

Eq. (4.36) and the bound in Eq. (4.37) coincide for $N = 1$, as well as if there exists a Kraus representation, i.e., h , such that $\|\beta_{\tilde{K}}\| = 0$ (in this case one can show [43] that the second inequality in Eq. (4.37) is saturated). In the latter case, it might still be convenient to consider Kraus representations such that $\|\beta_{\tilde{K}}\| \neq 0$ and the optimal h in Eq. (4.37) for each finite value of N . This provides the so-called *finite- N channel extension* method, which plays a crucial role in frequency estimation, in order to determine how the optimal evaluation time depends on N and, hence, the best possible scaling of the precision obtained by optimizing also over t [39, 43]. In any case, the bound requires intensive numerical effort, but can be cast into a semidefinite program to perform the minimization efficiently [35, 43]. Note that, besides this channel extension method, also other methods have been proposed and developed in the literature [35, 42, 252].

4.3.3. Saturation of the (Quantum-)CRB

Let us now discuss the attainability of the (Q)CRB. The first thing one has to keep in mind is that one is free to choose $t \ll T$ which increases the number of repetitions $\nu = T/t$. This provides more measurement data gathered over the total time T , and hence can lead to a better precision which then improves at a classical rate $\sim 1/\nu$.

The chain of inequalities for the (Q)CRB mentioned so far is given by

$$\Delta^2 \hat{\omega} \cdot T \stackrel{(1)}{\geq} \min_t \frac{t}{F_{\text{cl}}} \stackrel{(2)}{\geq} \min_t \frac{t}{F_Q} \stackrel{(3)}{\geq} \min_t \frac{t}{\mathcal{F}} \stackrel{(4)}{\geq} \min_t \frac{t}{\mathcal{F}^\uparrow}, \quad (4.38)$$

which has been bounded by several optimization procedures.

Inequality (1). — In fact, one should keep in mind that the saturability of inequality (1) is a non-trivial issue and strongly depends on the properties of the estimator and therefore classical data processing [10]. We already mentioned that any efficient estimator which is unbiased will achieve the CRB, however, such an estimator may not even exist *globally*, i.e. for any arbitrary value of ω_0 .

An often constructed estimator is the *maximum likelihood estimator* (MLE) which profits from the collection of a large data set (Consider for example the estimator for a sample mean $\bar{x} = \sum_{i=1}^{\nu} x_i / \nu$). Specifically, it is the estimator maximizing the likelihood $p_{\omega_0}(\vec{x})$ from Section 4.2.1. One can show that the asymptotic probability distribution of the MLE is a normal distribution with mean ω_0 and variance F_{cl} , i.e. saturating the CRB [29]. While always being consistent, one also has to keep in mind that an MLE may only be *asymptotically unbiased*, i.e. the bias β vanishes asymptotically for a large sample size.

On the other hand, in the regime of a finite data set, saturation is as mentioned not guaranteed in general. More specifically, this is true at least on a global level, i.e. irrespective of the true value ω_0 . In particular, a globally efficient estimator can only be found if the underlying probability density belongs to the so called exponential family [29]. Crucially, the normal distribution belongs to that family and hence the asymptotic saturability can be understood as an instance of the central-limit-theorem [29, 253].

However, one can always follow a *local approach* to saturate the CRB locally at a point $\omega_0 = \omega_L$, where one constructs a *locally unbiased estimator* which satisfies a local unbiasedness condition [12, 254],

$$\left. \frac{\partial}{\partial \omega_0} \langle \hat{\omega}(\vec{x}) \rangle_{\vec{x}} \right|_{\omega_0 = \omega_L} = 1. \quad (4.39)$$

Indeed, when this condition is imposed during the derivation of the CRB, one exactly obtains Eq. (4.9) with the only restriction that it is only valid (i.e. equality can be reached) for an interval $\omega_0 = \omega_L \pm \delta\omega$, as one also restricts the FI to this interval, which on the other hand is a local quantity anyway, see Eq. (4.11). One is tempted to believe that such a constraint renders the whole formalism impractical, as this restriction is very much present in nearly every estimation scheme since a globally unbiased estimator can almost never be constructed in a useful manner, or can't even be found for the problem at hand [29]. The usefulness of the local approach traces back to the fact that one often possesses preliminary information about the parameter, such that the scheme becomes applicable to the measurement of small fluctuations in the parameter as it is done in atomic clocks [232], gravitational wave detectors [236, 238] or as in a quantum sensing scenario named "slope detection" [13] employing for example nitrogen-vacancy centers in diamond [229] for magnetometry. Furthermore, one can think of the protocol as a "second step estimation", where one roughly determines the parameter first and applies the presented protocol for further refinement. Indeed, the local approach may be considered as the one giving the lowest bound hence its analysis may be regarded as the most optimistic one, therefore the derived limits can be considered fundamental. Additionally, the call for locality may be relaxed by allowing adaptive measurements, that is a sequence of MLE estimators based on locally unbiased estimates is consistent and asymptotically efficient [254]. For an approach employing an estimation of the whole parameter range, one has to resort to Bayesian inference techniques to frequency estimation [255]. Here one requires a new notion of the Heisenberg limit, in particular $\Delta^2 \hat{\omega} \sim \pi^2 / N^2$ [256]. Saturation of the latter is then achieved employing adaptive schemes, as examined in [257].

Inequality (2). — The second inequality turns into an equality by choosing the POVM which

maximizes the FI F_{cl} . In particular, this POVM is given in terms of the projectors into the eigenbasis of the SLD operator [41], which in most cases turns out not to be a practical, realizable choice. In the specific case of a unitary evolution we know that Eq. (4.29) holds, and then the optimal measurement (and input state!) are given by an equally weighted superposition of eigenstates belonging to the Hamiltonian H , as this state maximizes the variance [19], compare Eq. (4.29). More precisely, for the Hamiltonian $H = \sum_{n=1}^N \omega_0 H_{\text{red}}^{(n)}$ (where all $H_{\text{red}}^{(n)}$ are identical), the SQL is achieved by the product state $|\psi\rangle^{\otimes N}$ where

$$|\psi\rangle = \underset{|\phi\rangle}{\operatorname{argmax}} \Delta^2 H_{\text{red}}|_{|\phi\rangle}, \quad (4.40)$$

while the HL is achieved by

$$|\psi^{(N)}\rangle = \frac{|\mu_{\text{max}}\rangle^{\otimes N} + |\mu_{\text{min}}\rangle^{\otimes N}}{\sqrt{2}}, \quad (4.41)$$

with $|\mu_{\text{max/min}}\rangle$ the eigenvectors belonging to the maximal (minimal) eigenvalues of H_{red} . These states are trivially also the ones maximizing the cQFI and are therefore able to saturate all bounds given in Eq. (4.38).

Inequality (3). — The saturation of the bound given by the cQFI \mathcal{F} is given if all the conditions set by the maximization procedures of the FI are fulfilled. This requires the knowledge of an optimal (here, optimal is referred to the scaling and not the saturation of the CRB) input state for the QFI. In the case of a unitary evolution, these can be found by maximizing the variance of the Hamiltonian, as mentioned in the previous paragraph. For a general open-system dynamics, i.e. an arbitrary quantum channel, the state maximizing the cQFI cannot be generally found explicitly. However, note that if one finds a state and a measurement procedure such that t/F_{cl} has the same scaling as t/\mathcal{F} , one can also argue that the optimal strategy will have such a scaling, as long as the classical CRB (1) is saturated as well.

Inequality (4). — This inequality may never be saturated, as the cQFI \mathcal{F}^\uparrow is an upper bound on the cQFI \mathcal{F} itself. However, its scaling with the probe number may be reached asymptotically ($N \rightarrow \infty$), apart from a possible parameter independent constant. Analogously to the arguing for inequality (3), if one finds a state and a measurement procedure such that t/F_{cl} has the same scaling as t/\mathcal{F}^\uparrow , given the saturation of the classical CRB (1), the optimal strategy will possess the same scaling.

4.4. Realistic Bounds on the Precision

The cFEP has been under heavy investigation, to determine the best precision achievable under different circumstances and, in particular, the different kinds of noise during the encoding time. The main question is whether the ultimate limit is given by the SQL, or how close one can reach the HL. Thereby one has to keep in mind that these limits have to be understood in an *asymptotic sense*, i.e. the number of available probes N is large and tends to infinity. That is, as we will see, due to the competition of the parameter encoding and the noise removing the imprinted information. Moreover, the noise may collapse the state such that no further encoding is even possible⁵. As the influence of the noise is stronger pronounced the more probes are involved in the entangled state, it is rather intuitive to assume that the optimal time when the measurement should be performed approaches zero when the number of probes is increased⁶. Therefore, the focus of interested is put on the ultimate limit one can achieve with any number of probes, i.e. "how fast" the precision decreases when N is increased.

As already explained in Section 4.3.3, the attainability of the QCRB employing the cQFI \mathcal{F} as a lower bound to the achievable precision can be shown (at least up to a constant factor) by evaluating the precision, as quantified by the FI, for a specific measurement and initial state. For that reason, let us note that for all the cases presented in this section, it is enough to consider GHZ-states as the input and the parity operator, $P_x = \bigotimes_{n=1}^N \sigma_{(n)}^x$ [258] as the subsequent measurement. Using error propagation, Eq. (4.14), and that $\Delta^2 P_x = \langle P_x(t)^2 \rangle - \langle P_x(t) \rangle^2 = 1 - \langle P_x(t) \rangle^2$ the error can be written as

$$\Delta^2 \hat{\omega}_P \cdot T = t \frac{1 - \langle P_x(t) \rangle^2}{|\langle \dot{P}_x(t) \rangle|^2}, \quad (4.42)$$

where further calculation can be found in [46,H3], Section 5.4 and Appendix A.2.7. That bound provides a chain of inequalities

$$\Delta^2 \hat{\omega}_P \cdot T \geq \Delta^2 \hat{\omega} \cdot T \geq \frac{t}{\mathcal{F}[\Lambda_{\omega_0,t}^{\otimes N}]} \geq \frac{t}{\mathcal{F}[(\Lambda_{\omega_0,t} \otimes \mathbb{1})^{\otimes N}]} \Rightarrow \Delta^2 \hat{\omega} \cdot T \sim \frac{1}{N^\kappa}, \quad (4.43)$$

where we justify the implication from the fact that when both sides approach 0 in the limit $N \rightarrow \infty$ as $N^{-\kappa}$, the same will be true for $\Delta^2 \hat{\omega} \cdot T$.

⁵Obviously, a state $\rho \sim \mathbb{1}$ has lost all its coherence and hence the phase can not evolve anymore.

⁶While from a physical perspective this statement may seems intuitive, at last for all noise dynamics where the steady state commutes with the parameter imprinting Hamiltonian, it is mathematically not clear a priori and has to be checked carefully. In fact, this has only been shown rigorously for the Zeno scaling presented in Section 4.4.1.

4.4.1. The Zeno-Limit under Phase-Covariant Noise

Let us start with a scenario where the induced noise during the evolution is phase-covariant, as explained in Section 1.5.

It has been shown that for any FEP where the encoding channel is phase-covariant, i.e. in accordance with Eq. (1.36), the ultimate precision is always bounded from below [39] by the asymptotic scaling

$$\Delta^2 \hat{\omega}_{\text{Zeno,PC}} \cdot T \geq \frac{C}{N^{3/2}}, \quad (4.44)$$

for a suitable (N -independent) constant C . Furthermore, it was shown that such a limit can always be achieved (at most up to the constant factor) by means of a GHZ state. First encounters with this scaling have been presented in [36, 37], where it has been linked to the quadratic decay of transition probabilities in the environment on short time scales and was hence called the *Zeno-Limit* (ZL). A general derivation for the case of pure dephasing can also be found in [38]. Indeed, as shown in [39], the Zeno scaling emerges for all evolutions whose dynamics deviate from a dynamical semigroup (see Section 1.4, Equation (1.10)) at short time scales, while the precision collapses immediately to the SQL when the rates $\gamma_j(t)$ in Eq. (1.7) are replaced by constants [34]. In particular, the optimal interrogation time has been proven to scale as

$$t_{\text{opt}}^{\text{Zeno,PC}} \propto \frac{1}{N^{1/2}}, \quad (4.45)$$

for any evolution (apart from the unrealistic case of a full revival), thus showing explicitly how the optimal estimation strategy relies on measurements on shorter and shorter time scales.

Note that a Lindbladian (semigroup) evolution corresponding to constant rates in Eq. (1.7) is generally an approximation to the real dynamics, as it relies on a coarse grained time resolution [2], which neglects times where the environmental correlation functions are not yet decayed. However, the total evolution of the system and the bath is always governed by a unitary evolution of a possibly time dependent Hamiltonian $H(t)$. Hence given an initial pure state of the system $|\psi_S\rangle$ and the total state $|\psi\rangle = |\psi_S\rangle \otimes |\psi_E\rangle$, the short time survival probability of the reduced state can be written as [39]

$$\langle \psi_S | \Lambda_t [|\psi_S\rangle \langle \psi_S|] | \psi_S \rangle = 1 - \alpha_S t^2 + O(t^3), \quad (4.46)$$

which is always of the order $O(t^2)$ and $\alpha_S = \langle \psi | H(0)^2 | \psi \rangle - \langle \psi_S | \text{tr}_E [H(0) | \psi \rangle \langle \psi | H(0)] | \psi_S \rangle$. Consequently we can understand a dynamics which is accurately described by a Lindblad master equation as a type of dynamics where the "Zeno regime" (i.e. the regime where terms

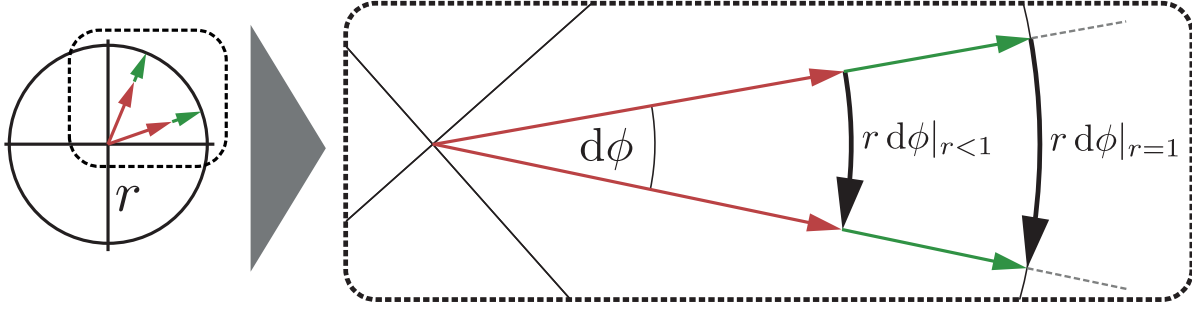


Figure 4.3.: **Geometric picture for the precision for a single probe ($N = 1$).** The distance of two quantum states, i.e. the distance between two neighboring probability distributions, can be visualized by two Bloch vectors of same length who only differ in a small phase angle $d\phi$. Note that rigorously one should understand these as the projection of some Bloch vectors into the xy plane. Decoherence processes decrease the length of these vectors (and their projections), hence the states are approaching each other, see the transition from green to red. (Figure first published in [H6])

quadratic in time are relevant) is not accessible. Moreover, since the information about ω_0 is encoded in the phase of the qubit's state, for the special single probe case (i.e. $N = 1$) it was possible to show that the length of the Bloch vector's projection into the xy plane determines the achievable precision. In this respect one may observe geometrically the balance between a long evolution time and the decoherence processes diminishing the achievable precision, for that compare also Fig. 4.3.

Both affect the distance between the projections of the two states $\rho_{\omega_0 t}$ and $\rho_{\omega_0 + d\omega_0 t}$, which is given by the line element $r(t) d\phi(t) = r(t) t d\omega_0$ where $r(t)$ is the length of the projection and $d\phi(t) = t d\omega_0$ the phase difference. Obviously, the function $r(t)$ and t counteract each other. While t increases the phase difference and hence provides a better distinguishability of the states, $r(t)$ pulls the projections towards the origin and thereby decreases the precision.

We want to emphasize again, that this limit is asymptotic, i.e. it is reached for a larger number of probes which in turn shifts the optimal interrogation time into the short time regime. This shifting can be motivated by the fact that entangled states do not only share their phase evolution, but also collectively gather fluctuations induced by the noise. Hence, the noise is naively speaking " $\sim N$ -times stronger", i.e. the phase evolution is lost quicker. In the short time regime, the only time order left to contribute is the second one as shown above, which then yields the mentioned scaling.

Remark.— Note that the Zeno scaling can also emerge non-asymptotically, when the function dictating the transversal contraction of the Bloch sphere is always of second order in time. Then

the scaling is immediately Zeno-like, e.g., for Gaussian decay envelopes as we will encounter in Section 9.3 for the NV center.

4.4.2. Transversal Noise

A special case is set by noise which is perpendicular to the direction of the frequency encoding, which is normally chosen as \hat{z} . Usually one speaks about the direction of the noise at the level of the master equation associated with the dynamics. That is, a dissipator of the form

$$\mathcal{D}(t)[\rho] = \gamma(t) \left(\alpha_x \sigma^x \rho \sigma^x + \alpha_y \sigma^y \rho \sigma^y - \rho \right), \quad (4.47)$$

with $\alpha_x + \alpha_y = 1$ induces transversal noise (i.e. the noise direction is perpendicular to the direction of the encoding, here \hat{z}). Specifically, for a constant rate $\gamma(t)$, this dissipator was analyzed in [45] and it was found that the ultimate precision is improved beyond the Zeno limit, yielding

$$\begin{aligned} \Delta^2 \hat{\omega}_{\perp, \text{SG}} \cdot T &\gtrsim \frac{1}{N^{5/3}}, \\ t_{\text{opt}}^{\perp, \text{SG}} &\sim N^{-1/3}. \end{aligned} \quad (4.48)$$

Crucially, transversal noise is not phase-covariant, i.e. the condition in Eq. (1.36) does not hold. In particular, the inclusion of PC breaking terms (which are exactly the ones neglected by the secular approximation [50, H3]), allows for non-isotropic contractions of the Bloch sphere in \hat{x} and \hat{y} direction. As will also be presented in Section 5.3.1, non-phase-covariant dynamics then become sensitive to the initial phase of input states of the cFEP, which is fixed by the relation of α_x and α_y . Indeed, a dependence of the initial phase was also predicted in [46], where the noise model was applied to a specific setup in atomic magnetometry [259].

For completeness, we do a leap ahead of Chapter 5 and already present the scaling for perpendicular but non-semigroup noise. The precision in such a scenario is ultimately bounded by

$$\begin{aligned} \Delta^2 \hat{\omega}_{\perp} \cdot T &\gtrsim \frac{1}{N^{7/4}}, \\ t_{\text{opt}}^{\perp} &\sim N^{-1/4}. \end{aligned} \quad (4.49)$$

Importantly, both scalings, Eq. (4.49) and (4.48), are reached by a parity measurement of GHZ states, see Section 5.4. The latter scaling, $N^{-7/4}$, is the best so far achieved using the cFEP employing the independent noise model.

4.4.3. Arbitrary, non-Phase-Covariant Noise

The dynamics under non-phase covariant, non transversal noise are a mostly unexplored category so far when regarded in the context of frequency estimation. It is not too long, that these types of dynamics became important, as the secular approximation performed in the master equation has been a rather standard procedure. Recent technological advances however presented methods to access timescales of the system's dynamics where the contribution of the non secular terms is not averaged out.

Since an NPC generator does not possess a specific form [conversely they are defined by not being PC, i.e. of the form in Eq. (1.38)], it is involved to derive analytic results for the QCRB. While again being a preview of Section 5.4, here we state the only numerical evidence so far. We found that the ultimate scaling may also be given by the Zeno limit iff the decay rate $\gamma(t)$ is time dependent and the noise is not completely orthogonal to the parameter encoding, i.e.

$$\Delta^2 \hat{\omega}_{\text{Zeno,NPC}} \cdot T \gtrsim \frac{1}{N^{3/2}}. \quad (4.50)$$

Indeed, pure dephasing components along the encoding of the parameter are *always* PC, hence they should limit the precision as explained in Sec. 4.4.1. Indeed, in Appendix A.2.6 we show that the information content in the FI is directly proportional to the length of the Bloch vector's projection into the xy plane, extending the result of [39], where it was already argued that pure dephasing is indeed the most detrimental noise in the estimation scheme. In other words, pure dephasing contributions are the limiting noise factors and when additional noise is added to the (even arbitrary small but not negligible dephasing) dynamics, the precision cannot increase. While this seems intuitive, we want to stress that this must not be the case when the asymptotic limit is not reached or when one has a probe-independent constant improvement in mind. In particular, in Sections 5.3.1 and 5.3.2 we demonstrate that NPC contributions can increase the single probe QFI on short times when the considered model is kept slightly more general.

4.4.4. Motivating Toy Model

To motivate the presented limits pictorially, we dedicate this section to a simple toy model. More precisely, the aim is to illustrate why transversal noise yields an improved scaling and any pure dephasing contribution automatically fixes the precision to be Zeno limited. Therefore recall that the Ramsey sequence effectively measures the evolved phase of a coherent input state and the precision is fixed by the variance of a corresponding observable which is

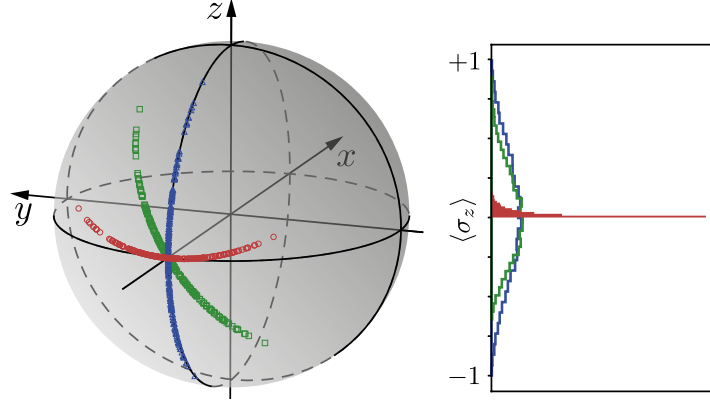


Figure 4.4.: **Toy model for the different directions of the noise.** After the protocol described in the main text (after the second $\pi/2$ rotation), the different outcomes of $\langle \sigma_z \rangle$ are marked with blue triangles ($\theta = \pi/2$), red squares ($\theta = 0$) and green circles ($\theta = \pi/4$). Every x component of the noise is along the positive x axis. The right panel shows a histogram of the appearances of the expectation value. Note the much narrower distribution for the transversal case. (Figure first published in [H6])

measured afterwards. For qubit probes, the variance of Pauli operators is completely determined by their expectation value. Let's assume that the dynamics during the free evolution is governed by the Hamiltonian

$$H = \frac{\omega_0}{2} \sigma^z + \eta [\sigma^x \cos(\theta) + \sigma^z \sin(\theta)] , \quad (4.51)$$

where η is the amplitude of a noise process. If an experiment including multiple runs is performed, a value for η is chosen at random, but it is fixed for the different runs of the experiment (corresponding to ν in Eq. (4.9)). We assume that the drawn amplitudes have zero mean and are distributed according to a Gaussian distribution. Consequently, we interpret the measured expectation as a single realization (corresponding to one specific realization of \vec{x}) drawn from the distribution of possible outcomes. In the experiment, for each run we prepare an equally weighted superposition of the σ^z eigenstates analogously to Section 4.2. Let us now consider 3 cases: (i) For pure dephasing we have $\theta = \pi/2$, (ii) for transversal noise we have $\theta = 0$ and for a third case (iii) we assume $\theta = \pi/4$. We simulate the evolution via the unitary generated by the Hamiltonian (4.51) such that we have a total evolution of $\omega_0 t = \pi/2$. Every result plotted on the Bloch sphere shown in Figure 4.4 corresponds to the outcome of a *different* experiment. A $\pi/2$ rotation around the x axis transforms the phase information of the states onto a population difference, where we can extract the distribution of $\langle \sigma_z \rangle$, see Figure 4.4, where the width of the distribution is drastically reduced for case (ii) when compared to the cases (i) and (iii), which themselves yield pretty similar results. Note that for case (i), the

non-negative expectation values are a result of the particular geometry in combination with small values of η .

To that end, this gives a motivation for why transversal noise is a special case, while any longitudinal component will reduce the scaling to the ZL.

4.5. Remarks

4.5.1. The Role of non-Markovianity

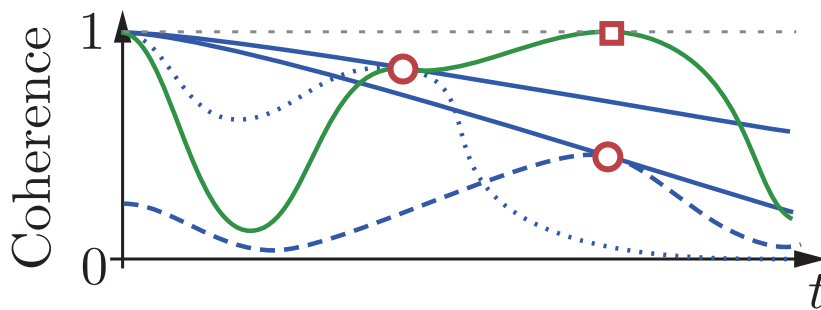


Figure 4.5.: **Role of non-Markovianity in pure dephasing.** Each optimal point (red circles) of a non-Markovian decay process (dashed and dotted blue lines) can be reached by Markovian processes (blue solid lines), therefore demonstrating that the solely non-Markovianity of the dynamics cannot provide an advantage over Markovian dynamics. The only exception is the case of a full revival as shown by the green curve and marked by the red square. This point cannot be reached via a Markovian dynamics and decay rates $\gamma_r > 0$. (Figure first published in [H6])

The role of non-Markovianity in topics referring to quantum metrology is, by far, not sorted out yet. For sure, this also due to the varying definitions around, see Section 1.4. However, we stress that for the configuration of the cFEP non-Markovianity does not play any role when it comes to the ultimate limits in the asymptotic regime. A detailed analysis and the proof for phase covariant noise is given in [39], but we give an intuition in the following.

As shown in [39] and argued in Sec. 4.4.1, performing measurements at shorter and shorter time scales is crucial in order to overcome the SQL. This not only implies that, as said, the key property is the violation of the semigroup composition law on short time scales (rather than a specific form of non-Markovianity), but one can also show that, apart from the unrealistic case of a full revival, performing a measurement on longer time scales (e.g. waiting for a back-flow of information) would be in any case detrimental and furthermore reducing the scaling of the

error to the SQL. Now, such a strong result is certainly a consequence of the asymptotic regime $N \rightarrow \infty$ taken into account in [39]. However, one can easily argue that non-Markovianity is not really a necessary resource for the FEP, even in the finite- N regime.

Crucially, note that all the FIs defined above are local quantities in time, i.e. they can not capture any temporal correlation in the evolution of the state. In other words, they only take the instantaneous state of the system into account. E.g. as mentioned already in Sec. 4.4.3, the achievable precision depends on the available coherence orthogonal to imprinting of ω_0 . Any dynamics, whose value of coherence coincide at a given point yield the same cQFI, which means that even if the cQFI increases in time during one evolution due to non-Markovianity, one will always find a different Markovian dynamics reaching the same QFI at the same time and thus providing the same precision. This argument is illustrated in Fig. 4.5. Nevertheless, we stress that non-Markovianity can be of course of practical advantage, given a specific setting and hence a restricted set of available dynamics.

Moreover, note that the temporal derivative of the QFI has been proposed as a measure of non-Markovianity as it quantifies the information flow between the system and the environment [260].

4.5.2. Precision, Accuracy and Sensitivity

In this paragraph we would like to clarify some terms commonly encountered in the literature and often used interchangeably. The notions of an accurate and precise measurement can be linked to properties of the estimator [30]. Any unbiased estimator is accurate. Therefore, asymptotic unbiasedness also guarantees an accurate measurement in the asymptotic regime. The notion of precision is surely connected to the variance of the estimator and for unbiased estimators it is equal to the MSE. Importantly, precision is a term describing the closeness of results obtained by repeated performances of the experiment (as long as the true value does not change), the results may still be biased away from the true value, see the illustration in Fig. 4.6. Note that any efficient estimator is accurate and precise as it is consistent. In particular, any MLE is precise and accurate in the asymptotic regime. A further term often used when quantifying the performance of quantum sensing experiments is *sensitivity* [13, 229]. Note that this term may be misleading in a broader context, since other communities use the term *noise equivalent power* (NEP) η while referring to the same concept [261, 262]. At the same time, sensitivity is then referred to the slope of the response curve [263, 264]. NEP is a measure of the *signal-to-noise ratio* (SNR), specifically it is defined as the signal yielding the $\text{SNR} = 1$. Since this depends on the resources at hand, one usually chooses a fixed total time of $T = 1$ s.

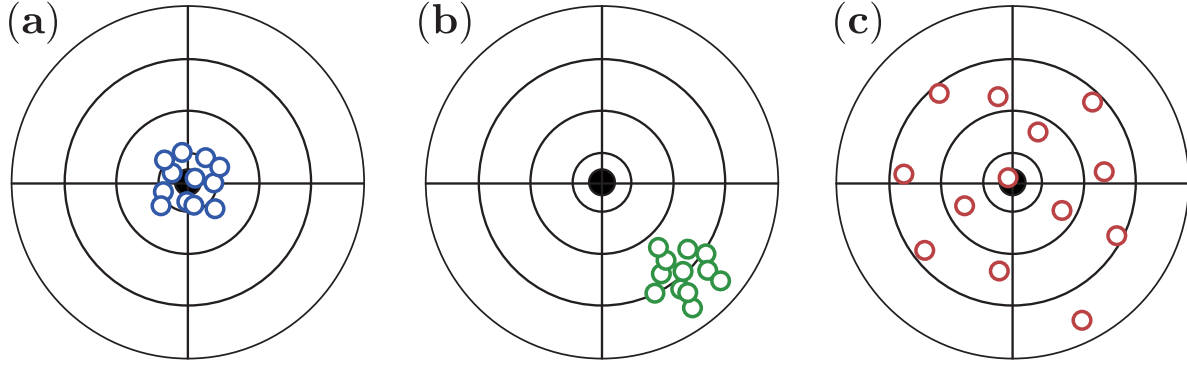


Figure 4.6.: **Precision and Accuracy.** Imagine throws onto a dartboard, each consecutive hit is marked with a circle. The player of board (a) is accurate and precise, as his throws have a small spread and are distributed around the center. The player on (b) is very precise but lacks accuracy. His throws also possess a narrow distribution, however around a point which is displaced from the center of the target. The throws of the last player on (c) are evenly but widely distributed around the center, therefore he is accurate without possessing any precision. To connect this illustration with the estimation task treated in this work, every throw onto the dartboard has to be associated with a whole experiment which is conducted. (Figure first published in [H6])

For a response curve or signal $S_T(\omega_0)$ and the noise $\sigma_T(\omega_0)$ we have the SNR

$$\text{SNR} = \frac{S_T(\omega_0)}{\sigma_T(\omega_0)}. \quad (4.52)$$

Here we include the possibility to repeat measurements and denote the affiliation to the specific total time in the index T . This may change the response itself but crucially the repetitions reduce the noise, typically by a factor $\sqrt{T/t}$ where t is the duration of a single run, compare the discussion in Section 4.1. We emphasize that in practical applications $\sigma_T(\omega_0)$ is a sum of noise contributions from different sources, e.g. electrical noise, counting errors of quantized signals like photons or precisely the quantum shot noise (or projection noise) [28].

In principal the NEP is given by $S_T(\omega_0) = \sigma_T(\omega_0)$ for $T = 1s$, however it is convenient to express it in terms of the quantity to estimate. Since the sensor needs to be calibrated to a known reference point ω_L , we express the response as (recall $\omega_0 = \omega_L + \delta\omega$)

$$S_T(\omega_0) \approx S_T(\omega_L) + \left. \frac{\partial S_T(\omega_0)}{\partial \omega_0} \right|_{\omega_0=\omega_L} \delta\omega, \quad (4.53)$$

and therefore we arrive at the NEP (note that the $\sqrt{\text{Hz}}$ is required to obtain the desired units of

η)

$$\delta\omega = \sigma_T(\omega_0) \left[\left[\frac{\partial S_T(\omega_0)}{\partial \omega_0} \right]_{\omega_0=\omega_L} \right]^{-1} \Big|_{T=1\text{ s}} = \eta \sqrt{\text{Hz}}. \quad (4.54)$$

Thereby the value of $S_T(\omega_L)$ is a bias which is known via the calibration and we set it to zero without any loss of generality and we prefer $\delta\omega$ to be positive, hence we take the absolute value of the derivative. The NEP shares similarities with the error propagation Eq. (4.13) and we may indeed interpret $\delta\omega$ as the upper limit in precision when we understand the sensing experiment as a task of frequency matching, where we aim to tune ω_L as close as possible to ω_0 . Particularly, $S_T(\omega_0)$ is then the expectation value of a quantum mechanical observable and $\sigma_T(\omega_0)$ its standard deviation. Furthermore, the requirement of local estimation is implied by Eq. (4.53) where the derivative is the sensitivity of the sensor. However, as mentioned, one needs to keep in mind that some communities refer to the concept of NEP as sensitivity of the sensor. Consequently, they require a different term for the local slope $\partial S_T/\partial \omega_0$ and hence introduce the concept of *responsivity* [262].

For illustration purposes, let us rederive the NEP (i.e. the sensitivity) of a single probe Ramsey experiment as used for magnetometry of a magnetic field, i.e. $\omega_0 = \gamma_a B$ is determined by the Zeeman interaction of the atomic probe (gyromagnetic ratio γ_a) with a magnetic field of amplitude B . Here, $S_T(\omega_0)$ is given by the survival probability of the initial state, Eq. (4.18), and $\sigma_T(\omega_0)$ represents the shot noise. As already mentioned, the shot noise is given by $\sigma_T(\omega_0) = \sqrt{S_T(\omega_0)[1 - S_T(\omega_0)]/\nu}$ with $\nu = T/t$. Plugging these expressions into Eq. (4.54) yields

$$\delta\omega = \frac{\sqrt{e^{-2\gamma t} - \cos^2(\omega t)}}{\sqrt{tT} |\sin(\omega t)|} \Big|_{T=1\text{ s}}, \quad (4.55)$$

which is minimized in two steps. A first optimization finds $\omega = \pi/(2t)$ and further minimizing over t yields the optimal time $t_{\text{opt}} = 1/(2\gamma)$. Translating this into the NEP for the field amplitude yields

$$\begin{aligned} \delta B &= \sqrt{\frac{2e}{\gamma_a/\gamma}} \frac{1}{1\text{ s}} = \sqrt{\frac{2e}{\gamma_a T_2^*}} \sqrt{\text{Hz}} \\ \Rightarrow \eta &= \sqrt{\frac{2e}{\gamma_a T_2^*}} \text{ and } [\eta] = [\text{B}] \sqrt{\text{Hz}}^{-1} \end{aligned} \quad (4.56)$$

In the last step we used that the coherence time of the probe is given by $T_2^* = 1/\gamma$. Note that

the NEP η is given in terms of the units of the parameter (here B) divided by $\sqrt{\text{Hz}}$ giving a reference to the integration time of $T = 1$ s.

4.5.3. Ultimate Precision without Entanglement

As we have seen, in parallel estimation strategies a necessary condition to overcome the SQL with respect to the number N of probes is the entanglement among the latter. However, it has been shown that the same precision can be achieved in a sequential strategy where, instead of N initially entangled probes, one has an N -step protocol with one single probe [265, 266]. For the case of a unitary operator $\exp(-it\omega_0\sigma^z/2)$ which is applied N times to an initially equally weighted superposition of $|0\rangle$ and $|1\rangle$, one obtains the state of the probe after the interrogation time as $(|0\rangle + e^{-iN\omega_0 t}|1\rangle)/\sqrt{2}$ and the survival probability is hence given by

$$p_{\omega_0 t} = \frac{1 + \cos(N\omega_0 t)}{2}, \quad (4.57)$$

yielding the scaling $1/N^2$ of the precision. However, note that in practice such a protocol is also challenging to implement, as the setup has to be stabilized, also against noise, during the total duration Nt of the experiment.

On the other hand, in case of a bosonic systems whose indistinguishable particles constitute the probe, it is more natural to treat them all together as an isolated quantum system. Then, from such a perspective, one may interpret the HL to be attainable with N bosonic particles, i.e., N excitations of a single bosonic mode (given a perfect phase reference) [227, 267]. However, one has to note that such states still carry particle entanglement which is, contrary to mode entanglement, necessary to obtain a quantum advantage in non-sequential schemes. Nevertheless, these details go far beyond the scope of this review but can be found in [12, 268].

4.5.4. Geometrical Distance of Quantum States

Let us briefly note the connection between the (quantum) Fisher-Information and the distinguishability of different quantum states. Therefore note that, besides in this work we are focusing on frequency estimation, the achievable precision for any other parameter λ can be analyzed using the formalism presented here by making the identification $\omega_0 \mapsto \lambda$ in the Eqs. (4.9) and (4.32)⁷.

⁷Thereby one has to keep in mind that this replacement concerns the derivative in the FI, while the functional dependence of the applied channel may not be a one-to-one replacement. For example, in the scenario of phase estimation one is interested to find the product $\lambda = \omega_0 t$.

As we already noted during the introduction, the problem of a finite estimation precision is emerging from the fact that probability theory is involved in the performance of measurements. Based on classical probability theory, in [269] a notion of statistical distance between two probability distributions was introduced. If one parameterizes these distributions as p_λ , the distance between p_{λ_1} and p_{λ_2} can be defined as the shortest path between the two, calculated in the space of all p_λ . An intuitive measure of the length is given in terms of the probabilities which can be distinguished along the path. In the case that p_λ is referred to N possible outcomes, the length (note the appearance of the FI)

$$l = \frac{1}{2} \int_{\lambda_1}^{\lambda_2} d\lambda \left\{ \sum_{n=1}^N \frac{1}{p_\lambda(n)} \left[\frac{dp_\lambda(n)}{d\lambda} \right]^2 \right\}^{\frac{1}{2}} \quad (4.58)$$

is minimized to yield the statistical distance

$$d(p_{\lambda_1}, p_{\lambda_2}) = \arccos \left(\sum_{n=1}^N \sqrt{p_{\lambda_1}(n) p_{\lambda_2}(n)} \right). \quad (4.59)$$

This result has then been transferred to the quantum regime where an N dimensional pure state $|\psi_\lambda\rangle$ is measured. Crucially, here the probabilities $p_\lambda(n)$ will depend on the chosen measurement basis and hence a further optimization can be performed. In particular, the optimal measurement basis includes one of the states itself, which yields

$$d(|\psi_{\lambda_1}\rangle, |\psi_{\lambda_2}\rangle) = \arccos |\langle \psi_{\lambda_1} | \psi_{\lambda_2} \rangle|. \quad (4.60)$$

Therefore, the distinguishability directly relates to the angle enclosed by two states in the Hilbert space. This result can be transformed into a metric for neighboring pure states $|\psi_\lambda\rangle$ and $|\psi_{\lambda+\delta\lambda}\rangle$ giving the Fubini-Study metric [270] and in [41] a generalization for mixed states is presented. The statistical distance for two states is then given by the Bures distance [117]

$$d_B(\rho_{\lambda_1}, \rho_{\lambda_2}) = \arccos F(\rho_{\lambda_1}, \rho_{\lambda_2}) = \arccos \text{tr} \left[\sqrt{\sqrt{\rho_{\lambda_1}} \rho_{\lambda_2} \sqrt{\rho_{\lambda_2}}} \right] \quad (4.61)$$

where F denotes the Fidelity [14]. Interestingly, for neighboring states this equation can be expanded yielding

$$d_B(\rho_{\lambda_1}, \rho_{\lambda_2}) = \frac{1}{2} \sqrt{F_Q[\rho_\lambda]} \delta\lambda + O(\delta\lambda^2), \quad (4.62)$$

which shows the connection between the QFI and the notion of statistical distance between quantum states.

4.6. Beyond the Independent Noise Model: Correlations and Control

By now it should be clear that the cFEP employing the independent noise model is an idealization. In addition, the bounds mentioned so far may be the ultimate bounds in an asymptotic regime, however, current realizations of the protocol in experimental setups struggles to achieve this regime. On top, there can be correlations in the noise affecting the individual probes and the probes may also interact with each other in principle. Furthermore one can think of control methods during the interrogation time, which may suppress noise, perform error correction, or increase the sensitivity to the frequency to be estimated. The details of these techniques go beyond the scope of this work, however we want to complete it by mentioning the recent progress in the field.

4.6.1. Correlated Noise and Interacting Probes

The cFEP sets fixed requirements onto the setup to be analyzed. Indeed, the boundary conditions of independent and identical noise are rather an idealization. Despite the fact that this provides an accurate description of the noise in many circumstances, there are certainly situations of interest where correlations of the noise are actually relevant. On top, the different probes are prohibited to interact during the interrogation time, also a necessity which is not always given. Especially in the context of probes which are desired to be prepared in an entangled state, where corresponding methods relying on the inter-probe interaction exist.

However, it is not a priori given that these flaws in a realization of the cFEP are a disadvantage. Considering pure dephasing, it was shown that noise which is spacially correlated along the used probes can beat the SQL with Lindbladian [271–273] and non-Lindbladian noise [274]. In particular, it was shown that for some antisymmetric entangled preparations of the input state, the correlations in the noise allow for the identification of decoherence free subspaces (DFS) which in turn even allow for the restoration of the HL. In [272] it was calculated that the spatial length over which the correlations decay is crucial for the achievable scaling and HL manifests for correlation lengths longer than the chain of probes. This infinite correlation length was implicitly assumed in [271] where a linear chain of trapped ions was investigated. To exemplify the latter, consider a master equation describing the evolution of total state evolving under

correlated dephasing. The state contains N probes, with N even. It may take the form

$$\frac{d}{dt}\rho_{\omega_0,t}^{(N)} = -i [H, \rho_{\omega_0,t}^{(N)}] + \gamma \left(V \rho_{\omega_0,t}^{(N)} V - \frac{1}{2} \{V^2, \rho_{\omega_0,t}^{(N)}\} \right),$$

when, e.g.,

(4.63)

$$H = \frac{\omega_1}{2} \sum_{n=1}^{N/2} \sigma_{(n)}^z + \frac{\omega_2}{2} \sum_{n=N/2+1}^N \sigma_{(n)}^z + \xi(t) \sqrt{\gamma} \sum_{n=1}^N \sigma_{(n)}^z,$$

where $V = \sum_{n=1}^N \sigma_{(n)}^z$ and $\xi(t)$ is a delta correlated, zero mean stochastic process, i.e. white noise. Note, that a state which is part of the DFS has to satisfy $V |\psi_{\text{DFS}}(t)\rangle = 0$ at all times. One way to construct such a subspace is the following. Therefore, note that the first two terms in the Hamiltonian can be rearranged as

$$H_0 = \frac{\omega_1 - \omega_2}{4} \left(\sum_{n=1}^{N/2} \sigma_{(n)}^z - \sum_{n=N/2+1}^N \sigma_{(n)}^z \right) + \frac{\omega_1 + \omega_2}{4} V. \quad (4.64)$$

Then, an input state of the form

$$|\psi\rangle = \frac{1}{\sqrt{2}} \left(\bigotimes_{n=1}^{N/2} |1\rangle \bigotimes_{n=N/2+1}^N |0\rangle + \bigotimes_{n=1}^{N/2} |0\rangle \bigotimes_{n=N/2+1}^N |1\rangle \right) \quad (4.65)$$

fulfills the DFS criteria and can be used to measure the frequency $\omega_0 = \omega_1 - \omega_2$. Interestingly, if one does not exploit the existence of these DFS, under the conditions of correlated noise GHZ states dephase on a timescale $\propto N^{-2}$ compared to an uncorrelated preparation when employed on conventional Ramsey spectroscopy, i.e. all ions possess an equal splitting. This effect was called *superdecoherence* [275], implying that GHZ states are strongly disadvantageous. Indeed, it was found that the precision using GHZ states is then independent of N , and furthermore, for optimized input states it was demonstrated that a constant, N independent part prevails in the precision, i.e.

$$\Delta^2 \hat{\omega} \approx \frac{\gamma C_1}{T} + \frac{\sqrt{\gamma} C_2}{\sqrt{T} N^{1.8}}, \quad (4.66)$$

where C_1 and C_2 are some constants determined numerically. To that end, the example presented may suggest that the assumption of local noise in the cFEP is an optimistic one, yielding a better precision than for correlated noise. On the other hand, this is no longer true in the special case of an appearing DFS where finally the HL can be reached. In any case, the precise comparison of the two scenarios is under investigation.

Another, until now only briefly investigated scenario are probes interacting among each other. Whether the parameter independent interaction of the probes can increase the precision is yet to be fully explored. It was shown that the estimation of the amplitude of a transverse field in an Ising-Hamiltonian can be performed with Heisenberg limited precision [276] and similar results have been derived for estimation procedures close to phase transitions [277]. Furthermore, there are investigations for the case when the frequency to be estimated is given by the coupling constant of k -body interactions. Precisely, the total encoding Hamiltonian has the form

$$H = \omega_0 \left(\sum_{n=1}^N h_0^{(n)} \right)^k \quad (4.67)$$

where $h_0^{(n)}$ is the same operator for each probe. Such a case is clearly operating outside the framework of the cFEP described until here, as the best precision achievable under such evolution scales as N^{-2k} [278, 279]. Remarkably, for initial product states this scaling is only slightly altered to $N^{-(2k-1)}$ and in specific cases it is enough to consider separable measurements to achieve the optimal scaling, while the scaling is also maintained under Lindbladian dephasing [280]. An experiment involving Bose-Einstein-Condensates was proposed [281] and performed [282]. Despite the simplified preparation of the initial input product state, the experimental difficulty is shifted to the generation of a k -body Hamiltonian (in this case $k = 2$ was realized). It is worth stressing that such a scheme also uses exclusive quantum resources as entanglement is generated during the interrogation time. This is in contrast to the cFEP introduced here, where the entanglement is injected during the input state preparation and interaction during the interrogation time is not considered.

4.6.2. External Control

A natural approach to an increase of precision is the suppression of noise acting on the probes. Within the cFEP, this corresponds to multiple applications of the channel during the interrogation time, but between the channels it is allowed to perform unitary operations. Assuming time-homogeneous Lindbladian noise, bounds under infinitely fast control have been found. In particular for qubit probes, it was shown that rank one Pauli noise can be eliminated completely, as long as it is not parallel to the imprinting of the parameter [283]. Therefore, assume a probe which evolves according to a semigroup generated by the master equation

$$\frac{d}{dt}\rho(t) = -i \left[\frac{\omega_0}{2} \sigma^z, \rho \right] + \gamma \left[\bar{\sigma} \rho(t) \bar{\sigma}^\dagger - \rho(t) \right], \quad (4.68)$$

where $\bar{\sigma} = \cos(\vartheta)\sigma^x + \sin(\vartheta)\sigma^z$, while it is initially prepared in an entangled GHZ state with a noiseless ancilla (we refer to Chapter 5 for further details on the ME). We define a logical qubit (the so called "code space") via the subspace $\{|\uparrow 1\rangle, |\downarrow 0\rangle\}$ with $\bar{\sigma} |\uparrow (\downarrow)\rangle = |\downarrow (\uparrow)\rangle$ and some arbitrary reference basis $\{|0\rangle, |1\rangle\}$ for the ancilla. Integrating the master equation over a small time step dt and projecting into the code space via $P_C = |\uparrow 1\rangle\langle\uparrow 1| + |\downarrow 0\rangle\langle\downarrow 0|$ and the error space (implicitly defined by $P_E = \mathbb{1} - P_C$) yields

$$\begin{aligned}\rho_C(dt) &= \rho(\mathbb{1} - \gamma dt) - i\frac{\omega_0}{2} [\kappa, \rho] dt + O(dt^2), \\ \rho_E(dt) &= \gamma \bar{\sigma} \rho \bar{\sigma} dt + O(dt^2),\end{aligned}\tag{4.69}$$

respectively. Note that we implicitly assume the tensor product $\otimes \mathbb{1}_A$ for the ancilla space. In case an error emerges, $\bar{\sigma}$ is applied to $\rho_E(dt)$, otherwise the system remains unmodified. After the correction, the system is in a mixed state $\rho(dt) = \rho_C(dt) + \bar{\sigma} \rho_E(dt) \bar{\sigma}$. Rearranging the terms, yields the differential equation

$$\frac{d}{dt}\rho = -i\frac{\omega_0}{2} [\kappa, \rho]\tag{4.70}$$

in the limit $dt \rightarrow 0$. This corresponds to a unitary evolution with the effective Hamiltonian $\kappa = \cos^2 \vartheta \sigma^z - \sin 2\vartheta \sigma^x/2$, hence the error correction rotates the encoding basis. However, now the analysis of Section 4.2.2 applies. The eigenvalues of κ are given by $\pm \cos \vartheta$, representing the only penalty of the scheme, which is a slower encoding of the parameter. Importantly, as soon as $\vartheta = \pi/2$, the noise and the encoding are parallel and the error correction also removes all information of ω_0 encoded during dt .

Importantly, this result has been generalized recently to any finite-dimensional probe [279, 284], showing that one can always restore the HL, if the encoding Hamiltonian is not contained in the linear span of the identity $\mathbb{1}$ and the Lindblad operators $V_k, V_k^\dagger, V_k^\dagger V_j, \forall k, j$. In particular, if there is a dephasing term $H = \alpha V_{\text{dephasing}}$ with some constant α , the HL can not be reached, confirming the detrimental role of pure dephasing (see Section 4.4.3 and the related discussion). Relaxing the requirement of a time-homogeneous noise process, it was shown that dynamical decoupling restores the ZL [285]. However, since dynamical decoupling is limited by the correlation time of the environment [192], one resorts to error correction schemes, which in general can be applied on the time scales of the effects of the noise [14, 286, 287]. While these base on the idea to prolong the coherence time [288, 289] (with an experimental implementation [290]), limiting processes as spontaneous emission may be corrected by observation of the environment [291]. Furthermore, a way to utilize open quantum systems is the engineering of noise processes which drive the probes back into the code space [292, 293]. A different

approach was aimed to preserve the QFI itself, rather than the input state [294]. Recently, it was also observed that for time-homogeneous processes a continuous measurement [295] of the environment [296] restores the HL. While the strict derivation of this result is challenging, one can intuitively understand that the observation of the environment closes the system and the evolution can be interpreted as unitary.

4.7. Time Dependent Encoding

Recently, interesting progress has been made for the case of time dependent encoding Hamiltonians. Before examining the setting we should stress that in that context the term "frequency estimation" is often referred to the frequency of an ac-signal [13] and thus differs from the definition we adapted in this work. Furthermore, instead of estimating the precision for the best scaling in N one is rather interested in the scaling with the available time T , which for time independent encodings is usually given as $\Delta^2\omega \sim T^{-2}$, compare Section 4.1, Section 4.2.3 and Section 4.2.2. However, with time dependent encodings this scaling can be overcome. A trivial example is the Hamiltonian

$$H_f(t) = f(\omega_0, t) G \quad (4.71)$$

where G is a time independent Hermitian operator and $f(\omega_0, t)$ a real valued function. Employing Eq. (4.29), the QFI yields

$$F_Q[U|\psi\rangle] = 4 \left(\frac{\partial \int_0^t f(\omega_0, \tau) d\tau}{\partial \omega_0} \right)^2 \Delta^2 G|_{|\psi\rangle}. \quad (4.72)$$

Obviously, depending on the form of $f(\omega_0, t)$ the precision $\Delta^2\omega \geq F_Q^{-1}$ can take different scalings in t or equivalently in T . As exploited in [297], the application of a suitable control Hamiltonian to some time dependent encoding may transform the Hamiltonian to the one in Eq. (4.71). An elegant way to construct a suitable control Hamiltonian for any time dependent encoding was presented in [298], starting from the observation that $F_Q[U|\psi\rangle] = 4\text{var}[\mathfrak{H}(\omega_0, t)]$, where $\mathfrak{H}(\omega_0, t) = -iU(\omega_0, t) \partial U(\omega_0, t) / \partial \omega_0$ and $U(\omega_0, t)$ is the unitary operator generating the evolution governed by an arbitrary time dependent Hamiltonian. It was shown that the applied control Hamiltonian should be constructed such that it steers the input state on the path of optimal sensing states as the system evolves. Analogously to the time independent case examined in [19], this state is always given by an equally weighted superposition of the

instantaneous eigenstates of $\xi(\omega_0, t)$ with the instantaneous maximum ($\mu_{\max}(t)$) and minimum ($\mu_{\min}(t)$) eigenvalues. Hence at each time t we have $|\psi_t\rangle \propto |\mu_{\max}(t)\rangle + |\mu_{\min}(t)\rangle$ with $\xi(\omega_0, t) |\mu_j(t)\rangle = \mu_j(t) |\mu_j(t)\rangle$ and the QFI yields

$$F_Q [|\psi_t\rangle] = \left[\int_0^t \mu_{\max}(\tau) - \mu_{\min}(\tau) d\tau \right]^2. \quad (4.73)$$

To consider an explicit example, it was shown that the precision in estimating ω_0 when encoded by $H(t) = -B [\sigma^x \cos(\omega_0 t) + \sigma^z \sin(\omega_0 t)]$ scales as $\Delta^2 \omega \geq 1/B^2 T^4$, which is then also the best precision achievable for that setting. Contrary, it is worth mentioning that estimating the amplitude B , i.e. the frequency we were focusing on in all other chapters of this review, scales as $\Delta^2 B \geq 1/4T^2$. The analytic form of the control Hamiltonian can be found in [298], but one should mention that in general this control depends on the frequency to be estimated. While this seems contradictory, it is enough to recall that the estimation is performed locally. Hence, using a close estimate for the frequency in the control Hamiltonian also improves the precision, as can be seen in [297]. Furthermore, [298] showed that one can use an adaptive scheme, where estimations of the parameter are used as a feedback for the control and the quartic scaling is then reached in an asymptotic regime of repetitions. A further example of the application of a control Hamiltonian can be found in [299], where the estimation of the speed of a Landau-Zener sweep also shows the quartic scaling in the total time.

A time dependent encoding of the form $H(t) = A \sin(\omega_0 t) \sigma^z$ has been studied experimentally, exploiting a nitrogen-vacancy center in diamond [300, 301] or involving a superconducting transmon circuit coupled to a waveguide cavity [302]. The latter used a control Hamiltonian constructed via the methods in [298], indeed showing a scaling $\sim T^{-4}$ for times shorter than the coherence time of the probe. Regarding the scheme employing nitrogen-vacancy centers, a different control was employed where the limiting factor was set by the coherence time of the signal itself. Dividing the total time into small blocks where a dynamical decoupling sequence and a subsequent measurement are performed, the total FI is the sum of the FI of the different measurements. That results in a scaling of

$$\Delta^2 \omega \sim \frac{1}{T^3 T_2}, \quad (4.74)$$

which holds as long as T is smaller than the coherence time of the signal and the coherence time of the probe T_2 .

CHAPTER 5

Realistic Bounds on the Precision: An Analysis Involving a Microscopic Noise Model

This chapter has been published in [H3] and large parts have been taken from there.

The analysis of precision bounds in quantum metrology is commonly performed by defining a master equation which describes the open system evolution. In the last years, that lead to a bunch of different results for the ultimate bounds, where each is valid for a specific type of dynamics (i.e. type of quantum channel), e.g. a pure dephasing semigroup [34], an NPC semigroup introducing orthogonal noise [45], non-markovian pure dephasing dynamics [38] and the most general result derived so far covering any PC dynamics [39] (see Section 4.4.1 for the latter). On the following pages, we will present a model which is microscopically motivated and is able to reproduce all of the bounds derived so far. Furthermore, it sheds light into the unexplored regime of NPC dynamics, where only the special case presented in [45] has been examined so far (see the first part of Section 4.4.2).

In particular, the model considered here is represented by a qubit as the probe, coupled to an environment consisting of an infinite number of non-interacting harmonic oscillators. Crucially, the coupling can be tuned to reproduce any coupling direction, from parallel to orthogonal. Depending on the operating regime, different approximations of the dynamics are valid yielding either NPC or PC, likewise as semigroup or non-semigroup dynamics. While hence providing

regimes where each of the previously derived limits apply, in Section 5.4 we also identify a completely unknown limit valid for the case of NPC orthogonal noise which does not form a semigroup. Moreover, we argue that any NPC noise that possess a noise component parallel to the parameter imprinting will ultimately follow the limits derived for PC.

The asymptotic limits set aside, another crucial aspect will be covered. When defining the quantum channel via an artificial master equation, the natural parameter dependence of the noise rates is usually neglected. Starting with Section 5.3, we will explore how the different properties of PC and NPC dynamics contribute to the QFI and that the contributions induced by the noise rates can change the QFI by non-negligible amounts.

5.1. Spin-Boson Model: Weak-Coupling Master Equation and Secular Approximation

As emphasized in Chapter 4, we assume that the probes are affected identically and independently by their environments, so that the global dynamics is fixed by the one-particle dynamics, see Figure 4.1 (c) and Equation (4.24). Therefore, we focus on the microscopic derivation of the open-system dynamics of one probe, which we present in the following. In particular, we model our sensing qubit with the widely used spin-boson model for quantum dissipation [44]. Within this model the environment corresponds to a set of non-interacting harmonic oscillators linearly coupled to the system, which may be directly interpreted as interactions with a radiation field or a phononic (crystal lattice) background. This model provides us with the most general description of the corresponding open two-level system dynamics, including special cases such as pure dephasing [2] or purely transversal noise [303]. The Hamiltonian of the spin-boson model consists of the two-level system Hamiltonian H_0 , the free Hamiltonian H_E of the environment and the interaction Hamiltonian H_I , which sum up to ($\hbar = 1$)

$$\begin{aligned}
 H = H_0 + H_E + H_I = & \frac{\omega_0 \sigma^z}{2} + \sum_n \omega_n a_n^\dagger a_n \\
 & + \left(\cos \vartheta \frac{\sigma^x}{2} + \sin \vartheta \frac{\sigma^z}{2} \right) \otimes \sum_n (g_n a_n + g_n^* a_n^\dagger).
 \end{aligned} \tag{5.1}$$

The system's frequency ω_0 represents the encoded frequency, while a_n and a_n^\dagger are the bosonic annihilation and creation operators of the bath mode n of frequency ω_n , which is coupled to the two-level system with the strength g_n . The parameter ϑ defines the *coupling angle*, i.e., the angle between the x -axis and the direction of the coupling operator (in the xz -plane): for

$\vartheta = \pi/2$ we have pure dephasing (or parallel, with respect to H_0) interaction, while for $\vartheta = 0$ we have purely transversal (or perpendicular) interaction.

Finally, note that the Hamiltonian is physically equivalent to a transformed Hamiltonian where the system only couples via σ^z to the environment, but both σ^z and σ^x are included in the system Hamiltonian; e.g., this would describe an experimental realization where the system is driven by the application of an off-axis magnetic field (see Appendix A.2.1).

5.1.1. Second-Order TCL-Master Equation

To obtain a closed form of the master equation ruling the evolution of the probe subject to the noise fixed by Equation (5.1), we exploit the perturbative approach of the TCL master equation introduced in Section 1.2.1, assuming that the system is weakly coupled to the environment. Recall that its general form in the interaction picture is given by

$$\frac{d\tilde{\rho}(t)}{dt} = - \int_0^t d\tau \operatorname{tr}_E [[H_I(t), [H_I(\tau), \tilde{\rho}(t) \otimes \rho_E]]],$$

where $H_I(t)$ is now the the interaction Hamiltonian H_I in the interaction picture with respect to $H_0 + H_E$ as fixed by the Hamiltonian in Eq. (5.1). In Appendix A.2.2, we describe how to get the desired master equation for the reduced system density matrix starting from the the general form of the TCL expansion, Eq. (1.13). At this point, let us just briefly introduce the main required quantities to define such a master equation, along with their physical meaning. First, the interaction Hamiltonian in the interaction picture is given by

$$H_I(t) = e^{iH_0 t} \left(\cos \vartheta \frac{\sigma^x}{2} + \sin \vartheta \frac{\sigma^z}{2} \right) e^{-iH_0 t} \otimes B(t), \quad (5.2)$$

where

$$B(t) = \sum_n \left(g_n e^{-i\omega_n t} a_n + g_n^* e^{i\omega_n t} a_n^\dagger \right) \quad (5.3)$$

is the interaction picture of the environmental operator appearing in the interaction Hamiltonian, see Equation (5.1). The partial trace over the environment introduces the two-time correlation function $\operatorname{tr}_E [B(t)B(\tau)\rho_E]$ of the environment under its free dynamics, along with its complex conjugate $\operatorname{tr}_E [B(\tau)B(t)\rho_E]$. This function encompasses the whole relevant information about the environment needed to characterize the open-system evolution in the weak coupling regime: as we will see, it fixes each coefficient of the master equation. In addition, if the initial state of the bath is thermal, i.e.

$$\rho_E(0) = \frac{\exp\{-\beta H_B\}}{Z}, \quad (5.4)$$

with the inverse temperature β and $Z = \text{tr} [\exp\{-\beta H_B\}]$, since $[H_B, \rho_E(0)] = 0$ the correlation function only depends on the difference of its time arguments $t - \tau$ ¹. Therefore we can define the correlation function $C(t)$ via

$$\text{tr}_E [B(t)B(\tau)\rho_E] = \text{tr}_E [B(t - \tau)B(0)\rho_E] \equiv C(t - \tau). \quad (5.5)$$

Using the definition of $B(t)$ in Equation (5.3), this expression can be written as

$$C(t) = \sum_n g_n^2 \left[N(\omega_n) e^{i\omega_n t} + (N(\omega_n) + 1) e^{-i\omega_n t} \right], \quad (5.6)$$

where $N(\omega_n) = \text{tr}_E [a_n^\dagger a_n \rho_E]$ represents the average number of excitations in the bath mode n . For the considered thermal state it is given by [2]

$$N(\omega) = \frac{1}{e^{\beta\omega} - 1} = \frac{1}{2} \left[\coth\left(\frac{\beta\omega}{2}\right) - 1 \right]. \quad (5.7)$$

The bath correlation function $C(t)$ is conveniently expressed in terms of the *spectral density* of the environment, which is defined by

$$J(\omega) = \sum_n g_n^2 \delta(\omega - \omega_n). \quad (5.8)$$

This quantity describes the density of the bath modes weighted with the square of their individual coupling strength to the system. In fact, the bath correlation function (5.6) can be written as

$$\begin{aligned} C(t) &= \int_0^\infty d\omega J(\omega) \left[N(\omega) e^{i\omega t} + (N(\omega) + 1) e^{-i\omega t} \right] \\ &= \int_{-\infty}^\infty d\omega e^{i\omega t} N(\omega) [J(\omega)\Theta(\omega) - J(-\omega)\Theta(-\omega)] \\ &\equiv \int_{-\infty}^\infty d\omega e^{i\omega t} j(\omega). \end{aligned} \quad (5.9)$$

In the second line we used the formal identity $-N(-\omega) = N(\omega) + 1$ [see Equation (5.7)] in order to introduce the function $j(\omega)$, i.e., the anti-Fourier transform of the bath correlation function².

¹This can be straightforwardly derived when using the noted commutation relation and the cyclic property of the trace: For $u(t) = e^{-itH_B}$ we have $\text{tr} [u(t)Bu^\dagger(t)u(\tau)Bu^\dagger(\tau)\rho_E(0)] = \text{tr} [u(t)Bu^\dagger(t)u(\tau)B\rho_E(0)u^\dagger(\tau)] = \text{tr} [u^\dagger(\tau)u(t)Bu^\dagger(t)u(\tau)B\rho_E(0)]$. Note also that $B(0) \equiv B$.

²Often $j(\omega)$ is referred to as the *spectrum* and corresponds to $S(\omega)$ introduced in Section 3.1. Nevertheless, note that there is a factor of 2π in the definition and we keep separate notations since $S(\omega)$ was introduced for a classical, stationary stochastic and Gaussian process, while here we consider the special case of a thermal state

The Heaviside stepfunction $\Theta(\omega)$ keeps track of the fact that $J(\omega)$ is defined only for positive frequencies. Finally, the relation in Equation (5.9) allows us to perform the continuum limit straightforwardly by replacing the spectral density in Equation (5.8) with a smooth function of the frequency bath modes [2].

As said, the bath correlation function $C(t)$ or, equivalently, the bath spectral density $J(\omega)$ along with the initial state of the bath fix the reduced master equation in the weak coupling regime: since we are dealing with the second order perturbative (TCL) expansion, only the two-time correlation function $C(t)$ is involved, while the bath multi-time correlation functions would only be involved in higher order terms (see also the recent [304]). As shown in Appendix A.2.2, the master equation (back in the Schrödinger picture) is then given by

$$\begin{aligned} \frac{d\rho(t)}{dt} = \mathcal{L}(t)[\rho(t)] = & -i \left[H_0 + H^{\text{LS}}(t), \rho(t) \right] \\ & + \sum_{j,k=\pm,z} b_{kj}(t) \left(\sigma_k \rho(t) \sigma_j^\dagger - \frac{1}{2} \{ \sigma_j^\dagger \sigma_k, \rho(t) \} \right), \end{aligned} \quad (5.10)$$

where we introduced the function

$$\Gamma(\varsigma, t) = \int_0^t d\tau e^{i\varsigma\tau} C(\tau) \quad (5.11)$$

for $\varsigma = \pm\omega_0, 0$ while the Hamiltonian correction is fixed by the elements

$$\begin{aligned} H_{11}^{\text{LS}}(t) &= \frac{\cos^2 \vartheta}{4} \text{Im}\{\Gamma(\omega_0, t)\} \\ H_{10}^{\text{LS}}(t) = H_{01}^{\text{LS}*}(t) &= -\frac{i \cos \vartheta \sin \vartheta}{4} \\ &\quad \times \left(\text{Re}\{\Gamma(0, t)\} - \frac{1}{2} (\Gamma^*(-\omega_0, t) + \Gamma(\omega_0, t)) \right) \\ H_{00}^{\text{LS}}(t) &= \frac{\cos^2 \vartheta}{4} \text{Im}\{\Gamma(-\omega_0, t)\}, \end{aligned} \quad (5.12)$$

for the bath and the second order TCL expansion. However, the most crucial difference is the symmetry the functions. It was assumed that $S(\omega) = S(-\omega)$, which is in general not true for $J(\omega)$. In Section 5.2 we show that this is only true if the initial state of the bath is at a high temperature.

with $H_{ij}^{\text{LS}}(t) = \langle i | H^{\text{LS}}(t) | j \rangle$ for $i, j = 0, 1$, and the coefficients read

$$\begin{aligned}
 b_{zz}(t) &= \frac{\sin^2 \vartheta}{2} \text{Re}\{\Gamma(0, t)\} \\
 b_{++}(t) &= \frac{\cos^2 \vartheta}{2} \text{Re}\{\Gamma(-\omega_0, t)\} \\
 b_{--}(t) &= \frac{\cos^2 \vartheta}{2} \text{Re}\{\Gamma(\omega_0, t)\} \\
 b_{+-}(t) &= b_{-+}^*(t) = \frac{\cos^2 \vartheta}{4} (\Gamma(-\omega_0, t) + \Gamma^*(\omega_0, t)) \\
 b_{z+}(t) &= b_{+z}^*(t) = \frac{\sin \vartheta \cos \vartheta}{4} (\Gamma(0, t) + \Gamma^*(-\omega_0, t)) \\
 b_{z-}(t) &= b_{-z}^*(t) = \frac{\sin \vartheta \cos \vartheta}{4} (\Gamma(0, t) + \Gamma^*(\omega_0, t)) .
 \end{aligned} \tag{5.13}$$

Let us stress that we did not invoke the Born-Markov approximation [2] in our derivation—the above time-local master equation includes fully general non-Markovian effects and it will provide us with a satisfactory description of the noisy evolution of the probes as long as the interaction with the environment is weak enough (i.e., the higher orders of the TCL expansion can be neglected). In addition, we are taking into account the dependence of the coefficients of the dissipative part of the master equation on the free system frequency ω_0 , see Equation (5.13), i.e., on the parameter to be estimated. This is a natural consequence of the detailed microscopic derivation of the system dynamics [2], in contrast with the phenomenological approaches, where the master equation is postulated on the basis of the noise effects to be described. Let us emphasize that only in the case of pure dephasing, for which $\vartheta = \pi/2$ and all dissipative terms in Eq. (5.13) apart from $b_{zz}(t)$ vanish, the dissipative part of the master equation can be assured not to depend on ω_0 . Otherwise, this is not generally the case unless a special choice of $J(\omega)$ is made (e.g., discussed later in Section 5.2.2).

5.1.2. Secular Approximation

Finding an explicit solution to the master equation in Equation (5.10) is in general a complicated task, even after fixing the explicit form of the spectral density of the bath modes. On the other hand, the structure of the dynamics can be simplified considerably by making the so-called *secular approximation* [2, 112, 186, 187], which relies on a time-scale separation between the system free-evolution time τ_0 and the relaxation time τ_R of the system subject to the interaction with the environment. Whenever the free dynamics is much faster than the dissipative one, i.e., $\tau_0 \sim \omega_0^{-1} \ll \tau_R$, one can neglect terms oscillating with $e^{\pm i\omega_0 t}$ because they will be averaged

out to 0 over a time interval of the order of τ_R . If we apply this approximation to the weak coupling master equation, see in particular Equation (A.14), all off-diagonal elements of the coefficient matrix $b_{kj}(t)$ in Equation (5.10) and the off-diagonal elements of the Hamiltonian in Equation (5.12) vanish, so that one is left with the master equation

$$\begin{aligned} \frac{d\rho(t)}{dt} = & -i \left[H_0 + \frac{H_{11}^{\text{LS}}(t)}{2} \sigma^z, \rho(t) \right] \\ & + b_{++}(t) \left(\sigma_+ \rho(t) \sigma_- - \frac{1}{2} \{ \sigma_- \sigma_+, \rho(t) \} \right) \\ & + b_{--}(t) \left(\sigma_- \rho(t) \sigma_+ - \frac{1}{2} \{ \sigma_+ \sigma_-, \rho(t) \} \right) \\ & + b_{zz}(t) (\sigma^z \rho(t) \sigma^z - \rho(t)), \end{aligned} \quad (5.14)$$

where all the non-zero coefficients are still those of Equation (5.13). This master equation can be explicitly solved for generic coefficients $b_{++}(t), b_{--}(t), b_{zz}(t)$ and $H_{11}^{\text{LS}}(t)$ (see, e.g., [39, 305]). Crucially, we see how the secular master equation in Equation (5.14) precisely corresponds to the most general form of a master equation associated with a PC qubit dynamics recalled in Section 1.5, see Equation (1.38). Hence the difference between secular and non-secular dynamics provides us with a direct physical explanation of the difference between PC and NPC dynamics. The complete (weak-coupling) dynamics described by the master equation in Equation (5.10) will generally lead to NPC dynamical maps, represented by generic matrices $\mathcal{D}^{\Lambda(t)}$ as in Equation (1.19) and corresponding to a completely general affine transformation of the Bloch sphere. Instead, if one applies the secular approximation, thus getting the master equation in Equation (5.14), the resulting dynamics is PC and will be then characterized by dynamical maps with a structure as in Equation (1.37), see also Figure 5.1(a) and (b). In other words, within this framework, the distinction between PC and NPC dynamics precisely corresponds to the distinction between dynamics within or outside the secular regime, i.e., the regime $\tau_0 \ll \tau_R$ where the secular approximation is well-justified. Needless to say, and as we will see explicitly in the next sections, the two kinds of dynamics describe also qualitatively different open-system evolutions. As a paradigmatic example, one can easily see how for any secular master equation the populations and coherences are decoupled, while the inclusion of non-secular terms leads to a coupling between them. The latter can be relevant for different phenomena, such as excitonic transport [89, 306], or the speed of the evolution in non-Markovian dynamics [307, 308]. Finally, note that general constraints on the variation of the coherences for a given variation of the populations in the presence of a generic completely positive phase covariant map have been recently derived in [50].

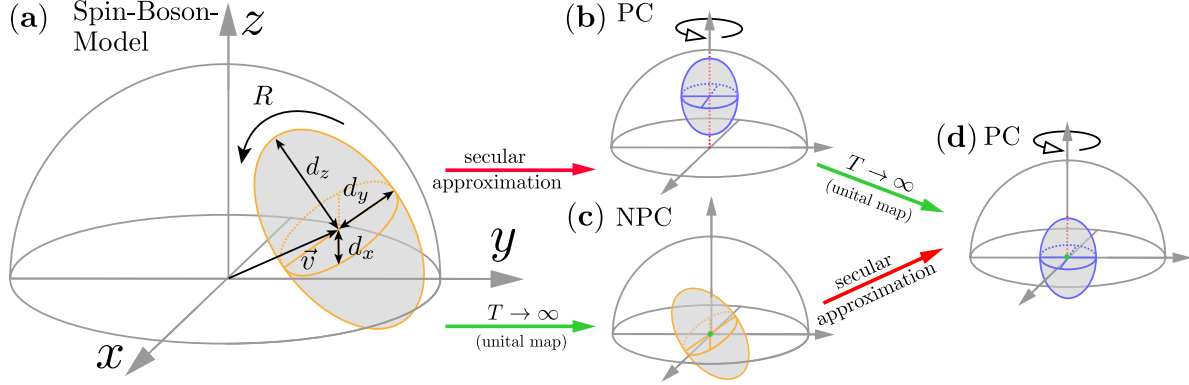


Figure 5.1.: **Various dynamical regimes of the weak-coupling spin-boson model in the Bloch sphere picture.** (a): The NPC dynamics specified by Eqs. (5.10-5.12) can be viewed as a general affine transformation Eq. (1.20) of the Bloch sphere, see also Sections 1.3 and 1.5. (b): PC dynamics Eq. (5.14) is then obtained by applying the secular approximation. (c): High-temperature limit of the spin-boson model forces a general map of the NPC dynamics to be *unital*, i.e., the translation, $\vec{v} = 0$, to vanish. (d): When both high-temperature and secular approximations apply, the resulting quantum map in the Bloch representation is both cylindrically symmetric and unital. (Figure first published in [H3])

5.2. Solutions in the High-Temperature Regime

In order to get analytic solutions for the NPC dynamics, which will also be useful to compare the different impact of NPC and PC dynamics on the metrological properties of the probes, let us restrict to the case of a bath at a high temperature. Because of that, we can treat the function $j(\omega)$ in the bath correlation function $C(t)$, see Equation (5.9), as a symmetric function of ω : for large values of the temperature, i.e., small values of β , one has that $N(\omega) \approx 1/(\beta\omega)$, see Equation (5.7), and therefore $j(\omega) \approx j(-\omega)$. Looking at the correlation function in Equation (5.9), we see that in this regime $C(t) \approx C^*(t)$ thus we have $\Gamma(-\omega_0, t) \approx \Gamma^*(\omega_0, t)$, see Equation (5.11). Together with Equation (5.13), we then obtain

$$\begin{aligned}
 b_{zz}(t) &= \frac{\sin^2 \vartheta}{2} \Gamma(0, t) \\
 b_{+-}(t) &= b_{-+}^*(t) = \frac{\cos^2 \vartheta}{2} \Gamma(-\omega_0, t) \\
 b_{++}(t) &= b_{--}(t) = \text{Re}\{b_{+-}(t)\} \\
 b_{z+}(t) &= b_{+z}^*(t) = b_{z-}^*(t) = b_{-z}(t) = \frac{\sin \vartheta \cos \vartheta}{4} (\Gamma(0, t) + \Gamma^*(-\omega_0, t)),
 \end{aligned} \tag{5.15}$$

while the Hamiltonian correction is given by

$$\begin{aligned} H_{11}^{\text{LS}}(t) &= \frac{\cos^2 \vartheta}{4} \text{Im}\{\Gamma(\omega_0, t)\} \\ H_{10}^{\text{LS}}(t) &= H^{\text{LS}*}(t)_{01}(t) = \frac{i \cos \vartheta \sin \vartheta}{4} (\text{Re}\{\Gamma(0, t)\} - \Gamma(-\omega_0, t)) \\ H_{00}^{\text{LS}}(t) &= \frac{\cos^2 \vartheta}{4} \text{Im}\{\Gamma(-\omega_0, t)\}. \end{aligned}$$

These identities can be exploited to simplify the structure of the master equation, and hence of the corresponding dynamical map. In [A.2.3](#), we show explicitly that the constraints in Equation (5.15) imply the matrix form

$$\mathbf{D}^{\Lambda(t)} = \begin{pmatrix} 1 & \vec{0}^T \\ \vec{0} & V(t) \end{pmatrix}, \quad (5.16)$$

so that the translations of the Bloch sphere can be neglected and thus the dynamics can be described by unital maps, i.e., such that $\Lambda(t)[\mathbb{1}] = \mathbb{1}$, see Figure [5.1\(c\)](#). Note that the unitality of the reduced map is a general consequence of the high temperature limit $T \rightarrow \infty$, in which the initial state of the bath becomes maximally mixed [\[309\]](#). By further applying the singular value decomposition to the matrix $V(t)$ one can get the geometrical picture associated with the dynamical map, in terms of rotations and contractions of the Bloch sphere, see Section [1.3](#). Indeed, an analogous result holds if we start from the PC master equation, see Equation (5.14), and in the Figure [5.1\(c-d\)](#) one can see a graphical representation of the corresponding transformations of the Bloch sphere.

We will present, in particular, two different solutions of the high-temperature master equations (the PC and NPC ones); namely, for short times and a generic spectral density, as well as for an Ohmic spectral density at any time.

5.2.1. The Short-Time Evolution

As explained in Appendix A.2.3, using the Dyson series of Equation (1.12) we obtain the short-time solution of master equation (5.10) as:

$$\mathbf{D}_{(3)}^{\Lambda(t)} = \begin{pmatrix} 1 & 0 & 0 & 0 \\ 0 & 1 - \frac{\omega_0^2 t^2}{2} - \frac{1}{2} \alpha t^2 \sin^2 \vartheta & -\omega_0 t + q & \frac{1}{2} \alpha t^2 \cos \vartheta \sin \vartheta \\ 0 & \omega_0 t - q & 1 - \frac{\omega_0^2 t^2}{2} - \frac{\alpha t^2}{2} & \frac{1}{3} \alpha \omega_0 t^3 \cos \vartheta \sin \vartheta \\ 0 & \frac{1}{2} \alpha t^2 \cos \vartheta \sin \vartheta & -\frac{1}{3} \alpha \omega_0 t^3 \cos \vartheta \sin \vartheta & 1 - \frac{1}{2} \alpha t^2 \cos^2 \vartheta \end{pmatrix} \quad (5.17)$$

where

$$\alpha = \int_{-\infty}^{\infty} d\omega j(\omega) \approx \int_0^{\infty} d\omega \frac{2J(\omega)}{\beta\omega} \quad \text{and} \quad (5.18)$$

$$q = \frac{\omega_0 t^3}{6} \left[\alpha(1 + 2 \sin^2 \vartheta) + \omega_0^2 \right]. \quad (5.19)$$

Truncating the Dyson series is justified due to the weak-coupling approximation, while we have kept the terms up to the third order (and *not* only to the second order) for a reason which will become clear when we evaluate the QFI of the corresponding evolved state in Section 5.3.1. Note that despite the precise value ω_0 is not known in the metrological scheme, we assume that the condition $\omega_0 \gg \alpha$ is satisfied. The short time dynamical maps do not depend on the specific form of spectral density, but only on the global parameter α . Furthermore, evaluating the eigenvalues of the Choi matrix reveals that the map is CP [109].

Repeating the same calculations for the PC master equation in Equation (5.14) in the secular approximation, we arrive at

$$\mathbf{D}_{(3),\text{PC}}^{\Lambda(t)} = \begin{pmatrix} 1 & 0 & 0 & 0 \\ 0 & 1 - \frac{\omega_0^2 t^2}{2} - \frac{\alpha t^2}{4} (1 + \sin^2 \vartheta) & -\omega_0 t + q & 0 \\ 0 & \omega_0 t - q & 1 - \frac{\omega_0^2 t^2}{2} - \frac{\alpha t^2}{4} (1 + \sin^2 \vartheta) & 0 \\ 0 & 0 & 0 & 1 - \frac{1}{2} \alpha t^2 \cos^2 \vartheta \end{pmatrix}. \quad (5.20)$$

5.2.2. Finite-Time Evolution for an Ohmic Spectral Density

Here, in order to be able to characterize the reduced dynamics at any time t , we focus on a particular specific spectral density of the bath—the Ohmic spectral density:

$$J(\omega) = \lambda \omega e^{-\omega/\omega_c}, \quad (5.21)$$

where λ quantifies the global strength of the system-environment interaction, while ω_c sets the cut-off frequency which defines the relevant environmental frequencies in the open-system dynamics. We further assume that $\omega_c \gg \omega_0$, so that the dependence of $\Gamma(\varsigma, t)$ on ς can be neglected and $\Gamma(\omega_0, t) \approx \Gamma(-\omega_0, t) \approx \Gamma(0, t)$, as then, see Eqs. (5.9) and (5.11):

$$\begin{aligned} \Gamma(\pm\omega_0, t) &\approx \frac{\lambda}{\beta} \int_0^t d\tau \int_{-\infty}^{\infty} d\omega e^{i(\pm\omega_0+\omega)\tau} \\ &\quad \times \left(e^{-\omega/\omega_c} \Theta(\omega) + e^{\omega/\omega_c} \Theta(-\omega) \right) \\ &= \frac{2\lambda}{\beta} \int_0^t d\tau e^{\pm i\omega_0\tau} \int_0^{\infty} d\omega e^{-\frac{\omega}{\omega_c}} \cos(\omega\tau) \\ &= \frac{2\lambda}{\beta} \int_0^t d\tau e^{\pm i\omega_0\tau} \frac{\omega_c}{1 + \omega_c^2 \tau^2} \approx \frac{2\lambda}{\beta} \int_0^t d\tau \frac{\omega_c}{1 + \omega_c^2 \tau^2}, \end{aligned} \quad (5.22)$$

where in the first and last approximated equalities we used the high-temperature condition and $\omega_0/\omega_c \ll 1$, respectively. The coefficients of the master equation in Equation (5.13) then simplify to

$$\begin{aligned} b_{zz}(t) &= \frac{\sin^2 \vartheta}{2} \Gamma(0, t) \\ b_{++}(t) &= b_{+-}(t) = b_{-+}(t) = b_{--}(t) = \frac{\cos^2 \vartheta}{2} \Gamma(0, t) \\ b_{z+}(t) &= b_{+z}(t) = b_{z-}(t) = b_{-z}(t) = \frac{\sin \vartheta \cos \vartheta}{2} \Gamma(0, t), \end{aligned} \quad (5.23)$$

while the Hamiltonian correction, $H^{\text{LS}}(t)$, vanishes. We stress that it is the specific choice of Ohmic spectral density that assures the coefficients of the master equation to be independent of ω_0 —a fact, typically taken for granted in quantum metrology scenarios [12, 39, 43, 45, 46, 284, 310].

Now, using Equation (5.23) one can easily see (e.g., by diagonalizing the matrix with elements given by the coefficients $b_{jk}(t)$) that the time-local master equation can be written as

$$\frac{d\rho(t)}{dt} = -i [H_0, \rho(t)] + \gamma(t) \left(\bar{\sigma} \rho(t) \bar{\sigma}^\dagger - \rho(t) \right), \quad (5.24)$$

where the rate $\gamma(t)$ and the dissipative operator $\bar{\sigma}$ are given by

$$\begin{aligned}\gamma(t) &= \frac{1}{2}\Gamma(0,t) = \frac{\lambda}{\beta} \arctan(\omega_c t) \\ \bar{\sigma} &= \cos \vartheta \sigma^x + \sin \vartheta \sigma^z.\end{aligned}\tag{5.25}$$

It is worth noting that the dissipative part of the master equation is fixed by one single operator $\bar{\sigma}$, i.e., we have the most general qubit rank-one Pauli noise, recently proved to be correctable in the semigroup case ($\gamma(t) = \text{const}$) in quantum metrology by ancilla-assisted error-correction [283] (see in particular Section 4.6.2), which has been demonstrated experimentally for transversal coupling, $\vartheta = 0$, in reference [290]. In addition, the only noise rate $\gamma(t)$ is a positive function of time, which, as introduced in Section 1.2.1, guarantees not only the CP of the dynamics, but also that the dynamical maps can be always split into CP terms. In this case, one speaks of (CP)-divisible dynamics, which coincides with the definition of Markovian quantum dynamics put forward in [103]; see also [82] and Section 1.4. As expected, in the limit of an infinite cut-off, $\omega_c \rightarrow \infty$, the rate goes to a positive constant value, $\gamma(t) \rightarrow \pi\lambda/(2\beta)$, so that we recover a Lindblad time-homogeneous (semigroup) dynamics [112]; see Appendix A.2.5, where we also give the explicit form of the corresponding dynamical maps for $\vartheta = 0, \pi/2$, i.e., transversal and pure dephasing noise-types, respectively.

Finally, note that a purely transversal interaction Hamiltonian ($\vartheta = 0$) yields a purely transversal master equation equation, i.e., the only dissipative operator $\bar{\sigma} = \sigma^x$ in Equation (5.24) is orthogonal to H_0 , which is generally not guaranteed for arbitrary spectral densities. $\bar{\sigma} = \sigma^x$ characterizes what is usually known in the literature [45, 46] as (and what we mentioned already in 4.4.2) transversal noise.

Let us now consider the corresponding dynamics under the secular approximation that provides us with a PC dynamics. The coefficients in the third line of Equation (5.23) along with $b_{+-}(t)$ are set to 0 and we are thus left with the PC master equation

$$\frac{d\rho(t)}{dt} = -i[H_0, \rho(t)] + \gamma(t) \sum_{j=\pm, z} d_j \left(\sigma_j \rho(t) \sigma_j^\dagger - \frac{1}{2} \{ \sigma_j^\dagger \sigma_j, \rho(t) \} \right) \tag{5.26}$$

with $d_+ = d_- = \cos^2 \vartheta$, while $d_z = \sin^2 \vartheta$. Once again, the dynamics is CP and due to the positivity of $\gamma(t)$ and the d_j s it is even CP-divisible. Despite having now three different dissipative operators, these claims hold because there is only one single time-dependent function which defines all the rates.

In Figure 5.2 we illustrate the different dynamics geometrically by comparing the different evolutions of the open system for the NPC dynamics described by Equation (5.25) and the

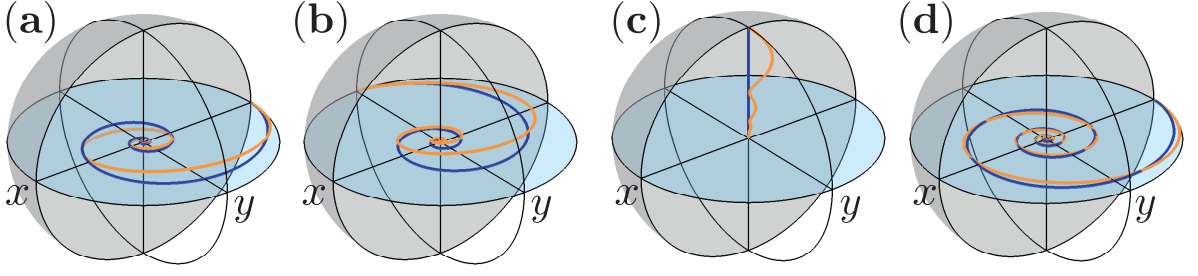


Figure 5.2.: **Qubit evolution in the Bloch sphere picture for the resulting NPC Eq. (5.24) and PC Eq. (5.26) dynamics** (orange and blue, respectively). In (a-c) the evolution parameter $\vartheta = \pi/4$ is chosen, so that when starting from an equator state, (a-b), the NPC dynamics clearly differs from PC leading to a rotation around an axis that is tilted away from z . Initializing the qubit in an excited state, (c), the PC dynamics yields just a decay to a completely mixed state, while for NPC the rotational behavior is still manifested. In (d), perfectly transversal ($\vartheta = 0$) coupling is considered to illustrate that even though for both NPC and PC an equatorial state evolves in the xy plane, the secular approximation of PC strongly modifies the speed of contraction. (Figure first published in [H3])

PC dynamics fixed by Equation (5.26), respectively, see Appendix A.2.4. In Figures 5.2(a-c), we report the evolution for the same dynamics (i.e., the same $\omega_0, \omega_c, \lambda, \beta$ and ϑ), for the three different initial conditions which correspond to the three canonical orthogonal axes in the Bloch sphere. Of course, this is enough to detect all the possible linear transformations that the set of states undergoes during the evolution. In the PC dynamics we have contractions and rotations about the z -axis, as well as equal contractions along the x - and y -axes. These are all transformations commuting with the unitary rotation about the z -axis, as recalled in Section 1.5. On the other hand, in the non-secular dynamics we can observe a rotation about an axis with components in the plane perpendicular to the z -axis, which clearly breaks the phase covariance of the dynamics. Figure 5.2(d) is devoted to illustrate another NPC effect, which is already present in the dynamics in Figures 5.2(a-c), but is not clearly observable due to the other transformations of the Bloch sphere. We consider a dynamics where $\vartheta = 0$, thus excluding any rotation apart from that about the z -axis³. As we see, the NPC dynamics introduces different contractions along the x and y directions, contrary to the PC case. The effects on parameter estimation of the rotations about the x - and y -axes, as well as the different contractions along them will be investigated in Section 5.3.2.

Finally, note that although the non-secular terms introduce a transient behavior, which departs from the secular (i.e., PC) evolution, the system relaxes, in any case, to the fully mixed state.

³Once again, this could be shown by exploiting a block-diagonal structure of the generator $\mathcal{L}(t)$ and thus of the resulting dynamical maps; compare with Appendix A.2.3.

When probe systems can be interrogated within the transient dynamics, metrological advances may arise, as discussed in the following sections.

5.3. Single-Qubit Quantum Fisher Information

We are now in a position to study the precision that can be reached in frequency estimation under the general dynamics considered here. We start by addressing the case of a single probe, which already enables us to point out some relevant differences in the behavior of the QFI under a PC and a NPC dynamics, respectively. In Section 5.4, we focus on the asymptotic scaling with the number N of probes.

As recalled in Section 4.3, the QFI fixes the maximum achievable precision via the QCRB in Equation (4.32). For a single qubit probe, one can directly evaluate the QFI by diagonalizing the state $\rho_{\omega_0}(t)$ at time t , see Equation (4.27). Here, instead, we use a different and equivalent formulation of the QFI [311], which directly connects it to the Bloch sphere picture of the probe dynamics. Given the Bloch vector $\vec{r}(0)$ associated with the initial state $\rho(0)$ and recalling that we are dealing only with unital dynamics, see Section 5.2, so that the affine transformation of the Bloch sphere in Equation (1.20) reduces at any time t and for any ω_0 to $\vec{r}(0) \rightarrow V_{\omega_0}(t)\vec{r}(0)$, the QFI at time $t > 0$ can be expressed as

$$F_Q[\rho_{\omega_0}(t)] = \left| \dot{V}_{\omega_0}(t)\vec{r}(0) \right|^2 + \frac{\left(V_{\omega_0}(t)\vec{r}(0) \cdot \dot{V}_{\omega_0}(t)\vec{r}(0) \right)^2}{1 - |V_{\omega_0}(t)\vec{r}(0)|^2}; \quad (5.27)$$

the second term is set to 0 for pure states, i.e., for times where $|V_{\omega_0}(t)\vec{r}(0)| = 1$. We remind that we mark the derivative with respect to the parameter by a dot, i.e., $\dot{V}_{\omega_0} \equiv \partial V_{\omega_0} / \partial \omega_0$. In the following, we focus on initially pure states, i.e., $|\vec{r}(0)| = 1$, since any mixture would decrease the QFI as a consequence of its convexity [12]. It is then convenient to move to spherical coordinates and adequately parametrize pure states by $\vec{r} = \{\sin \theta \cos \phi, \sin \theta \sin \phi, \cos \theta\}$.

5.3.1. Short-Time Limit

Thus, let us start by looking at the short-time expansion of the QFI in Equation (5.27). The spherical parametrization provides us with a clear relation among the short-time QFI for the NPC and PC dynamics, see Eqs. (5.17) and (5.20), respectively. As a matter of fact, the first non-trivial term (i.e., the first contribution to F_Q which is induced by the noise and therefore the first contribution where F_Q differs between NPC and PC dynamics) in the QFI is of the order t^4 and it is fixed by those terms up to t^3 in $V_{\omega_0}(t)$ and $\dot{V}_{\omega_0}(t)$. Let us motivate this directly via the

purification based representation of the QFI in Eq. (4.31)

$$F_Q[\rho(t)] = 4 \min_{\psi} \langle \psi | \dot{U}^\dagger(t) \dot{U}(t) | \psi \rangle = 4 \min_{\psi} \langle \psi | \sum_{k,l=0}^{\infty} \dot{U}_k^\dagger \dot{U}_l t^{k+l} | \psi \rangle, \quad (5.28)$$

where ψ are possible purifications of $\rho(t)$. Here we assumed that the unitary operators on the extended space possess the power series $U(t) = \sum_{k=0}^{\infty} U_k t^k$. Since it is required that $F_Q[\rho(0)] = 0$, a necessary condition⁴ is that $\dot{U}_0 = 0$ and hence the observation follows immediately, i.e. the n -th order in the QFI is fully determined by the order $n - 1$ of the linear map (which can always be expressed as a unitary on an extended Hilbertspace by virtue of Stinespring's dilation theorem).

After a straightforward calculation, we arrive in fact at

$$\begin{aligned} F_{Q,PC}^{(4)} &= \sin^2 \theta t^2 - \frac{1}{3} \alpha \sin^2 \theta (1 + \sin^2 \vartheta) t^4, \\ F_Q^{(4)} &= F_{Q,PC}^{(4)} + \alpha t^4 \sin \theta \left(\frac{1}{3} \cos \theta \sin 2\vartheta \cos \phi \right. \\ &\quad \left. + \frac{\sin^2 \phi (\sin \vartheta \cos \theta + \cos \vartheta \cos \phi \sin \theta)^2 / 4}{\cos \theta \cot \theta - 2 \tan \vartheta \cos \phi \cos \theta + (\cos^{-2} \vartheta - \cos^2 \phi) \sin \theta} \right). \end{aligned} \quad (5.29)$$

The maximum value of the QFI for a PC dynamics is obtained for $\vartheta = 0$, i.e., for a pure transversal Hamiltonian [45] and for $\theta = \pi/2$, i.e., for a state lying on the equator of the Bloch sphere; moreover, the dephasing noise, i.e., $\vartheta = \pi/2$, is the most detrimental in this regime. Although the expression for $F_Q^{(4)}$ in the NPC case is too cumbersome to yield a comprehensible analytical solution for a state which maximizes the QFI in the short time limit, even for a fixed value of the parameter ϑ , we report an approximated evaluation later in this Section 5.3.1.

As can be directly inferred comparing the two formulas in Equation (5.29), a crucial difference between PC and NPC dynamics is that in the former case the QFI only depends on the initial distance of the Bloch vector from the z -axis and hence on the angle θ , while the NPC terms introduce a dependence of the QFI on the direction of the Bloch vector itself and therefore on the angle ϕ . Such a dependence is a consequence of the non-commutativity of the encoding Hamiltonian with the action of the noise. For any PC dynamical map $\Lambda_{\omega_0,PC}$, if we rotate the state ρ about the z -axis by a certain angle ϕ , we have that

$$F_Q [\Lambda_{\omega_0,PC} \mathcal{U}_\phi [\rho]] = F_Q [\mathcal{U}_\phi \Lambda_{\omega_0,PC} [\rho]] = F_Q [\Lambda_{\omega_0,PC} [\rho]], \quad (5.30)$$

⁴Note that this is trivially given for any unitary which can be generated via a time independent Hamiltonian, i.e. $U(t) = e^{-it(H_{\omega_0} + H_A)}$ where H_A is the ancilla Hamiltonian acting on the extending space and H_{ω_0} is the encoding Hamiltonian.

by virtue of Equation (1.36) and equivalently the invariance of the QFI under rotations independent from the parameter to be estimated.

Now, the contributions due to the NPC terms are able to enhance the QFI, as can be seen in Figure 5.3(a), where we illustrate the behavior of the difference $\Delta F_Q \equiv F_Q^{(4)} - F_{Q,PC}^{(4)}$ as a function of the initial conditions. Besides the dependence on the initial phase ϕ , one can clearly observe the presence of several areas where the NPC terms do increase the QFI. Moreover, there are two maxima of the increment, one in the neighborhood of $\phi = 0$ and one in the neighborhood of $\phi = \pi$; we plot ΔF_Q for values $\phi \in [0, \pi]$, since it is a symmetric function under the reflection $\phi \rightarrow 2\pi - \phi$, see Equation (5.29). In the plot, we fixed $\vartheta = \pi/4$ but the behavior is qualitatively the same for different values of ϑ . Indeed, ΔF_Q goes to 0 for ϑ going to $\pi/2$ since for a pure dephasing Hamiltonian the secular approximation has no effect, so that the dynamical maps in Equation (5.17) and Equation (5.20) coincide.

Moreover, the presence of NPC terms can enhance the value of the QFI maximized over all the initial conditions and hence enlarge the maximal achievable precision. This is explicitly shown by taking into account the states lying on the equatorial plane of the Bloch sphere, which as said maximize $F_{Q,PC}^{(4)}$. For $\theta = \pi/2$, the second relation in Equation (5.29) reduces to

$$F_Q^{(4)} = F_{Q,PC}^{(4)} + \frac{\alpha t^4}{4} \left(\frac{\cos^4 \vartheta \cos^2 \phi \sin^2 \phi}{\sin^2 \vartheta \cos^2 \phi + \sin^2 \phi} \right), \quad (5.31)$$

which clearly shows that the maximum value of $F_{Q,PC}^{(4)}$ can be actually overcome for any value of $\vartheta \neq \pi/2$. In Figure 5.3 (b), we plot the increase of the QFI due to the NPC terms for $\theta = \pi/2$, while varying the initial phase ϕ and mixing angle ϑ . The QFI with the NPC terms is always bigger or equal than $F_{Q,PC}^{(4)}$ and the maximum enhancement occurs for ϕ close to $k\pi$ with $k = 0, 1, 2$ and the pure transversal noise corresponding to $\vartheta = 0$. However, the latter condition depends on the specific choice of the initial state: for $\theta \neq \pi/2$ one can have the maximal amplification due to the NPC terms for non-zero values of ϑ .

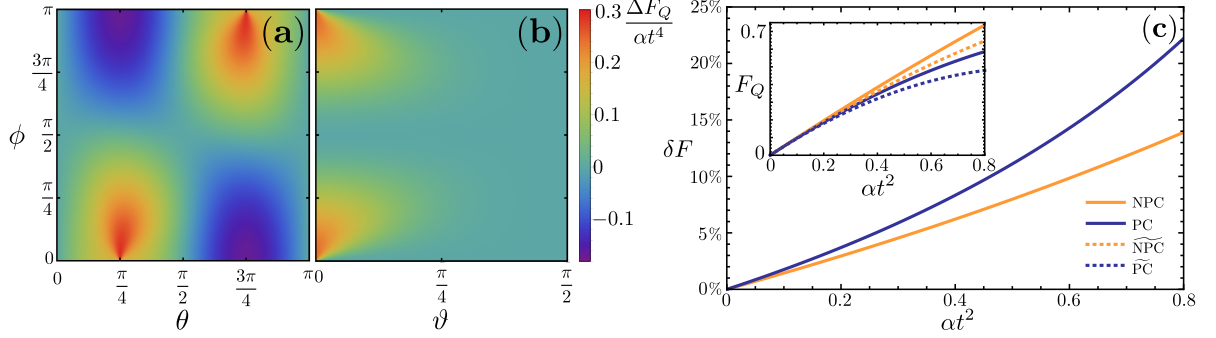


Figure 5.3.: **Difference between NPC and PC QFI at short time scales and contributions due to the dependence of the master-equation rates on ω_0 .** (a-b): Difference (adimensional) between the QFI of NPC and the PC dynamics, $\Delta F_Q / (\alpha t^4) = (F_Q^{(4)} - F_{Q,PC}^{(4)}) / (\alpha t^4)$, as a function of: (a) ϕ and θ for a fixed coupling angle $\vartheta = \pi/4$; (b) of ϕ and ϑ for states maximizing $F_{Q,PC}^{(4)}$ in Equation (5.31) at $\theta = \pi/2$. (c): Increase of the QFI at short time-scales for PC and NPC dynamics when the ω_0 dependence of the noise rates is taken into account, here $\delta F_Q = (F_Q - \tilde{F}_Q)/F_Q$. The inset shows the QFI plotted exactly and after neglecting the dependence of the noise rates on ω_0 (denoted by $\tilde{\bullet}$).

States Maximizing the Short Time NPC Expression

We provide an approximate evaluation of the maximum of the short-time expression of the NPC-QFI, see Equation (5.29), to gain some understanding of the dependence of the optimal QFI on the initial state also for NPC dynamics. Importantly, this explicitly demonstrates the dependence of the initial state on its initial phase. To second order in time, we have $F_Q^{(4)} = F_{Q,PC}^{(4)}$ and the QFI is maximal for $\theta = \pi/2$. We assume this to be around the optimal input even if the fourth order is considered. Taking the derivative of $F_Q^{(4)}$ with respect to ϕ we obtain

$$\left. \frac{\partial F_Q^{(4)}}{\partial \phi} \right|_{\theta=\pi/2} = \frac{\alpha \tau^4 \cos^4 \vartheta \sin \phi \cos \phi (\sin^2 \vartheta \cos^4 \phi - \sin^4 \phi)}{2 (\sin^2 \vartheta \cos^2 \phi + \sin^2 \phi)^2}. \quad (5.32)$$

The derivative can be solved for its root depending on ϕ which yields:

$$\theta_{\text{opt}} \approx \frac{\pi}{2} \quad \text{and} \quad \phi_{\text{opt}} = \arctan \left\{ \sqrt{\sin \vartheta} \right\}. \quad (5.33)$$

The (quasi-) optimality of this choice has been checked numerically, confirming that the value of the optimal ϕ_{opt} is more sensitive to changes in the bath-coupling angle ϑ than in the value of θ .

Different Contributions to the QFI.

To get a more quantitative and general understanding of the different contributions fixing the QFI in PC and NPC dynamics, let us move a step back and recall them explicitly.

First, the non-commutativity between the noise and the free evolution will induce some specific contributions to the QFI, typical of the NPC regime. For illustration, let us use the decomposition $\mathcal{L}(t) = \mathcal{H}(t) + \mathcal{D}(t)$, where $\mathcal{H}(t) = -i [H_0 + H^{\text{LS}}(t), \cdot]$ is the Hamiltonian term, while $\mathcal{D}(t) = \sum_{ij} b_{ij}(t) (\sigma_i \cdot \sigma_j^\dagger - (1/2) \{ \sigma_j^\dagger \sigma_i, \cdot \})$ represents the dissipator. In the PC case we have that $[\mathcal{H}(t), \mathcal{L}(t)] = 0$ which does not hold for NPC dynamics, as can be directly checked, for instance, by comparing Equation (5.14) and Equation (5.10). Recalling the Dyson expansion in Equation (1.12), we have to consider products of $\mathcal{H}(t)$ and $\mathcal{D}(t)$ at each different times, e.g., terms as $\mathcal{H}(t_1)\mathcal{D}(t_2) \dots \mathcal{H}(t_k)$, to obtain the dynamical maps fixing the evolution of the probes. If the Hamiltonian and the dissipative part do not commute, then the dependence on ω_0 within $\mathcal{H}(t)$ will mix with the dissipative terms contained in $\mathcal{D}(t)$ and will be thus spread among more parameters of the dynamical map at time t or, equivalently, on more features of the Bloch vector at time t , possibly enhancing the QFI. In particular, this mechanism leads to the dependence of the QFI on the phase of the probes initial state in the NPC case, a feature which is not shared with the PC case, see Equation (5.30).

Second, the noise terms themselves depend on ω_0 : As already pointed out in Section 5.1.1 the coefficients of the master equation will in general contain a dependence on the parameter to be estimated. To quantify explicitly such a phenomenon, we compared, for both PC and NPC dynamics, the QFI which is obtained including the dependence of the rates on ω_0 , with the QFI where such a dependence is disregarded. In particular, in the latter case we replace the dependence of the coefficients $b_{ij}(t)$, $H_{ij}^{\text{LS}}(t)$ on ω_0 with the dependence on a generic frequency Ω , and only after that the QFI has been evaluated, we set $\Omega = \omega_0$. Let us denote this auxiliary object as \tilde{F}_Q , contrary to the former calculations of the QFI which have been denoted by F_Q . We stress that that \tilde{F}_Q is actually the object utilized in more phenomenological approaches to quantum metrology, where the master equation is postulated to describe some specific kinds of noise, rather than microscopically derived so that the contributions due to the dependence of the rates on ω_0 are not accounted for. On the other hand, let us mention that in [312] the role of the dependence of the emission and absorption rates on the free system frequency for a qubit system coupled to a Gaussian classical noise has been investigated.

Figure 5.3(c) summarizes the effects of the two contributions described above. In the main panel we plot the percentage increase $\delta F_Q = 100(F_Q - \tilde{F}_Q)/F_Q$ for both PC and NPC QFI. We see that in both cases the dependence on ω_0 of the noise terms non-negligible and the compliance of these noise terms can increase the QFI way beyond the value of the auxiliary

QFI, e.g. reaching 10% for NPC and 15% for PC at $\alpha t^2 \approx 0.6$.

In the case of the PC dynamics, we can derive a very intuitive geometrical picture of the information encoding. In Appendix A.2.6 we show that the auxiliary QFI $\tilde{F}_{Q,PC}(t)$ is simply proportional to $t^2 D_z(t)^2$ where $D_z(t)$ is the length of the projection of the Bloch vector into the xy plane, see Equation (A.31). Hence the information about the frequency we want to estimate, i.e. the rotation speed about the z -axis, is fully enclosed into the distance of the Bloch vector from the rotation axis. Crucially, if we take the dependence of the rates on ω_0 into account, some further contributions to the QFI will appear, see Equation (A.32). There is one additional term due to the dependence of $D_z(t)$ on ω_0 and a second term in accordance with Equation (1.37), which contains the noise parameters $v_z(t)$ and $d(t)$. By construction, these two terms are positive for any PC dynamics, so that the dependence of the rates on ω_0 will always yield an improvement on the estimation precision, as already indicated in Figure 5.3(c).

The time course of the QFI provides us with direct access to the contribution of the non-commutativity by comparing $F_{Q,PC}$ and $F_{Q,NPC}$ in the inset of Figure 5.3(c). This effect is even more relevant than the contribution due to the dependence of the noise rates on ω_0 and, in any case we can further confirm that the inclusion of nonsecular terms modifies significantly the one-probe QFI, as already discussed referring to Figure 5.3(a) and (b).

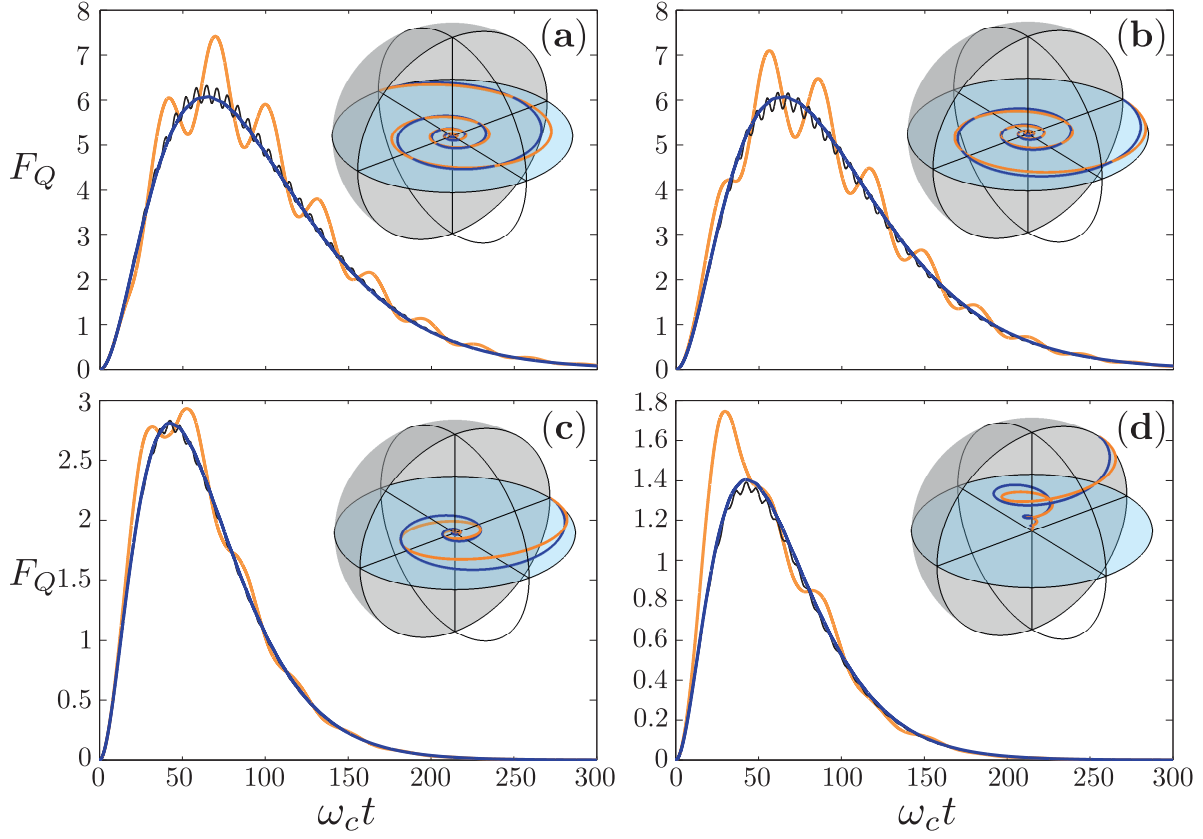


Figure 5.4.: **Difference at finite times between the QFIs of NPC and PC dynamics for baths of Ohmic spectral density.** Time evolution of the QFI for different initial states and values of ϑ . The NPC curves are shown in orange (light grey) and black for, respectively, $\omega_0 = 1$ and $\omega_0 = 5$, while the PC curve after the secular approximation is shown in blue (dark grey) and it describes both the case of $\omega_0 = 1$ and $\omega_0 = 5$; the noise parameter is $\lambda/\beta = 0.1$. The insets show the corresponding evolution of the Bloch vector, here NPC in orange (light grey), PC in blue (dark grey). The initial conditions are the following: a) $\phi = \pi/2, \theta = \pi/2, \vartheta = 0$, b) $\phi = 0, \theta = \pi/2, \vartheta = 0$, c) $\phi = 0, \theta = \pi/2, \vartheta = \pi/4$, d) $\phi = 0, \theta = \pi/4, \vartheta = \pi/4$. (Figure first published in [H3])

5.3.2. Finite-Time Analysis for the Ohmic Spectral Density

In this paragraph we examine the behavior of the QFI for finite times, when the dynamics are dictated by the master equation expressed in Eqs. (5.24) and (5.26). This will allow us to analyze more in detail the difference between the NPC and the PC contributions to the QFI. The results presented in this section are numeric, calculated using Equation (5.27) and the same parametrization of the Bloch vector as before. Figure 5.4 contains the foundation of the following discussion.

Let us first note that the dependence on the initial phase ϕ already mentioned above affects the whole time evolution of the NPC-QFI. Figures 5.4 (a-b) show the evolution with $\vartheta = 0$ for an initial state in an equally weighted superposition, i.e., a state in the $\hat{x} - \hat{y}$ plane of the Bloch sphere ($\theta = \pi/2$), but with initial phases $\phi = \pi/2$ and $\phi = 0$, respectively. Comparing the two figures, one observes that the initial phase is of no relevance for PC dynamics on the whole timescale, while the NPC dynamics introduces a dependence on ϕ . The NPC contributions enhance the maximum value of the QFI and shift its position, depending on the value of the initial phase.

For the Ohmic spectral density considered here, the noise terms do not depend on ω_0 , see Section 5.2.2, so that $\tilde{F}_Q(t) = F_Q(t)$ and the same result holds for the PC case. Hence, $F_{Q,PC}(t)$ is directly fixed by the distance of the Bloch vector from the z -axis, along with the elapsed time t , see Equation (A.31) in Appendix 5.3.1, while the further contributions within the NPC-QFI $F_Q(t)$ can be fully ascribed to the non-commutativity of the Hamiltonian and dissipative part, see the discussion in the previous paragraph.

While the independence of the QFI from the parameter to be estimated in the PC case can be readily shown [39, 43], we can see from Figure 5.4 that the NPC-QFI depends on ω_0 . In particular, with growing values ω_0 , the NPC-QFI converges to its PC counterpart: higher values of ω_0 imply a faster free dynamics of the system, which thus reduces the relevance of NPC terms and increases the validity of the secular approximation, see Section 5.1.2.

We further observe that the overall effect of the NPC terms can yield an increase or a decrease of the QFI, depending on the time interval considered. On the one hand, the NPC terms induce a contraction in the x - y plane, which is no longer isotropic. Comparing the evolution of the QFIs in Figures 5.4 (a-b) with the evolution of the Bloch vector in the insets, it is clear how the non-isotropic contractions can bring the Bloch vector further or closer to the z -axis, thus increasing or decreasing the QFI. On the other hand, as mentioned in the previous paragraph, due to the non-commutativity of the dynamics additional information about ω_0 is enclosed in other features of the Bloch vector; the action of decoherence itself adds some information about ω_0 to the information imprinted by the rotation about the z -axis given by the Hamiltonian encoding.

The delicate interplay of the different mechanisms of production and annihilation of the QFI is also illustrated in Figures 5.4 (c-d). Here we consider values of ϑ different from 0, so that the states initially on the equator of the Bloch sphere are no longer confined to the xy -plane. Comparing Figures 5.4 (b) and (c), we see how the introduced NPC rotation partially counterbalances the oscillations due to the non-isotropic contraction. Furthermore, the role of the different NPC terms strongly depends on the initial state. As an example, Figure 5.4 (d)

shows the strongest (relative) enhancement of the maximum value of the QFI due to the action of both the NPC rotations and contractions.

5.4. *N*-Probe Quantum Fisher Information and Achievable Metrological Limits

In this final section, we want to explore the QFI for an estimation utilizing multiple probes, up to the asymptotic limit $N \rightarrow \infty$. In this way, we will also provide a complete picture for the model at hand of the different scalings of the error in the presence of noise, including semigroup or non-semigroup noise, as well as phase-covariant or non phase-covariant one.

As recalled in Section 4.3.2, evaluating the QFI becomes a more and more difficult task, with the increasing of the dimensionality of the probing system. However, since we are assuming a non-interacting probe system subject to independent and identical noise, we can invoke the bound presented in Equation (4.36) exploiting the finite- N channel extension method [35, 43] to calculate $\mathcal{F} \left[(\Lambda_{\omega_0, t} \otimes \mathbb{1})^{\otimes N} \right]$. We emphasize again, that this method yields an upper bound on the cQFI $\mathcal{F} \left[\Lambda_{\omega_0, t}^{\otimes N} \right]$.

In addition, to investigate the attainability of the bound, we will consider a measurement of the parity operator $P_x = \bigotimes_{k=1}^N \sigma_{(k)}^x$ [258], which as mentioned in Section 4.4 will follow all the observed scalings in the examined cases. In particular, focusing on an initial GHZ state, one finds here

$$\langle P_x(t) \rangle = \frac{1}{2} \left\{ [\xi(t) + i\chi(t)]^N + [\xi(t) - i\chi(t)]^N + [1 - (-1)^N] \varsigma(t)^N \right\}, \quad (5.34)$$

where $\xi(t)$, $\chi(t)$ and $\varsigma(t)$ are proper time- and frequency-dependent functions depending on the single probe dynamics, obtained as in [46] and Appendix A.2.7, from which Equation (4.42) can be evaluated numerically. Note that the last term only contributes if N is an even number and hence the precision may heavily change when N is changed by one. However, for all the cases examined here, we have $\varsigma(t) = 0$.

We focus on the case of an Ohmic spectral density, which provides us with numerically easily solvable differential equations for any time t , cut-off frequency ω_C and coupling strength. Furthermore, by taking the limit $\omega_C \rightarrow \infty$ we recover the semigroup limit as mentioned in Sec. 5.2.2 and Appendix A.2.5, which will be useful to compare our results to those already known in the literature.

5.4.1. Asymptotic Scaling of the Ultimate Estimation Precision

The starting point is the master equation given by Equation (5.24). In particular, we considered three different NPC noise scenarios: the first two cases of a purely transversal noise, i.e., $\vartheta = 0$, for a non-semigroup [see Figure 5.5(a)] and for a semigroup [Figure 5.5(b)] dynamics. As a third case, we chose noise with a (small) longitudinal component fixed by $\vartheta = \pi/100$ for a non-semigroup dynamics [see Figure 5.5(c)]. In Figure 5.5(a-c) we report the numerical study of $t/\mathcal{F}^\uparrow[\rho^{(N)}(t)]$, which fixes a lower bound to the estimation error, see Eqs. (4.32) and (4.36), along with the estimation error for the parity measurement, $\Delta^2\hat{\omega}_{0,P}T$, see Equation (4.42). As clearly observed in Figure 5.5, the two quantities have the same asymptotic scaling, therefore the bound is achievable, at most up to a constant factor. Hence we can infer the scaling with respect to N of the error $\Delta^2\hat{\omega}T$ for the optimal estimation strategy by virtue of Equation (4.43) which we recall as

$$\Delta^2\hat{\omega}_PT \geq \Delta^2\hat{\omega}T \geq \frac{t}{\mathcal{F}[(\Lambda_{\omega_0,t} \otimes \mathbb{1})^{\otimes N}]} \Rightarrow \Delta^2\hat{\omega}T \propto \frac{1}{N^\eta}.$$

Table 5.1 contains the values of the optimal scaling η for the different NPC noise scenarios as inferred from our numerical analysis, along with the corresponding PC scaling behavior (i.e., those for the dynamics after the secular approximation, see Equation (5.26)) taken from [39, 43]. The optimal scaling of the estimation error for the full NPC dynamics is fixed by two key features: Whether we have a semigroup or a non-semigroup evolution and the direction of the noise fixed by the angle ϑ . The presence of a time-dependent rate $\gamma(t)$ as in Equation (5.25) always leads to an improved scaling, with respect to the constant rate γ of the semigroup evolution; in particular, for any $\vartheta \neq 0$ we have the Zeno $\eta = 3/2$ scaling, associated with the linear increase of the rate $\gamma(t)$ for short times [37, 39]. Moreover, we numerically find the novel $\eta = 7/4$ scaling for a non-semigroup, purely transversal noise.

We stress that for any value of ϑ different from 0 the full NPC dynamics leads to the same scaling behavior as in the corresponding PC case. We can say that the transversal noise represents a special case of NPC noise, which might be seen as a "purely NPC noise". For any $\vartheta \neq 0$, the dissipative part of the master equation given in Equation (5.24) together with the resulting dynamical maps, will have a component longitudinal to the parameter imprinting, fixing the asymptotic scaling to the less favorable one proper to PC dynamics and hence extending the Zeno regime recalled in Section 4.4.1 to the scenario governed by NPC noise. This result, already known for the semigroup regime [45] (see also Section 4.4.2), is here extended to the non-semigroup case. Summarizing, we can conclude that the ultimate achievable estimation precision can overcome the SQL whenever we have a non-semigroup

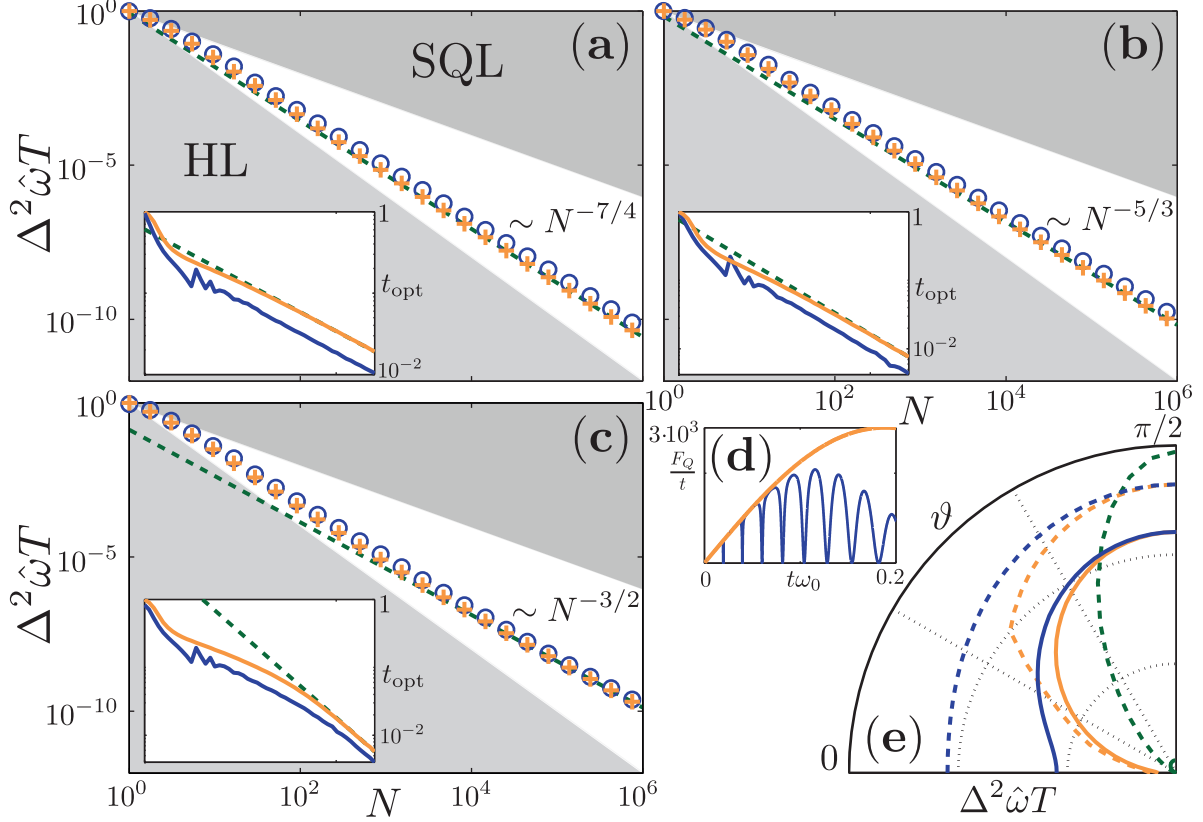


Figure 5.5.: **Sensing with N probes in parallel undergoing NPC Ohmic dynamics** Eq. (5.24). The panels (a) to (c) show the MSE as functions of N that is attained with the parity measurement and GHZ inputs, $\Delta^2 \hat{\omega}_{0,P} T$ of Equation (4.42) (blue circles), in comparison with the general lower bound on the error, $t/\mathcal{F}^\uparrow[\rho^{(N)}(t)]$ with \mathcal{F}^\uparrow defined in Equation (4.37) (orange crosses); both minimized over the round duration t with corresponding optimal t_{opt} plotted within the insets (in matching colors). In cases, (a) $\vartheta = 0$ and $\omega_c = 10$, (b, semigroup) for $\vartheta = 0$ and $\omega_c \rightarrow \infty$, and (c) $\vartheta = \pi/100$ and $\omega_c = 10$; in all the three cases $\alpha = 1$. All the curves are normalized with respect to their values at $N = 1$; the grey areas mark the regions below the HL and above the SQL scalings respectively, while the green dashed line follows the scaling $N^{-\eta}$, with the different η denoting the asymptotic scaling observed. The panel (d) shows the ratio \mathcal{F}^\uparrow/t (orange) for the upper bound on the QFI and the inverse error $1/(\Delta^2 \hat{\omega}_{0,P} T)$ (blue) for $N = 160$ and the same parameters shown in (a). Panel (e) illustrates the dependency of the MSE on ϑ for $N = 160$ as a polar plot. Solid lines correspond to $t/\mathcal{F}^\uparrow[\rho^{(N)}(t)]$, while dashed lines represent $\Delta^2 \hat{\omega}_{0,P} T$. NPC noise is colored in orange, PC noise in blue and the NPC semigroup limit in green. Note that the lines for the semigroup cases are reduced by a factor 200. (Figure first published in [H3])

η	NPC	PC	NPC, semigroup	PC, semigroup
$\vartheta = 0$	7/4	3/2	5/3	1
$\vartheta \neq 0$	3/2	3/2	1	1

Table 5.1.: **Ultimate scaling exponent**, η in Equation (5.4.1), of the optimal estimation error $\Delta^2 \hat{\omega}_0 T$ for different types of noise in the asymptotic limit of $N \rightarrow \infty$.

(short-time) evolution, irrespective of the direction of the noise, or in the cases where we have a purely transversal noise, irrespective of whether we have a semigroup or not.

Interestingly, similar results have been derived recently [313] for rather different, infinite dimensional probing systems. The probes are prepared in Gaussian states and undergo a Gaussian dynamics, possibly non-semigroup and NPC. The NPC contributions are induced by the presence of squeezing in the initial bath state. Also there the optimal asymptotic scaling of the error is also found to be the same for PC and NPC dynamics, going from the SQL for a semigroup to the Zeno limit for a linear increase of the dissipative rates. Such a transition for a PC evolution of a Gaussian system has been shown also in [314].

Analytic Estimation for Pure Dephasing

The calculation in this section has previously been published in [H6].

As an example, we show here that the induced Zeno scaling can also be calculated analytically if the noise is pure dephasing and hence PC. That is, the direction of the noise is parallel to the signal encoding, i.e. $\vartheta = \pi/2$. For a Ramsey measurement, we can calculate the CRB analogously to [37]. Employing GHZ states (compare also Sec.4.2.3) we determine the survival probability

$$p_{\omega_0, t} = \frac{1}{2} \left\{ 1 + \exp \left[-\frac{N\lambda}{\beta} \left(t \arctan(t\omega_c) - \frac{\log(1 + t^2\omega_c^2)}{2\omega_c} \right) \right] \cos(Nt\omega_0) \right\}. \quad (5.35)$$

Since the short time expansion yields $p_{\omega_0, t} \approx 1 - t^2(N^2\omega_0^2 - \lambda N\omega_c/\beta)/4 + O(t^3)$, we expect the precision to be bound by the Zeno limit. Calculating the CRB employing the survival probability in Eq. (5.35), the subsequent derivations of the CRB with respect to ω_0 and t yield

the optimality conditions,

$$\begin{aligned} t_{\text{opt}} &= \frac{k\pi}{2N\omega_0} \quad \text{and} \\ \beta &= 2N\lambda t_{\text{opt}} \arctan(\omega_C t_{\text{opt}}), \end{aligned} \tag{5.36}$$

where the second one is a transcendental equation. Expanding it to second order in t , which is justified by the results of [39], we find $t_{\text{opt}} \approx \sqrt{\beta/2\lambda\omega_CN}$ which results in the optimal precision as

$$\begin{aligned} \Delta^2 \hat{\omega} \cdot T &\gtrsim \sqrt{\frac{2\lambda\omega_C}{\beta N^3}} e^{\sqrt{\frac{2\lambda N}{\beta\omega_C}} \arctan\left(\sqrt{\frac{\beta\omega_C}{2\lambda N}}\right)} \left(1 + \frac{\beta\omega_C}{2\lambda N}\right)^{-\frac{\lambda N}{\beta\omega_C}} \\ &\rightarrow \sqrt{\frac{2\lambda\omega_C}{\beta}} \frac{1}{N^{3/2}} \quad (N \rightarrow \infty), \end{aligned} \tag{5.37}$$

and is indeed scaling according to the Zeno limit. Additionally, it is possible to show that an infinitely short Zeno regime immediately yields the SQL. Therefore, remember that the model is described by a Lindblad equation when taking the limit $\omega_C \rightarrow \infty$, which reduces the correlation time of the environment to zero. Estimating these limits in Eq. (5.35) and (5.36), we obtain $t_{\text{opt}} = \beta/\pi\lambda N$ and the optimal precision is scaling according to the SQL, $\Delta^2 \hat{\omega} \cdot T \geq \pi e \lambda / \beta N$.

Note that the Zeno scaling can also emerge non-asymptotically, when the function dictating the transversal contraction of the Bloch sphere, i.e., along \hat{x} and \hat{y} direction, is always of second order in time. Then the scaling is immediately Zeno-like, which is the case for, e.g., for Gaussian envelopes, as they are encountered in NV centers which we will examine in Section 9.3.

5.4.2. Finite- N Behavior

The plots in Figure 5.5 (a-c) allow us to get some interesting information also about the behavior of the estimation error for a finite number of probes, showing that the asymptotic scaling is approached in a possibly non-trivial way.

First of all, we note that for smaller values of N , the lower bound to the estimation precision $t/\mathcal{F}^\uparrow[\rho^{(N)}(t)]$ and the error under parity $\Delta^2 \hat{\omega}_{0,P} T$ seem to follow the SQL and then, only for intermediate and high values of N , the two quantities converge to the asymptotic behavior, approaching it always from above. This was already shown for a semigroup NPC noise, also with a longitudinal component (see [45], in particular Figure 5.1) and here we see how the same

happens for a non-semigroup NPC noise. Actually, the effect is even more pronounced for a non-semigroup non-transversal noise, where the asymptotic behavior emerges only if almost 10^4 probes are used, see Figure 5.5 (c). Additional numerical studies (not reported here) show that the asymptotic scaling is approached earlier when the coupling to the bath is increased. Even if it is clear that the finite- N behavior do not spoil the validity of the different scalings pointed out in the previous paragraph, it should also be clear the relevance of such behavior in many experimental frameworks, when, indeed, the high- N regime might be not achievable. In such situations, the experimental data would follow a scaling which is different from the asymptotic one for all practical purposes.

In addition, the behavior of the estimation error for finite values of N provides us with a more complete understanding of the specific role played by the geometry of the noise, i.e. the coupling angle ϑ . In Figure 5.5 (e) we study $t/\mathcal{F}^\uparrow[\rho^{(N)}(t)]$ and $\Delta^2\hat{\omega}_{0,P}T$, but now for different values of $\vartheta \in [0, \pi/2]$ and a fixed number of probes $N = 160$. For this value of N and $\vartheta = 0$ the two quantities have essentially already reached their asymptotic values, see Figure 5.5 (a), while this is not the case for $\vartheta \neq 0$, see Figure 5.5 (c). Now, Figure 5.5 (d) shows how both $t/\mathcal{F}^\uparrow[\rho^{(N)}(t)]$ and $\Delta^2\hat{\omega}_{0,P}T$ change continuously with the variation of ϑ . They increase from $\vartheta = 0$ up to $\vartheta = \pi/2$, with the increment being more pronounced for values of ϑ close to 0. The sudden transition between different scalings for, respectively, $\vartheta = 0$ and $\vartheta \neq 0$ is a peculiarity of the asymptotic limit, $N \rightarrow \infty$. Furthermore, this also confirms that noise in the direction of the parameter imprinting is more detrimental than any other direction, if the absolute noise strength is kept identical.

As a final remark, note that the optimal time of the estimation error for a parity measurement as a function of N has discrete jumps between smooth periods, see the lower insets in Figures 5.5 (a-c). These jumps originate from the fact that $\Delta^2\hat{\omega}_{0,P}T$ does possess multiple local maxima instead of one global maxima as $t/\mathcal{F}^\uparrow[\rho^{(N)}(t)]$ does, see Figure 5.5 (d). The jump occurs when the global maximum of $\Delta^2\hat{\omega}_{0,P}T$ changes to a different peak, which was only a local maximum before. On the other hand, for large values of N $\Delta^2\hat{\omega}_{0,P}T$ will converge to a function with only one local maximum, as the following ones have been damped off, so that the optimal time will stay a smooth function of N . The jumps in the optimal evaluation time for a parity measurement can be observed also in the polar plot in Figure 5.5 (e), in terms of non-smooth variation as a function of ϑ .

5.5. Conclusions

We have exploited a detailed analysis of the spin-boson model, which is a general, well-known and widely used noise model, to investigate how the ultimate achievable limits to frequency estimation are affected by the different microscopic features of the interaction between the quantum probes and their environment, and furthermore, provide a cohesive model realizing all the known limits so far. Hence, we used common tools of the theory of open quantum systems to extend the characterization of noisy quantum metrology beyond the common framework, where the description of the noise is usually postulated on a phenomenological basis.

First, we derived the master equation fixing the dynamics of the probes, employing the second order TCL expansion. Thereby, we clarified that the distinction between phase-covariant and non-phase-covariant noise, which plays a key role in frequency estimation [39], corresponds to the distinction between secular and non-secular dynamics. Moreover, we characterized explicitly the dependence of the noise rates, as well as of the correction to the system Hamiltonian, on the free frequency of the probes, i.e., on the parameter to be estimated. This is another aspect commonly overlooked in phenomenological approaches to noisy metrology.

Then, employing a solution to the master equation in the short time regime, valid for any spectral density, and a solution on the whole time scale for an Ohmic spectral density, we investigated the single probe QFI and hence how the microscopic details of the model influence the estimation precision. In particular, we compared the differences between the effects of, respectively, phase-covariant and non-phase-covariant dynamics. The non-secular contributions can both increase or decrease the QFI, also depending on the initial condition, as they lead to a dependence of the QFI on the initial phase of the probes state. However, in general, the maximum (over time) QFI is higher in the non-phase covariant case, due to the positive contributions induced by the non-commutativity of the noise and the free Hamiltonian. Furthermore, we examined the mentioned dependence of the noise terms on the estimated frequency. While for non-secular dynamics no definite statement can be made, we found that this dependence is always beneficial for secular dynamics.

In the last part of the chapter, we moved to the regime of multiple probes and gave a complete characterization of the possible asymptotic scalings of the estimation precision, putting results already existing in the literature onto a common ground, as well as exploring new regimes. In particular, we extended the validity of the super-classical Zeno scaling $N^{-3/2}$ onto non-phase-covariant, non-semigroup dynamics, as long as the noise possesses any infinitesimal component parallel to the encoding direction of the parameter (i.e. $\vartheta \neq 0$). Furthermore, we identified the novel $N^{-7/4}$ scaling for $\vartheta = 0$, i.e., for a non-phase-covariant and non-semigroup dynamics,

due to a coupling with the environment fully orthogonal to the direction of the encoding of the parameter.

Concluding, the analysis in this chapter offers a complete and physically motivated characterization of the scenarios where one can actually achieve super-classical precision in frequency estimation in the presence of (independent) noise. In addition, the microscopic characterization of the probes dynamics enabled us to present an in depth study of the influence of the microscopic details of the probe-environment interaction on the precision. The adopted scheme can be directly linked to widely used sensing scenarios as exploited with color-centers in diamond, superconducting qubits or optomechanical setups.

CHAPTER 6

Open Questions in Quantum Metrology

The field of quantum metrology truly is a rich field with multifaceted applications in other areas of physics. For example, the progress in the development of sensors operating in the quantum regime will enable to improve the detection of gravitational waves by the LIGO cooperation who have successfully demonstrated an enhanced sensitivity of their Michelson interferometer by employing squeezed states of light [236, 238, 315] as proposed by Caves in 1981 [316]. Furthermore, atomic clocks start employing protocols enhanced by quantum entanglement [231] and quantum enhanced position measurements of lipid granules have been demonstrated in living cells [317, 318]. The latter case exemplifies that quantum enhanced metrology is also useful to reduce other side effects of a measurement while maintaining a precision that may also be achievable employing a classical strategy. In the specific case, squeezed light reduced the required laser intensity on the living cells which prevented the sample from overheating and hence enabled to perform the measurements in the first place.

Despite the recent developments, the fundamental theory concerning the role of noise in quantum enhanced parameter estimation is still in its infancy. Let us draw the picture along the lines discussed in the previous Chapters 4 and 5. We have been able to fill gaps concerning the asymptotic scaling of the precision in the number of probes, however, a rigorous analytic proof of the results is pending, so far the results presented are only numeric. Likewise, the asymptotic behavior of the optimal encoding time was only proven for PC noise. Even if such an all-embracing proof arrives, sorting out the asymptotic scalings achievable for any type of dynamic appearing in the cFEP, whether PC or NPC, semigroup or non-semigroup, the most practical questions remain.

From which number of probes the scaling is considered to follow the asymptotics? Given the

dynamics during the encoding, is it possible to obtain that probe number in terms of the underlying microscopic model? Furthermore, it will be crucial to translate these optimal scalings back to actual physical setups. There is now a confined set of states that can be prepared employing multiple probes. Which state is the optimal one and which measurement should be performed? Although we proved the attainability of each scaling with a parity measurement of GHZ states, let us admit that this discovery followed rather from intuition than mathematical reasoning. There exists no procedure constructing the optimal measurement out of the QFI, under the restriction of physical implementability (thereby note that the measurement basis defined by the SLD-operator might not fulfill that criteria). Equivalently, there exists no reliable method to find the N -probe entangled state yielding the best performance. This state may obey a highly complex structure of correlations. For example, see already the early work by Huelga et. al. [34] where, even for a pure dephasing semigroup, the optimal state was not given by a GHZ state but a complicated partially entangled state. For sure the prepared initial state also influences the optimal measurement and possibly obeys a completely different structure for different values of N (although, one could imagine that this is only important until the asymptotic scaling is reached). Obviously, the optimal states also need to be confined to a set of states available in the experimental setup.

Let us now discuss the conditions required for the cFEP itself. How realistic is the assumption of uncorrelated environments? We have seen in Section 4.6.1 that taking correlations in the environment into consideration can change the situation completely. This question is more basic as one may consider at first and probably studied too little, given the amount of results taking that assumption for granted; even the generation of the initial state may correlate the otherwise disconnected environments, see for example a method for generating entanglement between two NV centers [319]. Crucially, the preparation of an entangled state takes time. Realistically, this preparation time should be included into the analysis of the cFEP, in particular since the preparation method itself will most probable also depend on the probe number and the same has to be assumed for the measurement stage. Moreover, during this preparation and readout time, noise will unavoidably already act on the system. While one may partially counteract this noise with control methods as DD or error correction, in the end the encoding time will be reduced, and importantly, this effect becomes more pronounced as entangled states are increasingly fragile when subjected to noise - which is the core of the challenge. Taking these considerations into account, what are the effects on the MSE? Are the ultimate scalings still attainable? Does this set an ultimate upper bound on the maximal number of probes itself, because otherwise during the preparation stage the state decoheres completely?

Control methods, such as error correction or dynamical decoupling are popular tools to prolong the coherence time or correct for flipping errors of the probe system. The first approaches to transfer these ideas into the framework of quantum metrology (we covered them briefly in Section 4.6.2) are promising but still suffering under two major constraints. Firstly, the assumption of "infinitely fast control" is by far not realizable in practice. Control pulses and error correction steps take finite amounts of time which need to be considered in future works. Secondly, the considered dynamics obey the semigroup composition law and hence exclude time-inhomogeneous and non-Markovian processes. Clearly, the later two are unarguably more involved to analyze, as after each correction step one needs to invoke the unique map $\Lambda_{t_{i+1} \leftarrow t_i}$. In particular, denoting the map performing the correction step by EC of length τ , the total channel has to be written as

$$\Lambda = \dots \circ \Lambda_{t_3 \leftarrow t_2 + \tau} \circ EC \circ \Lambda_{t_2 \leftarrow t_1 + \tau} \circ EC \circ \Lambda_{t_1 \leftarrow t_0}.$$

On the other hand, we stress that the main achievements of the results restoring the HL is not the restoration of the latter itself, but the ability to transform the open system into an effectively closed system. In principle, one can construct an argument along the lines of the one made for non-Markovianity in Section 4.5.1. The QCRB only takes the instantaneous state into account, the evolution beforehand does not play any role. Hence, the scaling for any control method imitating a free evolution with a possibly reduced amplitude of the encoded parameter will show the HL, as it determined by the QFI in Eq. (4.29). One should also remark, that these methods exclude noise which is parallel to the parameter encoding. However, these noises normally represent the main challenge since the states employed are most sensitive along the encoding direction. Furthermore, the additional resources necessary for the application of the control methods, like the energy required to correct flipping errors or the ancillas for error correction, should be taken into account.

To conclude, let us exemplary mention the work by Schmitt et. al. [300], where the total experimental time available has been used more efficiently. Here, instead of repeating a single measurement as in the cFEP, a scheme of subsequent measurements was used to detect the frequency of an oscillating field. This chronological order of observations allowed to extend the precision limit to the coherence time of the signal, while the coherence time of the probe takes a subordinate role (see also the last paragraph of Section 4.7). Taking experimental restrictions into account, the development of schemes employing control or neat measurement schemes making more efficient use, i.e., providing the ability to employ a more efficient estimator, out of

the given resources could be the spirit for short term applications. Moreover, the answers to the questions raised above, concerning realistic preparation and readout schemes, are essential for the design of experiments which aim to implement the quantum advantage of entanglement as a standard tool in quantum technologies beyond the current proofs of principle.

Part III.

Quantum Control

CHAPTER 7

Field Detection with Real Pulses

The following sections are based on the work published in [H2]. Reprinted excerpts with permission from [H2]. Copyright (2016) by the American Physical Society.

In Chapter 2 we introduced the NV center in diamond. In current quantum sensing experiments involving the latter, DD pulse sequences of Section 3.3 such as the CPMG [217, 218], or the XY family [71, 73, 221] are used to design a set of filter functions [64, 199, 210, 320] along the lines of Section 3.1. These filter functions are only transmissive for particular frequencies due to the refocusing of the undesired couplings.

The operating principle to detect an external signal, either classical or quantum [321], corresponds to having the NV center, i.e., the quantum sensor, evolving under the action of these decoupling pulses and the signal. Whenever the generated filter is permeable for a certain frequency component of the signal, the quantum sensor gathers a phase that will be subsequently measured leading to a spectrum that characterizes its environment [64, 68, 69, 205, 209, 322].

A filter function is created by a sequence of microwave π -pulses applied on the NV center. We covered the basics of DD, Section 3, under the premise of perfect, instantaneous pulses which are applied while the remaining dynamics are frozen. Nevertheless, what is observed in case this assumption is relaxed?

For standard DD sequences such as the CPMG or the XY family, the expected resonances can only occur at the frequencies $l\omega_{\text{DD}}$, where l are odd integers and $\omega_{\text{DD}} = \pi/t_{\text{free}}$ for a pulse interval of t_{free} [68, 205]. In the same manner DD schemes employing composite pulses, like the AXY-sequences in Section 3.3.2, admit a similar description [66]. However it has been

recently shown [74] that, due to the finite width of the applied pulses, the quantum sensor still accumulates a phase if $l\omega_{\text{DD}}/k$ matches the signal frequency ω_{ac} or, equivalently, $\omega_{\text{DD}} = \alpha\omega_{\text{ac}}$ with $\alpha = k/l$. Here $k \in \mathbb{N}$ with the maximum value of k defined by the outer period of the sequence, and odd numbers of k are excluded by symmetric sequences [74]. Therefore the spurious responses with $k \neq 1$ lead to spectral ambiguities and to a misinterpretation of the signals present in the environment. In particular, the $k = 4$ spurious resonance of a ^{13}C spin may be falsely interpreted as the $k = 1$ resonance of a hydrogen spin.

In this chapter we show that spurious responses in the measured spectrum can be identified and separated from the real ones by controlling the initial phase of the quantum sensor or the phase of the decoupling pulses. More specifically, we show how the intensity of the spurious peaks changes when we vary this phase while the real peaks do not change in the spectrum. Furthermore, we show how this method can be combined with the AXY-sequences to yield an accurate characterization of the spin environment.

We organized the chapter as follows: In Section 7.1 we cover the detection of classical fields and motivate our method by studying the behavior of the spurious signals in Section 7.2. In Sections 7.3 and 7.4 we apply the method to the quantum regime where, in particular, we will make use of an NV center in diamond as the quantum sensor. Furthermore we will combine our protocol with the AXY pulse sequences to demonstrate accurate spin detection [172, H1, H7].

7.1. Detection of a Classical AC-Signal

To understand the presence and detection of spurious resonances we first describe the detection of a classical signal by summarizing the necessary quantities introduced in Section 2. Therefore, we consider a sensor spin subjected to a static magnetic field, $\vec{B} = B_z \hat{z}$, and driven by a classical ac-field, i.e., the external signal, applied in the same \hat{z} direction with angular frequency ω_{ac} and amplitude B . For the case of an NV based sensor, we choose the \hat{z} -direction along the NV symmetry axis as described in Section 2.2. In addition we consider the action of microwave π -pulses for both coherence protection (compare Section 3) of the sensor spin and detection of the ac-field. The relevant Hamiltonian in a rotating frame with respect to the static B_z field reads ($\hbar = 1$, compare also Eq. (2.14))

$$H(t) = m_s \gamma_n B \sin(\omega_{\text{ac}} t + \theta) \frac{\sigma^z}{2} - \delta \frac{\sigma^z}{2} + H_c, \quad (7.1)$$

where $\sigma^\mu, \mu = x, y, z$ are Pauli matrices of the subspace $\{|0\rangle, |m_s\rangle\}$, θ is the initial phase of the ac-field, and δ a possible detuning of the driving field. The control Hamiltonian

$$H_c = \frac{1}{2}\Omega(t)[\cos(\varphi_i + \vartheta)\sigma^x + \sin(\varphi_i + \vartheta)\sigma^y] \quad (7.2)$$

is applied stroboscopically, i.e. $\Omega(t)$ switches periodically between 0 and a constant value Ω , leading to the action of the decoupling π -pulses on the sensor spin. The pulse-phase φ_i controls the rotation axis in the $x - y$ plane, while ϑ sets an overall phase on the pulses which we set to zero for the following calculations.

In the sensing protocol we are going to utilize, the sensor spin is initialized in the state described by the density matrix

$$\rho_0 = \frac{1}{2} \begin{pmatrix} 1 & e^{-i\phi} \\ e^{i\phi} & 1 \end{pmatrix}, \quad (7.3)$$

where ϕ corresponds to the initial phase of the state. After applying a DD pulse sequence, the density matrix of the central spin becomes $\rho_{\omega_{\text{DD}}}(t)$ and we consider the transition probability

$$P(\omega_{\text{DD}}) = 1 - \text{Tr}[\rho_{\omega_{\text{DD}}}(t)\rho_0] \quad (7.4)$$

as the *measured spectrum*. We stress that the dependencies in $\rho_{\omega_{\text{DD}}}(t)$ are not disconnected. In fact, fixing ω_{DD} and a number of DD periods automatically fixes t . Equivalently, fixing ω_{DD} and t fixes the number of DD periods to be applied. Throughout this work, we are rather using the number of periods, while the evolution time and number of pulses then depend on the chosen pulse sequence.¹

In NV based setups, the initial state can be achieved via optical polarization into the $|m_s = 0\rangle$ state and a subsequent $\pi/2$ -pulse to obtain ρ_0 . To find P , a second $\pi/2$ pulse is applied to $\rho_{\omega_{\text{DD}}}(t)$, converting collected phases into a difference in the populations which may then be read out as described in Section 2.1.2.

The effects of the control pulses and the ac-field on ρ_0 can be described by a sequence of rotations

$$R_{\hat{n}}(\kappa) = e^{-i\kappa\hat{n}\cdot\vec{\sigma}/2} \quad (7.5)$$

on the central spin, where $\vec{\sigma} = (\sigma^x, \sigma^y, \sigma^z)^T$. For instantaneous π -pulses around an axis lying in the $x - y$ plane we have $\kappa = \pi$, $\hat{n}_z = 0$ and the effect of each pulse corresponds to a

¹For example, for 10 repetitions of an XY-8 sequence where each repetition contains 4 DD periods, we have $M = 4 \cdot 10 = 40$ DD periods and thus $M \cdot N = 80$ pulses (recall Section 3.1, $N = 2$). When the pulse spacing is fixed as π/ω_{DD} , the length of one XY-8 sequence is immediately given by $T_{\text{XY-8}} = 8(2\pi/\omega_{\text{DD}})$ and hence we have $t = 10 \cdot T_{\text{XY-8}} = M \cdot (2\pi/\omega_{\text{DD}}) = 160\pi/\omega_{\text{DD}}$.

change $\sigma^z \mapsto -\sigma^z$, as it was already studied in Section 3. As indicated by Eq. (3.4), the free evolution between π -pulses corresponds to a rotation around the z -axis and gives rise to a phase accumulation

$$\begin{aligned}\kappa_{\text{free},j} &= \int_{t_j}^{t_{j+1}} d\tau \gamma_n B \sin(\omega_{\text{ac}}\tau + \theta) \\ &= \frac{\gamma_n B}{\omega_{\text{ac}}} \left[\cos(\omega_{\text{ac}}t_j + \theta) - \cos(\omega_{\text{ac}}t_{j+1} + \theta) \right],\end{aligned}\quad (7.6)$$

induced by the ac-field during the free evolution between the times t_j and t_{j+1} where the pulses are applied. In this manner one can find, for ideal control, that the measured signal is given by the total phase in Eq. (3.7), $P(\omega_{\text{DD}}) = \sin^2 \left[\sum_{j=0}^N (-1)^j \kappa_{\text{free},j} / 2 \right]$ [323], where N is as before the number of pulses applied. This signal depends on the initial signal phase θ , but is independent of the initial phase ϕ of the sensing state. The effect of the detuning δ , which can be treated as static noise as shown in Equation (7.1), would be ideally removed by the DD sequence. For instantaneous pulses, we calculate the signal achieved by a CPMG sequence with M periods (or equivalently an XY sequence as they realize the same modulation function, see Section 3.3) and obtain

$$P_{\text{CPMG}}(\omega_{\text{DD}}) = \sin^2 \left[\frac{2\gamma_n B \sec\left(\frac{\pi\omega_{\text{ac}}}{2\omega_{\text{DD}}}\right) \sin\left(\theta + \frac{2\pi M\omega_{\text{ac}}}{\omega_{\text{DD}}}\right) \sin^2\left(\frac{\pi\omega_{\text{ac}}}{4\omega_{\text{DD}}}\right) \sin\left(\frac{2\pi M\omega_{\text{ac}}}{\omega_{\text{DD}}}\right)}{\omega_{\text{ac}}} \right]. \quad (7.7)$$

Tuning the DD sequence on resonance, such that $\omega_{\text{DD}} = \omega_{\text{ac}}/l$ with l odd (i.e. using higher harmonics), one finds that

$$P_{\text{CPMG}}(\omega_{\text{DD}})|_{\text{resonance}} = \sin^2 \left(\frac{2\gamma_n M B \sin \theta}{\omega_{\text{ac}}} \right), \quad (7.8)$$

while for any even l the signal vanishes. For experiments where no control over θ is available, the signal would have to be averaged leading to a loss in contrast [67]. For example, the expectation value for a uniformly distributed phase for the CPMG signal above is given by

$$\begin{aligned}\langle P_{\text{CPMG}}(\omega_{\text{DD}}) \rangle_{\theta} &= \int_0^{2\pi} d\theta \frac{P_{\text{CPMG}}}{2\pi} \\ &= \frac{1}{2} \left\{ 1 - J_0 \left[\frac{4\gamma_n B \left| \sec\left(\frac{\pi\omega_{\text{ac}}}{2\omega_{\text{DD}}}\right) \right| \sin^2\left(\frac{\pi\omega_{\text{ac}}}{2\omega_{\text{DD}}}\right) \sin\left(\frac{2M\pi\omega_{\text{ac}}}{\omega_{\text{DD}}}\right)}{\omega_{\text{ac}}} \right] \right\},\end{aligned}\quad (7.9)$$

where $J_0[\bullet]$ is the zeroth Bessel function of the first kind.

7.2. Identifying Spurious Responses

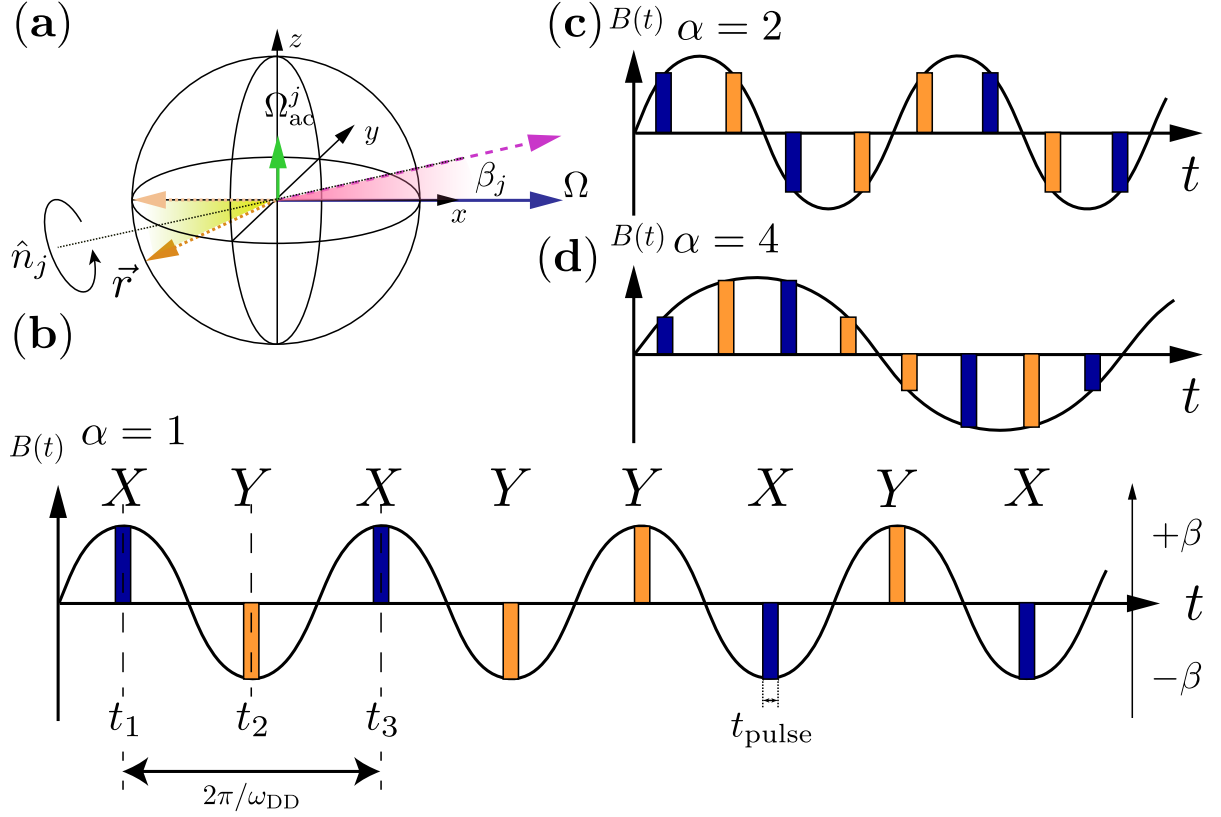


Figure 7.1.: **Interplay of the control- and driving fields.** (a) Visualization of the actual control axis at the present of signal fields on the Bloch sphere. The vectors of the driving field (blue) and the ac-field (green) add to the total driving (pink, chained) and set the angle β_j out of the $x - y$ plane. The rotation of the Bloch vector $\vec{r} = \langle \vec{\sigma} \rangle$ is shown in yellow (short chained). (b) Locations of the X (blue) and Y (orange) pulses with respect to the ac field for $\alpha = 1$ and $\theta = 0$. The height of each square pulse is proportional to the tilting angle β . (c) and (d) are the illustrations similar to (b) but for $\alpha = 2$ and $\alpha = 4$, respectively. (Reprinted figure with permission from [H2]. Copyright (2016) by the American Physical Society.)

The spurious resonances are caused by non-instantaneous π -pulses. To capture the physics of spurious resonances, recall that we consider π -pulses with constant amplitudes and with a pulse duration $t_{\text{pulse}} = \pi/\Omega$. For the sake of simplicity in the following discussion we will assume $\delta = 0$, see Equation (7.1). The presence of the ac-field during t_{pulse} of the j -th pulse changes the rotation axis by an angle β_j out of the $x - y$ plane, see Figure 7.1 (a). The value of β_j is set by the relative strengths of the ac-field and the j -th pulse at time t_j , i.e.,

$\beta_j = \tan^{-1} [\gamma_n B \sin(\omega_{ac} t_j + \theta) / \Omega]$. Here we assume that the ac field experiences almost no change during t_{pulse} , resulting in the condition² $t_{\text{pulse}} \ll 1/\omega_{ac}$. In the following we consider a typical experimental situation where the signal amplitude, $\gamma_n B$, is small compared with Ω leading to $\beta_j \approx \beta_{\max} \sin(\omega_{ac} t_j + \theta)$, where $\beta_{\max} \approx \gamma_n B / \Omega \ll 1$.

Now, we study the effect of β_j on the widely used XY-8 sequence [66] by tuning the ratio $\alpha = \omega_{DD} / \omega_{ac}$. The ideal signal after a single application of the XY-8 sequence is given by Eq. (7.8) with $M = 4$ (see also Appendix B.2.1, Eq. (B.5)). As expected, this ideal signal is completely independent of the initial phase ϕ of the sensor spin. In fact, for $\beta_{\max} \neq 0$ the influence of the tilt arises in higher orders of β_{\max} , which we characterize in the following.

As it can be seen in Figure 7.1 (b) we apply the DD sequence such that the tilt of the axis is maximal, which we expect to be the worst possible case, therefore we set $\theta = 0$. At the same time, as shown by Eq. (7.8), this sets the signal equal to zero when operating at resonance, such that the only signal accumulation is due to the tilting angle β_{\max} . In addition, we have that for $\alpha = 1$ and equally-spaced pulses, β_j is constant up to a sign change, i.e., $|\beta_j| = |\beta_{\max}| \forall j$, see Figure 7.1 (b). Hence, during pulses the state is rotated around the axis

$$\hat{n}_j^{\alpha=1} = \begin{pmatrix} \cos \varphi_j \cos \beta_{\max} \\ \sin \varphi_j \cos \beta_{\max} \\ (-1)^j \sin \beta_{\max} \end{pmatrix} \quad (7.10)$$

We apply an XY-8 sequence with 8 pulses, where the evolution operator is a generalization of Eq. (3.6),

$$\begin{aligned} U_{XY8}^{\alpha=1} = & R_{\hat{z}}(\kappa_{\text{free},8}) R_{\hat{n}_8^{\alpha=1}}(\pi) R_{\hat{z}}(\kappa_{\text{free},7}) R_{\hat{n}_7^{\alpha=1}}(\pi) R_{\hat{z}}(\kappa_{\text{free},6}) R_{\hat{n}_6^{\alpha=1}}(\pi) R_{\hat{z}}(\kappa_{\text{free},5}) R_{\hat{n}_5^{\alpha=1}}(\pi) R_{\hat{z}}(\kappa_{\text{free},4}) \\ & \times R_{\hat{n}_4^{\alpha=1}}(\pi) R_{\hat{z}}(\kappa_{\text{free},3}) R_{\hat{n}_3^{\alpha=1}}(\pi) R_{\hat{z}}(\kappa_{\text{free},2}) R_{\hat{n}_2^{\alpha=1}}(\pi) R_{\hat{z}}(\kappa_{\text{free},1}) R_{\hat{n}_1^{\alpha=1}}(\pi) R_{\hat{z}}(\kappa_{\text{free},0}), \end{aligned} \quad (7.11)$$

and find that for small tilting angles β_{\max} we have

$$P_{\alpha=1} = 16 \left[1 - \sin \left(\frac{2\gamma_n B}{\omega_{ac}} - 2\phi \right) \right] \beta_{\max}^6 + O(\beta_{\max}^7). \quad (7.12)$$

The result in Eq. (7.12) tells us that when the frequency ω_{DD} is tuned to ω_{ac} (note that $\alpha = 1$) the sensor is only marginally affected by the presence of the tilting angle. Therefore, a change

²This assumption means that the rotation axis is indeed constant during the pulse. Of course, in a real setting the rotation axis itself will be time depend as the instantaneous amplitude of the field changes. Hence it will rotate around an axis orthogonal to the directions fixed by the ac-field and the direction of the pulse, but always lies in the surface spanned by the two.

on the initial phase ϕ would have almost no effect on the observed spectrum.

In contrast, according to Figure 7.1 (c), for a decoupling frequency such that $\omega_{DD} = 2\omega_{ac}$ we have the rotation axis

$$\hat{n}_j^{\alpha=2} = \begin{pmatrix} \cos \varphi_j \cos \beta_j \\ \sin \varphi_j \cos \beta_j \\ \sin \beta_j \end{pmatrix}, \quad (7.13)$$

and after the application of an XY-8 sequence we obtain

$$P_{\alpha=2} = 8 \left\{ \cos \left(\frac{\gamma_n B}{\sqrt{2}\omega_{ac}} \right)^2 \times \left[1 + \sin \left(\frac{2(\sqrt{2}-1)\gamma_n B}{\omega_{ac}} + 2\phi \right) \right] \right\} \beta_{\max}^2 + O(\beta_{\max}^3). \quad (7.14)$$

Here the signal is already affected by the square of the tilting angle which is the reason for a spurious resonance to appear.

For the fourfold frequency, $\omega_{DD} = 4\omega_{ac}$, and $\gamma_n B/\omega_{ac} \ll 1$ we have that the transition probability is

$$P_{\alpha=4} \approx 2(\sqrt{2}-2) [\sin(2\phi) - 1] \beta_{\max}^2 + O(\beta_{\max}^3), \quad (7.15)$$

which also contains the second order of β_{\max} and as it can be seen in Figure 7.1 (d) the rotation axis corresponding to consecutive X (or Y) pulses are always different.

In Figure 7.2 (a) we have analytically computed [see Eq. (B.6) in Appendix B.2.2] the impact of the phase ϕ of the initial spin state on the factors accompanying the second order in the tilting angle. Thereby we consider different values of the ω_{DD} frequencies after the application of a single XY-8 sequence under the assumption $\gamma_n B/\omega_{ac} \ll 1$. From that figure we can extract important conclusions.

- For the frequencies ω_{DD} with $k = 1$ and $1/\alpha = l = 1, 3, 5, \dots$ there is no dependence on β_{\max}^2 . Hence these resonances are independent up to the order β_{\max}^6 , therefore the effect of ϕ is entirely negligible for short pulses. Note that for the case $\theta = \pi/2$ we will find no spurious contribution as the pulses are located on the nodes of the ac-field thus we have $\beta_{\max} = 0$.
- Importantly, for the cases $l = 3, 5, \dots$ the collected error is completely equivalent to the $l = 1$ case as the field in the moment of pulse application is exactly the same.

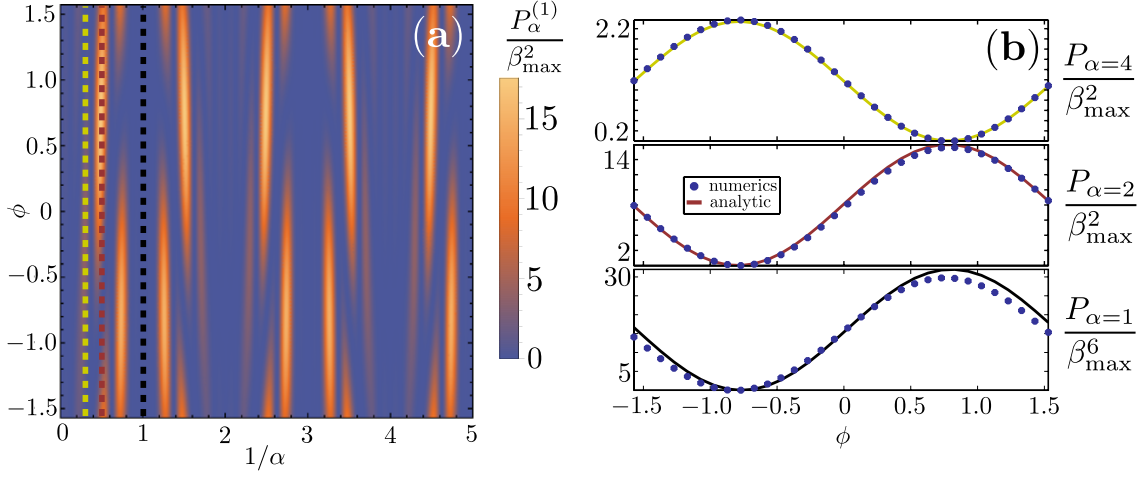


Figure 7.2.: **Phase dependence of the measured spectrum.** (a) Impact of the second order in the tilting angle for the XY-8 sequence as a function of $1/\alpha$ and the phase angle ϕ . The colored lines mark the corresponding cuts for (b) where we compare the analytical results (solid lines) of Eqs. (7.12), (7.14), and (7.15) with a numerical simulation (dots) of the behavior of the transition probability P under the Hamiltonian given in Eq. (7.1) for $\omega_{\text{ac}} = 2\pi \times 1$ MHz, $\gamma_n B = 2\pi \times 0.12$ MHz, $\theta = 0$, and $\beta_{\max} = 0.012$. (Reprinted figure with permission from [H2]. Copyright (2016) by the American Physical Society.)

- For other values of α where spurious resonances appear, the dependence on ϕ can be clearly observed.

Furthermore the vertical lines in Figure 7.2 (a) correspond to the cases $\alpha = 1, 2, 4$ that we have previously discussed in Eqs. (7.12), (7.14) and (7.15), respectively, and a numerical check shown in Figure 7.2 (b) stresses the agreement with those analytical expressions. In addition, Figure B.1 in the Appendix shows the equivalent of Figure 7.2 (a), but for three applications of the XY-8 sequence. Here, the phase-dependent accumulation is even more pronounced while the width of the resonances is decreased.

Crucially, the calculation shown in Appendix B.2.2 for three applications of the sequence also explains why there is no spurious resonance observed in the case that $\alpha = 3$. While for a single application the obtained signal is $P_3 \sim \beta_{\max}^2 \cos^2(\phi)$, after three consecutive applications the second order is canceled and one arrives at $P_3 \approx O(\beta_{\max}^3)$. Hence, the accumulation of the spurious signal is averaged out.

This dependence on the phase ϕ motivates the development of a criteria to identify spurious resonances as we will do in the following.

7.2.1. A Criteria to Detect Spurious Resonances

According to the behavior predicted by Eqs. (7.12), (7.14) and (7.15) we are able to suppress and enhance the signal by tuning the initial phase ϕ of sensor spin states when the resonances are spurious. Therefore, we can detect a spurious resonance by the oscillation of its associate peak's height when choosing different initial phases of the state. More specifically, after the first experiment and the recording of the spectrum P_{ϕ_1} , we repeat the experiment with a different initial phase to obtain P_{ϕ_2} . In this manner for every real resonance we will have

$$P_{\phi_1} = P_{\phi_2} + \mathcal{O}(\beta_{\max}^6) \approx P_{\phi_2}, \quad (7.16)$$

meaning that the effect of the tilting angle is negligible. On the contrary, spurious resonances differ already at the order β_{\max}^2 . Hence by comparing P_{ϕ_1} and P_{ϕ_2} the real resonances can be identified.

A further improvement concerning resolution on spurious peaks can be made by recording multiple initial phases to construct a spectrum of spurious resonances. In this respect one can define the following quantity

$$W = \max_{\phi_i, \phi_j} |P_{\phi_i} - P_{\phi_j}|, \quad (7.17)$$

where the maximum is taken over all recorded initial phases. W contains all the peaks but the real resonances because in this case $P_{\phi_i} \approx P_{\phi_j} \forall \phi_i, \phi_j$ leading to $W \approx 0$. It is important to stress that this criteria is one-directional. In particular, in the case of having multiple ac-fields with frequencies $\omega_{\text{ac},j}$ and some of them are integer multiples of another one, i.e. $\omega_{\text{ac},k} = \mu\omega_{\text{ac},l}$, the real resonances $\omega_{\text{ac},l}$ can not be distinguished from the spurious contribution of $\omega_{\text{ac},k}$.

7.2.2. Effects of Pulse Errors.

We derived the above criteria for pulses which are only disturbed by the action of the ac-field during the pulse time. However, a real situation will also suffer from the presence of a detuning δ , see Eq. (7.1), and flip-angle errors caused by fluctuations in the Rabi frequency Ω in H_c . For the following analysis we will consider static errors in δ and Ω . Note that this condition can be justified by assuming that both δ and Ω are slowly varying. The detuning δ of the applied control field from the transition frequency of the sensing qubit, see Eq. (7.1), tilts the rotation axis out of the $x - y$ plane by an angle γ that can be quantified as $\gamma = \tan^{-1}(\delta/\Omega) \approx \delta/\Omega$ if $\delta \ll \Omega$. In addition, an error on Ω results in non perfect π pulses with an angle of rotation $\pi + \xi$.

We can collect all possible deviations into a single parameter by defining $\beta_{\max} = \tilde{\beta}\eta$, $\gamma = \tilde{\gamma}\eta$, $\xi = \tilde{\xi}\eta$ and expand the signal with respect to η . Note that we assume all errors to be constant in time and small, but of the same order of magnitude such that the different proportionality constants are enough to characterize the impact of the error. A repetition of the calculation for finding Eq. (7.12) yields

$$P_{\alpha=1} = \frac{1}{4} \left[4\tilde{\beta}^2 - 4\tilde{\gamma}^2 + \tilde{\xi}^2 \right]^2 \times \left[(2\tilde{\beta} + \tilde{\xi}) \cos \phi + (2\tilde{\beta} - \tilde{\xi}) \sin \phi \right]^2 \eta^6 + O(\eta^7), \quad (7.18)$$

while $P_{\alpha=2}$ and $P_{\alpha=4}$ do not change in the second order of η , since the specific construction of the XY-8 sequences suppresses these errors, see Table 3.1 in Section 3.3. Therefore, our criteria is valid to identify spurious peaks under the presence of error sources.

7.2.3. Remark on Pulse Phases

It is worth to mention that the preparation of the initial state in the $x-y$ plane with different initial phases ϕ_j , or different choices of the rotation axis for the decoupling pulses are interchangeable. The later can be achieved by a variation of ϑ in Eq. (7.2). More specifically, a preparation in $\rho = |+_x\rangle\langle+_x|$ and choosing the rotation axis X_{ϑ_j} and $Y_{\vartheta_j} = X_{\vartheta_j + \frac{\pi}{2}}$ is equivalent to the situation described throughout the paper. When both phases are changed, the equations above still hold if one makes the identification $\phi \mapsto \phi - \vartheta$.

7.3. Detection of a Quantum Signal

In what follows, we replace the classical ac-field by a quantum system interacting with the sensor spin. The main concept however is equivalent to the classical signal illustrated in Section 7.1. The transition probability of the initial state ρ_0 to an orthogonal one still corresponds to the measured spectrum. However, the collected phase is now more challenging to calculate. Here we make use of the two approaches to dynamical decoupling presented in Chapter 3.

The first one being the filter formalism, which directly determines the coherence $\xi_{\omega_{\text{DD}}}(t)$ of the state $\rho_{\omega_{\text{DD}}}(t)$ in terms of the overlap integral given in Eq. (3.12) (where we also mark the explicit dependence on ω_{DD}). Independent of the initial phase, for the initial state in Eq. (7.3) one finds

$$P(\omega_{\text{DD}}) = \frac{1 - e^{-\xi_{\omega_{\text{DD}}}(t)}}{2}. \quad (7.19)$$

At this point, let us remark that this spectrum only takes values on the interval $[0, 1/2]$. However, any other definition of the spectrum where the value of $\xi_{\omega_{\text{DD}}}(t)$ is able to be extracted would be valid. For example, the length of the state's Bloch vector normalized to its initial value would also produce a usable spectrum. By varying the application frequency of the DD pulses via tuning of the spacing between the pulses, i.e. changing the modulation function, one shifts the position of the peaks in the filter function which ultimately determines the value of $\xi_{\omega_{\text{DD}}}(t)$, because as mentioned in Section 3.1, it is

$$\xi_{\omega_{\text{DD}}}(t) = \frac{1}{2\pi} \int_0^\infty d\omega S(\omega) f_\omega(t, \omega_{\text{DD}}). \quad (7.20)$$

From the measurement of the different $\xi_{\omega_{\text{DD}}}(t)$, the desired information about $S(\omega)$ can be subsequently extracted from $P(\omega_{\text{DD}})$, for example following the method presented in [209]. As mentioned before, this method allows for a general spectroscopic examination, as it captures the effect of the environment and the signal source in the spectral function $S(\omega)$, while the true underlying microscopic structure is of subordinate importance.

Contrary to that, the effective Hamiltonian approach in Section 3.2 requires detailed knowledge of the underlying dynamics, apart of the parameter values that should be determined. Furthermore, one has to assume some initial state of the quantum system the sensor is interacting with. Let's assume that the DD sequence is applied such that the resonance condition with the n -th spin (the target) in the bath is fulfilled. Then, employing the effective Hamiltonian in Eq. (3.25) and for an initial product state of the sensor and the target spin, $\rho_0 \otimes \rho_n$, we obtain the signal

$$P(\omega_n) = \frac{1 - \text{Re}\{\Xi(t)\}}{2} = \sin^2 \left(\frac{1}{8} a_n^\perp f_{l_{\text{DD}}} m_s t \right). \quad (7.21)$$

Here, $\Xi(t)$ is the coherence modulation of the sensor spin after the application of the partial trace over the target spin degrees of freedom. In particular,

$$\Xi(t) = \text{tr}_n \left[\langle m_s | e^{-itH_{\text{eff},n}} | m_s \rangle \rho_n \langle 0 | e^{itH_{\text{eff},n}} | 0 \rangle \right], \quad (7.22)$$

where the state ρ_n can be an arbitrary one. Note that, of course, here $H_{\text{eff},n}$ can be replaced with any Hamiltonian which is not in resonance, even a free one where no DD pulses are applied. This holds, as long as the underlying dynamics is pure dephasing which ensures the block diagonal structure of the Hamiltonian. In particular, for the NV center $H = \sum_{m_s} H_{m_s} |m_s\rangle \langle m_s|$ where $H_{m_s} = \langle m_s | H | m_s \rangle$. This construction only holds as long as no transitions between the $|m_s\rangle$ states are induced. Therefore, this provides an efficient way to perform numerical simulations starting from the Hamiltonian (3.15) to obtain the spectrum for arbitrary DD

frequencies. Of course, when the number of nuclear spins increases, one has to switch to numerical algorithms which allow the calculation of the high-dimensional system, like, e.g. the disjoint-cluster-expansion [177] (requires a diluted spin bath) or the cluster-correlation-expansion [324, 325].

On the other hand, the inclusion of real pulses of finite width t_{pulse} can only be performed by consideration of the full Hamiltonian which includes a pulse Hamiltonian analogous to the form of Eq. (2.14). Then, both the filter formalism approach and the effective Hamiltonian description fail.

7.4. Spurious Resonances of Quantized Signal Sources

7.4.1. A Scheme for Quantum Emitters

In the following we will demonstrate the transcription of the criteria for spurious resonances of signals emitted by a quantum system. For the theory derived in Section 7.2 to apply, we first need to identify the corresponding quantities. In a quantum setting the classical field is replaced by one or more nuclei, each of them oscillating at its own Larmor frequency, and coupled differently to the sensor spin, as it is also the case for NV centers, Section 2.2. For the sake of simplicity, we stick to a single remote spin. In that case the free evolution of the system is dictated by the Hamiltonian

$$H = \omega_c \sigma^z - \omega I_z + \vec{\sigma} \mathbb{A} \vec{I} \approx \omega_c \sigma^z - \omega I_z + \sigma^z \vec{A} \vec{I}, \quad (7.23)$$

where \mathbb{A} is the hyperfine tensor describing the interaction between the sensor and the target spin. We assumed that the energy splitting is much larger than the interaction with the remote spin, $\omega_c \gg |\mathbb{A}_{i,j}| \forall i, j = x, y, z$, while at the same time we demand $\omega_c \gg \omega$. Therefore the central spin does not flip and we applied the secular approximation which removes the corresponding flip-flop terms and leaves the hyperfine vector $(\vec{A})_j = \mathbb{A}_{z,j}$. In a rotating frame of the free energy terms $\omega_c \sigma^z - \omega I_z$ we obtain the following Hamiltonian

$$H_I(t) = \sigma^z \left[A_x \cos(\omega t) I_x - A_y \sin(\omega t) I_y + A_z I_z \right]. \quad (7.24)$$

Hence the levels of the central spin are shifted by the amplitudes A_i which are the analogue to the amplitude of the classical field. Note that the first two contributions at the right hand side of Eq. (7.24) reassemble the cases $\theta = 0$ and $\theta = \pi/2$ simultaneously. Thus, if we want to use our criteria for the identification of spurious resonances when driving the system with

the Hamiltonian presented in Eq. (7.2), we have to ensure that $|\vec{A}| \ll \Omega$ which is the condition giving rise to small tilting angles.

The regime where this condition holds is easily satisfied in NV based schemes, that we will comment below, as typical couplings to remote ^{13}C spins are around $2\pi \times 20 \text{ kHz}(\text{nm}d)^3$ (with d being the distance between the NV center and each nuclear spin), while driving frequencies can be easily selected around $2\pi \times 30 \text{ MHz}$.

7.4.2. Numerical Results in NV-based Schemes

A widely used sensor spin corresponds to an NV center, which we already reviewed intensively in this work. Consequently, we will employ it to exemplify the detection of spurious resonances. The Hamiltonian of an NV center and its surrounding nuclear spins within the secular approximation and without control is given in Eq. (2.7). As shown in Section 2.2.1 we restrict to the subspace containing only the electronic spin states $|m_s = 0\rangle$, $|m_s = 1\rangle$ which we choose as our sensing qubit. In the rotating frame of the NV electron spin we also add the control term given in Section 2.2.2, Eq. (2.14) and arrive at the Hamiltonian dictating the evolution under control

$$H(t) = - \sum_j \vec{\omega}_j \cdot \vec{I}_j + \frac{\sigma^z}{2} \sum_j \vec{A}_j \cdot \vec{I}_j - \sigma^z \frac{\delta}{2} + \frac{1}{2} \Omega(t) [\cos(\varphi_n) \sigma^x + \sin(\varphi_n) \sigma^y], \quad (7.25)$$

where $\Omega(t) = \Omega$ during the pulses and equal to zero otherwise. The pulse phase φ_n is adjusted according to the n -th pulse of the chosen DD sequence defined in Section 3.3. Every nuclear spin rotates with its own Larmor frequency $|\vec{\omega}_j| = |\gamma_j B \hat{z} - \frac{1}{2} \vec{A}_j|$, see Eq. (2.9).

In Fig. 7.3 we illustrate the oscillation of spurious peaks which we use for their detection and discrimination from real peaks. We present the spectrum that results from the interaction of an NV center with a remote ^{13}C spin ($\gamma_C = 2\pi \times 1.0705 \text{ kHz/G}$) at a distance of $r \approx 1.19 \text{ nm}$ from the NV center and located in one of the available diamond lattice positions. This gives rise to a hyperfine coupling $\vec{A} = 2\pi \times (15.0 \ 6.4 \ 11.9)^T \text{ kHz}$. The applied field strength of the external magnetic field reads $B_z = 100 \text{ G}$. Concerning the possible error sources we have taken into account that the nitrogen atom inherent to the NV center might change the energy splitting of the electronic spin due to a hyperfine interaction of up to $\sim 2\pi \times 1 \text{ MHz}$ [61, 74] when the intrinsic nitrogen spin is not polarized. The detuning is stable because of the long T_1 time of the nitrogen spin. Therefore, we choose $\delta = 2\pi \times 1 \text{ MHz}$ in our numerical simulations and include a relatively large 3% error in the Rabi-frequency Ω which is set to be $2\pi \times 30 \text{ MHz}$. We compare the spectra obtained for AXY-8 and XY-8 sequences for 70 periods of the corresponding DD protocols, meaning 2800 pulses for AXY-8 and 560 pulses for XY-8.

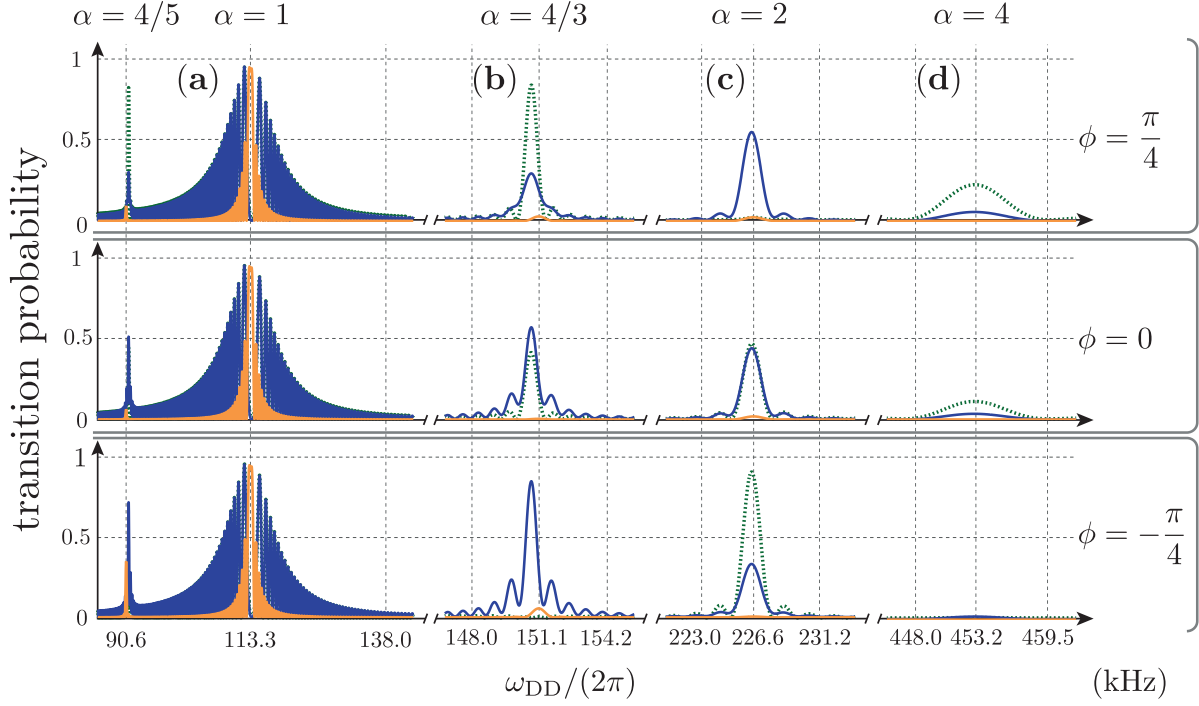


Figure 7.3.: **Simulation of P_ϕ for a NV center coupled to a single spin.** P_ϕ , employing the XY-8 (blue) and AXY-8 (orange) sequence and different initial phases of $\pi/4, 0, -\pi/4$ is shown in each row from top to bottom. The graphs in column (a) show the large resonance for $\alpha = 1$ and the smaller $\alpha = 4/5$ resonance. In the columns (b),(c),(d) the spurious peaks for $\alpha = 4/3, 2, 4$ are displayed respectively. The $\alpha = 1$ resonance corresponds to a sensing time of $T \approx 2.4$ ms. The green chained curves represent an XY8 sequence but with no error in the Rabi-frequency. (Reprinted figure with permission from [H2]. Copyright (2016) by the American Physical Society.)

We choose $\Omega(t)$ in a way such that the AXY-8 sequence is assembled with $f_1 = 4/(5\pi)$ (see Section 3.3.2), while the coefficient for XY-8 is always fixed to $f_1 = 4/\pi$ for the first harmonic contribution. We run the simulation with three initial phases $\phi = 0$ and $\phi = \pm\pi/4$. The important parts of the spectra are shown in Fig. 7.3. We can clearly distinguish the spurious peaks from the real peaks. The spurious resonances in Fig. 7.3 (b), (c) and (d) change the peak heights under the varying initial phase which makes them easy to detect. The AXY-8 sequence shows less amplitude in the $\alpha > 1$ spurious peaks, as it reduces the effective coupling to the remote spins by f_1 (a fraction of $1/5$ as compared to the one of XY-8) and therefore reduces the tilting angle. In addition it employs rotations around 6 axis instead of 2 as XY-8 does and is therefore more robust against the accumulation of the fake signal. Also see the green dashed line which illustrates the sensitivity of XY8 with respect to errors in the Rabi-frequency in

comparison with the blue line. The occurrence of the $\alpha = 4/3$ resonance [Figure 7.3 (b)] in the AXY-8 sequence is due to the large detuning and the high peak at $\alpha = 4/5$ [Figure 7.3 (a)] results because of the larger Fourier coefficient for f_5 compared to a standard XY sequence with equally spaced pulses. However, this resonance is also easy to detect.

7.4.3. Distinguishing Close Peaks

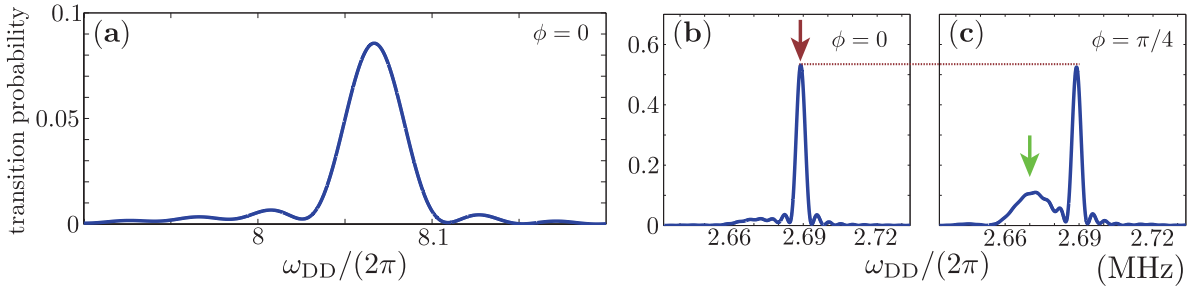


Figure 7.4.: **Simulation of P_ϕ for an NV center with a hydrogen and a strongly coupled carbon spin under the control of AXY sequences.** (a) and (b) show results for $f_1 = 4/(1.2\pi)$ and $f_3 = 4/(1.2\pi)$ respectively. The red (dark grey) arrow in (b) indicates the position of the hydrogen resonance, the green (light grey) arrow in (c) the ^{13}C resonance. (b) and (c) show the effect when changing the initial phase from 0 to $\pi/4$. All calculations are performed with $\Delta = 2\pi \times 1$ MHz, $\Omega = 2\pi \times 20$ MHz and $\delta = 0.03 \times \Omega t_{\text{pulse}}$. Here, 1920 decoupling pulses are used which corresponds to a sensing time $T \approx 23.9 \mu\text{s}$ for the $\alpha = 1$ and $T \approx 71.7 \mu\text{s}$ for the $\alpha = 1/3$ resonance of the hydrogen atom. (Reprinted figure with permission from [H2]. Copyright (2016) by the American Physical Society.)

Spurious resonances can induce false identification of detected nuclear spins [74]. For example, ^1H has a gyromagnetic ratio of $\gamma_{^1\text{H}} = 2\pi \times 4.2576$ kHz/G thus with $B_z = 600$ G we expect a resonance peak at $\approx 2\pi \times 2.555$ MHz. Unfortunately, NV center based detection of hydrogen suffers from the natural occurrence of ^{13}C spins in the diamond lattice [74]. These carbon spins produce a spurious resonance peak at approximately 1.0057 times the resonance frequency of the hydrogen spin since their Larmor frequency at this field is around $2\pi \times 0.642$ MHz. Hence their $\alpha = 4$ resonance will appear around the Larmor frequency of the hydrogen.³ As long as the absence of ^{13}C is not ascertained by independent means, the detection of hydrogen can not be achieved unambiguously. We use our recently introduced AXY-8 sequence and the above defined criteria to identify the spurious resonances.

³We stress here, that this is *not* an instance where the single spin addressing condition in Equation (3.20) fails, since it takes only real resonances into account.

For the following simulations we are guided by the data presented in [74]. Here, a hydrogen spin with $\vec{A}_H = 2\pi \times (14.5 \ 0 \ 500)^T$ kHz is considered. We assume a carbon spin with $\vec{A}_C = 2\pi \times (103, 103, 73)^T$ kHz ($r_C \approx 0.59$ nm) at one of the possible positions in the diamond lattice surrounding the NV center. The magnetic field is tuned to $B = 1836$ G.

Figure 7.4 (a) shows the transition probability in the region of the expected hydrogen resonance for $\alpha = 1$ ($k = l = 1$) and $f_1 = 4/(1.2\pi)$ using the parameters mentioned below the plot. From here it is not clear, to which element this peak has to be assigned, whether this peak indeed represents a real resonance or if it is spurious. Increasing the selectivity of the AXY-8 sequence by changing the sequence to $\alpha = 1/3$ ($k = 1, l = 3$) and $f_1 = 0$, as well as $f_3 = 4/(1.2\pi)$, leads to the spectrum (b). This choice of parameters clearly shows the resonance peak of the hydrogen and marks the spurious ^{13}C resonance, which can be identified undoubtedly by changing the phase as shown in Figure 7.4 (c). Again, note that even if there would be no ^{13}C present, the constant height of the hydrogen peak under the phase cycling proofs that the peak is a real resonance of a present interacting spin.

7.5. Conclusion

We have illustrated the field detection employing a quantum sensor using pulse sequences, both from classical oscillating fields, as well as quantum fields. In particular, we left the regime of instantaneous pulses and explored the appearing effect of abnormal phase collection, leading to additional resonance peaks. Subsequently we have defined a criteria that allows the identification of these spurious resonances as they appear in widely used dynamical decoupling schemes of the XY-family which can be easily implemented in existing experimental setups as it only requires a phase change of the applied pulses. To understand its working mechanism, we first calculated the effect of a XY-8 decoupling sequence for detection of a single classical ac-field and motivated the definition by the different leading orders of the tilting angle of the rotation axis, which is responsible for the appearance of spurious resonances. A further calculation verified the validity of the criteria in a quantum setting under the sufficient condition of a strong enough driving field used for the π -pulses. Later, we applied the criteria to an NV center coupled to a single spin where we illustrated the working principle in a fully quantum setting. As a second example, we solved the detection uncertainty of hydrogen atoms when using NV centers by employing the AXY-8 sequence.

CHAPTER 8

Soft Control of Quantum Interactions

The technique presented in this chapter has been proposed in [H4]. Reprinted excerpts with permission from [H4]. Copyright (2018) by the American Physical Society.

The quest of identifying suitable platforms to pursue applications in quantum information [22, 180, 326], quantum simulation [23] or quantum sensing [13], is by far more than a scouting challenge of different materials or artificial architectures [327–329], which assemble the "hardware" of the desired quantum device. Technological applications [8, 15, 330] do not solely require the provision of physical qubits. Often these qubits are arranged as an interacting quantum cluster, for instance the ^{13}C nuclear spins employed in diamond [59, 69, 331–333] or the ^{29}Si nuclear spins that appear in silicon carbide [334, 335], as well as Eu^{3+} ions in stoichiometric rare-earth crystals [336, 337].

Another integral part on the journey to future applications is the development of proper "software" that allows the realization of manipulations on single constituents and exerts desired protocols providing selective coupling among multiple parties assembling that cluster of quantum systems. One example of such software is given by the dynamical decoupling sequences in Chapter 3, where the *individual addressing* of nuclear spins represents the major challenge. In fact, the individual addressing represents a crucial requirement in applications where the "hardware", like the NV center, is employed as a quantum sensor. It allows the determination of the 3D structure of single molecules of interest in bio-chemistry and medicine [5, 9, 185, 338–341, H7] and enables the utilization of nearby single spins as a memory to design quantum sensing protocols that show enhanced sensitivity and resolution [54, 55, 219, 290, 342, 343]. Likewise,

these nuclear spins could serve as a quantum register to assemble a quantum repeater [57], or when coupled to an electron spin, are an important resource to build a robust optical interface for quantum networks [58, 63].

Let us examine the addressability problem in more detail. It can be reduced to the situation shown in Figure 8.1 (a) where a control qubit (CQ) interacts with multiple resource qubits (RQs) [344, 345]. In order to exert control on a certain RQ the characteristic frequency ω_0 of the CQ is tuned to the resonance frequency ω_j of the RQ via a continuous drive that exploits the Hartmann-Hahn resonance [322, 346, 347] (see also Appendix B.3.4) or the application of pulsed dynamical decoupling [66, 68, 204–206] (Section 3.2). As we will show in Section 8.1.1, the time independent coupling c_j between the CQ and each RQ is responsible for the slow decay of the spectral responses which are proportional to $c_j/\delta_{0,j}$. In particular, these responses decay in a power-law manner with respect to the energy mismatch $\delta_{0,j} = \omega_0 - \omega_j$ ($j > 0$ for RQs). As a result, when the energy distribution of the different RQ is too dense compared to their coupling strength, other off-resonant RQs will considerably perturb the CQ and vice versa, see Figure 8.1 (b). This prohibits the high-fidelity addressing of the desired target RQ. Note that this is a practical instance of the second decoupling condition in Eq. (3.21), which is particularly challenging for realistic settings where the RQs only slightly differ in their resonance frequencies.

In this chapter, we are tackling the addressability problem and propose the technique of *soft temporal quantum control*. The key characteristic of this control method is shaping of the interactions, such that they are weakened at the beginning and the end of the evolution. This technique enables on-resonant coupling within a desired set of target systems, while efficiently avoiding unwanted off-resonant contributions originating from other systems in the environment. With the specific case of Gaussian soft control, off-resonant effects are suppressed by the mismatch $\delta_{0,j}$ as $\exp(-\sigma^2 \delta_{0,j}^2/2)$, see Figure 8.1 (c), achieving high-selective coupling. In order to explain the working mechanism of the technique, we develop an average Hamiltonian theory, Section 8.1.1, which deals with the cases of either a constant or a time-dependent coupling and illustrates the exponential decay of the couplings with respect to the frequency mismatch. Next, we take high-order virtual transitions into account by invoking the quantum adiabatic theorem in Section 8.1.2. Thus we provide an accurate description of the dynamics even for situations involving strong perturbations (i.e. couplings) and long evolution times. Subsequently, we present a protocol to implement the soft Gaussian control via dynamical decoupling. More specifically, we will show how the AXY sequences from Section 3.3.2 are suitable to realize the Gaussian temporal modulation of the coupling. Then two applications of our method are following. First, Section 8.3.1 illustrates the realization of an efficient RWA,

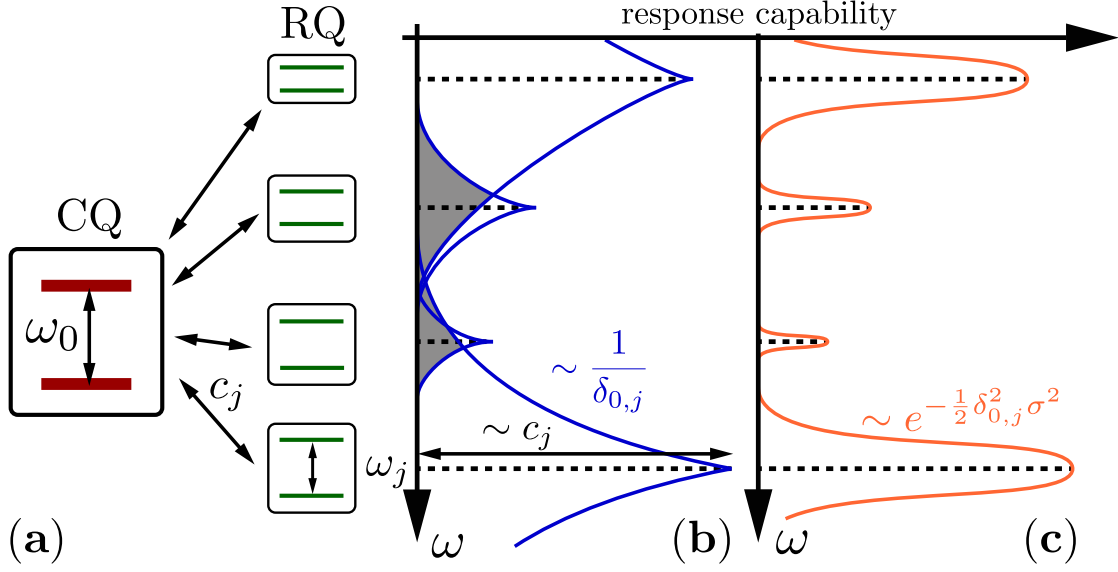


Figure 8.1.: **Advantages of a temporal shaping of the coupling.** (a) Illustration for the control qubit and resource qubits. (b) For the case of constant a coupling c_j , the off-resonant response decays slowly $c_j/\delta_{0,j}$ (blue lines) with the energy mismatch $\delta_{0,j}$. The overlaps (grey areas) on the frequency response prohibit high-fidelity selective coupling. (c) With the soft coupling proposed in this work the off-resonant response decays exponentially (see the orange lines), which allows high-fidelity addressing. (Reprinted figure with permission from [H4]. Copyright (2018) by the American Physical Society.)

where we strongly suppress all fast oscillating terms in a three-body Hamiltonian. Second, Section 8.3.2 contains a demonstration how the method adjusts frequency spectra obtained via dynamical decoupling by removing side oscillations and enables highly-selective two-qubit gates for quantum sensing and computing.

8.1. Generic Model for Temporal Control of Quantum Interactions

Let us explore the effects emerging from temporal control exerted on the coupling between quantum systems. For that, we consider the standard Hamiltonian used to describe open quantum systems as given in Eq. (1.2). However, the distinction between H_S and H_E is not necessary here, since for the desired application the roles of system and environment are diluted. For example, in a central spin model like we have for the NV center, every ^{13}C is a potential RQ while at the same time it acts as noise when not addressed. Furthermore, the approach we

are going to present does not require tracing over environmental degrees of freedom. Hence the distinction is not required. Thus we unite $H_0 = H_S + H_E$ and consider the Hamiltonian $H = H_0 + H_{\text{int}}$, where now H_0 is the free Hamiltonian for the the quantum registers, while

$$H_{\text{int}} = \lambda(t) \sum_{\alpha} c_{\alpha} V_{\alpha} \quad (8.1)$$

describes their interactions which we aim to control selectively. To model the soft control, we introduced $\lambda(t)$ which is a dimensionless, time-dependent global factor. The coupling operators V_{α} may contain single-body or n -body operators with strength c_{α} (i.e. the norm of V_{α} is equal to one). Note that α labels an arbitrary number of interaction terms.

Considering the eigenvalues ω_j and the projection operators $\mathbb{P}(\omega_j) = |\omega_j\rangle\langle\omega_j|$, the free Hamiltonian can be diagonalized yielding $H_0 = \sum_j \omega_j \mathbb{P}(\omega_j)$. Consequently, we write the interaction in the same basis such that

$$H_{\text{int}} = \lambda(t) \sum_{\alpha, j, k} c_{\alpha} V_{\alpha}^{\omega_j, \omega_k}, \quad (8.2)$$

where each $V_{\alpha}^{\omega_j, \omega_k} \equiv \mathbb{P}(\omega_j) V_{\alpha} \mathbb{P}(\omega_k)$ fulfills¹

$$[H_S, V_{\alpha}^{\omega_j, \omega_k}] = (\omega_j - \omega_k) V_{\alpha}^{\omega_j, \omega_k}. \quad (8.3)$$

The terms $V_{\alpha}^{\omega_j, \omega_k}$ describe the interactions between states of the total system with an energy mismatch of $\delta_{j,k} \equiv \omega_j - \omega_k$. In coupled quantum networks, the free states with energies ω_j are determined by (possibly) multiple constituents of the network.² For the sake of enhanced selectivity, our target is to suppress the terms $V_{\alpha}^{\omega_j, \omega_k}$ in Eq. (8.2) for which $\omega_j \neq \omega_k$, and to keep those with $\delta_{j,k} = 0$. Especially, these are terms where the coupled states $|\omega_j\rangle$ and $|\omega_k\rangle$ are degenerate. We will achieve this goal by an adequate shaping of the parameter $\lambda(t)$.

8.1.1. Leading-Order Effects and Soft Quantum Control

The calculation of an effective Hamiltonian can give precious insight to the underlying dynamics. Analogously to the procedure presented in Section 3.2, we employ a rotating frame with respect

¹The operators $V_{\alpha}^{\omega_j, \omega_k}$ are thus called *eigenoperators* of H_0 corresponding to the eigenfrequency $\omega_j - \omega_k$.

²Assume for example two qubits with $H_0 = (\nu_1 \sigma_1^z + \nu_2 \sigma_2^z)$, then $\omega_{1,4} = \pm(\nu_1 + \nu_2)/2$ and $\omega_{2,3} = \pm(\nu_1 - \nu_2)/2$, where the corresponding states are $|\omega_1\rangle = |11\rangle$, $|\omega_2\rangle = |10\rangle$, $|\omega_3\rangle = |01\rangle$, $|\omega_4\rangle = |00\rangle$. If the two qubits are tuned to resonance, this corresponds to the formation of pair of degenerate states, i.e. for $\nu_1 = \nu_2$ we have $\omega_2 = \omega_3 = 0$.

to H_0 and use Eq. (8.3). It is then straightforward to calculate that H_{int} becomes

$$H'_{\text{int}}(t) = \lambda(t) \sum_{\alpha,j,k} c_{\alpha} V_{\alpha}^{\omega_j, \omega_k} e^{i\delta_{j,k}t}. \quad (8.4)$$

In the absence of a modulation of λ , i.e. $\lambda(t) = \lambda_0$, unwanted terms in V_{α} may be neglected by the RWA provided that $\delta_{j,k}$ is sufficiently large compared with $\lambda_0 c_{\alpha}$. To motivate how the modulation of $\lambda(t)$ improves this situation, we calculate the leading-order average Hamiltonian in the rotating frame by using the Magnus expansion [79, 348] for a time interval $[-T/2, T/2]$. This average Hamiltonian reads

$$\bar{H}_{\text{int}}^{(1)} = \frac{1}{T} \int_{-T/2}^{T/2} dt H'_{\text{int}}(t) = \sum_{\alpha,j,k} c_{\alpha} g(\delta_{j,k}) V_{\alpha}^{\omega_j, \omega_k}, \quad (8.5)$$

where the averaging factor

$$g(\delta_{j,k}) = \frac{1}{T} \int_{-T/2}^{T/2} dt \lambda(t) e^{i\delta_{j,k}t} \quad (8.6)$$

is completely determined by $\lambda(t)$. For the conventional case of a constant $\lambda(t) = \lambda_0$, we have

$$g(\delta_{j,k}) = g_C(\delta_{j,k}) \equiv \lambda_0 \frac{\sin(T\delta_{j,k}/2)}{(T\delta_{j,k}/2)}. \quad (8.7)$$

In this manner, unwanted terms in V_{α} are suppressed by a large energy mismatch $\delta_{j,k}$ as they are decreasing the value of $g_C(\delta_{j,k})$. We remark that although the special matching condition $T\delta_{j,k}/2 = n\pi$ ($n = 1, 2, \dots$) for $g(\delta_{j,k}) = 0$ can be achieved for a single RQ with special values of the evolution time T , it is hard to accomplish for multiple RQs. Alternatively, by selecting λ_0 sufficiently small, the off-resonant interactions can be more efficiently suppressed with the associated improvement in the addressing for the resonant terms. This is the precise effect when higher harmonics are used in dynamical decoupling, see Section 3.2 and specifically Eq. (3.21), or the employment of an AXY sequence where the corresponding Fourier coefficient is tuned sufficiently small, see Section 3.3.2, which also tries to ensure Eq. (3.21). See also [H7] for an specific application of the latter.

However, from Eqs. (8.5) and (8.7) the effects introduced by off-resonant terms decay slowly as a power law $\lambda_0 c_{\alpha} / \delta_{j,k}$ with respect to the energy mismatch $\delta_{j,k}$. A natural way to increase the selectivity is then to decrease λ_0 . However, that as well carries the undesired effect of reducing the coupling with the resonant terms $\delta_{j,k} = 0$, since $g(0) = \lambda_0$. Crucially, the decrease of the

desired coupling prolongs the time which is required to collect phase for sensing or perform gates for computation. Hence, both operations become more influenced by present noise.

From Eq. (8.6), we find that by using a time-dependent soft modulation, i.e., $\lambda(t)$ is small at the beginning and at the end of the quantum evolution, the non-resonant terms can be removed with greater fidelity. More specifically, we find that the Gaussian temporal modulation

$$\lambda(t) = \lambda_0 \exp \left[-t^2/(2\sigma^2) \right], \quad (8.8)$$

has the corresponding averaging factor

$$g(\delta_{j,k}) = g_M(\delta_{j,k}) \equiv \lambda_0 \eta(\sigma, T) \exp \left(-\frac{1}{2} \sigma^2 \delta_{j,k}^2 \right), \quad (8.9)$$

where

$$\eta(\sigma, T) = \sqrt{\frac{\pi}{2}} \frac{\sigma}{T} \left[\operatorname{erf} \left(\frac{T - 2i\sigma^2 \delta_{j,k}}{2\sqrt{2}\sigma} \right) + \operatorname{erf} \left(\frac{T + 2i\sigma^2 \delta_{j,k}}{2\sqrt{2}\sigma} \right) \right] \quad (8.10)$$

and $\operatorname{erf}(x) = \frac{2}{\sqrt{\pi}} \int_0^x dz e^{-z^2}$ is the error function. A simple inspection of Eq. (8.9) reveals that the effective couplings $c_\alpha g_M(\delta_{j,k})$ decay exponentially with $\delta_{j,k}$. Hence, we expect the selectivity to be dramatically improved. We want to remark that this temporal shaping scheme shares interesting similarities with the control by Gaussian pulses of classical fields [56], however, in that case, the shaping is exerted on the coupling between quantum systems where quantum back-action plays a significant role on both sides [349].

8.1.2. Higher-Order Effects and Adiabatic Average Hamiltonian

Although the leading-order average Hamiltonian $\tilde{H}_{\text{int}}^{(1)}$ in Eq. (8.5) describes well the dynamics for $T \ll 1/\max|c_\alpha|$, if strong coupling constants are present, higher-order corrections [79, 348] have to be included in order to have an accurate description of the dynamics for larger times. While the evaluation of higher order terms is involved in the general case, we will now show that the soft quantum control scheme allows for an easy description of the system propagator including high-order corrections when executed in an adiabatic manner. To this end we first analyze the propagator

$$U_D(T) = e^{-i \int_{-T/2}^{T/2} dt H_D(t)}, \quad (8.11)$$

which is fixed by $H_D(t) = H_0 + \lambda(t) \sum_\alpha c_\alpha \sum_j V_\alpha^{\omega_j \omega_j}$, i.e., the free Hamiltonian together with

the desired on-resonance interactions. In the latter, all $V_\alpha^{\omega_j, \omega_j}$ operators commute with H_0 , see Eq. (8.3). Hence $H_D(t)$ can be diagonalized in the common eigenbasis $|\psi_n^D\rangle$ ($n = 1, 2, \dots$) of H_0 and $V_\alpha^{\omega_j, \omega_j}$. Note that this commutativity is also the reason that the evolution operator in Eq. (8.11) does not require a time-ordering and since H_0 is constant, the eigenstates $|\psi_n^D\rangle$ are also constant.³ Therefore $U_D(T) = \sum_n e^{-i\phi_n^D(T)} |\psi_n^D\rangle\langle\psi_n^D|$ is as well diagonal in the basis $\{|\psi_n^D\rangle\}$ and the dynamic phases $\phi_n^D(T)$ include the effect of energy shifts coming from $V_\alpha^{\omega_j, \omega_j}$.

If the whole Hamiltonian H is considered, the time-ordered evolution

$$U = \mathcal{T}_\leftarrow \exp \left[-i \int_{-T/2}^{T/2} H(t) dt \right] \quad (8.12)$$

is generally non-diagonal in the basis $\{|\psi_n^D\rangle\}$ and the terms not-commuting with H_0 , i.e. all $V_\alpha^{\omega_j, \omega_k}$ where $j \neq k$, will cause unwanted transitions between the different $|\psi_n^D\rangle$ states. However, when the soft control is included one can efficiently eliminate the unwanted interactions caused by $V_\alpha^{\omega_j, \omega_k}$, even for long evolution times T . At the boundaries of the interaction times, $-T/2$ and $T/2$, $\lambda(t)$ has negligible values and therefore the system's eigenstates coincide with those of $H_D(\pm T/2)$, since $H_D(\pm T/2) \approx H_0$ and $H(\pm T/2) \approx H_0$. More precisely, under the condition of adiabatic evolution [350, 351], there are no transitions among the different states $|\psi_n^D\rangle$. In particular, this is due to the instantaneous eigenstates $|\psi_n^H(t)\rangle$ of $H(t)$ being non-interacting. Consequently, the propagator at the end of the evolution is $U \approx \sum_n e^{-i\phi_n(T)} |\psi_n^D\rangle\langle\psi_n^D|$, where $\phi_n(T)$ are the associated dynamic phases, while the geometric phases vanish because $\lambda(t)$ returns to its original value [80] see Appendix B.3.1. In this manner U takes the same form as U_D and the adiabatic average Hamiltonian and the corresponding evolution operator for the soft quantum control scheme

$$\begin{aligned} \bar{H} &= \sum_n [\phi_n(T)/T] |\psi_n^D\rangle\langle\psi_n^D|, \\ \bar{U} &= e^{-i\bar{H}T} = \sum_n e^{-i\phi_n(T)} |\psi_n^D\rangle\langle\psi_n^D| \end{aligned} \quad (8.13)$$

are diagonal in the same basis as H_D . Furthermore, \bar{U} includes all the high-order energy shifts. In the following we illustrate our general theory via two important applications.

³Note that this argument is in principle the same as for noisy pure dephasing dynamics, where no transitions between eigenstates of the system Hamiltonian can be introduced.

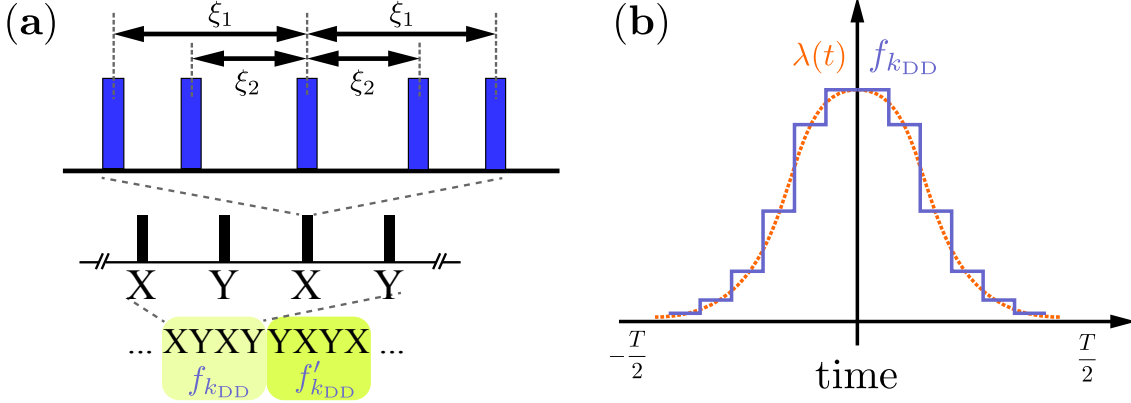


Figure 8.2.: **The protocol of soft control implemented via the AXY sequences.** For optimal robustness, the AXY sequences are executed in their AXY-8 pulse scheme, where after each four composite pulses the spacing in the latter is changed. Panel (a) shows is this procedure in the lowest row, while the upper rows are basically taken from Figure 3.3. Changing the parameters ξ_1 , ξ_2 accordingly, results in panel (b) where f_{lDD} assembles the continuous function $\lambda(t)$ in discrete steps. (Reprinted figure with permission from [H4]. Copyright (2018) by the American Physical Society.)

8.2. An Implementation using Dynamical Decoupling

Let us dedicate this section to the demonstration of how the soft quantum control might be implemented into an experimental scheme employing dynamical decoupling. Surely, the results derived above indicate appealing properties when employed for the control of resources qubits. However, not every physical platform provides a direct control over the couplings. Crucially, the type and strength of the coupling is given by the nature of the system itself, e.g. for NV centers the direction and the strength of the hyperfine coupling vector is set according to Eq. (2.4), i.e. by the relative position of the NV and impurity.

For the sake of simplicity, we consider a central spin model where the central spin undergoes pure dephasing dynamics. In a frame rotating with the free energy terms, we may write the corresponding Hamiltonian with time dependent coupling as [compare Eqs. (3.16) and (3.18)]

$$H(t) = \lambda(t) \frac{1}{2} \sigma_0^z \sum_j \left[a_j^\perp \left(\sigma_j^+ e^{i\omega_j t} + \sigma_j^- e^{-i\omega_j t} \right) + a_j^\parallel \sigma_j^z \right]. \quad (8.14)$$

Here, $\lambda(t)$ directly reminds of the modulation function $F(t)$ used in Section 3, except this function is only allowed to take the values ± 1 , see Eq. (3.10). In the following, we now show

a way to circumvent this issue. Therefore, recall Section 3.2 which discusses the effective Hamiltonian approach to DD, where a critical point in the derivation of the effective Hamiltonian was the value of the chosen Fourier coefficient $f_{l_{DD}}$, which in the end determined the coupling strength to the target frequency. Furthermore, recall the AXY-sequences introduced in Section 3.3.2 which enable control over these coefficients. Thereby it is important to note that the desired coefficient is created through the periodicity of the modulation, i.e. one requires at last one period of two composite pulses. We hence use the AXY-sequences to construct $\lambda(t)$ via the coefficients $f_{l_{DD}}$ in a digitalized manner, by changing the interpulse spacing every four composite pulses. Figure 8.2 (a) shows the added layer of complexity to the AXY-sequences illustrated in Figure 3.3, Figure 8.2 (b) the digitalized function $\lambda(t)$. Hence, we call the resulting sequence *Gaussian AXY-sequences*.

To that end, let us mention a few important points concerning this implementation. The pulse spacing is changed every four composite pulses to maintain the robustness against pulse errors including the first order. Nevertheless, according to Table 3.1, AXY-8 also removes the second order of the pulse errors. Hence we shift every second AX-4 period by a phase of $\pi/2$, which then assembles one AXY-8 period in terms of the pulse phases. If we assume that $f_{l_{DD}}$ changes only slightly between each four composite pulses, i.e., they are almost the same, this will lead to a comparable robustness to the AXY-8 sequence. Furthermore, for symmetric modulations as the Gaussian one in Figure 8.2 (b), each block of four composite pulses that appears in the first half of the sequence, appears with pulse phase shifted by $\pi/2$ and exactly the same pulse spacing in the second half of the sequence. If the errors are static, this may also yield an improved robustness.

We also emphasize, that the implementation via DD has a welcoming advantage. Crucially, it protects the control qubit against unwanted noise terms which are not faded by the Gaussian control. More explicitly, in the central spin model considered here, the terms $\sim a_j^\parallel \sigma_j^z$ do not oscillate and hence are not detuned from the central spin. These terms result in a fluctuating magnetic field which emerges from the collection of the nuclear spins and destroys the central spin's coherence (see also Section 3.1). Naturally, under DD these terms are averaged out and the coherence is protected.

8.3. Applications

8.3.1. Improving the Rotating Wave Approximation

In this section, we apply the soft quantum control to a generic model of two body interactions. More specifically, we demonstrate how the soft quantum control mechanism is suitable for an efficient elimination of the counter rotating (or often also called non-energy-conserving), but also fast oscillating terms over a continuous time-interval and even for long evolution times. The persistent impact of the fast oscillating terms is difficult to remove due to the limit of available resources for selective control on realistic quantum systems (e.g., for singlet-triplet qubits in semiconductor quantum dots [352, 353]). As an example, we consider a control qubit (index 0) and two equally strong coupled resource qubits (index 1, 2) with the interaction Hamiltonian

$$\begin{aligned} H_{\text{int}} &= c\lambda(t)\sigma_0^x (\sigma_1^x + \sigma_2^x) = c\lambda(t) (P_{0,1} + Q_{0,1} + \sigma_0^x \sigma_2^x) \quad \text{where} \\ P_{0,1} &= \sigma_0^+ \sigma_1^- + \sigma_0^- \sigma_1^+, \\ Q_{0,1} &= \sigma_0^+ \sigma_1^+ + \sigma_0^- \sigma_1^-. \end{aligned} \quad (8.15)$$

Here, $Q_{0,1}$ is the counter rotating term.⁴ We aim to couple qubit 0 purely with qubit 1 via the flip-flop term $P_{0,1}$ without involving the perturbation $Q_{0,1}$. Therefore we choose the energies

$$H_0 = \frac{\omega}{2} (\sigma_0^z + \sigma_1^z) + \frac{\omega_2}{2} \sigma_2^z \quad (8.16)$$

such that qubit 2 is off-resonant with $\omega_2 = 3\omega$. In a regime where the RWA can be applied efficiently, we are able to approximate a high-fidelity swap gate between the qubits 0 and 1. The perfect swap gate would be generated by the corresponding target Hamiltonian

$$H_{\text{target}} = \frac{1}{2}\tilde{\omega} (\sigma_0^z + \sigma_1^z) + \frac{1}{2}\tilde{\omega}_2 \sigma_2^z + \tilde{c} (\sigma_0^+ \sigma_1^- + \text{H.c.}), \quad (8.17)$$

which governs the dynamics via the associated propagator $U_{\text{target}} = e^{-iH_{\text{target}}T}$. The frequencies and coupling marked with a tilde correspond to corrected energies and couplings, where the shifts appear due to the interaction among the different qubits. These corrected energies can be obtained by using the adiabatic average Hamiltonian according to Eq. (8.13) (see also Appendix B.3.2 for an analytic example considering two qubits).

Let us now formulate the task as follows. Our aim is to tune $\lambda(t)$ such that the evolution

⁴Note, there exist also such terms for the second qubit, i.e. $Q_{0,2}$ and $P_{0,2}$. However, here we want to suppress all terms involving the second qubit.

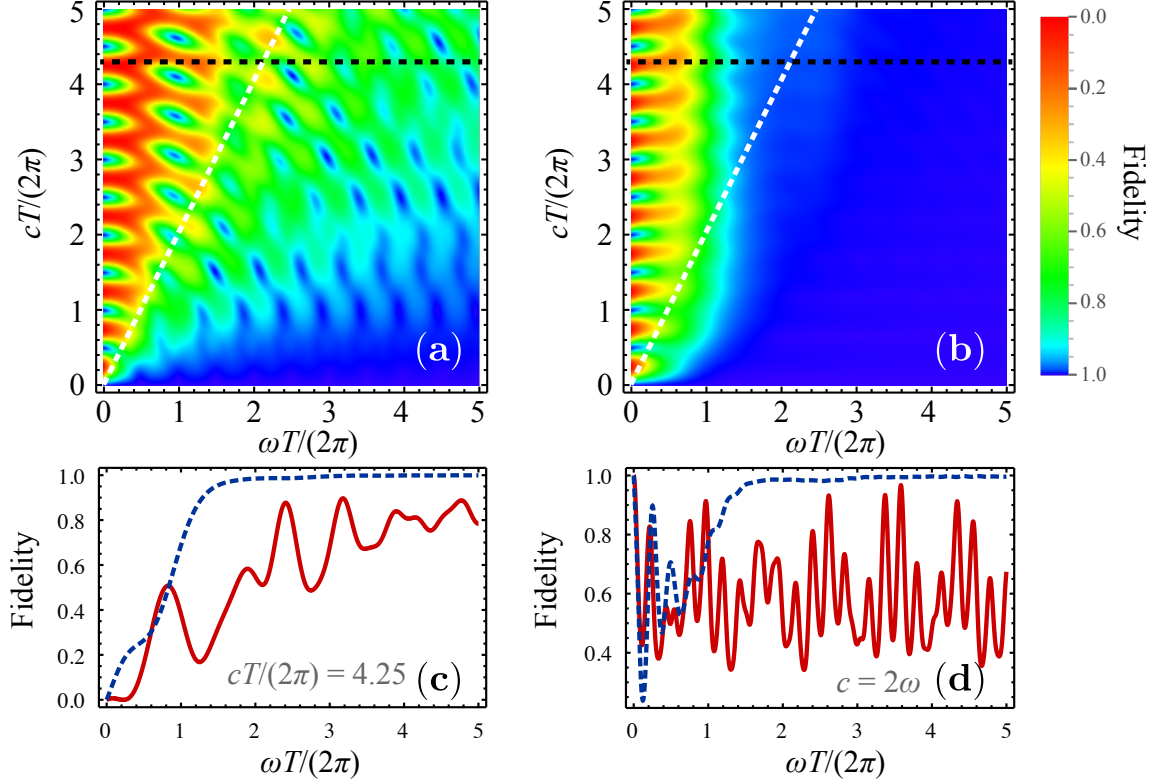


Figure 8.3.: **Fidelities under the RWA.** (a) Fidelity to the target evolution without unwanted coupling by using the constant-amplitude coupling. (b) As in (a) but using the Gaussian soft coupling such that we obtain the same target evolution. Curves in (c) and (d) show cross-sectional plots [cuts marked with black dashed lines for (c) and white dashed lines for (d)] in the constant-amplitude case of (a) [red solid lines], or for the Gaussian shaped coupling case of (b) [blue dashed lines]. It is easy to see that the soft quantum control scheme keeps a high fidelity even for a relatively large ratios c/ω at long evolution times T . (Reprinted figure with permission from [H4]. Copyright (2018) by the American Physical Society.)

governed by $H(t) = H_0 + H_{\text{int}}(t)$ and the one generated by H_{target} at the final time are effectively the same. In particular, we aim to achieve

$$U(T) = \mathcal{T}_{\leftarrow} e^{-i \int_{-T/2}^{T/2} d\tau H_0 + H_{\text{int}}(\tau)} = e^{-iT H_{\text{target}}} = U_{\text{target}}(T), \quad (8.18)$$

where $U(T)$ is the evolution under the soft quantum control. To succeed, we select the following parametrization for the Gaussian,

$$\sigma = \frac{T}{4\sqrt{2}} \quad \text{and} \quad \lambda_0 = \left[\sqrt{2\pi}\sigma \operatorname{erf}\left(\frac{T}{2\sqrt{2}\sigma}\right) \right]^{-1}. \quad (8.19)$$

Naturally, the width of the Gaussian, σ , is the most crucial but also most sensitive parameter participating in the problem. To decouple of resonant transitions efficiently, the width has to be chosen as large as possible, since this results in a narrow frequency window where interactions are not suppressed. This is an intuitive result from the averaging function in Eq. (8.6), which can be understood as a Fourier transform. On the other hand, when σ is chosen too large, one obtains a constant coupling as the limiting case.

We measure the gate fidelity according to [354]

$$F = \frac{|\text{tr}[U_{\text{target}}U^\dagger]|}{\text{tr}[UU^\dagger]}. \quad (8.20)$$

The numerical results for various energies and couplings are displayed in Figure 8.3 (a) for the standard constant coupling, i.e., no modulation, and in (b) for the Gaussian modulation. Inspection of the plots reveals that the soft quantum control reaches much higher fidelities over a wide range of parameters (blue region), and we stress that in particular this is the case for strong couplings ($c > \omega$) where the RWA usually starts to fail. Panels (c) and (d) in Figure 8.3 show cuts through the maps in panels (a) and (b), the constant coupling with a red solid line and the Gaussian coupling as a blue dashed line. From here, one can clearly observe that the constant coupling requires much longer averaging times to approach a high fidelity. Naturally during these times, relaxation and decoherence processes will decrease the fidelity further. Furthermore, locating the points of high fidelity in the standard approach becomes increasingly difficult when more qubits are involved. For that, compare also Appendix B.3.3 where we illustrate the same example without the off resonant qubit 2.

Note that our approach is fundamentally different from adiabatic elimination [355, 356]. Adiabatic elimination is aimed at *coupling* certain target levels by a virtual transfer of excitations through other mediator states that are removed from the dynamics, thus generating an evolution in the *reduced* Hilbert space of the target states. Instead our objective is to efficiently *suppress* unwanted interaction terms in the Hamiltonian through a soft modulation of the coupling constants, without reducing the dimension of the whole Hamiltonian and without having to use other states as mediators. Hence, our method allows to switch off unwanted interactions among the qubits in a highly selective manner and to perform high-fidelity quantum gates as we will demonstrate later.

8.3.2. Sensing and Quantum Gates

The soft quantum control mechanism allows high-fidelity interactions between weakly coupled qubits while it avoids perturbations that arise from the surroundings. As we have seen in the last section, these could arise due to other, possibly strongly coupled qubits. In this section, we will take the mechanism a step further and illustrate its capabilities when implemented via DD, employing the digitized formalism we described in Section 8.2.

As usual throughout this work, the platform of choice is the NV center in diamond. Despite this growing habit, this platform is especially suitable here since the electron-nuclear hyperfine coupling offers a medium to control the ^{13}C nuclear spins via the NV electron spin and we thus have exactly the arrangement displayed in Figure 8.1. Furthermore, the NV center represents an excellent platform for quantum information processing, quantum sensing and quantum networks [5, 9, 13, 23, 58, 63, 345], while it offers extraordinary capabilities to be manipulated by a huge number of DD pulses [137, 180]. The calculations in Chapter 3 show that under pulsed DD (or a continuous drive [322, 347], see Appendix B.3.4) on two NV electron states forming the control qubit, the ^{13}C Larmor frequencies ω_j are shifted by their individual hyperfine coupling [see Eq. (2.8)], providing the frequency differences $\delta_{j,n} = \omega_j - \omega_n$ for selective addressing, as stated in Eq. (3.24). Nevertheless, the equation also reveals that the frequency differences are on the level of the hyperfine coupling, i.e.

$$|\delta_{j,n}| \approx |\vec{A}_j - \vec{A}_n|. \quad (8.21)$$

Consequently, the electron-nuclear interactions are typically of the same order of magnitude which imposes an enormous challenge on the design of highly-selective coupling. Especially when the number of accessible nuclear spins in such a register should be increased which is typically achieved for a higher concentration of ^{13}C , the individual addressing becomes incomparably more difficult.

To demonstrate the advantages of the soft quantum control, we compare different protocols for single spin addressing in Figure 8.4, by using a model with two spectrally close nuclear spins. The couplings among themselves are small but taken into account in the simulations. Thereby we choose a strongly coupled (spin A) and a weakly coupled spin (spin B) whose Larmor frequencies are separated by less than 5 kHz in a magnetic field of $B_z = 400$ G. The couplings are shown in Table 8.1.

Table 8.1.: **Parameters of the spins used for the simulation presented in Figure 8.4.** The Larmor frequencies are calculated for ^{13}C spins in a magnetic field $B_z = 400$ G.

	$\frac{\omega}{2\pi \text{ kHz}}$	$\frac{a^{\parallel}}{2\pi \text{ kHz}}$	$\frac{a^{\perp}}{2\pi \text{ kHz}}$
spin A, weak	441.91	27.25	17.45
spin B, strong	437.54	16.93	55.45

We start with the presentation of frequency spectra as introduced in Chapter 7, obtained via various methods.

As shown in Figure 8.4 (a) a frequency scan obtained via a continuous, constant drive exploiting the Hartmann-Hahn resonance condition [322, 347] (see also Appendix B.3.4) does not resolve the two ^{13}C nuclei even for a longer sensing time T because of the slow power-law decay of the signal around the resonance position. Importantly, note that the width of the peak is about $2\pi \times 75$ kHz.

As a next step, we implement a standard AXY sequence from Section 3.3.2 employing a small $f_{l_{\text{DD}}} = f_3 = 0.271$ at the third harmonic $l_{\text{DD}} = 3$. The signal of 128 composite pulses is plotted in Figure 8.4 (b) with a red line. The obtained signal reveals greater details than the scheme employing the continuous drive, however it also reduces the coupling to the target spins. The resonance position of the weakly coupled spin A is expected at $3\omega_{\text{DD}} = 441.91$ kHz and marked with the white (dashed) line. However it turns out that the resonance signal of spin A is heavily disturbed by the influence of the strongly coupled spin B, causing the indentation in the signal. Indeed, this can be seen directly from the single spin signals we computed by neglecting the other spin respectively. These curves are shown with dotted lines in green and blue. At the resonance position of spin A, there is a significant contribution of the strongly coupled spin B caused by one of its side oscillations. Hence, we can conclude that spin A is impossible to address individually using the AXY sequences, since the width of addressed frequencies is still too large.

For the simulation of the curve in panel (c), we employ the Gaussian AXY sequence as described in Section 8.2. Changing $f_{l_{\text{DD}}}$ (with $l_{\text{DD}} = 3$) in the AXY sequences for every unit with four composite pulses, we implement $\lambda(t)$ in a digitized manner while preserving the robustness of the sequences against experimental control errors. We choose $\lambda_0 = \max_t \lambda(t) = 0.6171$, while σ corresponds to 11 periods of the DD sequence. For the precise values of f_3 , i.e. $\lambda(t)$, we refer to Appendix B.3.5. This yields the red solid curve in Figure 8.4 (c) which demonstrates the significant enhancement in the addressability and resolves the weak spin flawlessly. In addition, it removes all side peaks around the spin resonances, which is of great advantage

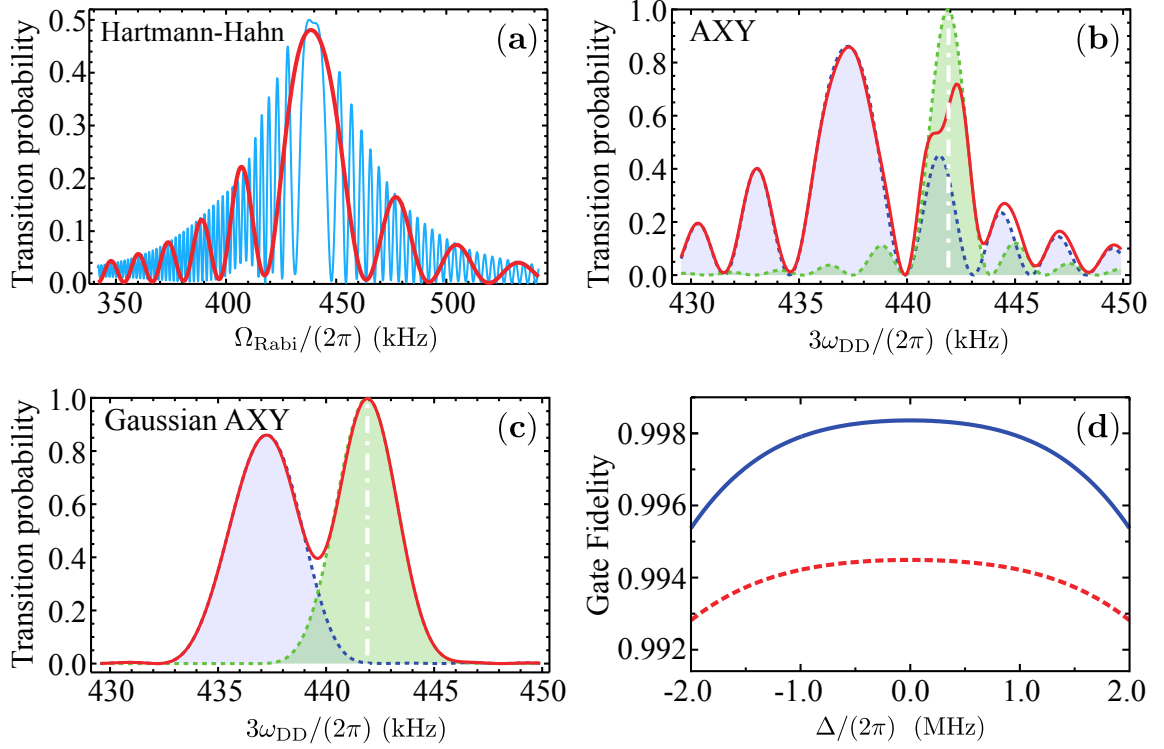


Figure 8.4.: **The soft quantum control employed via AXY-sequences.** (a)-(c) Signal of transition probabilities, originating from two nuclear spins with the Larmor frequencies $\omega_A = 2\pi \times 441.91$ kHz and $\omega_B = 2\pi \times 437.54$ kHz. More details can be found in Table 8.1. (a) Hartmann-Hahn resonance spectrum with a total sensing time $T \approx 54 \mu\text{s}$ (red) or $T \approx 435 \mu\text{s}$ (blue). (b) Signal for the AXY sequences (red solid line) operating at the third harmonic employing 128 composite pulses. The single-spin contributions are drawn with dashed lines and corresponding shading. The Fourier coefficient $f_3 = 0.271$ is chosen to maximize the signal (green) one from the spin with Larmor frequency ω_A . The target signal centered at the vertical white dashed-dotted line is destroyed by the strong perturbation (blue) originating from spin B. (c) Varying f_3 of the AXY sequences in (b) according to the Gaussian shape clearly resolves the two spins. (d) The fidelity (blue solid curve) of the gate $U_{\text{target}} = e^{-i\frac{\pi}{4}\sigma_0^z\sigma_1^x} \otimes \mathbb{I}_2$ as a function of the microwave detuning error δ by using the Gaussian AXY sequence with a Rabi frequency $\Omega = 2\pi \times 20$ MHz in the rectangular pulses. The red dashed line is the case for a mismatch of 5% in Ω . To realize the gate U_{target} , f_3 has been reduced by a factor of two when using the parameters indicated by the vertical dashed-dotted line in (c). (Reprinted figure with permission from [H4]. Copyright (2018) by the American Physical Society.)

when fitting dense signals [69] and avoids false identification of the signal peaks in particular in the presence of spurious resonances like in Section 7.4.3 [74, 357, H2].

This great addressability suggests the employment of the Gaussian AXY sequence as a method to apply robust, high-fidelity quantum gates on desired nuclear qubits. For example, a perfect gate rotating spin A around its \hat{x} -axis by an angle ϕ possesses the evolution operator

$$U_{\text{target}} = e^{-i\frac{\phi}{2}\sigma^z\sigma_A^x} \otimes \mathbb{I}_B. \quad (8.22)$$

Note that this operator corresponds exactly to an evolution according to the effective Hamiltonian (3.25) where $m_s f_{\text{DD}} a_A^\perp / 4 = \phi / t$. For the soft control, we adapt that notion to

$$\phi = m_s \frac{a_A^\perp}{4} \int_{-T/2}^{T/2} d\tau \lambda(\tau) = m_s \frac{a_A^\perp}{4} \int_{-T/2}^{T/2} d\tau \lambda_0 e^{-\frac{\tau^2}{(2\sigma)^2}}. \quad (8.23)$$

We calculate the fidelity for the gate for the same sequence parameters as employed for the spectrum given in Figure 8.4 (c) but choose the variation of f_3 such that the target spin only performs a half rotation, i.e. $\phi = \pi/2$. In fact, this corresponds to half the λ_0 employed for the simulations in Figure 8.4 (c), since at the resonance position a π rotation is fulfilled (see also Figure B.3). We include an energy shift of the strongly coupled nuclear spin equivalent to the example above, Section 8.3.1, and choose the Rabi frequency of the pulses as $\Omega = 2\pi \times 20$ MHz. The fidelity is shown in Figure 8.4 (d) for different values of possible detunings of the decoupling pulses, where the blue curve represents a perfect match of the Rabi frequency and the pulse time t_{pulse} while the red curve includes a five percent error in Ω . Remarkably, the obtained fidelity is always well above 99%, even for detunings of 2 MHz which is twice as much as we would expect in an NV based setting [61, 74]. On the contrary, the fidelities achieved by the Hartmann-Hahn or AXY protocol under the same conditions are very low (e.g., 57% for AXY) because of the poor spin addressing [see Figure 8.4 (a),(b)].

Note that the enhanced spectral resolution by the soft control can be used to improve the controllability of interacting spin clusters [180, 185, 219, 338, H7] and nuclear-spin decoherence-free subspaces [326].

8.4. Conclusions

We proposed the mechanism of soft quantum control which enables highly selective coupling between different on-resonance constituents of composite quantum systems. The method

introduces a time-dependent, Gaussian shaped modulation of the coupling constants in addition to the matching of resonance frequencies. This results in an exponentially improved suppression of off-resonant couplings. We motivated the form of the modulation by a first order average Hamiltonian. To include strongly interacting quantum systems which are not covered by the average Hamiltonian theory, we furthermore we established an adiabatic theory. Here, we developed an average adiabatic Hamiltonian, which is even valid under the presence of strong coupling terms to undesired parts of the Hilbert space.

To underline the capabilities of our model, we showed two direct applications of our protocol. First an improved RWA, which is now also valid in the strong coupling regime, that is when the energy splitting of the resonant systems is on the same order of magnitude as their coupling strength. Moreover, the method guaranties continuous intervals of high fidelity with the approximated Hamiltonian. That is, the averaging effect of the fast oscillating terms is not only valid for isolated points in time. Second, we demonstrated how the soft quantum control can be combined with DD techniques. In particular, we showed how it can introduces effectively by modifying the AXY sequences developed in an earlier work. This enables the addressing of weakly coupled nuclear spins under the presence of strong perturbations, originating from impurities with close resonance frequencies. We presented a realistic example employing the NV center in diamond. Moreover, the method is of general applicability and can be useful for the coherent manipulations of quantum registers and spectroscopic challenges in a wide range of systems such as stoichiometric rare earth ion systems, spin defects and single dopants in solids, as well as spin-boson systems.

Finally, we also remark that the technique goes well beyond realizing the proposed Gaussian shape. In principle, many different shapes can be realized. The presented method hence also provides the possibility to engineer the shape of the averaging factor in Eq. (8.6), or equivalently the filter function in DD based scheme, Eq. (3.12), to meet the needs of the problem at hand. For example, windows at other frequencies than odd multiplies of ω_{DD} can be introduced by adding an oscillatory component to $\lambda(t)$. A Gaussian shape of small width yields a broad window where one can address a wide range of target frequencies at once. This might be of interest for schemes that, e.g., employ frequency specific Hamiltonian engineering for hyperpolarization [358].

CHAPTER 9

Controllable Non-Markovianity for an Electron Spin in Diamond

The results presented in this chapter are published in [H5]. Reprinted excerpts with permission from [H5]. Copyright (2018) by the American Physical Society.

What ever quantum system is under investigation, there is always, the unavoidable impact of undesired noise altering the state of the observed system [1–4]. With quantum technologies striving for commercial applications [5, 8, 9, 15, 21], it is essential to understand, first the origin of the noise, but second, also the effect of the noise onto the employed quantum state and the accompanied consequences for the application of interest, as there are quantum computing [14], quantum cryptography [359], quantum simulation [24], quantum sensing [13] and quantum metrology [18]. In some cases, the structure and the coupling of the environment allow for a mutual exchange of information, and more specifically, information once drained out of the system of interest may flow back at a later time. One usually denotes such a dynamic as non-Markovian.

Apparently, different properties of the noise may render its impact less harmful. For example, the Chapters 4 and 5 demonstrate that colored noise outperforms white noise (i.e. uncorrelated noise) in terms of the achievable precision when estimating the transition frequency of a qubit. Moreover, dynamical decoupling, as introduced in Chapter 3, solely keeps its refocusing abilities when the noise possesses a finite correlation time. Further practical applications of these non-Markovian processes have been recognized in the creation of entangled states [86, 360],

energy transport in biological complexes [87, 89] and several other fields [37, 39, 85, 86, 88, 90, 361, 362, H3].

We dedicated Section 1.4 to the theoretical description of non-Markovianity and how it can be introduced to characterize the dynamics of open quantum systems. As mention there, in the last years, numerous works appeared developing methods and tools to quantify the degree of non-Markovianity [82, 83, 102, 103, 130–132, 363]. More specifically, several measures have been defined with the aim to quantify, how (non-)Markovian a dynamics is. These works are accompanied by experimental investigations enabling extended control over this degree, with realizations in trapped ions [100] and photonic setups [93–99].

In this chapter, we are theoretically and experimentally investigating the realization of a system which enables continuous tunability of its degree of non-Markovianity, i.e., its quantification according to a specific measure. More specifically, the NV center in diamond provides this flexible platform where the inherent nitrogen nuclear spin acts as a natural source of non-Markovianity during the genuine open-system evolution of the electron spin. For the control, we manipulate the polarization of the nitrogen spin to induce collapses and revivals on the electronic spin coherence, while the polarization direction of the nitrogen spin defines the amplitude of these collapses and revivals. In other words, one of the system's key features is the fact that the source of non-Markovianity is intrinsic to the system itself, instead of being artificially generated by an external signal generator acting as a source of correlated noise.

Here, we performed the data analysis using Bayesian inference to keep the amount of necessary data acquisition to a minimum. Hence, we start this chapter with an introduction to the concept and terminology concerning the latter in Section 9.1. Following in Section 9.2 is the theoretical description of the model and the underlying processes leading to the non-Markovian dynamics. The experimental investigation afterwards is divided into two parts. First, we analyze an FID measurement performed on the NV center in Section 9.3.1. The reason for the latter is the environment of the NV center. As described in Section 2.2, it may be highly complex and in some instances, e.g., when single strongly coupled ^{13}C spins are present, is already able to induce non-Markovianity. In fact, we ensure that the only source of non-Markovianity in our selected probe is the nitrogen nuclear spin, which in turn allows to set the degree of non-Markovianity to zero, and importantly, allows an interpolation of the non-Markovianity measure from data collected at short evolution times after initialization. Second, the dynamics of the NV centers electron spin is tuned through different degrees of non-Markovianity by specific preparations of the nitrogen spin. The details of the analysis and results are contained in Section 9.4.2.

9.1. Introduction to Bayesian Inference

The problem of assigning observed outcomes to possible causes, is a daily faced problem in science. We may categorize possible causes with numbers which we call probabilities. Contrary to a frequentist approach, where these probabilities are understood as the relative number of occurrences of precisely that cause (in the limit of infinite observations), the Bayesian approach takes probabilities as a measure of certainty, i.e., how much one believes a certain cause to be the true one. Within the Bayesian approach, all causes, e.g. parameters to be inferred are probability distributions themselves, while the frequentist approach assumes them to be constant. For an in-depth review on Bayesian inference, see the references [104–106].

We denote a random variable for the parameters by Θ and a corresponding value by θ . Note that in general θ can be a vector. The corresponding probability distribution is then written as $\mathcal{P}(\Theta)$. Let us introduce a second random variable for the measured data, \mathcal{X} , where a specific realization is denoted by x . The probability, to make certain observation $\mathcal{X} = x$, i.e. a data point or a whole set of data, given some model Θ is then the conditional probability

$$\mathcal{P}(\mathcal{X} = x | \Theta = \theta) = \frac{\mathcal{P}(\mathcal{X} = x, \Theta = \theta)}{\mathcal{P}(\Theta = \theta)}. \quad (9.1)$$

Note that the probability in the nominator on the r.h.s. denotes the probability to find x and θ , while the l.h.s. is the probability to find x given θ . From now on we will drop the notation like $\Theta = \theta$ for probabilities and use the value alone, while we keep the calligraphic random variables for the probability distributions.

Instead of the probability to make a specific observation x , we are rather interested in the parameter θ . Hence, we can formulate the conditional probability the other way round, i.e.

$$\mathcal{P}(\theta | x) = \frac{\mathcal{P}(x, \theta)}{\mathcal{P}(x)}. \quad (9.2)$$

Usually, we do not have access to $\mathcal{P}(x, \theta)$. Hence, we combine Eqs. (9.1) and (9.2) to obtain Bayes theorem,

$$\mathcal{P}(\theta | x) = \frac{\mathcal{P}(x | \theta) \mathcal{P}(\theta)}{\mathcal{P}(x)}. \quad (9.3)$$

This theorem describes the desired object, i.e. the posterior probability distribution $\mathcal{P}(\Theta | \mathcal{X} = x)$. This object quantifies how certain we are that a given $\Theta = \theta$ is the cause of the outcome $\mathcal{X} = x$. The r.h.s. of the theorem is specified in the following way. The likelihood function for Θ is $\mathcal{P}(\mathcal{X} | \Theta)$. While it is a probability distribution for \mathcal{X} given Θ , we can also think of it as a function weighting the values of Θ to the usually fixed, since observed, values $\mathcal{X} = x$. The so

called prior distribution $\mathcal{P}(\Theta)$ is a powerful way to include prior knowledge of the parameter. For example, a flat distribution would correspond to no prior information. However, in the application described in the main text, e.g. for estimates of a coupling constant, we may choose a Gaussian distribution with a mean value determined in earlier experiments. The only remaining quantity is the evidence $\mathcal{P}(X)$. While we are able to express

$$\mathcal{P}(X) = \int d\theta \mathcal{P}(X|\Theta = \theta) \mathcal{P}(\Theta = \theta), \quad (9.4)$$

we note that this quantity only serves as a normalization constant, hence we can neglect it and write Bayes theorem as

$$\mathcal{P}(\Theta|X) \propto \mathcal{P}(X|\Theta) \mathcal{P}(\Theta) \quad (9.5)$$

Therefore, the posterior distribution is always totally determined by the likelihood function and the prior distribution.

Possessing the posterior distribution allows the calculation of marginal probabilities, in case Θ has more than one dimension. The marginal distribution for one specific dimension of Θ quantifies the probability distribution for this dimension alone, irregardless of the distributions in other dimensions. In other words, if we have the parameter $\theta = (\theta_1, \theta_2, \dots, \theta_n)$ then the marginal distribution for θ_i is given by

$$\mathcal{P}(\theta_i|x) = \int_S d\theta_1 d\theta_2 \dots d\theta_{i-1} d\theta_{i+1} \dots d\theta_n \mathcal{P}(\theta|x), \quad (9.6)$$

where S is the image of $\tilde{\theta} = (\theta_1, \dots, \theta_{i-1}, \theta_{i+1}, \dots, \theta_n)$.

We can also use the posterior distribution to calculate a posterior predictive. Integrating over θ yields the posterior predictive distribution

$$\mathcal{P}(\mathcal{Y}|X = x) = \int_{\Theta} d\theta \mathcal{P}(\Theta = \theta|X = x) \mathcal{P}(\mathcal{Y}|\Theta = \theta) \quad (9.7)$$

where \mathcal{Y} is a second set of observations, which has not yet been detected in a real experiment. This is a powerful tool to first validate the obtained posterior distribution, but it can also be used to predict further observations due to the causes specified with the parameters in Θ .

Usually, the posterior distribution cannot be calculated analytically and even a numerical solution requires increasingly large effort, when the number of random variables increases. However, one can use Markov-Chain-Monte-Carlo (MCMC) methods to sample the r.h.s. of Eq. (9.3) efficiently. This technical detail goes far beyond the scope of this thesis and

many examples of these methods can be found in [105, 106]. Here we use the No-U-Turn Sampler [364], an extension to the Hamilton-Monte-Carlo MCMC algorithm [365]. The models in this thesis have been implemented using the PyMC3 software package for the Python programming language [366].

Using these algorithms, the obtained posterior distribution is given in terms of the relative frequencies with which a specific realization of Θ appears. Calculating the marginals, gives the relative frequencies of the values of a single parameter. The point estimate, which we denote by an overbar $\bar{\bullet}$, is then given by the median of the marginal posterior distribution (we neglect multimodal distributions in this work). However, the uncertainty in this value is determined by the shape of the distribution. A natural way to summarize the form of the distribution with least effort is the interval of highest posterior density (HPD). The HPD specifies the interval of values, which all have a higher probability than the values outside the HPD. Usually, the HPD is taken to cover a larger proportion of the distribution, e.g., as we also chose in the main text, 95% of all values which occurred during the sampling. An easy analogy is the width of a standard derivation, which contains 95.45% of its values within a region of width 4σ around its mean value. In case the marginal posterior distribution would be Gaussian, the HPD and the 4σ region would be equivalent.

9.2. Modeling and Measuring the Sample Dynamics

Chapter 2 already contains an extensive introduction into NV centers. However, let us quickly recall the necessary terminology and quantities, along with the specific details required for this very specific setup. The diamond used in this chapter is a low nitrogen (< 1 ppb) electronic grade diamond, grown by chemical vapor deposition with a depleted ^{13}C concentration of 0.2 % (natural concentration 1.1 %) to prolong the coherence time. Interaction with the inherent nitrogen nuclear spin results in a hyperfine splitting of the $|\pm 1\rangle$ states (see Figure 2.1), depending on the nitrogen isotope, here ^{14}N ($I = 1$), which possesses a parallel hyperfine coupling of $A_{\parallel} \approx 2\pi \cdot 2.14$ MHz [101]. We identified a native NV center, located deep (few μm) below the diamond surface to reduce its detrimental impact. The Hamiltonian of this configuration is given by [61] (compare also Section 2.2)

$$\begin{aligned}
 H_{\text{lab}} = & \Delta S_z^2 + \gamma_e B_z S_z + Q I_z^2 + \gamma_N B_z I_z \\
 & + S_z A_{\parallel} I_z + A_{\perp} (S_x I_x + S_y I_y) + H_R
 \end{aligned}
 \tag{9.8}$$

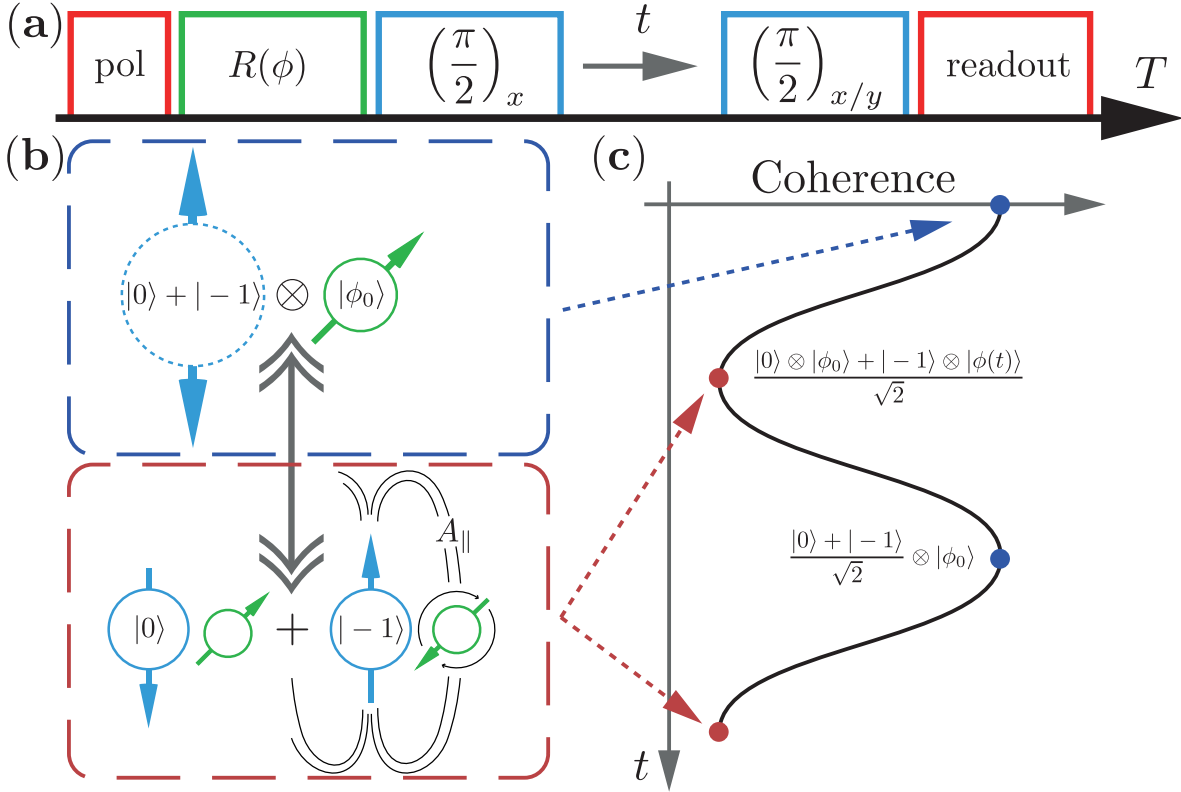


Figure 9.1.: Pulse scheme and theoretical modeling of the dynamics. The sequence for the Ramsey experiments in (a) consists of a preparation phase, where the polarization pulse initializes the electron spin in $|0\rangle$, the pulse $R(\phi)$ controls the population of the ^{14}N spin, two $\pi/2$ pulses (either x or y phase) on the electron spin and the subsequent readout. During the free period t , the spins undergo the conditional evolution illustrated in (b). If the electron spin populates $|-1\rangle$, it produces a hyperfine field which induces rotations of the ^{14}N spin. Therefore the pair switches continuously between a product (top) and an entangled state (bottom). Note that the roles of ^{14}N and electron spin are interchangeable. This switching coincides with the oscillations in the coherence in (c), where the points of maximal correlation correspond to the points of minimal coherence. (Reprinted panels (a) and (b) with permission from [H5]. Copyright (2018) by the American Physical Society)

where I_μ ($\mu = x, y, z$) are the ^{14}N spin-1 operators, the ^{14}N gyromagnetic ratio is labeled by γ_N and we have the quadrupole splitting Q and orthogonal interaction A_\perp . An applied field of $B_z = 453 \text{ G}$ lifts the degeneracy between the $|\pm 1\rangle$ states as usual, but further allows initialization into the $|m_s = 0, m_I = 1\rangle$ state as shown in Section 2.1.2. The Hamiltonian H_R contains all remaining terms originating from the environment of the NV, e.g., ^{13}C spins and other nitrogen impurities, including their coupling to the electron spin, but may also be seen as an effective Hamiltonian responsible for experimental imperfections [171, 181]. Couplings

between the ^{13}C spins to ^{14}N spins are neglected, since their dipolar coupling strength is about $0.63 \text{ Hz}(\text{nm}/d)^3$, where d is their separation in nm. Hence their interaction will not appear on the microsecond timescale observed in the following.¹ We apply the secular approximation due to the large zero field splitting $\Delta \gg A_{\perp} \approx 2\pi \cdot 2.70 \text{ MHz}$ [101], which prohibits flips of the ^{14}N spin and also removes all terms in H_R not coupling to S_z [181] (ensuring that $[S_z, H_R] = 0$). Because all free energy terms commute with the remaining interaction Hamiltonian $S_z A_{\parallel} I_z$, these terms can be removed in a rotating frame yielding

$$H = S_z A_{\parallel} I_z + H_R. \quad (9.9)$$

We employ the electron spin as a noise sensor for the environment choosing the subspace spanned by the $|0\rangle$ and $|-1\rangle$ state as an artificial qubit. Because of the pure dephasing Hamiltonian, the reduced density matrix of the electron spin only experiences a modulation of the coherence elements. Hence, the FID is efficiently measured by a Ramsey experiment, whose scheme is sketched in Figure 9.1 (a). The electron spin preparation and readout is achieved optically, utilizing the mechanisms presented in Chapter 3. A wire spanned over the diamond surface is used to realize coherent manipulations of the electron spin transition (microwave) or nitrogen spin transitions (radio-frequency).² At the chosen strength of the magnetic field, the nitrogen nuclear spin is polarized in the $|m_I = 1\rangle$ state by optical pumping [168] and it can be rotated by a radio frequency pulse $R(\phi)$ to a desired state $\rho^{(N)}$. It is not a crucial requirement that this state is coherent. We will examine the role of the ^{14}N spin in more detail in Section 9.2.1.

After polarization, a $\pi/2$ pulse flips the electron spin to the superposition state $|\psi\rangle = (|0\rangle + |-1\rangle)/\sqrt{2}$. For a time t the system will evolve freely, depending on the electron spin state as depicted in Figure 9.1 (b), i.e. according to the conditional Hamiltonian $H_i = \langle i| H |i\rangle$. Assuming an initial product state, $\rho = \rho^{(e)} \otimes \rho^{(N)} \otimes \rho^{(R)}$, with $\rho^{(e)} = |\psi\rangle\langle\psi|$ and $\rho^{(R)}$ arbitrary, the dynamic of the electron spin is completely described by the coherence modulation, i.e.

$$\rho_{0,-1}^{(e)}(t) = \langle 0| \text{tr}_{N,R} [\rho(t)] |-1\rangle \propto \text{tr}_{N,R} \left[e^{-itH_0} \rho^{(N)} \otimes \rho^{(R)} e^{itH_{-1}} \right], \quad (9.10)$$

where $\text{tr}_{N,R}[\bullet]$ denotes the partial trace over the nitrogen and the bath degrees of freedom. Assuming no residual population left in $|1\rangle$, the length of the Bloch vector associated with the

¹Note that a similar argument would hold for a bath of electron spins, e.g., emerging from P_1 centers. Their coupling to the nitrogen spin of the NV is around $5 \text{ kHz}(\text{nm}/d)^3$ and therefore becomes important on the microsecond timescale.

²The corresponding Hamiltonians are suppressed in Eq. (9.8) as they are only utilized for preparation and readout and therefore are not part of the dynamics of interest.

qubit in the $\{|0\rangle, |-1\rangle\}$ subspace is equivalent to the coherence. This length can directly be calculated as

$$\begin{aligned} r(t) &= \sqrt{\text{tr} [\sigma_{(e)}^x \rho_{0,-1}^{(e)}(t)]^2 + \text{tr} [\sigma_{(e)}^y \rho_{0,-1}^{(e)}(t)]^2} \\ &= |L(t)| \sqrt{p_0^2 + p_1^2 + p_{-1}^2 + 2p_0(p_1 + p_{-1}) \cos(A_{\parallel} t) + 2p_1 p_{-1} \cos(2A_{\parallel} t)}, \end{aligned} \quad (9.11)$$

where $L(t) = \text{tr} [e^{-it\langle 0|H_R|0\rangle} \rho^{(R)} e^{it\langle -1|H_R|-1\rangle}]$ and p_i is the initial population in the state $|m_I = i\rangle$ of the nitrogen spin, while $\sigma_{(e)}^{\mu}$, $\mu = x, y$ are the Pauli operators in the $\{|0\rangle, |-1\rangle\}$ subspace of the electron spin. Using the normalization constraint $p_1 + p_{-1} + p_0 = 1$, we parametrize $p_1 = p \cos^2(\phi/2)$, $p_0 = p \sin^2(\phi/2)$ and $p_{-1} = 1 - p$ where ϕ is a mixing angle and p the amount of population in the desired subspace of $|m_I = 0, 1\rangle$. For the readout, the electron spin is rotated back to the z-axis (either around x or y , such that the respective component of the Bloch vector is measured) and after a subsequent readout pulse the fluorescence light is recorded proportional to $r(t)$. During the measurement, we refocus the position of the NV center every 40 seconds to overcome drifts in the optical setup. A precise measurement of the microwave transition frequency of the electron spin every 300 seconds ensures the elimination of possible transition frequency detunings during the experiment.

The detailed calculation of $L(t)$ quickly becomes tedious, as it requires explicit knowledge about the Hamiltonian H_R . On timescales well below the T_1 relaxation time of the population decay, the pure dephasing dynamics assumed above has been verified by a wide range of experiments [181] and analytic calculations [175]. We stress again, that this is a consequence of the large zero field splitting Δ . One of the main contributions to H_R are impurities in the diamond sample like the ^{13}C spins. Furthermore, H_R can contain effects originating from the surface of the diamond probe, which have been examined by noise spectroscopy in [171] showing that it is sufficient to consider a model only inducing dephasing noise. At last, the mentioned drifts in the optical setup or temperature fluctuations during the experiment time slightly shift the resonance line of the electron spin. While being reduced by repeated refocusing steps during the data collection, this effect leads to random phase fluctuations between repetitions of the same experimental runs which ultimately results in an effective decoherence process when averaging over the experimental data (see also the definition of the T_2^* time in Section 2.1.1). While the noise originating from impurities could be written explicitly in the case the exact couplings would be known [see Chapter 2.2, in particular the last three terms in Eq. (2.7)], due to their large number it is justified to model their effect by a magnetic field randomly fluctuating in amplitude according to a classical Gaussian process [174, 214, 299], that we have also considered in Section 3.1. The effect of the surface and the experimental subtleties can

also be included into the statistics of the process.

Indeed, taking all these effects into account results in a challenging estimation of $L(t)$. However, it can often be modeled effectively as an exponential function $L(t) = \exp \left[- \left(t/T_2^* \right)^n \right]$, where $n = 1$ for ensemble measurements and $n = 2$ for single realizations [175].

To measure the degree of non-Markovianity in the system, we recall Section 1.4.1 where we introduced the trace distance as a suitable quantification. In particular, the example of a pure dephasing qubit dynamics fits exactly to the model introduced here. Therefore, we measure the non-Markovianity using Eq. (1.35), i.e.,

$$\mathcal{N} = \sum_m r(\tau'_m) - r(\tau_m),$$

where $r(t)$ is now given by Eq. (9.11) and the sum collects all intervals (τ_m, τ'_m) with $r(\tau'_m) - r(\tau_m) > 0$.

9.2.1. The Role of Correlations and a non-Markovian Evolution

In case of a noiseless evolution and perfect pulses, the evolution of the total system of electron and nitrogen spin can be exemplified as follows. The state after application of the radio frequency pulse on the ^{14}N spin is given by

$$|\psi_0\rangle = \frac{|0\rangle + |-1\rangle}{\sqrt{2}} \otimes |\phi_0\rangle, \quad (9.12)$$

where $|\phi_0\rangle = \sin \frac{\phi}{2} |m_I = 0\rangle + \cos \frac{\phi}{2} |m_I = 1\rangle,$

and we kept the parametrization of the nitrogen spin state as in the previous section. During the evolution governed by the Hamiltonian in Eq. (9.9), we have the state

$$|\psi(t)\rangle = \frac{|0\rangle \otimes |\phi_0\rangle + |-1\rangle \otimes |\phi(t)\rangle}{\sqrt{2}}, \quad (9.13)$$

where $|\phi(t)\rangle = \sin \frac{\phi}{2} |m_I = 0\rangle + \cos \frac{\phi}{2} e^{itA_{\parallel}} |m_I = 1\rangle.$

The state $|\psi(t)\rangle$ may represent an entangled state between the electron and nitrogen spin. Hence, correlations have built up between the two subsystems, which are responsible for the coherence oscillations of the reduced electron spin state, see also Figure 9.2.1. For $\langle \phi(t) | \phi_0 \rangle = 0$, we even obtain a Bell-state and the coherence of the electron spin after tracing vanishes completely. We plot the overlap of the states $|\phi_0\rangle$ and $|\phi(t)\rangle$ in Figure 9.2 (a) and the length of the electron

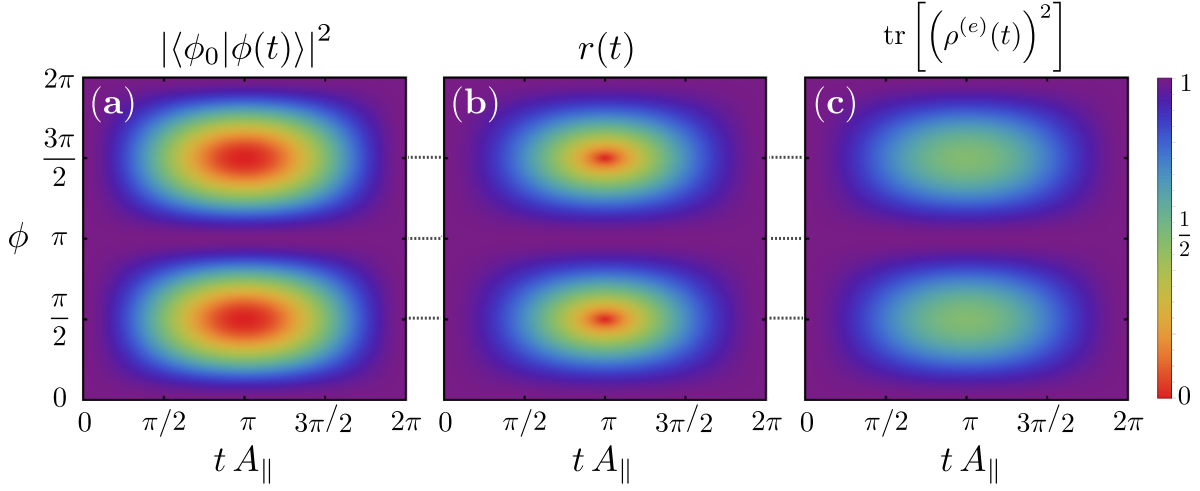


Figure 9.2.: **Connection of the entanglement, Bloch vector length and purity.** In (a) the overlap of the states $|\phi_0\rangle$ and $|\phi(t)\rangle$ is plotted. Clearly, at points where these are orthogonal the length of the Bloch vector in (b) is zero, hence the total state represents a Bell state. As a consequence, the purity of the electron spin in (c) shows its minimal value at these points, indicating that the state is maximally mixed. Subsequently, when $t A_{||}$ progresses, the ^{14}N nuclear and the NV electron spin get decorrelated which results in an increasing coherence and purity.

spin's Bloch vector in Figure 9.2 (c), where the connection between the electron spin coherence and the overlap of the ^{14}N spin states is clearly observable. After a minimum (red area), the overlap increases and the state $|\psi(t)\rangle$ becomes separable again. Note that this situation is also shown in explicitly in Figure 9.1 (c). Furthermore, performing the partial trace over the nitrogen degrees of freedom yields the reduced state of the electron spin

$$\rho^{(e)}(t) = \frac{1}{2} (|0\rangle\langle 0| + |-1\rangle\langle -1|) + \frac{1}{2} \left[\left(\sin^2 \frac{\phi}{2} + \cos^2 \frac{\phi}{2} e^{itA_{||}} \right) |-1\rangle\langle 0| + \text{h.c.} \right]. \quad (9.14)$$

From here, we calculate the purity of the state as shown in Figure 9.2, which, as expected, shows the same behavior as the length of the Bloch vector. Hence, this case clearly illustrates the connection between the entanglement of the two spin qubits, the coherence of the electron spin and the purity of the latter.

Importantly, the reduced state of the electronic spin, Eq. (9.14) is independent of coherences in the nitrogen spin. In particular, the same reduced electronic state is obtained, whatever mixing of the nitrogen is assumed. Following the reasoning in Section 7.3, the state of the electron spin

during the free evolution can be written as

$$\rho^{(e)}(t) = \frac{1}{2} (|0\rangle\langle 0| + |-1\rangle\langle -1|) + \frac{1}{2} \left[\text{tr}_N \left[e^{-itA_{\parallel}I_z} \rho^{(N)} \right] |-1\rangle\langle 0| + \text{H.c.} \right], \quad (9.15)$$

where the coherences of the nitrogen spin state are irrelevant. For example, we may have

$$\rho^{(N)} = \sin^2\left(\frac{\phi}{2}\right) |m_I = 0\rangle\langle m_I = 0| + \cos^2\left(\frac{\phi}{2}\right) |m_I = 1\rangle\langle m_I = 1|. \quad (9.16)$$

After performing the trace, this yields exactly Eq. (9.14). Therefore, the nature of the correlations between the two spins it is not as important since they cannot be distinguished by a measurement on the electron spin only.

9.3. Measuring the Free Induction Decay

In a preliminary experiment we explore the agreement of the FID envelope induced by H_R with a monotonic decay to exclude contributions to a non-Markovian evolution. Therefore, polarization of the ^{14}N spin is performed such that $p_0 = 1$, and $R(\phi) \equiv \mathbb{1}$. This enables a measurement of $|L(t)|$, see Eq. (9.11). Figure 9.3 shows the FID envelope in terms of the collected photoluminescence (PL). We model the observed likelihood distribution by a normal distribution with a mean $\mu = r(t) \exp(-c_0) + d$ and $|L(t)| = \exp\left(-\sum_{i=1}^5 a_i t^i\right)$. For a detailed description of the modeling, see also Section 9.3.1 below. Here, c_0 is a constant to normalize the measured contrast and d a possible bias in the asymptotic regime. After 50000 iterations of the chosen sampling algorithm (see the introduction to Bayesian estimation in Section 9.1), we plot the red curve using the medians of the sampled parameters and the marginals of the posterior distribution for all a_i in the insets. The experimentally measured contrast at specific times is shown with black dots. The FID envelope is well characterized by $L(t) = \exp\left[-\left(t/T_2^*\right)^2\right]$, i.e., the dynamic is fully (time-inhomogeneous) Markovian. Crucially, note that non-Markovian characteristics can only appear if at least one of the a_i is negative, i.e., the polynomial $\sum_{i=1}^5 a_i t^i$ is decreasing at some arbitrary time. We extract the characteristic timescale from the marginal of a_2 (we take the median as the point estimate and denote it by $\bar{\bullet}$) and obtain $T_2^* = 22.262 \mu\text{s}$ where the 95% high posterior density interval (HPD) (i.e. 95% of sampling values lie in that region) is $[21.878, 22.868] \mu\text{s}$. Coherence envelopes of this form are extremely useful for frequency estimation using entangled states, since the Gaussian decay ensures a super-classical scaling of the estimation error with the number of probes [37, 39, H3], see also Section 4.4.1. A careful examination of the short time regime reveals oscillations in the FID curve (see inset

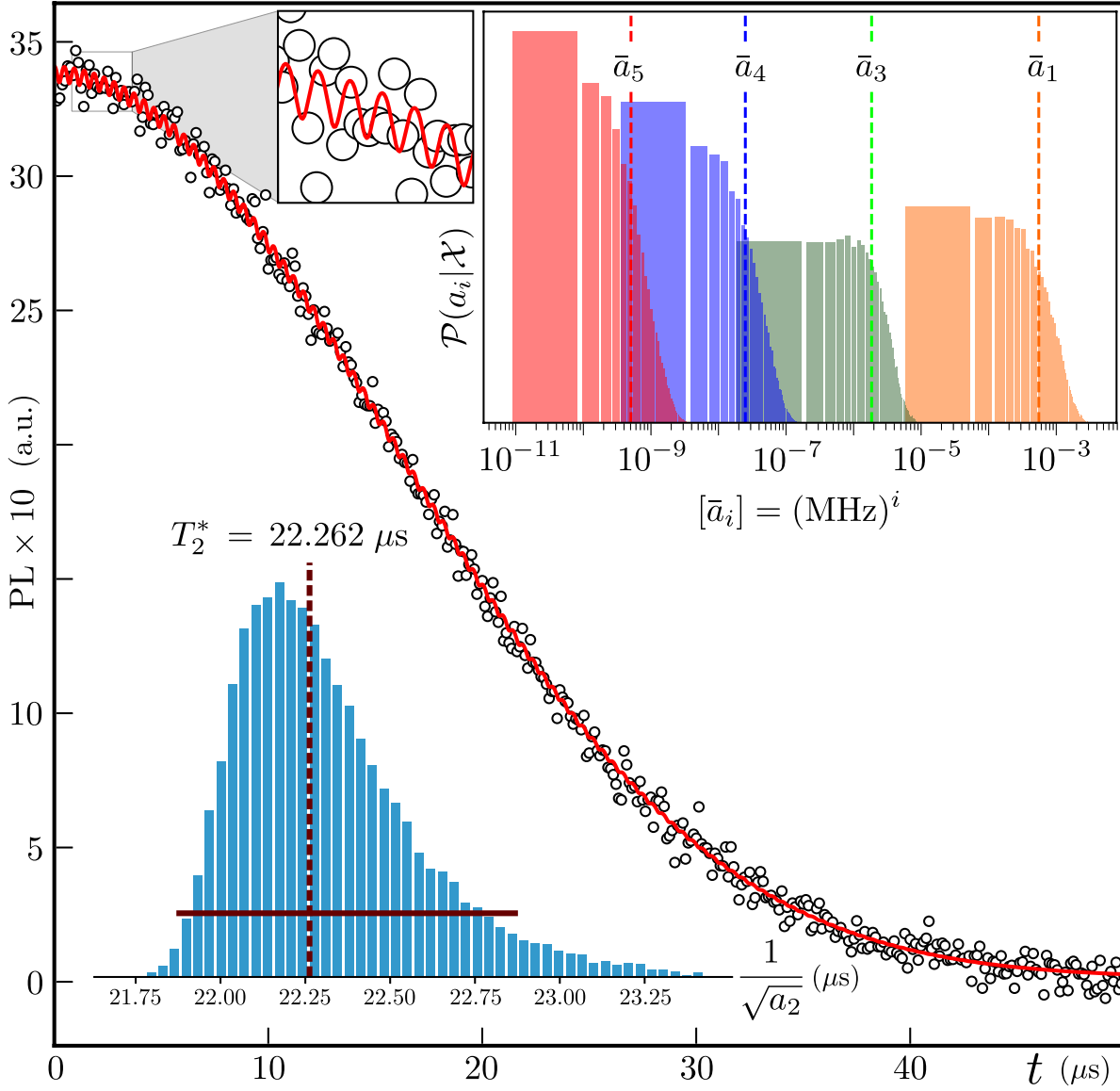


Figure 9.3.: **FID of curve of the NV center in units of the measured photoluminescence (PL).** The negligible values of the decay constants \bar{a}_i in the top right histogram of sampled values supports the purely Gaussian shape of $L(t)$. The histogram in the lower left assembles the distribution for T_2^* with the HPD interval marked by the horizontal line. From the initial oscillations at short times, the Bayesian method can extract also other parameters (distributions not shown), as $p = 0.972$ with HPD $[0.943, 1]$, $\phi = 0.191$ with HPD $[0.151, 0.227]$ and $A_{\parallel} = 2\pi \cdot 2.143 \text{ MHz}$ where HPD $2\pi \cdot [2.137, 2.148] \text{ MHz}$. (Reprinted figure with permission from [H5]. Copyright (2018) by the American Physical Society.)

in Figure 9.3), suggesting that the nitrogen spin is not fully polarized, as confirmed by the Bayesian method exploiting Eq. (9.11) of our model. The procedure is able to extract the

different contributions to the decay stemming from the bath, which are collected $L(t)$, but also the parameters describing the ^{14}N spin. For the latter, we obtain the coupling strength A_{\parallel} and the parameters ϕ, p (values see Figure 9.3) for the population distribution, up to the symmetry in $|m_I = \pm 1\rangle$ which is not resolvable in such experiment, see Eq. (9.11).

9.3.1. Bayesian Modeling of Free Induction Decay

Recall the expression for the length of the Bloch vector, Eq. (9.11), where our assumption for $L(t)$ is of the form

$$L(t) = e^{-\sum_{i=1}^5 a_i t^i}. \quad (9.17)$$

As a first step, we define the parameters to be inferred. We remind ourselves that due to the normalization of the probabilities, we have the parametrization $p_1 = p \cos^2(\phi/2)$, $p_0 = p \sin^2(\phi/2)$ and $p_{-1} = 1 - p$. Therefore, we define the parameters $\theta = (\{a_i\}, \phi, p, A_{\parallel}, d, c_0, \sigma)$. We are looking for the coefficients $\{a_i\}$ fixing the FID envelope, the populations of the nitrogen spin, the parallel coupling constant A_{\parallel} and the asymptotic bias of the readout contrast d . The parameter c_0 represents the normalization constant of the measured PL. To account for further errors, we define σ as the standard deviation of the measurements in the experiment. Each data point j of the FID envelope in Figure 9.3 is uniquely determined by its time t_j and its value, let us call it x_j . We construct the likelihood function in the following way, also sketched in Figure 9.4 (a). Each value x_j of the corresponding random variable in $\mathcal{X} = (X_1, \dots, X_n)$ is assumed to be a draw from a normal distribution with variance σ^2 and an expectation value $\mu(t_j) = [r(t_j) - c_0 + d]_{\theta}$, i.e. we have

$$\mathcal{P}(\mathcal{X}|\theta) \propto \exp \left\{ -\frac{[\mathcal{X} - \mu(T)|_{\theta}]^2}{2\sigma^2} \right\} \quad (9.18)$$

where we use the vector of measurement times $T = (t_1, \dots, t_n)$. Prior distributions for the parameters θ are also assumed either to be normal distributions around their expected value, e.g., $A_{\parallel} \sim N(2\pi \cdot 2.14 \text{ MHz}, \sigma_{A_{\parallel}})$, or a positive half normal distribution, since c_0 and all $a_i \geq 0$. Note that the origin of σ is not explicitly specified, but it is an inherent quantity of the model. As mentioned above, it accounts for error sources not explicitly specified in the model. On the other hand, an unnaturally large σ may also indicate a falsely specified model.

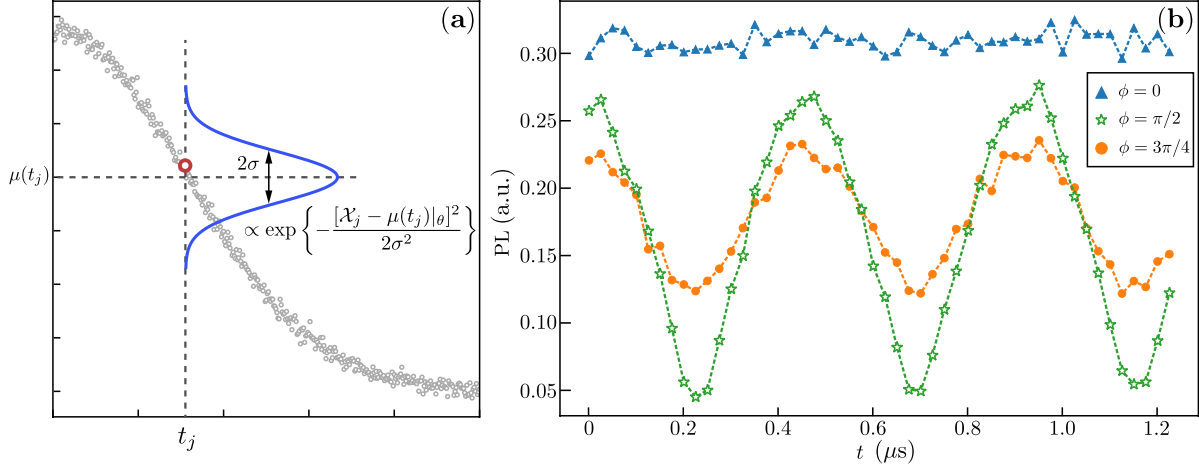


Figure 9.4.: **Sketch of the Bayesian FID modeling and oscillations in the length of the electron spin's Bloch vector.** (a) - Each measurement result, like the one marked in red is assumed to be the result of a random draw with the probability distribution sketched in blue. (b) - The curves show oscillations in the Bloch vector length for three initial preparations of the nitrogen spin. Note the difference in amplitude and offset but equality in frequency and phase. The curve for $\phi = 0$ (blue triangles) is supposed to show no oscillations theoretically, but of course it is influenced in practice by fluctuations in the measurement. (Reprinted figure with permission from [H5]. Copyright (2018) by the American Physical Society.)

9.4. Tuning the Non-Markovianity

An imperfectly polarized ^{14}N spin, i.e., a coherent or incoherent mixture of I_z eigenstates, induces oscillations of the electron spin coherence (see Figure 9.3 and Section 9.2.1). Consequently the reduced electron spin state undergoes a non-Markovian evolution. Vice versa, any population of the ^{14}N spin state undergoes the conditional evolution governed by the Hamiltonian (9.9). At the point of maximal achievable correlations [Figure 9.1 (b), bottom], the reduced state of the electron spin has reached its point of minimal coherence. Following is an increase in coherence corresponding to a reduction of correlations between the two spins. For an incoherent mixture of the nitrogen spin, the correlation would be classical. However, the induced effect on the reduced state of the electron spin would be the same as it is discussed in Section 9.2.1. Consequently, changing the orientation of the polarization of the nitrogen spin allows to control the non-Markovianity of the electron spin in a continuous manner.

In order to measure experimentally the amount of non-Markovianity, we follow again the Ramsey scheme, Figure 9.1 (a). Subsequently to the polarization, the nitrogen spin population

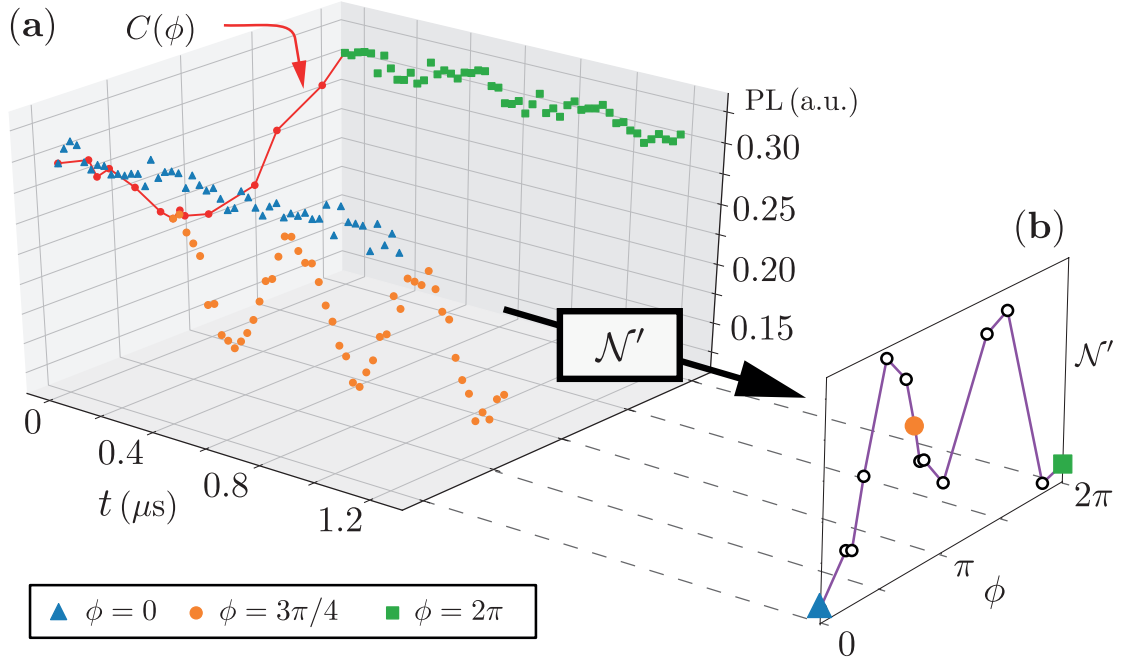


Figure 9.5.: **Illustration of the collected data and the connection to the non-Markovianity measure.** For the sale of visibility in plot (a), we only show 3 exemplary data sets of the total 14 which have been collected. The angle of each set collected for the analysis is shown via a red dot at $t = 0$, which also illustrates the measurement contrast depending on the polarization direction of the nitrogen spin. All curves have two full revivals at the same position as the one for $\phi = 3\pi/4$ (orange dots). From this data, one can compute the modified measure of non-Markovianity \mathcal{N}' which results in panel (b). Each curve for a single instance of ϕ results in a single point of \mathcal{N}' (compare also the next Figure 9.6). (Reprinted figure with permission from [H5]. Copyright (2018) by the American Physical Society.)

can be manipulated coherently by a resonant radio-frequency pulse $R(\phi)$ to create the nuclear spin state $|\psi_I\rangle = \sin(\phi/2)|m_I = 0\rangle + \cos(\phi/2)|m_I = 1\rangle$. The corresponding pulse length is previously determined by a Rabi measurement between the two spin states ($|m_I = -1\rangle$ is not used in this work). Since observed shifts of the electronic transition (microwave-)frequency do not exceed $\sim 2\pi \cdot 10$ kHz, the transition (radio-)frequency between the nitrogen nuclear spin states is assumed to be constant due to the smaller gyromagnetic ratio.³ Hence, it is not refocused during the measurement. We track the evolution of the electron spin for 14 different values of ϕ up to a maximum time of $T = 1.226 \mu\text{s}$ and record the oscillations in the coherence, where some examples are shown in Figure 9.4 (b) and Figure 9.5 (a). The fluorescence signal

³The shifts in the transition frequencies are mainly due to drifts in the applied magnetic field, hence the induced detunings are proportional to the individual gyromagnetic ratio.

corresponds to the absolute value of the Bloch vector length⁴, which changes due to continuous correlation and decorrelation of the electron spin and nitrogen nuclear spin. Furthermore, due to the pure diamond sample and the short evolution time, we may regard the evolution as essentially decoherence free, since for the coherence time determined by the FID measurements we have $L(T) = \exp[-(T/T_2^*)^2] \approx 1$.

Let us now briefly describe the probabilistic model for this specific setup, while the following Section 9.4.1 contains a detailed description of the modeling. First, note that a theoretical measure of non-Markovianity as defined in Eq. (1.35) requires post-processed data, e.g., fits. Otherwise, fluctuations will dominate the measure, e.g., for a constant coherence function fluctuations of the measurement results accumulate and give a positive measure. For example, observe the blue curve in Figure 9.4 (b) corresponding to $\phi = 0$. Here, fluctuations would introduce non-Markovianity artificially, while according to Eq. (9.11) a vanishing measure of non-Markovianity is expected. To avoid this issue, we exploit the oscillatory nature of the modulation and stop the recording of the oscillation before finishing an integer number of periods, i.e., for a time that is not an integer multiple of $2\pi/A_{\parallel}$. The requirement for an increase of the coherence in Eq. (1.35) is then relaxed and the sum runs over all intervals, such that the fluctuations in the data are averaged out, resulting in a measurement proportional to the oscillation amplitude. The model for the measure then possesses the simple form $\mathcal{N}'(\phi) = C(\phi)\{r[\phi, p(\phi), T] - 1\}$ where $C(\phi)$ is a parameter describing the variable measurement contrast [182] outlined in Section 2.1.2 and $1 - p(\phi)$ the population left in $|m_I = -1\rangle$. The modeling of these functions will be given in the next section via Eq. (9.20) and Eq. (9.21), respectively. However, Figure 9.5 illustrates the connection between the measured coherence oscillations, the observed values of $\mathcal{N}'(\phi)$ and the contrast $C(\phi)$.

We infer the model on the measured data to obtain the information of these functional dependencies along the lines of the scheme laid out in the upper part of Figure 9.6. As shown in Figure 9.5, the Ramsey measurements are used to evaluate $\mathcal{N}'(\phi)$. Crucially, all of these data sets are interpreted as observations and fed into the likelihood distribution, which we construct in detail in Section 9.4.1. However, as before, the expectation values are determined according to the theoretical models of $\mathcal{N}'(\phi)$ and $r(\phi, t)$, while the prior distributions are taken as normal distributions around physically reasonable values (see Section 9.4.2). Afterwards, the obtained posterior distribution and the corresponding HPD parameter set $\bar{\Theta}$ are used to predict $\mathcal{N}'(\phi)$ for different values of ϕ by drawing multiple samples of possible parameter sets Θ from the posterior distribution $\mathcal{P}(\Theta|\mathcal{X})$, where \mathcal{X} is now associated with the measured Data.

⁴As mentioned above, the second $\pi/2$ -pulse is either performed along the \hat{x} or the \hat{y} axis, giving the respective components of the Bloch vector. From these values the length of the vector can be calculated.

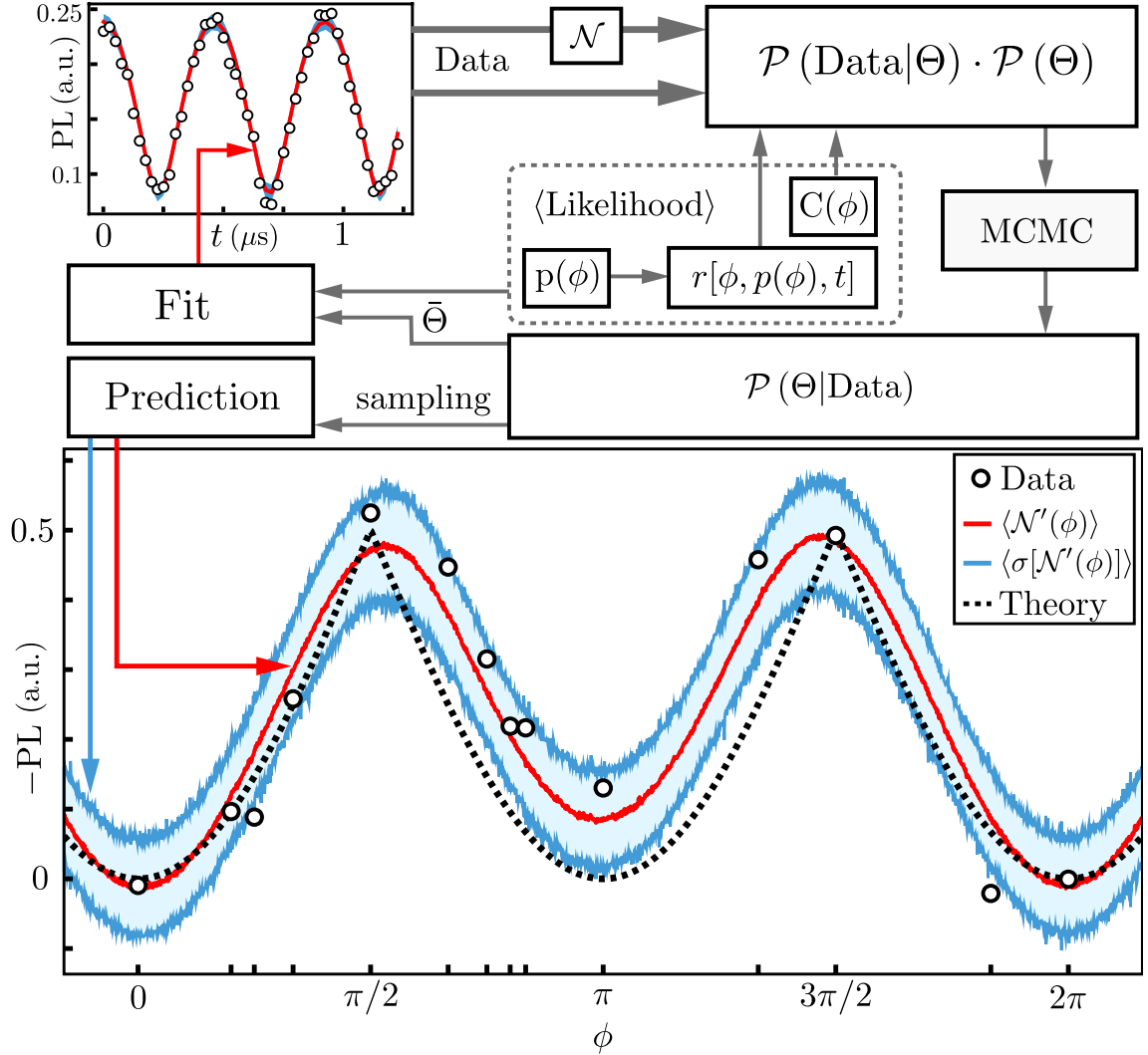


Figure 9.6.: **Scheme and Results of the Bayesian analysis for the measure of non-Markovianity.** Ramsey measurements are performed for different values of ϕ (top left, only $\phi = 2\pi/3$ is shown, black circles) and the non-Markovianity measure \mathcal{N}' (lower plot, black circles) is evaluated, which are both fed as observations into the likelihood distribution. The expectation value of the likelihood is constructed according to \mathcal{N}' , while the prior distributions are taken as normal distributions. The HPD parameter set $\bar{\Theta}$ can be plugged into the model defining the likelihood, which results in the maximum a posteriori inference (red curve) to the Ramsey data. The posterior distribution is sampled for different and, crucially, not measured values of ϕ . This results in an expectation value $\langle \mathcal{N}' \rangle$ which is taken with respect to the posterior, shown as the red curve in the lower plot along with the blue region marking the standard deviation. The black dotted line corresponds to the theory result neglecting the varying readout contrast and remaining population in $|m_I = -1\rangle$. (Reprinted figure with permission from [H5]. Copyright (2018) by the American Physical Society.)

The theoretical and experimental results are reported in Figure 9.6. In the lower part, black dots mark $\mathcal{N}'(\phi)$ for the 14 measured instances of ϕ . The theory curve according to Eq. (1.35) in black (dotted) is rescaled to match the values of the contrast. Its deviation from the red curve, which illustrates the expectation value of $\mathcal{N}'(\phi)$ sampled with respect to the posterior distribution, is due to the fact that the Bayesian model includes the angle dependent contrast and the nitrogen population left in $|m_I = -1\rangle$. In other words, the posterior distribution predictions of our parameters, together with the model in Eq.(9.11) enable us to estimate further measurement outcomes of the experiment. We show the standard deviation of the sampling as the blue region, which covers most of the actual measurements. This standard deviation is due to error sources not included explicitly in the model, e.g., remaining population of the electron spin in $|m_s = 1\rangle$ or drifts in the experimental setup.

9.4.1. Bayesian Inference Model for Tuneable non-Markovianity

Analogously to Section 9.3.1, let us illustrate the model employed for the inference of the parameters describing the non-Markovian dynamics of the NV center. Given the pure dephasing dynamics of the electron spin, it is enough to monitor its modulated coherence evolution as outlined in Section 9.2. To demonstrate controllable non-Markovianity, we monitored the length of the Bloch vector for 14 different initial preparations of the nitrogen spin, i.e., different values for ϕ determining the pulse length of the radio frequency field in Figure 9.1 (a). In the following, we want to illustrate the construction of the model used for the Bayesian inference.

1. We aim to describe the whole collected data by a common function, i.e., a model which gives the value of the coherence depending on the given point in time and the rotation angle of the nitrogen spin. The Bloch vector is still described by Eq. (9.11). Since we parametrized the population of the nitrogen spin in terms of ϕ and p , we have

$$r(t, \phi) = \left\{ 2(1 - p)p \cos(2A_{\parallel}t) \cos^2\left(\frac{\phi}{2}\right) + \frac{4 - p(8 - 7p) + p^2 \cos(2\phi)}{4} + p \cos(A_{\parallel}t)[2 - p + p \cos(\phi)] \sin^2\left(\frac{\phi}{2}\right) \right\}^{\frac{1}{2}}. \quad (9.19)$$

Since the final time of the free evolution was chosen as $t \leq T = 1.226 \mu\text{s}$, we assume $L(T) \approx L(0) \approx 1$ because of the long coherence time provided by the low ^{13}C concentration.

2. Three of the 14 data sets are shown in Figure 9.5 (a). The red curve at $t = 0$ (red circles mark the position of other data sets) illustrate the dependence of the readout contrast

on ϕ . See Section 2.1.2 for an explanation of this effect. To take this dependence into account, we model the contrast via

$$C(\phi) = C_a \cos(C_\nu \phi) + C_b, \quad (9.20)$$

where C_β are unknown constants to model amplitude (a), frequency (ν) and offset (b) of the modulation. Each of these is chosen as normally distributed.

3. Analogously to the contrast, we need to parametrize p in terms of ϕ . This is less straight forward, however a suitable parametrization can be found by mimicking Rabi oscillations found in driven three level systems in a ladder configuration, i.e., the dynamics governed by the Hamiltonian in (2.11) where the driving term is off-resonant to the desired transition. We assume

$$p(\phi) = 1 - \left[p_b + p_a \sin(p_\nu \phi + p_\varphi) \right]. \quad (9.21)$$

4. Next, we need to define the measure of non-Markovianity. Note the fluctuations for $\phi = 0$ (blue triangles) and $\phi = 2\pi$ (green squares) in Figure 9.5. Ideally, these measurements would correspond to a constant which results in a zero value of the non-Markovianity measure. However, equally distributed fluctuations will be eliminated when we sum over all differences instead of only the positive ones. This results in the definition of the measure \mathcal{N}' . Calculating the measure analytically, we arrive at

$$\begin{aligned} \mathcal{N}'(\phi) &= C(\phi) \sum_{i=1}^{n-1} \left[r(t_{i+1}, \phi)|_{p=p(\phi)} - r(t_i, \phi)|_{p=p(\phi)} \right] \\ &= C(\phi) \left[r(T, \phi)|_{p=p(\phi)} - 1 \right], \end{aligned} \quad (9.22)$$

which was already given in the previous section. The result for the measured data sets is also shown in Figure 9.5 (b). Note that we always have $r(T, \phi) \leq 1$ leading always to $\mathcal{N}'(\phi) \leq 0$. However, because of the periodicity of $r(t, \phi)$ in time is fixed by A_{\parallel} for all angles ϕ , this does not change the meaningfulness of the measure. In particular, because the induced oscillation has the same frequency for all ϕ and at $t = T$ all trajectories of $r(t, \phi)$ are in phase, the amplitude of the oscillation is sufficient to quantify the non-Markovianity of the evolution.

5. The Bayesian inference model for the measure of non-Markovianity possesses a parallel structure. Crucially, our inferred parameters need to be fitted to the modulations of the

coherence, while they are at the same time required to describe the measure of non-Markovianity. That is, we have the parameters $\theta = (\{C_\beta\}, \{p_\alpha\}, A_{||})$ which need to hold for all observed coherence data X . However, we distinguish between the angle labels for the coherence ϕ and the non-Markovianity measure ϕ_N for clarity. We rewrite Bayes theorem as

$$\begin{aligned} \mathcal{P}(\theta, \sigma, \sigma_N | X) &\propto \mathcal{P}(X | \theta, \sigma, \sigma_N) \mathcal{P}(\theta, \sigma, \sigma_N) \\ &= \mathcal{P}_r(X_\phi | \theta, \sigma) \mathcal{P}_N(X_{\phi_N} | \theta, \sigma_N) \\ &\times \mathcal{P}(\theta) \mathcal{P}(\sigma) \mathcal{P}(\sigma_N), \end{aligned} \quad (9.23)$$

where we could split the likelihood function, since these variables are conditionally independent⁵ in our probability model and mutually just depend on deterministically collected data. By σ (σ_N) we mark the standard deviation of the normal distribution used to model the likelihood function \mathcal{P}_r (\mathcal{P}_N). These distributions have the expectation values $r(t, \phi)|_{p(\phi)}$ and $\mathcal{N}'(\phi_N)$ respectively [compare also Eq. (9.18)].

6. We formulate the posterior predictive distribution according to Eq. (9.7).

At last, let us formulate the following remark. The model presented here may appear to be too complicated. Obviously, as soon as the parameters $\theta = (\{C_\beta\}, \{p_\alpha\}, A_{||})$ have been inferred, the maximum posteriori inference curve $r(t, \phi)|_{p(\phi)}$ is known. Consequently, one can calculate $\mathcal{N}(\phi)$ on the whole parameter range of ϕ and t . Moreover, employing the parameters determined during the FID decay in Section 9.3.1 enables the calculation of the non-Markovianity even for evolution times greater than $T = 1.226 \mu\text{s}$. However, this would entail the calculation of an involved error propagation for all parameters involved. The circumnavigation of such aspects is the beauty of Bayesian inference, the errors are inherent to the model and manifest in the finite width of the obtained posterior distribution, together with explicit parameters modeling noise sources which are not taken into account explicitly in the model. Here, this role is played by the widths σ .

⁵Two events A and B conditioned on Y are conditional independent if $\mathcal{P}(A \cap B | Y) = \mathcal{P}(A | Y) \mathcal{P}(B | Y)$.

9.4.2. Details of the Obtained Posterior Distribution

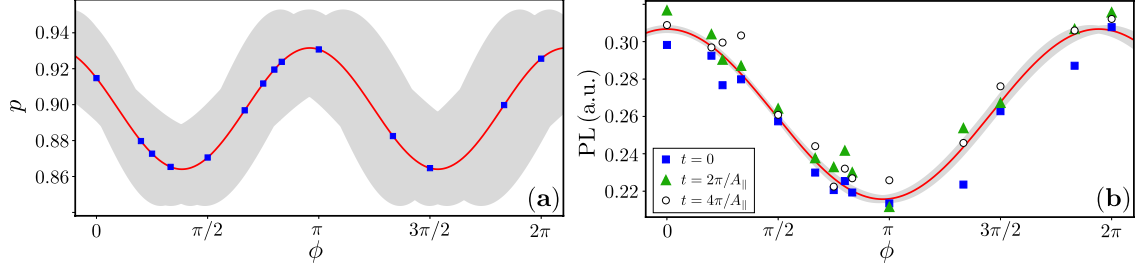


Figure 9.7.: **Resulting models with parameters inferred by the Bayesian analysis.** In (a) we plot the maximum posterior value (red curve) for the nitrogen population in the subspace $|m_I = 0, 1\rangle$. The HPD interval is marked by the grey area and the blue squares indicate angles for which we measured the length of the Bloch vector. We emphasize that the blue squares do not represent a measured value of the population. However, in (b) we are able to compare our modeling of the contrast (red curve) with the contrast directly after initialization (blue squares) and the first two full revivals (green triangles, black circles). The HPD interval is set by the grey area. (Reprinted figure with permission from [H5]. Copyright (2018) by the American Physical Society.)

We infer the posterior distribution for the model of the non-Markovianity measure as introduced above. The results are summarized in the following Table 9.1, where the first two columns specify the properties of the prior normal distribution and the second two columns the point estimate (median of the marginal) and the HPD interval.

Table 9.1.: **Parameters of the Bayesian Inference for the non-Markovianity measure.**

	μ	σ	point estimate	HPD
C_a	1	0.1	0.046	[0.044, 0.047]
C_v	0.3	0.1	1.030	[1.011, 1.050]
C_b	1	0.1	0.261	[0.260, 0.262]
p_a	0.02	0.01	0.034	[0.023, 0.044]
p_v	1.5	0.1	1.738	[1.611, 1.858]
p_b	0.02	0.01	0.102	[0.091, 0.112]
p_ϕ	0	0.3	-0.528	[-0.904, -0.134]
$A_{ } / (\text{rad}/\mu\text{s})$	4.2π	0.5	2π 2.169	2π [2.165, 2.173]
σ_N	0	1	0.060	[0.037, 0.096]

The value for the σ values describing the standard deviations of each coherence function is not

explicitly shown here, but the maximum posterior value for the largest of these is 0.018.

In Figure 9.7 we illustrate the dependence of the population $p(\phi)$ and the contrast $C(\phi)$ on the polarization direction of the nitrogen spin. The plot in panel (a) shows the amount of population in the desired subspace of $|m_I = 0, 1\rangle$. We remark again that the analytic solutions cannot distinguish between $|m_I = \pm 1\rangle$. We assign the finite offset from unity to an imperfect polarization (i.e. $< 100\%$) of the nitrogen before the radio-frequency pulse. At $\phi = 0$ we can get a hint of the efficiency of the polarization. The red curves shows the maximum posterior value $\bar{p}(0) = 0.915$, while the HPD interval (grey area) is fixed by $[0.891 \ 0.943]$. During the pulse, population leaks to the $|m_I = -1\rangle$ state due to a non-vanishing Rabi frequency between $|m_I = 0\rangle$ and $|m_I = -1\rangle$, which is leading to the shown curve.

The change of contrast is plotted in Figure 9.7 (b). Along with the inferred curve, we also plotted the coherence data at $t = 0$ [blue squares, corresponds to the red curve in Figure 9.5 (a)] and the first two full revivals (green triangles, black circles), i.e. $r(t_k, \phi) = 1$, which occur at

$$t_k = k \frac{2\pi}{A_{\parallel}}, \quad k \in \mathbb{N}. \quad (9.24)$$

These times correspond to a totally decorrelated product state (see Section 9.2.1), i.e., the state of the electron spin is equivalent at all these points. Therefore the contrast is only determined by the polarization direction of the nitrogen spin which enables the comparison with our modeling of the contrast without calculating the impact of correlations. We remark, that from this plot we can again confirm that the assumption of a decoherence free evolution, i.e., $L(t) \approx 1$, is justified. Otherwise, the coherence values of later times would strictly show less contrast than the ones at earlier times, which is not the case here. In particular, this is due to the long coherence time of the sample and the Gaussian shape of the envelope.

9.5. Conclusions

In this chapter, we experimentally demonstrated the control of the degree of non-Markovianity in the dynamics of an NV electron spin. To that end, we first developed the theory to model the origin of the coherence modulations induced by a continuous correlation and decorrelation process with the nitrogen spin. In a first step, we examined the FID envelope and employed a Bayesian probabilistic model to ensure that the degree of non-Markovianity induced by the residual noise background in the diamond host is actually zero. This background is mainly resulting from the nuclear spin environment of the NV center. Subsequently, we exploited the

inherent ^{14}N spin to induce modulations on the electron spin coherence. The ^{14}N provides us with a natural source of non-Markovianity, which, depending on its initial preparation, will be able to exchange a certain amount of information with the electron spin, influencing the evolution of the latter. Despite of the initial control the ^{14}N remains a natural source of non-Markovianity as no further interventions after the preparation have to be performed. The experimental effort for data collection is kept sufficiently low by using Bayesian techniques. These methods allow to predict the shape of the considered non-Markovianity measure, while also modeling the peculiarities that appear in the experimental realization.

Let us also mention that the scheme presented may be extended by the utilization of strongly coupled ^{13}C spins or interacting NV centers. Two NV centers located close enough are dipolar coupled to each other and evolve exactly under the same type of Hamiltonian, Eq. (9.9), as the coupled pair of electron and nitrogen spin in a single NV center. Surely, I_z has to be replaced by S_z of the second NV center's electron spin, while the coupling constant will also be different. In particular, this has been exploited to create entangled states between two NV centers [319]. However, we want to mention that the deterministic creation of such suitable pairs still represents a challenge [142], although it offers the possibility to achieve different modulation frequencies by varying the distance between the NV centers which affects the coupling constant. Hence, the construction of a network consisting of NV centers to explore non-Markovian evolutions, indeed represents a challenging but also promising approach to introduce further possibilities to control the induced dynamics.

Using the same technique as described here, additional parameters to shape the evolution can be introduced. Further modifications could be implemented as well via a classical driving with random, but temporally correlated amplitude.

In summary, the configuration investigated here allows the assembly of an experimental platform with intrinsic non-Markovianity. This provides a building block for the systematic investigation of memory effects in the performance of, e.g., quantum sensors and quantum metrology protocols, as well as facilitating the controllable inclusion of memory in quantum simulations of open quantum system dynamics.

Concluding Remarks - Outlook

This thesis provides novel ways to manipulate, explore and exploit systems evolving according to quantum dynamics. We proposed a technique, that employs a time dependent coupling between different constituents of a complex quantum system to remove off-resonant interactions. Moreover, a variable platform to test the impact of non-Markovian dynamics has been demonstrated, accompanied with an elaborate data analysis to reduce the necessary experimental effort. The thesis further contributes to the understanding of fundamental limits in frequency estimation employing entangled quantum probes. Throughout the whole work, a clear emphasis lies on the microscopic approach to derive, characterize and classify the obtained results.

The chapters 4 and 5 extensively discuss the role of entanglement in quantum metrology under the impact of noise. From a fundamental point of view, the ultimate scaling of the achievable precision in the number of probes employed is close to be settled. At least in the widely used parallel estimation scheme of identical probes, where all the fundamental limits have been presented in the thesis at hand and are summarized in Table 5.1. Eventually, the only remaining piece of theory to be fully addressed is a rigorous analytic proof for non-phase-covariant noise. For a detailed discussion of the issues going beyond this analysis we refer to Chapter 6, which already raises important questions and uncovers possible directions for future works. However, we highlight that these open questions mainly concern real world implementations. The available theory thins out when dealing with interacting probes and correlated noise. Crucially, the achievable precision in these settings can differ drastically from the one obtained for the parallel estimation scheme employing non-interacting probes and environments, but also provide new perspectives, such as decoherence-free subspaces [272, 274]. A further important direction is the development of techniques or algorithms that find an optimal input state for a given quantum channel that encodes the parameter. Concurrently, such an algorithm would optimally take the constraints of the physical platform, employed for the realization of the scheme, into account. Moreover, including quantum control into the framework of quantum metrology is a promising candidate to increase the achievable precision, without necessarily introducing entanglement.

Quantum control by itself is an integral component of quantum information science and technology. From the preparation of demanded states and the engineering of desired dynamics, to the transformation into states that one is able to read out, it is key to any application that will successfully exploit quantum features in the future. Importantly, all these operations have to be performed taking the restrictions of the physical platform one utilizes to realize the experiment into account. One of the most basic requirements of a developed control technique is ease of implementation, but moreover robustness against control errors. That is, it should not introduce further errors in the dynamics that it aims to engineer. In fact, the latter is highly challenging but encouraging progress is made. While DD sequences are already well developed and robust sequences consisting over 10000 pulses [180] or qubits with a coherence time of six hours [224] have been demonstrated, quantum error correction is catching up. In particular, the "break-even" point, i.e., the point at which the lifetime of a logical qubit is increased beyond the lifetimes of the physical qubits, has been reached very recently [367].

In the context of quantum sensing, the fields of quantum control and metrology are strictly connected. Recent theoretical results suggest that the combination of the latter, especially error correction, can lead to very effective suppression of environmental noise and therefore increase the precision in the estimation of Hamiltonian parameters [279, 283, 284, 310]. Nevertheless, these approaches suffer from the assumption of an infinitely fast control and future works need to relax that requirement. Very recent results have taken a different direction, i.e., employing quantum control techniques that provide access to measurement data which has advantages in classical data processing [297, 300–302]. This route has also been shown to resolve chemical shifts with a resolution of 1 Hz in nanoscale NMR [368]. For future extensions of these methods, they may also be combined with entanglement, which should yield an even higher precision by making use of the advantage provided by this unique quantum feature. In any case, until entanglement can be incorporated efficiently into the sensor architecture, neat data acquisition protocols are a promising intermediate step and moreover, they will not lose their importance once the quantum advancement is reached.

Additionally, high selectivity and suppression of noise to enhance the T_2 times which typically limit the achievable precision, require the application of hundreds of DD pulses. Furthermore, as we have discussed in Chapter 7, high amplitude pulses are more favorable as they minimize the impact of the free dynamics due to their short duration. These short pulses are achieved by utilizing high amplitudes in the driving field realizing the pulses. In practice, these conditions ultimately lead to heating processes in the employed sensing device. Especially in applications

involving biological material or even in vivo probes, heating is detrimental. In optical spectroscopy experiments, squeezed light is an option to enhance the resolution without increasing the intensity of the used light [230,318]. However current solid state quantum sensors have not been able to employ this quantum advantage effectively. Other solutions to these crucial issues can be the development of shaped pulses that reduce the irradiated power but effectively act as box pulses [369], or techniques that reshuffle the succession of pulses employed by conventional sequences to exhaust their addressing capabilities. The latter idea lead to the soft quantum control protocol presented in Chapter 8.

The presented soft quantum control is not only applicable in quantum sensing tasks. It further provides a method to selectively address and control different constituents of large, interacting quantum cluster by means of one control qubit. This is of particular interest for quantum information, quantum simulation and quantum communication tasks. We demonstrated the protocol on an NV center in diamond, which is a promising candidate to be the control qubit of q register of nuclear spin qubits. For example, entanglement distillation [58], quantum teleportation between NV centers separated by three meters [370], but also control over five carbon nuclear spins [63] has been achieved. However, the deterministic creation of NV centers, especially their positioning in the host material, still represents an unsolved challenge which deserves high priority in future research. On the other hand also ion traps [371,372] or superconducting circuits [20,373] are promising platforms were first realizations of computing devices with up to nineteen qubits [374] have already been demonstrated [375–377].

In all applications mentioned so far, noise plays a fundamental role due to its ubiquitous appearance in all practical realizations involving quantum systems. Nevertheless, it has been shown that the impact of noise can be at least partially diminished by exploiting suitable features that it may have. For example, non-Markovian noise has been proven to enable quantum teleportation with mixed states [88]. Moreover, it is experimentally verified that temporal correlations lead to an increasing robustness for quantum communication employing superdense coding [378] and it also manifests that non-Markovian effects may play an integral part in energy harvesting biomolecular structures [89]. Another interesting area is dissipative state preparation, where it was already shown that non-Markovianity enables the generation of entangled states [86,379]. These findings certainly motivate the further exploration of the characteristics of non-Markovian noise and its associated advantages.

In Chapter 9 of the thesis, we presented the electron spin of an NV center as a versatile and simple platform for characterizing non-Markovian dynamics in a well controlled environment. The control of non-Markovianity in an NV center via the manipulation of the natural sources of

noise in the system at hand represents a relevant step towards the full control of non-Markovian dynamics in solid-state systems. In particular, since the non-Markovian noise can be generated at will. Indeed, this property will have an important impact on different fields, in particular when the system's size is extended, maybe exploiting one of the proposals made in Section 9.5. The thus created architecture might then be employed for the quantum simulation of a dynamics which is affected by colored noise.

More importantly, however, as a fully controllable system, it may yield further insight on how to engineer a specific open system evolution which fully exhausts the features provided by the environment, whether it is for quantum computing, simulation or high precision sensing.

Bibliography

- [1] H. Carmichael. *An Open Systems Approach to Quantum Optics*. Springer Verlag, Berlin (1993).
- [2] H.-P. Breuer and F. Petruccione. *The theory of open quantum systems*. Oxford University Press, New York (2002).
- [3] C. Gardiner, P. Zoller and P. Zoller. *Quantum noise: a handbook of Markovian and non-Markovian quantum stochastic methods with applications to quantum optics*. Springer, Berlin (2004).
- [4] Á. Rivas and S. F. Huelga. *Open Quantum Systems*. Springer, New York (2012).
- [5] R. Schirhagl, K. Chang, M. Loretz and C. L. Degen. Nitrogen-Vacancy Centers in Diamond: Nanoscale Sensors for Physics and Biology. *Phys. Rev. A* **65**, 83 (2014).
- [6] J. P. Dowling and K. P. Seshadreesan. Quantum Optical Technologies for Metrology, Sensing, and Imaging. *J. Light. Technol.* **33**, 2359 (2015).
- [7] W. P. Schleich, K. S. Ranade, C. Anton, M. Arndt, M. Aspelmeyer, M. Bayer, G. Berg, T. Calarco *et al.* Quantum technology: from research to application. *Appl. Phys. B* **122**, 130 (2016).
- [8] F. J. Heremans, C. G. Yale and D. D. Awschalom. Control of Spin Defects in Wide-Bandgap Semiconductors for Quantum Technologies. *Proc. IEEE* **104**, 2009 (2016).
- [9] Y. Wu, F. Jelezko, M. B. Plenio and T. Weil. Diamond Quantum Devices in Biology. *Angew. Chem., Int. Ed. Engl.* **55**, 6586 (2016).
- [10] M. G. A. Paris. Quantum Estimation for Quantum Technology. *Int. J. Quantum Inf.* **7**, 125 (2009).

-
- [11] G. Tóth and I. Apellaniz. Quantum metrology from a quantum information science perspective. *J. Phys. A: Math. Theor.* **47**, 424006 (2014).
 - [12] R. Demkowicz-Dobrzański, M. Jarzyna and J. Kołodyński. Quantum Limits in Optical Interferometry. *Progress in Optics* **60**, 345 (2015).
 - [13] C. L. Degen, F. Reinhard and P. Cappellaro. Quantum sensing. *Rev. Mod. Phys.* **89**, 035002 (2017).
 - [14] M. A. Nielsen and I. L. Chuang. *Quantum Computation and Quantum Information*. Cambridge University Press, New York (2010).
 - [15] E. Prati and T. Shinada. *Single-Atom Nanoelectronics*. Pan Stanford (2013).
 - [16] V. V. Dobrovitski, G. D. Fuchs, A. L. Falk, C. Santori and D. D. Awschalom. Quantum Control over Single Spins in Diamond. *Annu. Rev. Condens. Matter Phys.* **4**, 23 (2013).
 - [17] D. T. Gillespie. The mathematics of Brownian motion and Johnson noise. *Am. J. Phys.* **64**, 225 (1996).
 - [18] V. Giovannetti, S. Lloyd and L. Maccone. Quantum-Enhanced Measurements: Beating the Standard Quantum Limit. *Science* **306**, 1330 (2004).
 - [19] V. Giovannetti, S. Lloyd and L. Maccone. Quantum Metrology. *Phys. Rev. Lett.* **96**, 010401 (2006).
 - [20] G. Wendin. Quantum information processing with superconducting circuits: a review. *Rep. Prog. Phys.* **80**, 106001 (2017).
 - [21] A. M. Stoneham, A. H. Harker and G. W. Morley. Could one make a diamond-based quantum computer? *J. Phys. Condens. Matter* **21**, 364222 (2009).
 - [22] J. Casanova, Z.-Y. Wang and M. B. Plenio. Noise-Resilient Quantum Computing with a Nitrogen-Vacancy Center and Nuclear Spins. *Phys. Rev. Lett.* **117**, 130502 (2016).
 - [23] J. Cai, A. Retzker, F. Jelezko and M. B. Plenio. A large-scale quantum simulator on a diamond surface at room temperature. *Nat. Phys.* **9**, 168 (2013).
 - [24] I. M. Georgescu, S. Ashhab and F. Nori. Quantum simulation. *Rev. Mod. Phys.* **86**, 153 (2014).
 - [25] C. W. Helstrom. Quantum detection and estimation theory. *J. Stat. Phys.* **1**, 231 (1969).

-
- [26] V. Giovannetti, S. Lloyd and L. Maccone. Advances in quantum metrology. *Nat. Photonics* **5**, 222 (2011).
- [27] C. W. Helstrom. *Quantum detection and estimation theory*. Academic Press, London (1976).
- [28] W. M. Itano, J. C. Bergquist, J. J. Bollinger, J. M. Gilligan, D. J. Heinzen, F. L. Moore, M. G. Raizen and D. J. Wineland. Quantum Projection Noise: Population Fluctuations in Two-Level Systems. *Phys. Rev. A* **47**, 3554 (1993).
- [29] S. M. Kay. *Fundamentals of Statistical Signal Processing: Estimation Theory*. Prentice Hall (1993).
- [30] A. van den Bos. *Parameter estimation for scientists and engineers*. Wiley-Interscience, New Jersey (2007).
- [31] D. J. Wineland, J. J. Bollinger, W. M. Itano and F. L. Moore. Spin squeezing and reduced quantum noise in spectroscopy. *Phys. Rev. A* **46**, R6797 (1992).
- [32] D. J. Wineland, J. J. Bollinger, W. M. Itano and D. J. Heinzen. Squeezed atomic states and projection noise in spectroscopy. *Phys. Rev. A* **50**, 67 (1994).
- [33] J. J. . Bollinger, W. M. Itano, D. J. Wineland and D. J. Heinzen. Optimal frequency measurements with maximally correlated states. *Phys. Rev. A* **54**, R4649 (1996).
- [34] S. F. Huelga, C. Macchiavello, T. Pellizzari, A. K. Ekert, M. B. Plenio and J. I. Cirac. Improvement of Frequency Standards with Quantum Entanglement. *Phys. Rev. Lett.* **79**, 3865 (1997).
- [35] R. Demkowicz-Dobrzański, J. Kołodyński and M. Guţă. The elusive Heisenberg limit in quantum-enhanced metrology. *Nat Commun* **3**, 1063 (2012).
- [36] Y. Matsuzaki, S. C. Benjamin and J. Fitzsimons. Magnetic field sensing beyond the standard quantum limit under the effect of decoherence. *Phys. Rev. A* **84**, 012103 (2011).
- [37] A. W. Chin, S. F. Huelga and M. B. Plenio. Quantum Metrology in Non-Markovian Environments. *Phys. Rev. Lett.* **109**, 233601 (2012).
- [38] K. Macieszczak. Zeno limit in frequency estimation with non-Markovian environments. *Phys. Rev. A* **92**, 010102 (2015).

-
- [39] A. Smirne, J. Kołodyński, S. F. Huelga and R. Demkowicz-Dobrzański. Ultimate Precision Limits for Noisy Frequency Estimation. *Phys. Rev. Lett.* **116**, 120801 (2016).
- [40] C. Helstrom. Minimum mean-squared error of estimates in quantum statistics. *Phys. Lett. A* **25**, 101 (1967).
- [41] S. L. Braunstein and C. M. Caves. Statistical distance and the geometry of quantum states. *Phys. Rev. Lett.* **72**, 3439 (1994).
- [42] B. M. Escher, R. L. de Matos Filho and L. Davidovich. General framework for estimating the ultimate precision limit in noisy quantum-enhanced metrology. *Nat. Phys.* **7**, 406 (2011).
- [43] J. Kołodyński and R. Demkowicz-Dobrzański. Efficient tools for quantum metrology with uncorrelated noise. *New J. Phys.* **15**, 073043 (2013).
- [44] A. J. Leggett, S. Chakravarty, A. T. Dorsey, M. P. A. Fisher, A. Garg and W. Zwerger. Dynamics of the dissipative two-state system. *Rev. Mod. Phys.* **59**, 1 (1987).
- [45] R. Chaves, J. B. Brask, M. Markiewicz, J. Kołodyński and A. Acín. Noisy Metrology beyond the Standard Quantum Limit. *Phys. Rev. Lett.* **111**, 120401 (2013).
- [46] J. B. Brask, R. Chaves and J. Kołodyński. Improved Quantum Magnetometry beyond the Standard Quantum Limit. *Phys. Rev. X* **5**, 031010 (2015).
- [47] A. S. Holevo. A note on covariant dynamical semigroups. *Rep. Math. Phys.* **32**, 211 (1993).
- [48] A. S. Holevo. Covariant quantum Markovian evolutions. *J. Math. Phys.* **37**, 1812 (1996).
- [49] B. Vacchini. Covariant Mappings for the Description of Measurement, Dissipation and Decoherence in Quantum Mechanics. *Lect. Notes Phys.* **787**, 39 (2010).
- [50] M. Lostaglio, K. Korzekwa and A. Milne. Markovian evolution of quantum coherence under symmetric dynamics. *Phys. Rev. A* **96**, 032109 (2017).
- [51] S. J. DeVience, L. M. Pham, I. Lovchinsky, A. O. Sushkov, N. Bar-Gill, C. Belthangady, F. Casola, M. Corbett *et al.* Nanoscale NMR spectroscopy and imaging of multiple nuclear species. *Nat. Nanotechnol.* **10**, 129 (2015).
- [52] I. Schwartz, J. Rosskopf, S. Schmitt, B. Tratzmiller, Q. Chen, L. P. McGuinness, F. Jelezko and M. B. Plenio. Blueprint for nanoscale NMR. *ArXiv:1706.07134* (2017).

-
- [53] N. Aslam, M. Pfender, P. Neumann, R. Reuter, A. Zappe, F. Fávoro de Oliveira, A. Denisenko, H. Sumiya *et al.* Nanoscale nuclear magnetic resonance with chemical resolution. *Science* **357**, 67 (2017).
- [54] S. Zaiser, T. Rendler, I. Jakobi, T. Wolf, S.-Y. Lee, S. Wagner, V. Bergholm, T. Schulte-Herbrüggen *et al.* Enhancing quantum sensing sensitivity by a quantum memory. *Nat. Commun.* **7**, 12279 (2016).
- [55] T. Rosskopf, J. Zopes, J. M. Boss and C. L. Degen. A quantum spectrum analyzer enhanced by a nuclear spin memory. *npj Quantum Inf.* **3**, 33 (2017).
- [56] L. M. K. Vandersypen and I. L. Chuang. NMR techniques for quantum control and computation. *Rev. Mod. Phys.* **76**, 1037 (2005).
- [57] L. Childress, J. M. Taylor, A. S. Sørensen and M. D. Lukin. Fault-tolerant quantum repeaters with minimal physical resources and implementations based on single-photon emitters. *Phys. Rev. A* **72**, 052330 (2005).
- [58] N. Kalb, A. A. Reiserer, P. C. Humphreys, J. J. W. Bakermans, S. J. Kamerling, N. H. Nickerson, S. C. Benjamin, D. J. Twitchen *et al.* Entanglement distillation between solid-state quantum network nodes. *Science* **356**, 928 (2017).
- [59] T. T. H., C. J., van der Sar T., D. V. V. and H. R. Universal control and error correction in multi-qubit spin registers in diamond. *Nat. Nanotechnol.* **9**, 171 (2014).
- [60] F. Jelezko and J. Wrachtrup. Single defect centres in diamond: A review. *Phys. Status Solidi A* **203**, 3207 (2006).
- [61] M. W. Doherty, N. B. Manson, P. Delaney, F. Jelezko, J. Wrachtrup and L. C. L. Hollenberg. The nitrogen-vacancy colour centre in diamond. *Phys. Rep.* **528**, 1 (2013).
- [62] L. Childress and R. Hanson. Diamond NV centers for quantum computing and quantum networks. *MRS Bull.* **38**, 134 (2013).
- [63] A. Reiserer, N. Kalb, M. S. Blok, K. J. M. van Bemmelen, T. H. Taminiau, R. Hanson, D. J. Twitchen and M. Markham. Robust Quantum-Network Memory Using Decoherence-Protected Subspaces of Nuclear Spins. *Phys. Rev. X* **6**, 021040 (2016).
- [64] L. Cywiński, R. M. Lutchyn, C. P. Nave and S. Das Sarma. How to enhance dephasing time in superconducting qubits. *Phys. Rev. B* **77**, 174509 (2008).

-
- [65] A. M. Souza, G. A. Álvarez and D. Suter. Robust Dynamical Decoupling for Quantum Computing and Quantum Memory. *Phys. Rev. Lett.* **106**, 240501 (2011).
- [66] A. M. Souza, G. A. Álvarez and D. Suter. Robust dynamical decoupling. *Philos. Trans. Royal Soc. A* **370**, 4748 (2012).
- [67] G. de Lange, D. Ristè, V. V. Dobrovitski and R. Hanson. Single-Spin Magnetometry with Multipulse Sensing Sequences. *Phys. Rev. Lett.* **106**, 080802 (2011).
- [68] N. Zhao, J. Honert, B. Schmid, M. Klas, J. Isoya, M. Markham, D. Twitchen, F. Jelezko *et al.* Sensing single remote nuclear spins. *Nat. Nanotechnol.* **7**, 657 (2012).
- [69] C. Müller, X. Kong, J. M. Cai, K. Melentijević, A. Stacey, M. Markham, D. Twitchen, J. Isoya *et al.* Nuclear magnetic resonance spectroscopy with single spin sensitivity. *Nat. Commun.* **5** (2014).
- [70] W. Ma, F. Shi, K. Xu, P. Wang, X. Xu, X. Rong, C. Ju, C.-K. Duan *et al.* Resolving remote nuclear spins in a noisy bath by dynamical decoupling design. *Phys. Rev. A* **92**, 033418 (2015).
- [71] A. Maudsley. Modified Carr-Purcell-Meiboom-Gill sequence for NMR fourier imaging applications. *J. Magn. Reson.* **69**, 488 (1986).
- [72] M. H. Levitt. Composite pulses. *Prog. Nucl. Magn. Reson. Spectrosc.* **18**, 61 (1986).
- [73] T. Gullion, D. B. Baker and M. S. Conradi. New, compensated Carr-Purcell sequences. *J. Magn. Reson.* **89**, 479 (1990).
- [74] M. Loretz, J. M. Boss, T. Rosskopf, H. J. Mamin, D. Rugar and C. L. Degen. Spurious Harmonic Response of Multipulse Quantum Sensing Sequences. *Phys. Rev. X* **5**, 021009 (2015).
- [75] I. I. Rabi, J. R. Zacharias, S. Millman and P. Kusch. A New Method of Measuring Nuclear Magnetic Moment. *Phys. Rev.* **53**, 318 (1938).
- [76] E. M. Purcell, H. C. Torrey and R. V. Pound. Resonance Absorption by Nuclear Magnetic Moments in a Solid. *Phys. Rev.* **69**, 37 (1946).
- [77] F. Bloch, W. W. Hansen and M. Packard. The Nuclear Induction Experiment. *Phys. Rev.* **70**, 474 (1946).

-
- [78] N. F. Ramsey. A Molecular Beam Resonance Method with Separated Oscillating Fields. *Phys. Rev.* **78**, 695 (1950).
- [79] U. Haeberlen and J. S. Waugh. Coherent Averaging Effects in Magnetic Resonance. *Phys. Rev.* **175**, 453 (1968).
- [80] D. J. Griffiths. *Introduction to quantum mechanics*. Pearson Prentice-Hall, New Jersey (2005).
- [81] A. Ajoy, G. A. Álvarez and D. Suter. Optimal pulse spacing for dynamical decoupling in the presence of a purely dephasing spin bath. *Phys. Rev. A* **83**, 032303 (2011).
- [82] Á. Rivas, S. F. Huelga and M. B. Plenio. Quantum non-Markovianity: characterization, quantification and detection. *Rep. Prog. Phys.* **77**, 094001 (2014).
- [83] H.-P. Breuer, E.-M. Laine, J. Piilo and B. Vacchini. Colloquium: Non-Markovian dynamics in open quantum systems. *Rev. Mod. Phys.* **88**, 021002 (2016).
- [84] L. Li, M. J. W. Hall and H. M. Wiseman. Concepts of quantum non-Markovianity: a hierarchy. *ArXiv:1712.08879* (2017).
- [85] R. Vasilé, S. Olivares, M. G. A. Paris and S. Maniscalco. Continuous-variable quantum key distribution in non-Markovian channels. *Phys. Rev. A* **83**, 042321 (2011).
- [86] S. F. Huelga, Á. Rivas and M. B. Plenio. Non-Markovianity-Assisted Steady State Entanglement. *Phys. Rev. Lett.* **108**, 160402 (2012).
- [87] A. W. Chin, J. Prior, R. Rosenbach, F. Caycedo-Soler, S. F. Huelga and M. B. Plenio. The role of non-equilibrium vibrational structures in electronic coherence and recoherence in pigment–protein complexes. *Nat. Phys.* **9**, 113 (2013).
- [88] E.-M. Laine, H.-P. Breuer and J. Piilo. Nonlocal memory effects allow perfect teleportation with mixed states. *Sci. Rep.* **4**, 4620 (2014).
- [89] S. Oviedo-Casado, J. Prior, A. W. Chin, R. Rosenbach, S. F. Huelga and M. B. Plenio. Phase-dependent exciton transport and energy harvesting from thermal environments. *Phys. Rev. A* **93**, 020102 (2016).
- [90] Y. Dong, Y. Zheng, S. Li, C.-C. Li, X.-D. Chen, G.-C. Guo and F.-W. Sun. Non-Markovianity-assisted high-fidelity Deutsch-Jozsa algorithm in diamond. *npj Quant. Inf.* **4**, 3 (2018).

-
- [91] G. Torre and F. Illuminati. Non-Markovianity-assisted optimal continuous variable quantum teleportation. *Phys. Rev. A* **98**, 012124 (2018).
- [92] D. Suter and G. A. Álvarez. Colloquium: Protecting quantum information against environmental noise. *Rev. Mod. Phys.* **88**, 041001 (2016).
- [93] B.-H. Liu, L. Li, Y.-F. Huang, C.-F. Li, G.-C. Guo, E.-M. Laine, H.-P. Breuer and J. Piilo. Experimental control of the transition from Markovian to non-Markovian dynamics of open quantum systems. *Nat. Phys.* **7**, 931 (2011).
- [94] S. Cialdi, D. Brivio, E. Tesio and M. G. A. Paris. Programmable entanglement oscillations in a non-Markovian channel. *Phys. Rev. A* **83**, 042308 (2011).
- [95] J.-S. Tang, C.-F. Li, Y.-L. Li, X.-B. Zou, G.-C. Guo, H.-P. Breuer, E.-M. Laine and J. Piilo. Measuring non-Markovianity of processes with controllable system-environment interaction. *EPL* **97**, 10002 (2012).
- [96] A. Chiuri, C. Greganti, L. Mazzola, M. Paternostro and P. Mataloni. Linear Optics Simulation of Quantum Non-Markovian Dynamics. *Sci. Rep.* **2**, 968 (2012).
- [97] B.-H. Liu, D.-Y. Cao, Y.-F. Huang, C.-F. Li, G.-C. Guo, E.-M. Laine, H.-P. Breuer and J. Piilo. Photonic realization of nonlocal memory effects and non-Markovian quantum probes. *Sci. Rep.* **3**, 1781 (2013).
- [98] J. Jin, V. Giovannetti, R. Fazio, F. Sciarrino, P. Mataloni, A. Crespi and R. Osellame. All-optical non-Markovian stroboscopic quantum simulator. *Phys. Rev. A* **91**, 012122 (2015).
- [99] S. Cialdi, M. A. C. Rossi, C. Benedetti, B. Vacchini, D. Tamascelli, S. Olivares and M. G. A. Paris. All-optical quantum simulator of qubit noisy channels. *Appl. Phys. Lett.* **110**, 081107 (2017).
- [100] M. Wittemer, G. Clos, H.-P. Breuer, U. Warring and T. Schaetz. Measurement of quantum memory effects and its fundamental limitations. *Phys. Rev. A* **97**, 020102 (2018).
- [101] S. Felton, A. M. Edmonds, M. E. Newton, P. M. Martineau, D. Fisher, D. J. Twitchen and J. M. Baker. Hyperfine interaction in the ground state of the negatively charged nitrogen vacancy center in diamond. *Phys. Rev. B* **79**, 075203 (2009).
- [102] H.-P. Breuer, E.-M. Laine and J. Piilo. Measure for the Degree of Non-Markovian Behavior of Quantum Processes in Open Systems. *Phys. Rev. Lett.* **103**, 210401 (2009).

-
- [103] Á. Rivas, S. F. Huelga and M. B. Plenio. Entanglement and Non-Markovianity of Quantum Evolutions. *Phys. Rev. Lett.* **105**, 050403 (2010).
- [104] D. S. Sivia and J. Skilling. *Data Analysis - A Bayesian Tutorial*. Oxford University Press, New York (2006).
- [105] J. Kruschke. *Doing Bayesian Data Analysis*. Academic Press, Boston (2015).
- [106] S. Sharma. Markov Chain Monte Carlo Methods for Bayesian Data Analysis in Astronomy. *Annu. Rev. Astron. Astrophys.* **55**, 213 (2017).
- [107] T. Baumgratz, M. Cramer and M. B. Plenio. Quantifying Coherence. *Phys. Rev. Lett.* **113**, 140401 (2014).
- [108] A. Jamiołkowski. Linear transformations which preserve trace and positive semidefiniteness of operators. *Rep. Math. Phys.* **3**, 275 (1972).
- [109] M.-D. Choi. Completely positive linear maps on complex matrices. *Linear Algebra Appl.* **10**, 285 (1975).
- [110] V. Gorini, A. Kossakowski and E. C. G. Sudarshan. Completely positive dynamical semigroups of N-level systems. *J. Math. Phys.* **17**, 821 (1976).
- [111] G. Lindblad. On the generators of quantum dynamical semigroups. *Commun. Math. Phys.* **48**, 119 (1976).
- [112] H.-P. Breuer, B. Kappler and F. Petruccione. The Time-Convolutionless Projection Operator Technique in the Quantum Theory of Dissipation and Decoherence. *Ann. Phys.* **291**, 36 (2001).
- [113] S. Nakajima. On Quantum Theory of Transport Phenomena Steady Diffusion. *Progr. Theor. Exp. Phys.* **20**, 948 (1958).
- [114] R. Zwanzig. Ensemble Method in the Theory of Irreversibility. *J. Chem. Phys.* **33**, 1338 (1960).
- [115] Á. Rivas, A. D. K. Plato, S. F. Huelga and M. B. Plenio. Markovian master equations: a critical study. *New J. Phys.* **12**, 113032 (2010).
- [116] C. King and M. B. Ruskai. Minimal entropy of states emerging from noisy quantum channels. *IEEE Trans. Inf. Theory* **47**, 192 (2001).

-
- [117] I. Bengtsson and K. Życzkowski. *Geometry of quantum states: An introduction to quantum entanglement*. Cambridge University Press, New York (2006).
- [118] E. Andersson, J. D. Cresser and M. J. W. Hall. Finding the Kraus decomposition from a master equation and vice versa. *J. Mod. Opt.* **54**, 1695 (2007).
- [119] M. Asorey, A. Kossakowski, G. Marmo and E. C. G. Sudarshan. Dynamical maps and density matrices. *J. Phys. Conf. Ser.* **196**, 012023 (2009).
- [120] D. Chruściński and A. Kossakowski. Non-Markovian Quantum Dynamics: Local versus Nonlocal. *Phys. Rev. Lett.* **104**, 070406 (2010).
- [121] D. Chruściński, A. Kossakowski, P. Aniello, G. Marmo and F. Ventriglia. A Class of Commutative Dynamics of Open Quantum Systems. *Open Syst. Inf. Dyn.* **17**, 255 (2010).
- [122] A. Smirne and B. Vacchini. Nakajima-Zwanzig versus time-convolutionless master equation for the non-Markovian dynamics of a two-level system. *Phys. Rev. A* **82**, 022110 (2010).
- [123] E.-M. Laine, J. Piilo and H.-P. Breuer. Measure for the non-Markovianity of quantum processes. *Phys. Rev. A* **81**, 062115 (2010).
- [124] H.-S. Zeng, N. Tang, Y.-P. Zheng and G.-Y. Wang. Equivalence of the measures of non-Markovianity for open two-level systems. *Phys. Rev. A* **84**, 032118 (2011).
- [125] I. L. Chuang and M. A. Nielsen. Prescription for experimental determination of the dynamics of a quantum black box. *J. Mod. Opt.* **44**, 2455 (1997).
- [126] M. Mohseni, A. T. Rezakhani and D. A. Lidar. Quantum-process tomography: Resource analysis of different strategies. *Phys. Rev. A* **77**, 032322 (2008).
- [127] T. Baumgratz, A. Nüßeler, M. Cramer and M. B. Plenio. A scalable maximum likelihood method for quantum state tomography. *New J. Phys.* **15**, 125004 (2013).
- [128] S. Wißmann, A. Karlsson, E.-M. Laine, J. Piilo and H.-P. Breuer. Optimal state pairs for non-Markovian quantum dynamics. *Phys. Rev. A* **86**, 062108 (2012).
- [129] S. Wißmann, H.-P. Breuer and B. Vacchini. Generalized trace-distance measure connecting quantum and classical non-Markovianity. *Phys. Rev. A* **92**, 042108 (2015).
- [130] M. M. Wolf, J. Eisert, T. S. Cubitt and J. I. Cirac. Assessing Non-Markovian Quantum Dynamics. *Phys. Rev. Lett.* **101**, 150402 (2008).

-
- [131] S. Lorenzo, F. Plastina and M. Paternostro. Geometrical characterization of non-Markovianity. *Phys. Rev. A* **88**, 020102 (2013).
- [132] D. Chruściński and S. Maniscalco. Degree of Non-Markovianity of Quantum Evolution. *Phys. Rev. Lett.* **112**, 120404 (2014).
- [133] C. M. Breeding and J. E. Shigley. The "Type" Classification system of diamonds and its importance in gemology. *Gems Gemology* **45**, 96 (2009).
- [134] G. Davies and M. F. Hamer. Optical Studies of the 1.945 eV Vibronic Band in Diamond. *Proc. R. Soc. Lond. A Math. Phys. Sci.* **348**, 285 (1976).
- [135] J. H. N. Loubser and J. A. Van Wyk. Optical spin-polarisation in a triplet state in irradiated and annealed type 1b diamonds. *Diamond Research* **9**, 11 (1977).
- [136] G. Balasubramanian, P. Neumann, D. Twitchen, M. Markham, R. Kolesov, N. Mizuochi, J. Isoya, J. Achard *et al.* Ultralong spin coherence time in isotopically engineered diamond. *Nat. Mater.* **8**, 383 (2009).
- [137] N. Bar-Gill, L. M. Pham, A. Jarmola, D. Budker and R. L. Walsworth. Solid-state electronic spin coherence time approaching one second. *Nat. Commun.* **4**, 1743 (2013).
- [138] T. Gaebel, M. Domhan, I. Popa, C. Wittmann, P. Neumann, F. Jelezko, J. R. Rabeau, N. Stavrias *et al.* Room-temperature coherent coupling of single spins in diamond. *Nat. Phys.* **2**, 408 (2006).
- [139] J. C. Angus and C. C. Hayman. Low-Pressure, Metastable Growth of Diamond and "Diamondlike" Phases. *Science* **241**, 913 (1988).
- [140] J. E. Butler, Y. A. Mankelevich, A. Cheesman, J. Ma and M. N. R. Ashfold. Understanding the chemical vapor deposition of diamond: recent progress. *J. Phys. Condens. Matter* **21**, 364201 (2009).
- [141] R. C. Burns, A. I. Chumakov, S. H. Connell, D. Dube, H. P. Godfried, J. O. Hansen, J. Härtwig, J. Hozowska *et al.* HPHT growth and x-ray characterization of high-quality type IIa diamond. *J. Phys. Condens. Matter* **21**, 364224 (2009).
- [142] I. Jakobi, S. A. Momenzadeh, F. Fávaro de Oliveira, J. Michl, F. Ziem, M. Schreck, P. Neumann, A. Denisenko *et al.* Efficient creation of dipolar coupled nitrogen-vacancy spin qubits in diamond. *J. Phys. Conf. Ser.* **752**, 012001 (2016).

-
- [143] S. Becker, N. Raatz, S. Jankuhn, R. John and J. Meijer. Nitrogen implantation with a scanning electron microscope. *Sci. Rep.* **8**, 32 (2018).
- [144] K. Ohno, F. Joseph Heremans, L. C. Bassett, B. A. Myers, D. M. Toyli, A. C. Bleszynski Jayich, C. J. Palmstrøm and D. D. Awschalom. Engineering shallow spins in diamond with nitrogen delta-doping. *Appl. Phys. Lett.* **101**, 082413 (2012).
- [145] K. Ohashi, T. Roskopf, H. Watanabe, M. Loretz, Y. Tao, R. Hauert, S. Tomizawa, T. Ishikawa *et al.* Negatively Charged Nitrogen-Vacancy Centers in a 5 nm Thin 12C Diamond Film. *Nano Lett.* **13**, 4733 (2013).
- [146] C. Osterkamp, J. Lang, J. Scharpf, C. Müller, L. P. McGuinness, T. Diemant, R. J. Behm, B. Naydenov *et al.* Stabilizing shallow color centers in diamond created by nitrogen delta-doping using SF₆ plasma treatment. *Appl. Phys. Lett.* **106**, 113109 (2015).
- [147] C. Kittel. *Introduction to solid state physics*. Wiley New York (2004).
- [148] G. Davies, S. C. Lawson, A. T. Collins, A. Mainwood and S. J. Sharp. Vacancy-related centers in diamond. *Phys. Rev. B* **46**, 13157 (1992).
- [149] Y. Mita. Change of absorption spectra in type-Ib diamond with heavy neutron irradiation. *Phys. Rev. B* **53**, 11360 (1996).
- [150] J. P. Goss, R. Jones, S. J. Breuer, P. R. Briddon and S. Öberg. The Twelve-Line 1.682 eV Luminescence Center in Diamond and the Vacancy-Silicon Complex. *Phys. Rev. Lett.* **77**, 3041 (1996).
- [151] A. Lenef and S. C. Rand. Electronic structure of the N- V center in diamond: Theory. *Phys. Rev. B* **53**, 13441 (1996).
- [152] J. P. Goss, R. Jones, P. R. Briddon, G. Davies, A. T. Collins, A. Mainwood, J. A. van Wyk, J. M. Baker *et al.* Comment on “Electronic structure of the N-V center in diamond: Theory”. *Phys. Rev. B* **56**, 16031 (1997).
- [153] N. B. Manson, J. P. Harrison and M. J. Sellars. Nitrogen-vacancy center in diamond: Model of the electronic structure and associated dynamics. *Phys. Rev. B* **74**, 104303 (2006).
- [154] T. Gaebel, M. Domhan, C. Wittmann, I. Popa, F. Jelezko, J. Rabeau, A. Greentree, S. Praver *et al.* Photochromism in single nitrogen-vacancy defect in diamond. *Appl. Phys. B* **82**, 243 (2006).

-
- [155] A. Gali, M. Fyta and E. Kaxiras. *Ab initio* supercell calculations on nitrogen-vacancy center in diamond: Electronic structure and hyperfine tensors. *Phys. Rev. B* **77**, 155206 (2008).
- [156] M. W. Doherty, N. B. Manson, P. Delaney and L. C. L. Hollenberg. The negatively charged nitrogen-vacancy centre in diamond: the electronic solution. *New J. Phys.* **13**, 025019 (2011).
- [157] M. W. Doherty, F. Dolde, H. Fedder, F. Jelezko, J. Wrachtrup, N. B. Manson and L. C. L. Hollenberg. Theory of the ground-state spin of the NV^- center in diamond. *Phys. Rev. B* **85**, 205203 (2012).
- [158] J. H. N. Loubser and J. A. van Wyk. Electron spin resonance in the study of diamond. *Rep. Prog. Phys.* **41**, 1201 (1978).
- [159] D. A. Redman, S. Brown, R. H. Sands and S. C. Rand. Spin dynamics and electronic states of N-V centers in diamond by EPR and four-wave-mixing spectroscopy. *Phys. Rev. Lett.* **67**, 3420 (1991).
- [160] N. Reddy, N. Manson and E. Krausz. Two-laser spectral hole burning in a colour centre in diamond. *J. Lumin.* **38**, 46 (1987).
- [161] E. van Oort, N. B. Manson and M. Glasbeek. Optically detected spin coherence of the diamond N-V centre in its triplet ground state. *J. Phys. C* **21**, 4385 (1988).
- [162] X.-F. He, N. B. Manson and P. T. H. Fisk. Paramagnetic resonance of photoexcited N-V defects in diamond. II. Hyperfine interaction with the ^{14}N nucleus. *Phys. Rev. B* **47**, 8816 (1993).
- [163] P. D. Bloch, W. S. Brocklesby, R. T. Harley and M. J. Henderson. Effects of Microwave Excitation on Spectral Hole-Burning in Colour Centre Systems. *J. Phys. Colloques* **46**, 527 (1985).
- [164] V. M. Acosta, A. Jarmola, E. Bauch and D. Budker. Optical properties of the nitrogen-vacancy singlet levels in diamond. *Phys. Rev. B* **82**, 201202 (2010).
- [165] L. J. Rogers, M. W. Doherty, M. S. J. Barson, S. Onoda, T. Ohshima and N. B. Manson. Singlet levels of the NV^- centre in diamond. *New J. Phys.* **17**, 013048 (2015).

-
- [166] F. Jelezko, I. Popa, A. Gruber, C. Tietz, J. Wrachtrup, A. Nizovtsev and S. Kilin. Single spin states in a defect center resolved by optical spectroscopy. *Appl. Phys. Lett.* **81**, 2160 (2002).
- [167] J. Harrison, M. Sellars and N. Manson. Optical spin polarisation of the N-V centre in diamond. *J. Lumin.* **107**, 245 (2004).
- [168] V. Jacques, P. Neumann, J. Beck, M. Markham, D. Twitchen, J. Meijer, F. Kaiser, G. Balasubramanian *et al.* Dynamic Polarization of Single Nuclear Spins by Optical Pumping of Nitrogen-Vacancy Color Centers in Diamond at Room Temperature. *Phys. Rev. Lett.* **102**, 057403 (2009).
- [169] R. S. Balmer, J. R. Brandon, S. L. Clewes, H. K. Dhillon, J. M. Dodson, I. Friel, P. N. Inglis, T. D. Madgwick *et al.* Chemical vapour deposition synthetic diamond: materials, technology and applications. *J. Phys. Condens. Matter* **21**, 364221 (2009).
- [170] B. A. Myers, A. Das, M. C. Dartiailh, K. Ohno, D. D. Awschalom and A. C. Bleszynski Jayich. Probing Surface Noise with Depth-Calibrated Spins in Diamond. *Phys. Rev. Lett.* **113**, 027602 (2014).
- [171] Y. Romach, C. Müller, T. Uden, L. J. Rogers, T. Isoda, K. M. Itoh, M. Markham, A. Stacey *et al.* Spectroscopy of Surface-Induced Noise Using Shallow Spins in Diamond. *Phys. Rev. Lett.* **114**, 017601 (2015).
- [172] J. Wang, W. Zhang, J. Zhang, J. You, Y. Li, G. Guo, F. Feng, X. Song *et al.* Coherence times of precise depth controlled NV centers in diamond. *Nanoscale* **8**, 5780 (2016).
- [173] B. A. Myers, A. Ariyaratne and A. C. B. Jayich. Double-Quantum Spin-Relaxation Limits to Coherence of Near-Surface Nitrogen-Vacancy Centers. *Phys. Rev. Lett.* **118**, 197201 (2017).
- [174] F. Reinhard, F. Shi, N. Zhao, F. Rempp, B. Naydenov, J. Meijer, L. T. Hall, L. C. L. Hollenberg *et al.* Tuning a Spin Bath through the Quantum-Classical Transition. *Phys. Rev. Lett.* **108**, 200402 (2012).
- [175] L. T. Hall, J. H. Cole and L. C. L. Hollenberg. Analytic solutions to the central-spin problem for nitrogen-vacancy centers in diamond. *Phys. Rev. B* **90**, 075201 (2014).
- [176] E. L. Hahn. Spin Echoes. *Phys. Rev.* **80**, 580 (1950).

-
- [177] J. R. Maze, J. M. Taylor and M. D. Lukin. Electron spin decoherence of single nitrogen-vacancy defects in diamond. *Phys. Rev. B* **78**, 094303 (2008).
- [178] N. Zhao, S.-W. Ho and R.-B. Liu. Decoherence and dynamical decoupling control of nitrogen vacancy center electron spins in nuclear spin baths. *Phys. Rev. B* **85**, 115303 (2012).
- [179] S. Takahashi, R. Hanson, J. van Tol, M. S. Sherwin and D. D. Awschalom. Quenching Spin Decoherence in Diamond through Spin Bath Polarization. *Phys. Rev. Lett.* **101**, 047601 (2008).
- [180] M. H. Abobeih, J. Cramer, M. A. Bakker, N. Kalb, M. Markham, D. J. Twitchen and T. H. Taminiau. One-second coherence for a single electron spin coupled to a multi-qubit nuclear-spin environment. *Nat. Commun.* **9**, 2552 (2018).
- [181] J. R. Maze, A. Dréau, V. Waselowski, H. Duarte, J.-F. Roch and V. Jacques. Free induction decay of single spins in diamond. *New J. Phys.* **14**, 103041 (2012).
- [182] M. Steiner, P. Neumann, J. Beck, F. Jelezko and J. Wrachtrup. Universal enhancement of the optical readout fidelity of single electron spins at nitrogen-vacancy centers in diamond. *Phys. Rev. B* **81**, 035205 (2010).
- [183] G. D. Fuchs, V. V. Dobrovitski, R. Hanson, A. Batra, C. D. Weis, T. Schenkel and D. D. Awschalom. Excited-State Spectroscopy Using Single Spin Manipulation in Diamond. *Phys. Rev. Lett.* **101**, 117601 (2008).
- [184] J. R. Maze, A. Gali, E. Togan, Y. Chu, A. Trifonov, E. Kaxiras and M. D. Lukin. Properties of nitrogen-vacancy centers in diamond: the group theoretic approach. *New J. Phys.* **13**, 025025 (2011).
- [185] N. Zhao, J.-L. Hu, S.-W. Ho, J. T. K. Wan and L. B. Atomic-scale magnetometry of distant nuclear spin clusters via nitrogen-vacancy spin in diamond. *Nat. Nanotechnol.* **6**, 242 (2011).
- [186] S. Maniscalco, F. Intravaia, J. Piilo and A. Messina. Misbeliefs and misunderstandings about the non-Markovian dynamics of a damped harmonic oscillator. *J. Opt. B Quantum. Semiclassical. Opt.* **6**, S98 (2004).
- [187] C. Fleming, N. I. Cummings, C. Anastopoulos and B. L. Hu. The rotating-wave approximation: consistency and applicability from an open quantum system analysis. *J. Phys. A. Math. Theo.* **43**, 405304 (2010).

-
- [188] L. Childress, M. V. Gurudev Dutt, J. M. Taylor, A. S. Zibrov, F. Jelezko, J. Wrachtrup, P. R. Hemmer and M. D. Lukin. Coherent Dynamics of Coupled Electron and Nuclear Spin Qubits in Diamond. *Science* **314**, 281 (2006).
- [189] Z.-H. Wang and S. Takahashi. Spin decoherence and electron spin bath noise of a nitrogen-vacancy center in diamond. *Phys. Rev. B* **87**, 115122 (2013).
- [190] G. Grynberg, A. Aspect and C. Fabre. *Introduction to quantum optics: from the semi-classical approach to quantized light*. Cambridge University Press, New York (2010).
- [191] L. Viola and S. Lloyd. Dynamical suppression of decoherence in two-state quantum systems. *Phys. Rev. A* **58**, 2733 (1998).
- [192] L. Viola, E. Knill and S. Lloyd. Dynamical Decoupling of Open Quantum Systems. *Phys. Rev. Lett.* **82**, 2417 (1999).
- [193] D. Vitali and P. Tombesi. Using parity kicks for decoherence control. *Phys. Rev. A* **59**, 4178 (1999).
- [194] P. Zanardi. Symmetrizing evolutions. *Phys. Lett. A* **258**, 77 (1999).
- [195] K. Khodjasteh and D. A. Lidar. Fault-Tolerant Quantum Dynamical Decoupling. *Phys. Rev. Lett.* **95**, 180501 (2005).
- [196] G. S. Uhrig. Keeping a Quantum Bit Alive by Optimized π -Pulse Sequences. *Phys. Rev. Lett.* **98**, 100504 (2007).
- [197] W. Yao, R.-B. Liu and L. J. Sham. Restoring Coherence Lost to a Slow Interacting Mesoscopic Spin Bath. *Phys. Rev. Lett.* **98**, 077602 (2007).
- [198] G. Gordon, N. Erez and G. Kurizki. Universal dynamical decoherence control of noisy single- and multi-qubit systems. *J. Phys. B At. Mol. Opt. Phys.* **40**, S75 (2007).
- [199] M. J. Biercuk, H. Uys, A. P. VanDevender, N. Shiga, W. M. Itano and J. J. Bollinger. Experimental Uhrig dynamical decoupling using trapped ions. *Phys. Rev. A* **79**, 062324 (2009).
- [200] M. J. Biercuk, H. Uys, A. P. VanDevender, N. Shiga, W. M. Itano and J. J. Bollinger. Optimized dynamical decoupling in a model quantum memory. *Nature* **458**, 996 (2009).
- [201] J. Du, X. Rong, N. Zhao, Y. Wang, J. Yang and R. B. Liu. Preserving electron spin coherence in solids by optimal dynamical decoupling. *Nature* **461**, 1265 (2009).

-
- [202] B. Naydenov, F. Dolde, L. T. Hall, C. Shin, H. Fedder, L. C. L. Hollenberg, F. Jelezko and J. Wrachtrup. Dynamical decoupling of a single-electron spin at room temperature. *Phys. Rev. B* **83**, 081201 (2011).
- [203] T. van der Sar, Z. H. Wang, M. S. Blok, H. Bernien, T. H. Taminiau, D. M. Toyli, D. A. Lidar, D. D. Awschalom *et al.* Decoherence-protected quantum gates for a hybrid solid-state spin register. *Nature* **484**, 82 (2012).
- [204] T. H. Taminiau, J. J. T. Wagenaar, T. van der Sar, F. Jelezko, V. V. Dobrovitski and R. Hanson. Detection and Control of Individual Nuclear Spins Using a Weakly Coupled Electron Spin. *Phys. Rev. Lett.* **109**, 137602 (2012).
- [205] S. Kolkowitz, Q. P. Unterreithmeier, S. D. Bennett and M. D. Lukin. Sensing Distant Nuclear Spins with a Single Electron Spin. *Phys. Rev. Lett.* **109**, 137601 (2012).
- [206] W. Yang, Z.-Y. Wang and R.-B. Liu. Preserving qubit coherence by dynamical decoupling. *Front. Phys.* **6**, 2 (2011).
- [207] J.-M. Cai, B. Naydenov, R. Pfeiffer, L. P. McGuinness, K. D. Jahnke, F. Jelezko, M. B. Plenio and A. Retzker. Robust dynamical decoupling with concatenated continuous driving. *New J. Phys.* **14**, 113023 (2012).
- [208] A. Stark, N. Aharon, T. Uden, D. Louzon, A. Huck, A. Retzker, U. L. Andersen and F. Jelezko. Narrow-bandwidth sensing of high-frequency fields with continuous dynamical decoupling. *Nat. Commun.* **8**, 1105 (2017).
- [209] G. A. Álvarez and D. Suter. Measuring the Spectrum of Colored Noise by Dynamical Decoupling. *Phys. Rev. Lett.* **107**, 230501 (2011).
- [210] A. G. Kofman and G. Kurizki. Universal Dynamical Control of Quantum Mechanical Decay: Modulation of the Coupling to the Continuum. *Phys. Rev. Lett.* **87**, 270405 (2001).
- [211] M. J. Biercuk, A. C. Doherty and H. Uys. Dynamical decoupling sequence construction as a filter-design problem. *J. Phys. B At. Mol. Opt. Phys.* **44**, 154002 (2011).
- [212] I. Almog, Y. Sagi, G. Gordon, G. Bensky, G. Kurizki and N. Davidson. Direct measurement of the system–environment coupling as a tool for understanding decoherence and dynamical decoupling. *J. Phys. B At. Mol. Opt. Phys.* **44**, 154006 (2011).

-
- [213] A. Albrecht and M. B. Plenio. Filter design for hybrid spin gates. *Phys. Rev. A* **92**, 022340 (2015).
- [214] W. M. Witzel, K. Young and S. Das Sarma. Converting a real quantum spin bath to an effective classical noise acting on a central spin. *Phys. Rev. B* **90**, 115431 (2014).
- [215] W. Yang, W.-L. Ma and R.-B. Liu. Quantum many-body theory for electron spin decoherence in nanoscale nuclear spin baths. *Rep. Prog. Phys.* **80**, 016001 (2017).
- [216] N. Zhao, J. Wrachtrup and R.-B. Liu. Dynamical decoupling design for identifying weakly coupled nuclear spins in a bath. *Phys. Rev. A* **90**, 032319 (2014).
- [217] H. Y. Carr and E. M. Purcell. Effects of Diffusion on Free Precession in Nuclear Magnetic Resonance Experiments. *Phys. Rev.* **94**, 630 (1954).
- [218] S. Meiboom and D. Gill. Modified Spin-Echo Method for Measuring Nuclear Relaxation Times. *Rev. Sci. Instrum.* **29**, 688 (1958).
- [219] Z.-Y. Wang, J. Casanova and M. B. Plenio. Delayed entanglement echo for individual control of a large number of nuclear spins. *Nat. Commun.* **8**, 14660 (2017).
- [220] C. A. Ryan, J. S. Hodges and D. G. Cory. Robust Decoupling Techniques to Extend Quantum Coherence in Diamond. *Phys. Rev. Lett.* **105**, 200402 (2010).
- [221] M. A. Ali Ahmed, G. A. Álvarez and D. Suter. Robustness of dynamical decoupling sequences. *Phys. Rev. A* **87**, 042309 (2013).
- [222] D. Farfurnik, A. Jarmola, L. M. Pham, Z. H. Wang, V. V. Dobrovitski, R. L. Walsworth, D. Budker and N. Bar-Gill. Optimizing a dynamical decoupling protocol for solid-state electronic spin ensembles in diamond. *Phys. Rev. B* **92**, 060301 (2015).
- [223] A. Ajoy, Y.-X. Liu, K. Saha, L. Marseglia, J.-C. Jaskula, U. Bissbort and P. Cappellaro. Quantum interpolation for high-resolution sensing. *Proc. Natl. Acad. Sci. U.S.A.* **114**, 2149 (2017).
- [224] M. Zhong, M. P. Hedges, R. L. Ahlefeldt, J. G. Bartholomew, S. E. Beavan, S. M. Wittig, J. J. Longdell and M. J. Sellars. Optically addressable nuclear spins in a solid with a six-hour coherence time. *Nature* **517**, 177 (2015).
- [225] K. Saeedi, S. Simmons, J. Z. Salvail, P. Dluhy, H. Riemann, N. V. Abrosimov, P. Becker, H.-J. Pohl *et al.* Room-Temperature Quantum Bit Storage Exceeding 39 Minutes Using Ionized Donors in Silicon-28. *Science* **342**, 830 (2013).

-
- [226] L. Pezzè, A. Smerzi, M. K. Oberthaler, R. Schmied and P. Treutlein. Quantum metrology with nonclassical states of atomic ensembles. *ArXiv:1609.01609* (2016).
- [227] D. Braun, G. Adesso, F. Benatti, R. Floreanini, U. Marzolino, M. W. Mitchell and S. Pirandola. Quantum enhanced measurements without entanglement. *ArXiv:1701.05152* (2017).
- [228] D. Budker and M. Romalis. Optical magnetometry. *Nat. Phys.* **3**, 227 (2007).
- [229] J. M. Taylor, P. Cappellaro, L. Childress, L. Jiang, D. Budker, P. R. Hemmer, A. Yacoby, R. Walsworth *et al.* High-sensitivity diamond magnetometer with nanoscale resolution. *Nat. Phys.* **4**, 810 (2008).
- [230] M. A. Taylor and W. P. Bowen. Quantum metrology and its application in biology. *Phys. Rep.* **615**, 1 (2016).
- [231] I. D. Leroux, M. H. Schleier-Smith and V. Vuletić. Orientation-Dependent Entanglement Lifetime in a Squeezed Atomic Clock. *Phys. Rev. Lett.* **104**, 250801 (2010).
- [232] A. D. Ludlow, M. M. Boyd, J. Ye, E. Peik and P. O. Schmidt. Optical atomic clocks. *Rev. Mod. Phys.* **87**, 637 (2015).
- [233] B. P. Abbott, R. Abbott, T. D. Abbott, M. R. Abernathy, F. Acernese, K. Ackley, C. Adams, T. Adams *et al.* Observation of Gravitational Waves from a Binary Black Hole Merger. *Phys. Rev. Lett.* **116**, 061102 (2016).
- [234] B. P. Abbott, R. Abbott, T. D. Abbott, M. R. Abernathy, F. Acernese, K. Ackley, C. Adams, T. Adams *et al.* GW150914: The Advanced LIGO Detectors in the Era of First Discoveries. *Phys. Rev. Lett.* **116**, 131103 (2016).
- [235] R. Schnabel, N. Mavalvala, D. E. McClelland and P. K. Lam. Quantum metrology for gravitational wave astronomy. *Nat. Commun.* **1**, 121 (2010).
- [236] T. L. S. Collaboration. A gravitational wave observatory operating beyond the quantum shot-noise limit. *Nat. Phys.* **7**, 962 (2011).
- [237] R. Demkowicz-Dobrzański, K. Banaszek and R. Schnabel. Fundamental quantum interferometry bound for the squeezed-light-enhanced gravitational wave detector GEO 600. *Phys. Rev. A* **88**, 041802 (2013).

-
- [238] J. Aasi, J. Abadie, B. P. Abbott, R. Abbott, T. D. Abbott, M. R. Abernathy, C. Adams, T. Adams *et al.* Enhanced sensitivity of the LIGO gravitational wave detector by using squeezed states of light. *Nat. Photonics* **7**, 613 (2013).
- [239] J. A. Jones, S. D. Karlen, J. Fitzsimons, A. Ardavan, S. C. Benjamin, G. A. D. Briggs and J. J. L. Morton. Magnetic Field Sensing Beyond the Standard Quantum Limit Using 10-Spin NOON States. *Science* **324**, 1166 (2009).
- [240] S. Simmons, J. A. Jones, S. D. Karlen, A. Ardavan and J. J. L. Morton. Magnetic field sensors using 13-spin cat states. *Phys. Rev. A* **82**, 022330 (2010).
- [241] S. Dooley, W. J. Munro and K. Nemoto. Quantum metrology including state preparation and readout times. *Phys. Rev. A* **94**, 052320 (2016).
- [242] D. M. Greenberger, M. Horne and A. Zeilinger. Going Beyond Bell's Theorem. In M. Kafatos, editor, *Bell's Theorem, Quantum Theory and Conceptions of the Universe*, vol. 37 of *Fundamental Theories of Physics*, pp. 69–72. Springer Netherlands (1989).
- [243] S. L. Braunstein, C. M. Caves and G. Milburn. Generalized Uncertainty Relations: Theory, Examples, and Lorentz Invariance. *Ann. Phys.* **247**, 135 (1996).
- [244] L. Pezzé and A. Smerzi. Entanglement, Nonlinear Dynamics, and the Heisenberg Limit. *Phys. Rev. Lett.* **102**, 100401 (2009).
- [245] R. Demkowicz-Dobrzański and L. Maccone. Using Entanglement Against Noise in Quantum Metrology. *Phys. Rev. Lett.* **113**, 250801 (2014).
- [246] R. Augusiak, J. Kołodyński, A. Streltsov, M. N. Bera, A. Acín and M. Lewenstein. Asymptotic role of entanglement in quantum metrology. *Phys. Rev. A* **94**, 012339 (2016).
- [247] L. Seveso, M. A. C. Rossi and M. G. A. Paris. Quantum metrology beyond the quantum Cramér-Rao theorem. *Phys. Rev. A* **95**, 012111 (2017).
- [248] G. Kitagawa. An algorithm for solving the matrix equation $X = FXF^T + S$. *Int. J. Control* **25**, 745 (1977).
- [249] A. Fujiwara. Quantum channel identification problem. *Phys. Rev. A* **63**, 042304 (2001).
- [250] A. Fujiwara and H. Imai. A fibre bundle over manifolds of quantum channels and its application to quantum statistics. *J. Phys. A: Math. Theor.* **41**, 255304 (2008).

-
- [251] R. T. Rockafellar. *Convex Analysis*. Princeton University Press, Princeton, New Jersey (1970).
- [252] S. Alipour, M. Mehboudi and A. T. Rezakhani. Quantum Metrology in Open Systems: Dissipative Cramér-Rao Bound. *Phys. Rev. Lett.* **112**, 120405 (2014).
- [253] M. Guță and A. Jenčová. Local asymptotic normality in quantum statistics. *Commun. Math. Phys.* **276**, 341 (2007).
- [254] A. Fujiwara. Strong consistency and asymptotic efficiency for adaptive quantum estimation problems. *J. Phys. A: Math. Gen.* **39**, 12489 (2006).
- [255] K. Macieszczak, M. Fraas and R. Demkowicz-Dobrzański. Bayesian quantum frequency estimation in presence of collective dephasing. *New J. Phys.* **16**, 113002 (2014).
- [256] M. Jarzyna and R. Demkowicz-Dobrzański. True precision limits in quantum metrology. *New J. Phys.* **17**, 013010 (2015).
- [257] D. W. Berry, B. L. Higgins, S. D. Bartlett, M. W. Mitchell, G. J. Pryde and H. M. Wiseman. How to perform the most accurate possible phase measurements. *Phys. Rev. A* **80**, 052114 (2009).
- [258] J. Ma, X. Wang, C. Sun and F. Nori. Quantum spin squeezing. *Phys. Rep.* **509**, 89 (2011).
- [259] W. Wasilewski, K. Jensen, H. Krauter, J. J. Renema, M. V. Balabas and E. S. Polzik. Quantum Noise Limited and Entanglement-Assisted Magnetometry. *Phys. Rev. Lett.* **104**, 133601 (2010).
- [260] X.-M. Lu, X. Wang and C. P. Sun. Quantum Fisher information flow and non-Markovian processes of open systems. *Phys. Rev. A* **82**, 042103 (2010).
- [261] P. L. Richards. Bolometers for infrared and millimeter waves. *J. Appl. Phys.* **76**, 1 (1994).
- [262] G. D. Boreman. *Basic electro-optics for electrical engineers*, vol. 31. SPIE Optical Engineering Press, Bellingham (1998).
- [263] A. D'Amico and C. D. Natale. A contribution on some basic definitions of sensors properties. *IEEE Sens. J.* **1**, 183 (2001).

-
- [264] J. Fraden. *Handbook of modern sensors: physics, designs, and applications*. Springer-Verlag, New York (2004).
- [265] A. Luis. Phase-shift amplification for precision measurements without nonclassical states. *Phys. Rev. A* **65**, 025802 (2002).
- [266] B. L. Higgins, D. W. Berry, S. D. Bartlett, H. M. Wiseman and G. J. Pryde. Entanglement-free Heisenberg-limited phase estimation. *Nature* **450**, 393 (2007).
- [267] F. Benatti and D. Braun. Sub-shot-noise sensitivities without entanglement. *Phys. Rev. A* **87**, 012340 (2013).
- [268] N. Killoran, M. Cramer and M. B. Plenio. Extracting Entanglement from Identical Particles. *Phys. Rev. Lett.* **112**, 150501 (2014).
- [269] W. K. Wootters. Statistical distance and Hilbert space. *Phys. Rev. D* **23**, 357 (1981).
- [270] G. Gibbons. Typical states and density matrices. *J. Geom. Phys.* **8**, 147 (1992).
- [271] U. Dorner. Quantum frequency estimation with trapped ions and atoms. *New J. Phys.* **14**, 043011 (2012).
- [272] J. Jeske, J. H. Cole and S. F. Huelga. Quantum metrology subject to spatially correlated Markovian noise: restoring the Heisenberg limit. *New J. Phys.* **16**, 073039 (2014).
- [273] L.-S. Guo, B.-M. Xu, J. Zou and B. Shao. Magnetic field sensing subject to correlated noise with a ring spin chain. *Sci. Rep.* **6**, 33254 (2016).
- [274] R. Yousefjani, S. Salimi and A. Khorashad. Enhancement of frequency estimation by spatially correlated environments. *Ann. Phys.* **381**, 80 (2017).
- [275] T. Monz, P. Schindler, J. T. Barreiro, M. Chwalla, D. Nigg, W. A. Coish, M. Harlander, W. Hänsel *et al.* 14-Qubit Entanglement: Creation and Coherence. *Phys. Rev. Lett.* **106**, 130506 (2011).
- [276] M. Skotiniotis, P. Sekatski and W. Dür. Quantum metrology for the Ising Hamiltonian with transverse magnetic field. *New J. Phys.* **17**, 073032 (2015).
- [277] M. M. Rams, P. Sierant, O. Dutta, P. Horodecki and J. Zakrzewski. At the Limits of Criticality-Based Quantum Metrology: Apparent Super-Heisenberg Scaling Revisited. *Phys. Rev. X* **8**, 021022 (2018).

-
- [278] S. Boixo, S. T. Flammia, C. M. Caves and J. Geremia. Generalized Limits for Single-Parameter Quantum Estimation. *Phys. Rev. Lett.* **98**, 090401 (2007).
- [279] R. Demkowicz-Dobrzański, J. Czajkowski and P. Sekatski. Adaptive Quantum Metrology under General Markovian Noise. *Phys. Rev. X* **7**, 041009 (2017).
- [280] S. Boixo, A. Datta, S. T. Flammia, A. Shaji, E. Bagan and C. M. Caves. Quantum-limited metrology with product states. *Phys. Rev. A* **77**, 012317 (2008).
- [281] S. Boixo, A. Datta, M. J. Davis, S. T. Flammia, A. Shaji and C. M. Caves. Quantum Metrology: Dynamics versus Entanglement. *Phys. Rev. Lett.* **101**, 040403 (2008).
- [282] M. Napolitano, M. Koschorreck, B. Dubost, N. Behbood, R. J. Sewell and M. W. Mitchell. Interaction-based quantum metrology showing scaling beyond the Heisenberg limit. *Nature* **471**, 486 (2011).
- [283] P. Sekatski, M. Skotiniotis, J. Kołodyński and W. Dür. Quantum metrology with full and fast quantum control. *Quantum* **1**, 27 (2017).
- [284] S. Zhou, M. Zhang, J. Preskill and L. Jiang. Achieving the Heisenberg limit in quantum metrology using quantum error correction. *Nat. Commun.* **9**, 78 (2018).
- [285] P. Sekatski, M. Skotiniotis and W. Dür. Dynamical decoupling leads to improved scaling in noisy quantum metrology. *New J. Phys.* **18**, 073034 (2016).
- [286] P. W. Shor. Scheme for reducing decoherence in quantum computer memory. *Phys. Rev. A* **52**, R2493 (1995).
- [287] D. A. Herrera-Martí, T. Gefen, D. Aharonov, N. Katz and A. Retzker. Quantum Error-Correction-Enhanced Magnetometer Overcoming the Limit Imposed by Relaxation. *Phys. Rev. Lett.* **115**, 200501 (2015).
- [288] G. Arrad, Y. Vinkler, D. Aharonov and A. Retzker. Increasing Sensing Resolution with Error Correction. *Phys. Rev. Lett.* **112**, 150801 (2014).
- [289] E. M. Kessler, I. Lovchinsky, A. O. Sushkov and M. D. Lukin. Quantum Error Correction for Metrology. *Phys. Rev. Lett.* **112**, 150802 (2014).
- [290] T. Uden, P. Balasubramanian, D. Louzon, Y. Vinkler, M. B. Plenio, M. Markham, D. Twitchen, A. Stacey *et al.* Quantum Metrology Enhanced by Repetitive Quantum Error Correction. *Phys. Rev. Lett.* **116**, 230502 (2016).

-
- [291] M. B. Plenio and S. F. Huelga. Sensing in the presence of an observed environment. *Phys. Rev. A* **93**, 032123 (2016).
- [292] O. Oreshkov and T. A. Brun. Continuous quantum error correction for non-Markovian decoherence. *Phys. Rev. A* **76**, 022318 (2007).
- [293] F. Reiter, A. S. Sørensen, P. Zoller and C. A. Muschik. Dissipative quantum error correction and application to quantum sensing with trapped ions. *Nat. Commun.* **8**, 1822 (2017).
- [294] X.-M. Lu, S. Yu and C. H. Oh. Robust quantum metrological schemes based on protection of quantum Fisher information. *Nat. Commun.* **6**, 7282 (2015).
- [295] S. Gammelmark and K. Mølmer. Fisher Information and the Quantum Cramér-Rao Sensitivity Limit of Continuous Measurements. *Phys. Rev. Lett.* **112**, 170401 (2014).
- [296] F. Albarelli, M. A. C. Rossi, D. Tamascelli and M. G. Genoni. Restoring Heisenberg scaling in noisy quantum metrology by monitoring the environment. *ArXiv:1803.05891* (2018).
- [297] T. Gefen, F. Jelezko and A. Retzker. Control methods for improved Fisher information with quantum sensing. *Phys. Rev. A* **96**, 032310 (2017).
- [298] S. Pang and A. N. Jordan. Optimal adaptive control for quantum metrology with time-dependent Hamiltonians. *Nat. Commun.* **8**, 14695 (2017).
- [299] J. Yang, S. Pang and A. N. Jordan. Quantum parameter estimation with the Landau-Zener transition. *Phys. Rev. A* **96**, 020301 (2017).
- [300] S. Schmitt, T. Gefen, F. M. Stürner, T. Uden, G. Wolff, C. Müller, J. Scheuer, B. Naydenov *et al.* Submillihertz magnetic spectroscopy performed with a nanoscale quantum sensor. *Science* **356**, 832 (2017).
- [301] J. M. Boss, K. S. Cujia, J. Zopes and C. L. Degen. Quantum sensing with arbitrary frequency resolution. *Science* **356**, 837 (2017).
- [302] M. Naghiloo, A. N. Jordan and K. W. Murch. Achieving Optimal Quantum Acceleration of Frequency Estimation Using Adaptive Coherent Control. *Phys. Rev. Lett.* **119**, 180801 (2017).

-
- [303] G. Clos and H.-P. Breuer. Quantification of memory effects in the spin-boson model. *Phys. Rev. A* **86**, 012115 (2012).
- [304] G. Gasbarri and L. Ferialdi. Recursive approach for non-Markovian time-convolutionless master equations. *Phys. Rev. A* **97**, 022114 (2018).
- [305] J. Lankinen, H. Lyyra, B. Sokolov, J. Teittinen, B. Ziaei and S. Maniscalco. Complete positivity, finite-temperature effects, and additivity of noise for time-local qubit dynamics. *Phys. Rev. A* **93**, 052103 (2016).
- [306] J. Jeske, D. J. Ing, M. B. Plenio, S. F. Huelga and J. H. Cole. Bloch-Redfield equations for modeling light-harvesting complexes. *J. Chem. Phys.* **142**, 064104 (2015).
- [307] Z. Sun, J. Liu, J. Ma and X. Wang. Quantum speed limits in open systems: Non-Markovian dynamics without rotating-wave approximation. *Sci. Rep.* **5**, 8444 (2015).
- [308] Y.-J. Zhang, W. Han, Y.-J. Xia, J.-P. Cao and H. Fan. Classical-driving-assisted quantum speed-up. *Phys. Rev. A* **91**, 032112 (2015).
- [309] K. Życzkowski and I. Bengtsson. On duality between quantum maps and quantum states. *Open Syst. Inf. Dyn.* **11**, 3 (2004).
- [310] W. Dür, M. Skotiniotis, F. Fröwis and B. Kraus. Improved Quantum Metrology Using Quantum Error Correction. *Phys. Rev. Lett.* **112**, 080801 (2014).
- [311] W. Zhong, Z. Sun, J. Ma, X. Wang and F. Nori. Fisher information under decoherence in Bloch representation. *Phys. Rev. A* **87**, 022337 (2013).
- [312] P. Szańkowski, M. Trippenbach and J. Chwedeńczuk. Parameter estimation in memory-assisted noisy quantum interferometry. *Phys. Rev. A* **90**, 063619 (2014).
- [313] M. Jarzyna and M. Zwierz. Parameter estimation in the presence of the most general Gaussian dissipative reservoir. *Phys. Rev. A* **95**, 012109 (2017).
- [314] C. L. Latune, I. Sinayskiy and F. Petruccione. Quantum force estimation in arbitrary non-Markovian Gaussian baths. *Phys. Rev. A* **94**, 052115 (2016).
- [315] R. Schnabel. Squeezed states of light and their applications in laser interferometers. *Phys. Rep.* **684**, 1 (2017).
- [316] C. M. Caves. Quantum-mechanical noise in an interferometer. *Phys. Rev. D* **23**, 1693 (1981).

-
- [317] M. A. Taylor, J. Janousek, V. Daria, J. Knittel, B. Hage, H.-A. Bachor and W. P. Bowen. Biological measurement beyond the quantum limit. *Nat. Photonics* **7**, 229 (2013).
- [318] M. A. Taylor, J. Janousek, V. Daria, J. Knittel, B. Hage, H.-A. Bachor and W. P. Bowen. Subdiffraction-Limited Quantum Imaging within a Living Cell. *Phys. Rev. X* **4**, 011017 (2014).
- [319] F. Dolde, I. Jakobi, B. Naydenov, N. Zhao, S. Pezzagna, C. Trautmann, J. Meijer, P. Neumann *et al.* Room-temperature entanglement between single defect spins in diamond. *Nat. Phys.* **9**, 139 (2013).
- [320] R. de Sousa. *Electron Spin as a Spectrometer o Nuclear-Spin Noise and Other Fluctuations*, pp. 183–220. Springer Berlin Heidelberg, Berlin, Heidelberg (2009).
- [321] G. Balasubramanian, I. Y. Chan, R. Kolesov, M. Al-Hmoud, J. Tisler, C. Shin, C. Kim, A. Wojcik *et al.* Nanoscale imaging magnetometry with diamond spins under ambient conditions. *Nature* **455**, 648 (2008).
- [322] P. London, J. Scheuer, J.-M. Cai, I. Schwarz, A. Retzker, M. B. Plenio, M. Katagiri, T. Teraji *et al.* Detecting and Polarizing Nuclear Spins with Double Resonance on a Single Electron Spin. *Phys. Rev. Lett.* **111**, 067601 (2013).
- [323] A. Z. Chaudhry. Utilizing nitrogen-vacancy centers to measure oscillating magnetic fields. *Phys. Rev. A* **90**, 042104 (2014).
- [324] W. Yang and R.-B. Liu. Quantum many-body theory of qubit decoherence in a finite-size spin bath. *Phys. Rev. B* **78**, 085315 (2008).
- [325] W. Yang and R.-B. Liu. Quantum many-body theory of qubit decoherence in a finite-size spin bath. II. Ensemble dynamics. *Phys. Rev. B* **79**, 115320 (2009).
- [326] M. A. Perlin, Z.-Y. Wang, J. Casanova and M. B. Plenio. Controlling Spectrally Indistinguishable Nuclear Spins for a Decoherence-Free Subspace. *ArXiv:1708.09414* (2017).
- [327] Y. Makhlin, G. Schön and A. Shnirman. Quantum-state engineering with Josephson-junction devices. *Rev. Mod. Phys.* **73**, 357 (2001).
- [328] I. Buluta, S. Ashhab and F. Nori. Natural and artificial atoms for quantum computation. *Rep. Prog. Phys.* **74**, 104401 (2011).

-
- [329] J. M. Gambetta, J. M. Chow and M. Steffen. Building logical qubits in a superconducting quantum computing system. *npj Quant. Inf.* **3**, 2 (2017).
- [330] X. Rong, D. Lu, X. Kong, J. Geng, Y. Wang, F. Shi, C.-K. Duan and J. Du. Harnessing the power of quantum systems based on spin magnetic resonance: from ensembles to single spins. *Adv. Phys. X* **2**, 125 (2017).
- [331] G.-Q. Liu, H. C. Po, J. Du, R.-B. Liu and X.-Y. Pan. Noise-resilient quantum evolution steered by dynamical decoupling. *Nat. Commun.* **4**, 2254 (2013).
- [332] G. Waldherr, Y. Wang, S. Zaiser, M. Jamali, T. Schulte-Herbrüggen, H. Abe, T. Ohshima, J. Isoya *et al.* Quantum error correction in a solid-state hybrid spin register. *Nature* **506**, 204 (2014).
- [333] V. V. Mkhitarian, F. Jelezko and V. V. Dobrovitski. Highly selective detection of individual nuclear spins with rotary echo on an electron spin probe. *Sci. Rep.* **5**, 15402 (2015).
- [334] P. G. Baranov, I. V. Il'in, E. N. Mokhov, M. V. Muzafarova, S. B. Orlinskii and J. Schmidt. EPR identification of the triplet ground state and photoinduced population inversion for a Si-C divacancy in silicon carbide. *J. Exp. Theor. Phys. Lett.* **82**, 441 (2005).
- [335] H. Seo, A. L. Falk, P. V. Klimov, K. C. Miao, G. Galli and D. D. Awschalom. Quantum decoherence dynamics of divacancy spins in silicon carbide. *Nat. Commun.* **7**, 12935 (2016).
- [336] R. Ahlefeldt, W. Hutchison and M. Sellars. fill me. *J. Lumin.* **130**, 1594 (2010).
- [337] R. L. Ahlefeldt, M. R. Hush and M. J. Sellars. Ultranarrow Optical Inhomogeneous Linewidth in a Stoichiometric Rare-Earth Crystal. *Phys. Rev. Lett.* **117**, 250504 (2016).
- [338] F. Shi, X. Kong, P. Wang, F. Kong, N. Zhao, R.-B. Liu and J. Du. Sensing and atomic-scale structure analysis of single nuclear-spin clusters in diamond. *Nat. Phys.* **10**, 21 (2013).
- [339] W.-L. Ma and R.-B. Liu. Angstrom-Resolution Magnetic Resonance Imaging of Single Molecules via Wave-Function Fingerprints of Nuclear Spins. *Phys. Rev. Applied* **6**, 024019 (2016).

-
- [340] J. M. Boss, K. Chang, J. Armijo, K. Cujia, T. Rosskopf, J. R. Maze and C. L. Degen. One- and Two-Dimensional Nuclear Magnetic Resonance Spectroscopy with a Diamond Quantum Sensor. *Phys. Rev. Lett.* **116**, 197601 (2016).
- [341] W.-L. Ma and R.-B. Liu. Proposal for Quantum Sensing Based on Two-Dimensional Dynamical Decoupling: NMR Correlation Spectroscopy of Single Molecules. *Phys. Rev. Applied* **6**, 054012 (2016).
- [342] I. Lovchinsky, A. O. Sushkov, E. Urbach, N. P. de Leon, S. Choi, K. De Greve, R. Evans, R. Gertner *et al.* Nuclear magnetic resonance detection and spectroscopy of single proteins using quantum logic. *Science* **351**, 836 (2016).
- [343] Y. Matsuzaki, T. Shimo-Oka, H. Tanaka, Y. Tokura, K. Semba and N. Mizuochi. Hybrid quantum magnetic-field sensor with an electron spin and a nuclear spin in diamond. *Phys. Rev. A* **94**, 052330 (2016).
- [344] Q. Chen, I. Schwarz and M. B. Plenio. Dissipatively Stabilized Quantum Sensor Based on Indirect Nuclear-Nuclear Interactions. *Phys. Rev. Lett.* **119**, 010801 (2017).
- [345] J. Casanova, Z.-Y. Wang and M. B. Plenio. Arbitrary nuclear-spin gates in diamond mediated by a nitrogen-vacancy-center electron spin. *Phys. Rev. A* **96**, 032314 (2017).
- [346] S. R. Hartmann and E. L. Hahn. Nuclear Double Resonance in the Rotating Frame. *Phys. Rev.* **128**, 2042 (1962).
- [347] J. Cai, F. Jelezko, M. B. Plenio and A. Retzker. Diamond-based single-molecule magnetic resonance spectroscopy. *New J. Phys.* **15**, 013020 (2013).
- [348] E. S. Mananga and T. Charpentier. On the Floquet–Magnus expansion: Applications in solid-state nuclear magnetic resonance and physics. *Phys. Rep.* **609**, 1 (2016).
- [349] N. Zhao, Z.-Y. Wang and R.-B. Liu. Anomalous Decoherence Effect in a Quantum Bath. *Phys. Rev. Lett.* **106**, 217205 (2011).
- [350] Z.-Y. Wang and M. B. Plenio. Necessary and sufficient condition for quantum adiabatic evolution by unitary control fields. *Phys. Rev. A* **93**, 052107 (2016).
- [351] K. Xu, T. Xie, F. Shi, Z.-Y. Wang, X. Xu, P. Wang, Y. Wang, M. B. Plenio *et al.* Breaking the quantum adiabatic speed-limit by jumping along geodesics. *ArXiv:1711.02911* (2017).

-
- [352] M. P. Wardrop and A. C. Doherty. Exchange-based two-qubit gate for singlet-triplet qubits. *Phys. Rev. B* **90**, 045418 (2014).
- [353] J. M. Nichol, L. A. Orona, S. P. Harvey, S. Fallahi, G. C. Gardner, M. J. Manfra and A. Yacoby. High-fidelity entangling gate for double-quantum-dot spin qubits. *npj Quant. Inf.* **3**, 3 (2017).
- [354] X. Wang, C.-S. Yu and X. Yi. An alternative quantum fidelity for mixed states of qudits. *Phys. Lett. A* **373**, 58 (2008).
- [355] B. T. Torosov and N. V. Vitanov. Adiabatic elimination of a nearly resonant quantum state. *J. Phys. B At. Mol. Opt. Phys.* **45**, 135502 (2012).
- [356] N. V. Vitanov, A. A. Rangelov, B. W. Shore and K. Bergmann. Stimulated Raman adiabatic passage in physics, chemistry, and beyond. *Rev. Mod. Phys.* **89**, 015006 (2017).
- [357] J. E. Lang, J. Casanova, Z.-Y. Wang, M. B. Plenio and T. S. Monteiro. Enhanced Resolution in Nanoscale NMR via Quantum Sensing with Pulses of Finite Duration. *Phys. Rev. Applied* **7**, 054009 (2017).
- [358] I. Schwartz, J. Scheuer, B. Tratzmiller, S. Müller, Q. Chen, I. Dhand, Z. Wang, C. Mueller *et al.* Pulsed polarisation for robust DNP. *ArXiv:1710.01508* (2017).
- [359] N. Gisin, G. Ribordy, W. Tittel and H. Zbinden. Quantum cryptography. *Rev. Mod. Phys.* **74**, 145 (2002).
- [360] M. B. Plenio and S. F. Huelga. Dephasing-assisted transport: quantum networks and biomolecules. *New J. Phys.* **10**, 113019 (2008).
- [361] R. Schmidt, A. Negretti, J. Ankerhold, T. Calarco and J. T. Stockburger. Optimal Control of Open Quantum Systems: Cooperative Effects of Driving and Dissipation. *Phys. Rev. Lett.* **107**, 130404 (2011).
- [362] B. Bylicka, D. Chruscinski and S. Maniscalco. Non-Markovianity and reservoir memory of quantum channels: a quantum information theory perspective. *Sci. Rep.* **4**, 5720 (2014).
- [363] G. Torre, W. Roga and F. Illuminati. Non-Markovianity of Gaussian Channels. *Phys. Rev. Lett.* **115**, 070401 (2015).

-
- [364] M. D. Hoffman and A. Gelman. The No-U-turn Sampler: Adaptively Setting Path Lengths in Hamiltonian Monte Carlo. *J. Mach. Learn. Res.* **15**, 1593 (2014).
- [365] R. M. Neal. Probabilistic inference using Markov chain Monte Carlo methods. *Tech. Rep. Technical Report No. CRG-TR-93-1*, University of Toronto (1993).
- [366] J. Salvatier, T. V. Wiecki and C. Fonnesbeck. Probabilistic programming in Python using PyMC3. *PeerJ Comp. Sci.* **2**, e55 (2016).
- [367] N. Ofek, A. Petrenko, R. Heeres, P. Reinhold, Z. Leghtas, B. Vlastakis, Y. Liu, L. Frunzio *et al.* Extending the lifetime of a quantum bit with error correction in superconducting circuits. *Nature* **536**, 441 (2016).
- [368] D. R. Glenn, D. B. Bucher, J. Lee, M. D. Lukin, H. Park and R. L. Walsworth. High-resolution magnetic resonance spectroscopy using a solid-state spin sensor. *Nature* **555**, 351 (2018).
- [369] J. Casanova, Z.-Y. Wang, I. Schwartz and M. B. Plenio. Shaped Pulses for Energy Efficient High-Field NMR at the Nanoscale. *ArXiv:1805.01741* (2018).
- [370] W. Pfaff, B. J. Hensen, H. Bernien, S. B. van Dam, M. S. Blok, T. H. Taminiau, M. J. Tiggelman, R. N. Schouten *et al.* Unconditional quantum teleportation between distant solid-state quantum bits. *Science* **345**, 532 (2014).
- [371] C. Piltz, T. Sriarunothai, S. S. Ivanov, S. Wölk and C. Wunderlich. Versatile microwave-driven trapped ion spin system for quantum information processing. *Sci. Adv.* **2** (2016).
- [372] B. Lekitsch, S. Weidt, A. G. Fowler, K. Mølmer, S. J. Devitt, C. Wunderlich and W. K. Hensinger. Blueprint for a microwave trapped ion quantum computer. *Sci. Adv.* **3** (2017).
- [373] M. H. Devoret and R. J. Schoelkopf. Superconducting Circuits for Quantum Information: An Outlook. *Science* **339**, 1169 (2013).
- [374] J. S. Otterbach, R. Manenti, N. Alidoust, A. Bestwick, M. Block, B. Bloom, S. Caldwell, N. Didier *et al.* Unsupervised Machine Learning on a Hybrid Quantum Computer. *ArXiv:1712.05771* (2017).
- [375] R. Barends, A. Shabani, L. Lamata, J. Kelly, A. Mezzacapo, U. L. Heras, R. Babbush, A. G. Fowler *et al.* Digitized adiabatic quantum computing with a superconducting circuit. *Nature* **534**, 222 (2016).

- [376] A. Kandala, A. Mezzacapo, K. Temme, M. Takita, M. Brink, J. M. Chow and J. M. Gambetta. Hardware-efficient variational quantum eigensolver for small molecules and quantum magnets. *Nature* **549**, 242 (2017).
- [377] C. Neill, P. Roushan, K. Kechedzhi, S. Boixo, S. V. Isakov, V. Smelyanskiy, A. Megrant, B. Chiaro *et al.* A blueprint for demonstrating quantum supremacy with superconducting qubits. *Science* **360**, 195 (2018).
- [378] B.-H. Liu, X.-M. Hu, Y.-F. Huang, C.-F. Li, G.-C. Guo, A. Karlsson, E.-M. Laine, S. Maniscalco *et al.* Efficient superdense coding in the presence of non-Markovian noise. *EPL* **114**, 10005 (2016).
- [379] C. Cormick, A. Bermudez, S. F. Huelga and M. B. Plenio. Dissipative ground-state preparation of a spin chain by a structured environment. *New J. Phys.* **15**, 073027 (2013).

Appendix

APPENDIX A

Metrology

A.1. Derivation of CRB and FI

Let us first define the *Fisher score*, which is the derivative of the logarithm probability defining the frequency of outcomes [30], i.e.

$$s_{\omega_0} = \frac{\partial q_{\omega_0}(\vec{x})}{\partial \omega_0} \quad \text{where} \quad q_{\omega_0}(\vec{x}) = \ln p_{\omega_0}(\vec{x}). \quad (\text{A.1})$$

Using $\int d\vec{x} p_{\omega_0}(\vec{x}) = 1$ and derivation with respect to ω_0 , it is straight forward to show that $\langle s_{\omega_0} \rangle = 0$.

Now assume that \hat{g}_{ω_0} is the estimator of a function g_{ω_0} which is dependent on the parameter ω_0 . The estimator may possess a possibly parameter dependent bias, hence $\langle \hat{g}_{\omega_0}(\vec{x}) \rangle = g_{\omega_0} + \beta_{\omega_0}$. We further have

$$\frac{\partial}{\partial \omega_0} \langle \hat{g}_{\omega_0}(\vec{x}) \rangle = \langle \hat{g}_{\omega_0}(\vec{x}) s_{\omega_0} \rangle = \langle [\hat{g}_{\omega_0}(\vec{x}) - \langle \hat{g}_{\omega_0}(\vec{x}) \rangle] [s_{\omega_0} - \langle s_{\omega_0} \rangle] \rangle = \text{cov} [\hat{g}_{\omega_0}(\vec{x}), s_{\omega_0}], \quad (\text{A.2})$$

where the second equality is obtained by effectively adding zeros because of the vanishing expectation value of the Fisher score. Invoking the Cauchy-Schwarz-Inequality we arrive at the bound

$$\langle \hat{g}_{\omega_0}(\vec{x}) s_{\omega_0} \rangle^2 \leq \text{var} [\hat{g}_{\omega_0}(\vec{x})] \text{var} [s_{\omega_0}] \Leftrightarrow \text{var} [\hat{g}_{\omega_0}(\vec{x})] \geq \frac{\langle \hat{g}_{\omega_0}(\vec{x}) s_{\omega_0} \rangle^2}{\text{var} [s_{\omega_0}]}. \quad (\text{A.3})$$

This can be brought into form of the CRB introduced above. Therefore, note that for the MSE we have $\Delta^2 \hat{g}_{\omega_0} = \text{var} [\hat{g}_w] + \beta_{\omega_0}^2$ and the Fisher Information is exactly the variance of the fisher score. We hence obtain

$$\begin{aligned} \Delta^2 \hat{g}_{\omega_0} &\geq \frac{\left[\frac{\partial}{\partial \omega_0} \langle \hat{g}_{\omega_0}(\vec{x}) \rangle \right]^2}{F_{\text{cl}}[p_{\omega_0}]} + \langle \hat{g}_{\omega_0}(\vec{x}) - g_{\omega_0} \rangle^2 \\ &= \frac{\left[\frac{\partial}{\partial \omega_0} (g_{\omega_0} + \beta_{\omega_0}) \right]^2}{F_{\text{cl}}[p_{\omega_0}]} + \beta_{\omega_0}^2 \\ &\geq \frac{1}{F_{\text{cl}}[p_{\omega_0}]} \left(\frac{\partial g_{\omega_0}}{\partial \omega_0} \right)^2, \end{aligned} \quad (\text{A.4})$$

where the last inequality becomes equal for $\beta_{\omega_0} = 0$. The last line is exactly Eq. (4.12) and for $g_{\omega_0} \equiv \omega_0$ we arrive at the CRB stated in Eq. (4.9). Recall also that the FI is additive for uncorrelated events which provides the factor ν at the latter equation.

A.2. Microscopic Model

Large parts of this section are based on material previously published in [H3].

A.2.1. Equivalence with an Engineered Coupling Hamiltonian

Despite the fact that the Hamiltonian given in Equation (5.1) can arise as the natural model for specific systems, we can also engineer this type of coupling out of a pure dephasing spin-boson Hamiltonian by a continuous driving of the central spin. Therefore consider the Hamiltonian

$$\tilde{H} = \frac{\omega \sigma^z}{2} + \frac{\Omega \sigma^x \cos(\omega_L t)}{2} - \frac{\sigma^z}{2} \otimes \sum_n (g_n a_n + g_n^* a_n^\dagger) + H_B, \quad (\text{A.5})$$

where Ω is the associated Rabi frequency of the driving with the frequency ω_L , e.g. these correspond to amplitude and frequency of a driving laser. In a frame rotating with the frequency ω_L we employ the rotating wave approximation with respect to that frequency and arrive at

$$\tilde{H}' = \frac{\omega - \omega_L}{2} \sigma^z + \frac{\Omega}{2} \sigma^x - \frac{\sigma^z}{2} \otimes \sum_n (g_n a_n + g_n^* a_n^\dagger) + H_B. \quad (\text{A.6})$$

Inserting the substitutions $\omega - \omega_L = -\omega_0 \sin \vartheta$, $\Omega = -\omega_0 \cos \vartheta$ and transforming the Hamiltonian with the help of the unitary matrix

$$U = \begin{pmatrix} \frac{\sec(\vartheta)(\sin(\vartheta)-1)\sqrt{\sin(\vartheta)+1}}{\sqrt{2}} & \frac{\sqrt{1-\sin(\vartheta)}(\sec(\vartheta)+\tan(\vartheta))}{\sqrt{2}} \\ \frac{\sqrt{\sin(\vartheta)+1}}{\sqrt{2}} & \frac{1}{\sqrt{2}\sqrt{\sec(\vartheta)(\sec(\vartheta)+\tan(\vartheta))}} \end{pmatrix}, \quad (\text{A.7})$$

directly yields the Hamiltonian (5.1), $H = U^\dagger \tilde{H}' U$, described in the main text. Note that due to the linearity of the substitutions and the parameter-independent unitary transformation, if one knows the driving laser frequency and amplitude, ω_L and Ω , the parameter estimation of ω_0 is fully equivalent to the estimation of ω .

A.2.2. Derivation of the TCL Master Equation

In this Appendix, we briefly sketch the derivation of the weak-coupling master equation in Equation (5.10) and we provide the expression of the coefficients $b_{jk}(t)$ where $j, k = \{+, -, z\}$, as well as the correction to the Hamiltonian $H^{\text{LS}}(t)$ in terms of the bath correlation function $C(t)$.

Recall that we start from Equation (1.13), which is obtained as the second order term in the expansion of the TCL master equation in the interaction picture, assuming an initial product state but without any assumption about the form of the global state at time t [103]. The master equation is then readily obtained following the derivation described in [112], the only difference being that we keep the integration at the r.h.s. of Equation (1.13) from 0 to t , since we are *not* making the Born-Markov approximation. Hence, following [112], we expand the system operator in the interaction Hamiltonian in Equation (5.1), i.e.,

$$A = \left(\cos \vartheta \frac{\sigma^x}{2} + \sin \vartheta \frac{\sigma^z}{2} \right), \quad (\text{A.8})$$

via the projectors in the eigenspaces of the system free Hamiltonian,

$$H_0 = \sum_{\epsilon} \epsilon \Pi(\epsilon), \quad (\text{A.9})$$

where $\epsilon_1 = \omega_0/2$, $\epsilon_2 = -\omega_0/2$, $\Pi_1 = |1\rangle\langle 1|$ and $\Pi_2 = |0\rangle\langle 0|$. Thus, we define

$$A(\varsigma) = \sum_{\epsilon' - \epsilon = \varsigma} \Pi(\epsilon) A \Pi(\epsilon'), \quad (\text{A.10})$$

and we have

$$A = \sum_{\varsigma} A(\varsigma) = \sum_{\varsigma} A^{\dagger}(\varsigma). \quad (\text{A.11})$$

Note that in our case ς can take the values $\pm\omega_0$ and 0. Explicitly,

$$\begin{aligned} A(0) &= \frac{\sin \vartheta}{2} \sigma^z \\ A(-\omega_0) &= \frac{\cos \vartheta}{2} \sigma_+ \\ A(\omega_0) &= \frac{\cos \vartheta}{2} \sigma_-. \end{aligned} \quad (\text{A.12})$$

The decomposition of the interaction operator in Equation (A.11) allows us to express the interaction Hamiltonian $H_I(t)$ as

$$H_I(t) = \sum_{\varsigma} e^{-i\varsigma t} A(\varsigma) \otimes B(t) = \sum_{\varsigma} e^{i\varsigma t} A^{\dagger}(\varsigma) \otimes B(t). \quad (\text{A.13})$$

Replacing these expansions in Equation (1.13), using Equation (A.12) and replacing the integration variable τ with $t - \tau$, one arrives at [112]

$$\begin{aligned} \frac{d}{dt} \tilde{\rho}(t) &= \sum_{\varsigma \varsigma'} e^{i(\varsigma' - \varsigma)t} \Gamma(\varsigma, t) \left[A(\varsigma) \tilde{\rho}(t) A^{\dagger}(\varsigma') - A^{\dagger}(\varsigma') A(\varsigma) \tilde{\rho}(t) \right] + \text{H.c.} \\ &= \Gamma(0, t) \left\{ \frac{\sin \vartheta \cos \vartheta}{4} \left[e^{-i\omega_0 t} (\sigma^z \tilde{\rho}(t) \sigma_- - \sigma_- \sigma^z \tilde{\rho}(t)) + e^{i\omega_0 t} (\sigma^z \tilde{\rho}(t) \sigma_+ - \sigma_+ \sigma^z \tilde{\rho}(t)) \right] \right. \\ &\quad \left. + \frac{\sin^2 \vartheta}{4} [\sigma^z \tilde{\rho}(t) \sigma^z - \tilde{\rho}(t)] \right\} \\ &\quad + \Gamma(-\omega_0, t) \left\{ \frac{\cos^2 \vartheta}{4} [\sigma_+ \tilde{\rho}(t) \sigma_- - \sigma_- \sigma_+ \tilde{\rho}(t) + e^{2i\omega_0 t} \sigma_+ \tilde{\rho}(t) \sigma_+] \right. \\ &\quad \left. + \frac{\sin \vartheta \cos \vartheta}{4} e^{i\omega_0 t} [\sigma_+ \tilde{\rho}(t) \sigma^z - \sigma^z \sigma_+ \tilde{\rho}(t)] \right\} \\ &\quad + \Gamma(\omega_0, t) \left\{ \frac{\cos^2 \vartheta}{4} [e^{-2i\omega_0 t} \sigma_- \tilde{\rho}(t) \sigma_- + \sigma_- \tilde{\rho}(t) \sigma_+ - \sigma_+ \sigma_- \tilde{\rho}(t)] \right. \\ &\quad \left. + \frac{\sin \vartheta \cos \vartheta}{4} e^{-i\omega_0 t} [\sigma_- \tilde{\rho}(t) \sigma^z - \sigma^z \sigma_- \tilde{\rho}(t)] \right\} + \text{H.c.} \end{aligned} \quad (\text{A.14})$$

Here H.c. stands for Hermitian conjugate and we introduced the functions

$$\Gamma(\varsigma, t) = \int_0^t d\tau e^{i\varsigma \tau} C(\tau). \quad (\text{A.15})$$

Recall that $C(t)$ is defined in Equation (5.9). We still need to separate the Hamiltonian and the dissipative contributions of the dynamics. Before doing so, we go back to the Schrödinger picture via $\tilde{\rho}(t) = e^{iH_0 t} \rho(t) e^{-iH_0 t}$, which adds a contribution $-i [H_0, \rho(t)]$ and removes all the phase terms $e^{\pm i\omega_0 t}$ and $e^{\pm 2i\omega_0 t}$ in the previous equation (since $e^{-iH_0 t} \sigma_{\pm} e^{iH_0 t} = e^{\mp i\omega_0 t} \sigma_{\pm}$, while $e^{-iH_0 t} \sigma_z e^{iH_0 t} = \sigma_z$). If we now define

$$\begin{aligned} c_{\zeta\zeta'}(t) &= \Gamma(\zeta, t) + \Gamma^*(\zeta', t) \\ d_{\zeta\zeta'}(t) &= \frac{1}{2i} (\Gamma(\zeta, t) - \Gamma^*(\zeta', t)), \end{aligned} \quad (\text{A.16})$$

we can write Equation (A.14) in the Schrödinger picture as

$$\begin{aligned} \frac{d}{dt} \rho(t) &= -i \left[H_0 + \sum_{\zeta, \zeta'} d_{\zeta\zeta'}(t) A^\dagger(\zeta') A(\zeta), \rho(t) \right] \\ &+ \sum_{\zeta, \zeta'} c_{\zeta\zeta'}(t) \left(A(\zeta) \rho(t) A^\dagger(\zeta') - \frac{1}{2} \{ A^\dagger(\zeta') A(\zeta), \rho(t) \} \right), \end{aligned} \quad (\text{A.17})$$

which can be written as the master equation (5.10) in the main text, when Equation (A.12) is used. Thereby, exploiting Eq. (A.16), the coefficients are fixed as in Equation (5.13), i.e.,

$$\begin{aligned} b_{zz}(t) &= \frac{\sin^2 \vartheta}{2} \text{Re}\{\Gamma(0, t)\} = \frac{\sin^2 \vartheta}{2} \int_0^t d\tau \text{Re}\{C(\tau)\} \\ b_{++}(t) &= \frac{\cos^2 \vartheta}{2} \text{Re}\{\Gamma(-\omega_0, t)\} = \frac{\cos^2 \vartheta}{2} \int_0^t d\tau \text{Re}\{C(\tau) e^{-i\omega_0 \tau}\} \\ b_{--}(t) &= \frac{\cos^2 \vartheta}{2} \text{Re}\{\Gamma(\omega_0, t)\} = \frac{\cos^2 \vartheta}{2} \int_0^t d\tau \text{Re}\{C(\tau) e^{i\omega_0 \tau}\} \\ b_{+-}(t) &= b_{-+}^*(t) = \frac{\cos^2 \vartheta}{4} (\Gamma(-\omega_0, t) + \Gamma^*(\omega_0, t)) = \frac{\cos^2 \vartheta}{2} \int_0^t d\tau \text{Re}\{C(\tau)\} e^{-i\omega_0 \tau} \\ b_{z+}(t) &= b_{+z}^*(t) = \frac{\sin \vartheta \cos \vartheta}{4} (\Gamma(0, t) + \Gamma^*(-\omega_0, t)) = \frac{\sin \vartheta \cos \vartheta}{4} \int_0^t d\tau [C(\tau) + e^{i\omega_0 \tau} C^*(\tau)] \\ b_{z-}(t) &= b_{-z}^*(t) = \frac{\sin \vartheta \cos \vartheta}{4} (\Gamma(0, t) + \Gamma^*(\omega_0, t)) = \frac{\sin \vartheta \cos \vartheta}{4} \int_0^t d\tau [C(\tau) + e^{-i\omega_0 \tau} C^*(\tau)], \end{aligned} \quad (\text{A.18})$$

while the Hamiltonian contribution due to the interaction with the environment is given by $H^{\text{LS}}(t) = \sum_{\zeta, \zeta'} d_{\zeta\zeta'}(t) A^\dagger(\zeta') A(\zeta)$, which corresponds to Equation (5.12) in the main text, that

is,

$$H^{\text{LS}}(t) = \begin{pmatrix} H_{11}^{\text{LS}}(t) & H_{01}^{\text{LS}}(t) \\ H_{01}^{\text{LS}}(t) & H_{00}^{\text{LS}}(t) \end{pmatrix}, \quad (\text{A.19})$$

where

$$H^{\text{LS}}(t) = \begin{pmatrix} \frac{\cos^2 \vartheta}{4} \int_0^t d\tau \operatorname{Im}\{e^{i\omega_0 \tau} C(\tau)\} & i \frac{\sin \vartheta \cos \vartheta}{4} \int_0^t d\tau \operatorname{Re}\{C(\tau)\} (1 - e^{-i\omega_0 \tau}) \\ -i \frac{\sin \vartheta \cos \vartheta}{4} \int_0^t d\tau \operatorname{Re}\{C(\tau)\} (1 - e^{i\omega_0 \tau}) & \frac{\cos^2 \vartheta}{4} \int_0^t d\tau \operatorname{Im}\{e^{-i\omega_0 \tau} C(\tau)\} \end{pmatrix}. \quad (\text{A.20})$$

Summarizing, starting from the global Hamiltonian in Equation (5.1), after introducing the environmental correlation function $C(t)$ in Equation (5.9) and the system's operators in Equation (A.10), one directly gets the weak-coupling master equation via the Eqs. (A.15)-(A.17).

A.2.3. Solutions of the Master Equation in the High Temperature Limit

As said in the main text, we can use the approximation $j(\omega) \approx j(-\omega)$ to simplify the structure of the master equation in the high temperature regime. First, note that since $\mathcal{L}(t)$ is a linear map acting on the space of linear operators in \mathbb{C}^2 , we can represent it via a 4×4 matrix, using the same representation recalled in Section 1.3, see Equation (1.18). In particular, the coefficients in the dissipative part of the generator as in Equation (5.15) imply the matrix representation of $\mathcal{L}(t)$ as

$$\mathbf{D}^{\mathcal{L}(t)} = \begin{pmatrix} 0 & \vec{0}^T \\ \vec{0} & L(t) \end{pmatrix}. \quad (\text{A.21})$$

Explicitly, using the definition of $\Gamma(\omega_0, t)$ and $\Gamma(0, t)$ in Equation (5.11), as well as $H^{\text{LS}}(t)$ in Equation (A.19) and $j(\omega) \approx j(-\omega)$, we end up with

$$\mathbf{D}^{\mathcal{L}(t)} = \begin{pmatrix} 0 & 0 & 0 & 0 \\ 0 & -\sin^2(\vartheta) f_1(0, t) & -\omega_0 & \cos(\vartheta) \sin(\vartheta) f_1(\omega_0, t) \\ 0 & \omega_0 + \cos^2(\vartheta) f_2(\omega_0, t) & -\sin^2(\vartheta) f_1(0, t) & \cos(\vartheta) \sin(\vartheta) f_2(\omega_0, t) \\ 0 & \sin(\vartheta) \cos(\vartheta) f_1(0, t) & 0 & -\cos^2(\vartheta) f_1(\omega_0, t) \end{pmatrix}. \quad (\text{A.22})$$

where

$$\begin{aligned} f_1(\omega_0, t) &= \int_{-\infty}^{\infty} d\omega j(\omega) \frac{\sin(t(\omega - \omega_0))}{\omega - \omega_0} \\ f_2(\omega_0, t) &= \int_{-\infty}^{\infty} d\omega j(\omega) \frac{\cos(t(\omega - \omega_0)) - 1}{\omega - \omega_0}. \end{aligned} \quad (\text{A.23})$$

Indeed, applying the same constraint on the secular master equation in Equation (5.14), we get the PC master equation, where the coefficients in the last line of Equation (5.15) are set to 0, along with $H_{10}^{\text{LS}}(t) = H_{01}^{\text{LS}}(t)^*$ in Equation (A.19). The corresponding time-local generator is hence given by

$$\mathbf{D}_{\text{PC}}^{\mathcal{L}(t)} = \begin{pmatrix} 0 & 0 & 0 & 0 \\ 0 & -\sin^2(\vartheta)f_1(0, t) & -\omega_0 - \frac{\cos^2(\vartheta)}{2}f_2(\omega_0, t) & 0 \\ 0 & -\frac{\cos^2(\vartheta)}{2}f_1(\omega_0, t) & -\sin^2(\vartheta)f_1(0, t) & 0 \\ 0 & \omega_0 + \frac{\cos^2(\vartheta)}{2}f_2(\omega_0, t) & -\frac{\cos^2(\vartheta)}{2}f_1(\omega_0, t) & 0 \\ 0 & 0 & 0 & -\cos^2(\vartheta)f_1(\omega_0, t) \end{pmatrix}. \quad (\text{A.24})$$

Now, the form of the time-local generator as in Equation (A.21) implies the form for the dynamical map as in Equation (5.16). By means of the Dyson expansion, Equation (1.12), we see that the block-diagonal structure of the generator directly implies the same block-diagonal structure of the dynamical map. Thus, we get Equation (5.16) with

$$V(t) = T_{\leftarrow} e^{\int_0^t d\tau L(\tau)}. \quad (\text{A.25})$$

A.2.4. Differential Equations for the Density Matrix Elements in the case of Ohmic Spectral Densities

Due to the simple master equations in the Ohmic regime described in Section 5.2.2, Eqs. (5.25) and (5.26), it is more convenient to solve the dynamics taking into account the evolution of the elements of the system's density matrix, $\rho_{ij}(t) = \langle i | \rho(t) | j \rangle$ for $i, j = 0, 1$.

For the NPC dynamics, the master equation in Equation (5.25) is equivalent to the following

system of equations [of course, $\rho_{01}(t) = \rho_{10}^*(t)$ and $\rho_{00}(t) = 1 - \rho_{11}(t)$]:

$$\begin{aligned}\frac{d}{dt}\rho_{11}(t) &= \cos^2 \vartheta \gamma(t) (1 - 2\rho_{11}(t)) + 2 \cos \vartheta \sin \vartheta \gamma(t) \text{Re}\{\rho_{10}(t)\} \\ \frac{d}{dt}\rho_{10}(t) &= -i\omega_0 \rho_{10}(t) - \sin \vartheta \cos \vartheta \gamma(t) (1 - 2\rho_{11}(t)) \\ &\quad - (1 + \sin^2 \vartheta) \gamma(t) \rho_{10}(t) + \cos^2 \vartheta \gamma(t) \rho_{10}^*(t),\end{aligned}\tag{A.26}$$

which can be easily solved numerically. For the PC dynamics, Equation (5.26) leads us to

$$\begin{aligned}\frac{d}{dt}\rho_{11}(t) &= \cos^2 \vartheta \gamma(t) (1 - 2\rho_{11}(t)) \\ + \frac{d}{dt}\rho_{10}(t) &= (-i\omega_0 - (2 - \cos^2 \vartheta) \gamma(t)) \rho_{10}(t).\end{aligned}\tag{A.27}$$

Contrary to the NPC case, populations and coherences are decoupled. Indeed, the solution of this system of equations reads

$$\begin{aligned}\rho_{11}(t) &= e^{-2\cos^2 \vartheta \int_0^t d\tau \gamma(\tau)} \rho_{11}(0) + \cos^2 \vartheta \int_0^t d\tau e^{-2\cos^2 \vartheta \int_\tau^t d\tau' \gamma(\tau')} \gamma(\tau) \\ \rho_{10}(t) &= e^{-i\omega_0 t - (2 - \cos^2 \vartheta) \int_0^t d\tau \gamma(\tau)} \rho_{10}(0).\end{aligned}\tag{A.28}$$

In Figure 5.2 we reported the evolution of the Bloch vector $\vec{r}(t)$ for different initial conditions for $\rho(0)$. Indeed, the components of the vector $\vec{r}(t)$ are directly related to the matrix elements of the corresponding state, see Section 1.3. Finally, the CP of the dynamics is guaranteed by the master equations themselves, as mentioned in the main text of Section 5.2.2.

A.2.5. Semigroup Limit of the Ohmic Spectral Density

Taking the limit $\omega_C \rightarrow \infty$, the decay rate given by Equation (5.25) becomes time independent,

$$\gamma_s = \lim_{\omega_C \rightarrow \infty} \frac{\lambda}{\beta} \arctan(\omega_C t) = \frac{\pi}{2} \frac{\lambda}{\beta}.\tag{A.29}$$

In the NPC case, this yields the generator

$$\mathbf{D}_{\text{NPC}}^{\mathcal{L}}(t) = \begin{pmatrix} 0 & 0 & 0 & 0 \\ 0 & -2\gamma_s \sin^2(\vartheta) & -\omega_0 & \gamma_s \sin(2\vartheta) \\ 0 & \omega_0 & -2\gamma & 0 \\ 0 & \gamma_s \sin(2\vartheta) & 0 & -2\gamma_s \cos^2(\vartheta) \end{pmatrix}.\tag{A.30}$$

A.2.6. A General Formula for the Single Probe QFI of PC Dynamics

Using the characterization of PC dynamics presented in Section 1.5 and the formula for the QFI in Equation (5.27), we will provide some analytic formulas for the one-probe QFI of a PC dynamics; for the sake of generality, we will not restrict to the unital case (i.e., to the $T \rightarrow \infty$ regime for the spin-boson model, see Figure 5.1). Any PC dynamical map can be written as in Equation (1.37), where $\xi = \omega_0 t + \varphi$ and, in general, also the other coefficients v_z, d_z, d will depend both on ω_0 and on t . However, if we neglect for a moment the dependence of the noise rates (for a PC dynamics $b_{ii}(t), i = \pm, z$) on ω_0 , it is easy to see that the dependence on ω_0 will be enclosed only in ξ , that is the coefficient due to the unitary component of the map. In this case the QFI, which we denote as $\tilde{F}_{Q,PC}(t)$, will be simply given by

$$\tilde{F}_{Q,PC}(t) = \frac{t^2}{2} D_z(t)^2, \quad (\text{A.31})$$

where $D_z(t) = \sqrt{x(t)^2 + y(t)^2} = |d(t)|\sqrt{x(0)^2 + y(0)^2}$ is the distance of the state at time t from the z -axis and we have used Cartesian coordinates to define the Bloch vector $\vec{r}(t) = \{x(t), y(t), z(t)\}$. Instead, if we include the dependence of the noise parameters on ω_0 , we obtain the 'full' QFI

$$\begin{aligned} F_{Q,PC}(t) = & \frac{1}{2} \left(t^2 D_z(t, \omega_0)^2 + \dot{D}_z(t, \omega_0)^2 + \dot{z}(t, \omega_0)^2 \right) \\ & + \frac{1}{2} \frac{\left(D_z(t, \omega_0)^2 \dot{d}(t, \omega_0)/d(t, \omega_0) + z(t, \omega_0) \dot{z}(t) \right)^2}{1 - D_z(t, \omega_0)^2 - z^2(t, \omega_0)}, \end{aligned} \quad (\text{A.32})$$

where for the sake of compactness we used explicitly that $z(t, \omega_0) = v_z(t, \omega_0) + z(0)d_z(t, \omega_0)$. Note that all the contributions are positive; in particular $1 - D_z(t, \omega_0)^2 - z^2(t) \geq 0$ due to the positivity of the dynamics.

A.2.7. Expectation Value of the Parity Operator using GHZ-States

In the Heisenberg picture, the dynamics of the parity operator is governed by

$$P_x(t) = \bigotimes_{k=1}^N \Lambda_{t, \omega_0}[\sigma^x_{(k)}] = \bigotimes_{k=1}^N \left[\xi(t) \sigma^x_{(k)} + \chi(t) \sigma^y_{(k)} + \varsigma(t) \sigma^z_{(k)} \right], \quad (\text{A.33})$$

where the second equality is an expansion of $P_x(t)$ into the Pauli basis (note that $P_x(t)$ is traceless). Importantly, the expansion coefficients are independent of k since the channel acts

identically and independently on every probe. For the calculation of $\langle P_x(t) \rangle$ we exploit that the parity operator is still a product, hence employing the GHZ state in the basis of σ^z as defined in Equation (4.15), we directly arrive at Equation (5.34). Obviously, the coefficients depend on the dynamics induced by $\Lambda_{\omega_0,t}$, however, these can be efficiently evaluated numerically. An analytic solution for transversal semigroup noise is given in [46].

APPENDIX B

Quantum Control

B.1. Calculation of the Overlap Integral

Let us briefly describe how the final form of the overlap integral is derived. Therefore we start with Eq. (3.11). As mentioned, for a Gaussian process, it is only required to calculate the variance $\langle \mathbb{K}_{\text{free}}(t)^2 \rangle$. Importantly, the integral [here $\mathbb{K}_{\text{free}}(t)$] of a Gaussian process (here $b(t)$) is still Gaussian, i.e. the distribution for the random variable $\mathcal{K}(t)$, $P[\mathcal{K}(t) = \mathbb{K}_{\text{free}}(t)]$ is normal. Since we stated $\langle b(t) \rangle = 0$ it follows $\langle \mathbb{K}_{\text{free}}(t) \rangle = 0$. This implies that Wick's theorem holds, i.e.

$$\langle \mathbb{K}_{\text{free}}(t)^n \rangle = \begin{cases} 0, & n \text{ odd} \\ \frac{(2n)!}{2^n n!} \langle \mathbb{K}_{\text{free}}(t)^2 \rangle^{n/2}, & n \text{ even.} \end{cases} \quad (\text{B.1})$$

Using Eq. (B.1), it is straightforward to show the identity

$\langle \exp \{-i\mathbb{K}_{\text{free}}(t)\} \rangle = \exp \left\{ -\langle \mathbb{K}_{\text{free}}(t)^2 \rangle / 2 \right\}$. Due to the linearity of the expectation value we then write

$$\begin{aligned} \langle \mathbb{K}_{\text{free}}(t)^2 \rangle &= \int_0^t d\tau_1 \int_0^t d\tau_2 \langle b(\tau_1)b(\tau_2) \rangle F(\tau_1)F(\tau_2) \\ &= \int_0^t d\tau_1 \int_0^t d\tau_2 \langle b(0)b(\tau_1 - \tau_2) \rangle F(\tau_1)F(\tau_2) \\ &= \int_0^t d\tau_1 \int_0^t d\tau_2 \int_{-\infty}^{\infty} d\omega \frac{S(\omega)}{2\pi} e^{-i\omega(\tau_1 - \tau_2)} F(\tau_1)F(\tau_2), \end{aligned} \quad (\text{B.2})$$

where the first line is due to the linearity of the expectation value and for the second line we assumed that the process is stationary. In particular, the two-point correlation function $C(\tau_1, \tau_2) = \langle b(0)b(\tau_1 - \tau_2) \rangle = C(\tau_1 - \tau_2)$ of a stationary process only depends on the difference of the time arguments. For the last equality we employed the spectrum $S(\omega)$, i.e. the Fourier transform of the correlation function,

$$S(\omega) = \int_{-\infty}^{\infty} dt C(t) e^{i\omega t} \quad \text{and respectively} \quad C(t) = \frac{1}{2\pi} \int_{-\infty}^{\infty} d\omega S(\omega) e^{-i\omega t}. \quad (\text{B.3})$$

Noting that $F(t)$ is a real function, we write

$$f_{\omega}(t) = \int_0^t d\tau_1 e^{-i\omega\tau_1} F(\tau_1) \times \int_0^t d\tau_2 e^{i\omega\tau_2} F(\tau_2) = \left| \int_0^t d\tau e^{-i\omega\tau} F(\tau) \right|^2 \quad (\text{B.4})$$

Finally, to arrive at (3.12) we need to mention that $S(\omega)$ is an even function, hence we can restrict the integration starting at zero and compensate by a factor of two.

B.2. Signal for an XY-8 Sequence Employing Realistic Pulses

This section has already been published in [H2]. Reprinted excerpts with permission from [H2].

Copyright (2016) by the American Physical Society.

B.2.1. Ideal Signal after a single XY-8 Sequence

The definitions of the Hamiltonians and sequences in Section 7.1 allow us to calculate the first order of the signal in β_{\max} . It turns out, that the corresponding result is independent of the tilting angle to first order, hence represents the ideal signal after the application of a single unit of the XY-8 sequence (8 pulses):

$$P_{\alpha,\theta}^{(1)} = \frac{1}{2} \left\{ 1 - \cos \left[16B\gamma_n \left(\cos \left(\frac{3\pi}{4\alpha} \right) + \cos \left(\frac{5\pi}{4\alpha} \right) + \cos \left(\frac{11\pi}{4\alpha} \right) + \cos \left(\frac{13\pi}{4\alpha} \right) \right) \right. \right. \\ \left. \left. \times \frac{\sin \left(\frac{\pi}{4\alpha} \right)^3 \sin \left(\frac{4\pi}{\alpha} + \theta \right)}{\omega_{\text{ac}}} \right] \right\} + O(\beta_{\max}^2). \quad (\text{B.5})$$

Note that the zero-th order contribution in β_{\max} (i.e., $P_{\alpha,\theta}^{(1)}$ with $\beta_{\max} = 0$) is independent of ϕ . However, higher orders on β_{\max} can provide a dependence on ϕ . For $\beta_{\max} = 0$, this equation represents the ideal signal.

B.2.2. Impact of the Second Order

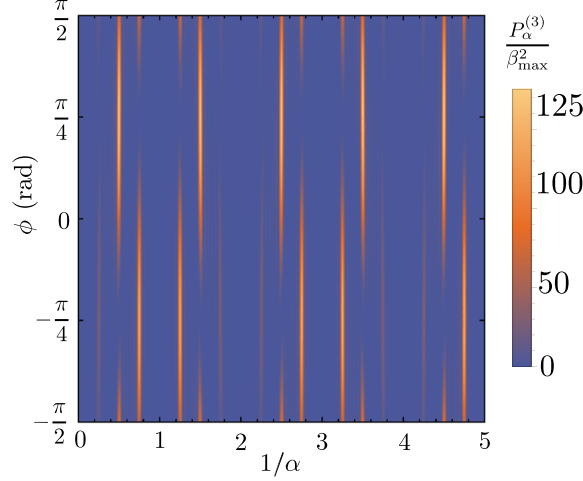


Figure B.1.: **Impact of the second order after three applications of the XY-8 sequence.**

The values for the figure are calculated using Eq. (B.7). (Reprinted figure with permission from [H2]. Copyright (2016) by the American Physical Society.)

With the definitions given in Section 7.1, we can calculate the spectrum for a single application of the XY-8 sequence (8 π -pulses) as

$$P_{\alpha}^{(1)} \approx \left\{ \left[\sin\left(\frac{\pi}{2\alpha}\right) - \sin\left(\frac{5\pi}{2\alpha}\right) + \sin\left(\frac{11\pi}{2\alpha}\right) - \sin\left(\frac{15\pi}{2\alpha}\right) \right] \cos \phi + \left[\sin\left(\frac{3\pi}{2\alpha}\right) - \sin\left(\frac{7\pi}{2\alpha}\right) + \sin\left(\frac{9\pi}{2\alpha}\right) - \sin\left(\frac{13\pi}{2\alpha}\right) \right] \sin \phi \right\}^2 \beta_{\max}^2 + O(\beta_{\max}^3), \quad (\text{B.6})$$

which is valid under the assumption $\gamma_n B / \omega_{\text{ac}} \ll 1$. This result gives $P_{\alpha=3}^{(1)} / \beta_{\max}^2 \approx 9 \cos^2(\phi) / 4$ and will thus oscillate under a changing initial phase. However, after three applications of the XY-8 sequence (24 π -pulses), we obtain the signal

$$P_{\alpha}^{(3)} \approx \left\{ 16 \cos\left(\frac{\pi}{4\alpha}\right)^4 \left[\sin\left(\frac{7\pi}{2\alpha}\right) - \sin\left(\frac{9\pi}{2\alpha}\right) + \sin\left(\frac{23\pi}{2\alpha}\right) - \sin\left(\frac{25\pi}{2\alpha}\right) + \sin\left(\frac{39\pi}{2\alpha}\right) - \sin\left(\frac{41\pi}{2\alpha}\right) \right]^2 \left[\cos \phi + 2 \cos\left(\frac{2\pi}{\alpha}\right) \cos \phi - \sin \phi + 2 \cos\left(\frac{\pi}{\alpha}\right) (\sin \phi - \cos \phi) \right]^2 \right\} \beta_{\max}^2 + O(\beta_{\max}^3). \quad (\text{B.7})$$

Interestingly, for $\alpha = 3$ we have $P_{\alpha}^{(3)} \approx O(\beta_{\max}^3)$. The same calculation can be done for other

odd numbers of $\alpha > 1$. Consecutive applications show that after $n\alpha$ sequences, for $\alpha > 1$ and $n \in \mathbb{N}$, the corresponding signal is again zero, thus for these resonances no accumulation of phase is accomplished. Fig. B.1 shows Eq. (B.7) for different values of $1/\alpha$ and ϕ . This sequence requires three times the evolution time as used for Figure 7.2 (a), thus the peaks are much narrower and it can be observed how the spurious signal accumulation is only present at certain relations of ω_{DD}/ω_{ac} while it is highly phase dependent.

B.3. High Selective Coupling using Soft Quantum Control

This appendix consists of material that has been partly published already in [H4]. Reprinted excerpts with permission from [H4]. Copyright (2018) by the American Physical Society.

B.3.1. Adiabatic evolution

In the following, we briefly describe the evolution generated by a time dependent Hamiltonian that changes in an adiabatic manner [80]. Starting from the initial time t_0 , a quantum state at time t may be always decomposed into the eigenstates of the Hamiltonian, i.e. we may write

$$|\Psi(t)\rangle = \sum_n c_n(t) e^{-i\phi_n(t)} |\psi_n(t)\rangle, \quad (\text{B.8})$$

where all the basis vectors fulfill the eigenvalue equation $H(t) |\psi_n(t)\rangle = E_n(t) |\psi_n(t)\rangle$ and we have the *dynamic phase*

$$\phi_n(t) = \int_0^t d\tau E_n(\tau). \quad (\text{B.9})$$

Using the Schrödinger Equation and the decomposition above, it is straightforward to show that the coefficients $c_n(t)$ fulfill the differential equation

$$\begin{aligned} \partial_t c_n(t) = & -c_n(t) \langle \psi_n(t) | [\partial_t |\psi_n(t)\rangle] \\ & - \sum_{m \neq n} c_m(t) \frac{\langle \psi_m(t) | [\partial_t H(t)] | \psi_n(t)\rangle}{E_n(t) - E_m(t)} e^{-i[\phi_n(t) - \phi_m(t)]}. \end{aligned} \quad (\text{B.10})$$

Note that energy crossings $E_n(t) - E_m(t) = 0$ are problematic, however, this issue can be solved by performing a more involved analysis [350]. Under the adiabatic theorem, we assume that the change in time of $H(t)$ is extremely small, hence we neglect the second line of the latest

equation. Using the solution given by that differential equation, we find that

$$|\Psi(t)\rangle = \sum_n c_n(0) e^{i\gamma_n(t)} e^{-i\phi_n(t)} |\psi_n(t)\rangle, \quad (\text{B.11})$$

where $\gamma_n(t)$ is the so called *geometric phase* given by the solution to Eq. (B.10),

$$\gamma_n(t) = i \int_0^t d\tau \langle \psi_n(\tau) | [\partial_\tau |\psi_n(\tau)\rangle]. \quad (\text{B.12})$$

Let us finally note the following concerning the case we are dealing with when employing the soft quantum control method. The time dependence of the states $|\psi_n(t)\rangle$ is due to the parameter $\lambda(t)$ in the Hamiltonian. Let us use

$$\partial_t |\psi_n(t)\rangle = \partial_\lambda |\psi_n[\lambda(t)]\rangle \partial_t \lambda(t), \quad (\text{B.13})$$

so that the geometric phase becomes

$$\gamma_n(t) = i \int_{\lambda(0)}^{\lambda(t)} d\lambda \langle \psi_n[\lambda(t)] | [\partial_\lambda |\psi_n(\lambda(t))\rangle], \quad (\text{B.14})$$

which is obviously equal to zero for $\lambda(0) = \lambda(t)$.

B.3.2. Calculation of Energy Shifts using the Adiabatic Theory

In Section 8.3.1 we have shown that the soft quantum control scheme can efficiently eliminate oscillating terms while keeping desired energy-conserving interactions. However, during the derivation of the effective evolution operator in Eq. (8.13), we mentioned that the dynamic phases may contain higher order energy shift. Here, we will exemplify the calculation of such shifts by considering a two-qubit Hamiltonian,

$$H(t) = \frac{\omega}{2} (\sigma_0^z + \sigma_1^z) + \lambda(t) c \sigma_0^x \sigma_1^x. \quad (\text{B.15})$$

To simplify the calculation, we first note that the subspaces $S_a = \{|11\rangle, |00\rangle\}$ and $S_b = \{|10\rangle, |01\rangle\}$ are disconnected in $H(t)$ by denoting as $|1(0)\rangle$ the eigenstates of σ_j^z with the eigenvalues 1 (-1). In terms of the Pauli operators for the pseudo spin in each of the two subspaces, the Hamiltonian $H(t)$ can be written as

$$H(t) = \omega \sigma_a^z + c \lambda(t) \sigma_a^x + c \lambda(t) \sigma_b^x, \quad (\text{B.16})$$

where $\sigma_a^z = |11\rangle\langle 11| - |00\rangle\langle 00|$ and $\sigma_a^x = |11\rangle\langle 00| + \text{H.c.}$ are the Pauli operators in the subspace S_a and $\sigma_b^x = |10\rangle\langle 01| + \text{H.c.}$ is the Pauli operator in the subspace S_b . Note that operators for different subspaces commute. The total field strength on the pseudo spin is given by the instantaneous eigenvalues of $H(t)$, in the subspace S_a it is fixed by the $\sqrt{\omega^2 + c^2\lambda^2(t)}$ while the field strength for S_b is $c\lambda(t)$ which can be obtained by diagonalizing Eq. (B.16). Similarly, we have

$$H_{\text{target}} = \tilde{\omega}\sigma_a^z + \tilde{c}\sigma_b^x, \quad (\text{B.17})$$

with the corresponding field strengths of $\tilde{\omega}$ and $\tilde{c} = c$. For adiabatic modulation on $\lambda(t)$ (including the cases for $\lambda(t) = 1$ and soft coupling), the dynamic phases [Eq. (B.9)] driven by $H(t)$ are the same as the case for H_{target} in case the field strength $\tilde{\omega}$ is given by

$$\tilde{\omega} = \frac{1}{T} \int_{-T/2}^{T/2} dt \sqrt{\omega^2 + c^2\lambda^2(t)} \quad (\text{B.18})$$

which we obtain by comparing the dynamic phase for the subspace S_a with the one generated by H_{target} . The energy shifts $\tilde{\omega} - \omega$ include all the high-order effects of the average Hamiltonian theory. The dynamic phase for the subspace S_b is $\int_{-T/2}^{T/2} dt c\lambda(t) = cT$.

B.3.3. Improved RWA: Two Qubits

To supplement the example given in Section 8.3.1, we remove the second resource qubit from the model. This simplifies the illustration of the incapability of the standard approach to suppress the RWA terms efficiently. The total Hamiltonian becomes

$$H(t) = \frac{\omega}{2} (\sigma_0^z + \sigma_1^z) + c\lambda(t)\sigma_0^x\sigma_1^x. \quad (\text{B.19})$$

As in the main text, we want to selectively preserve only the flip-flop interaction between the qubits. Explicitly, we would like to obtain the target Hamiltonian after RWA

$$H_{\text{target}} = \frac{1}{2}\tilde{\omega} (\sigma_0^z + \sigma_1^z) + \tilde{c} (\sigma_0^+\sigma_1^- + \text{H.c.}), \quad (\text{B.20})$$

where the parameters take into account the energy shifts as shown in Appendix B.3.2. In Fig. B.2 the equivalent of Figure 8.3 of the main text is shown. While the Gaussian modulation shows a smooth transition to constantly high fidelities, the standard method achieves high fidelity only for discrete values of ωT . Note that these discrete points for high fidelity in the standard method will change if there is a different number of qubits in the system (compare Figure 8.3) and in general are hard to predict in complex systems.

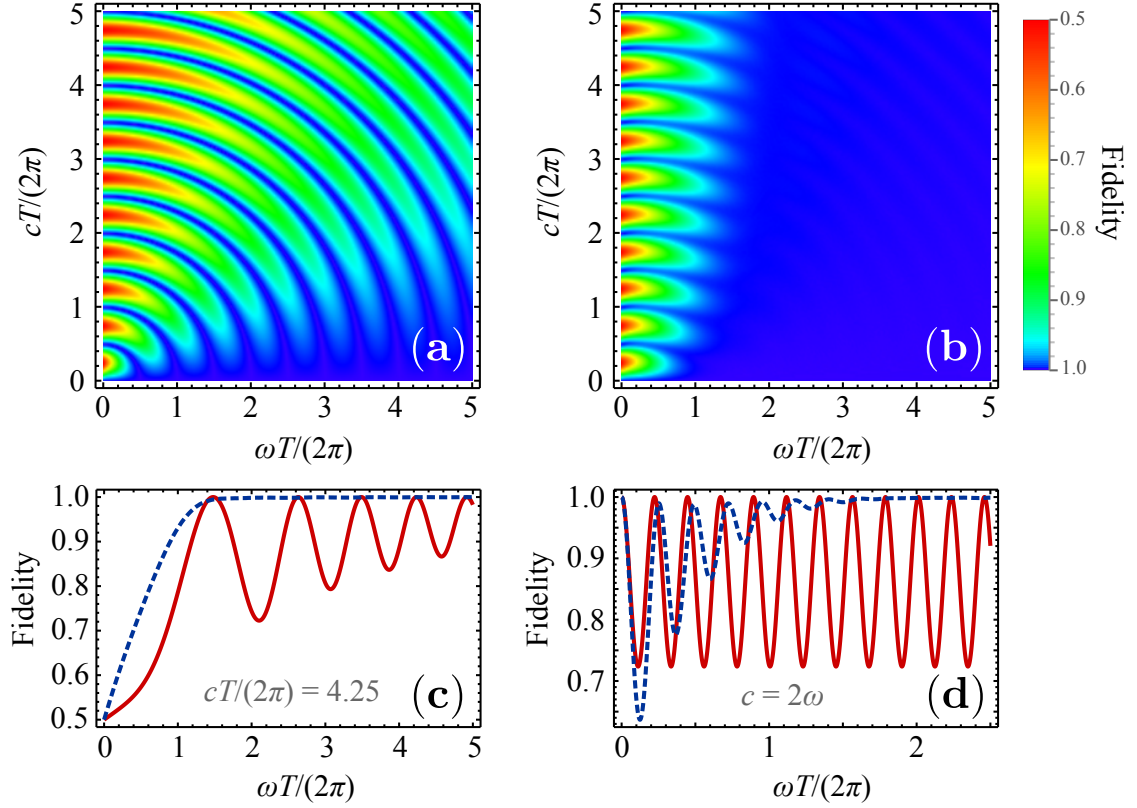


Figure B.2.: **Fidelities to the target two-qubit dynamics.** The figure is equivalent to Figure 8.3. The Gaussian shapes are realized with the parameters $\sigma = T/(4\sqrt{2})$ and $1/\lambda_0 = \sqrt{2\pi}\sigma \operatorname{erf}\left(\frac{T}{2\sqrt{2}\sigma}\right)$ which ensures the same target evolution as in the constant amplitude case. (a) and (b) show the constant amplitude and Gaussian modulation respectively. The curves for the Gaussian shapes [blue dashed lines in (c) and (d)] illustrate the same characteristic asymptotic behavior as for the three qubit case, while the constant amplitude undergoes significantly less modulation as only a single frequency is left in the model. (Reprinted figure with permission from [H4]. Copyright (2018) by the American Physical Society.)

B.3.4. Continuous Dynamical Decoupling and Hartmann-Hahn Resonance

Continuous dynamical decoupling is a different approach to the suppression of noise and sensing. It employs the dressed states formed by the application of a continuous drive and exploits the so called Hartmann-Hahn resonance. Starting from the total Hamiltonian in Eq. (2.11), we replace $\Omega(t)$ by a constant Rabi frequency Ω_{Rabi} . Following the same arguments as outlined in Section 2.2.2 and Section 2.2.1, the Hamiltonian is written in a frame rotating with the NV

center's free energy terms and the qubit approximation applied,

$$H_{\text{CD}} = \frac{\Omega_{\text{Rabi}}}{2} \sigma_0^x - \sum_j \vec{\omega}_j \vec{I}_j + \frac{m_s}{2} \sigma_0^z \sum_j \vec{A}_j \cdot \vec{I}_j. \quad (\text{B.21})$$

Here we made the convenient choice $\phi = 0$ and ω_{MW} is exactly on resonance with the driven transition determined by the choice of m_s .

Moving into a rotating frame with respect to the new free terms (the first two terms) yields the coupling Hamiltonian which is oscillating with the frequencies $\Omega_{\text{Rabi}} \pm \omega_j$. Provided that the couplings \vec{A}_j are large enough, we can neglect all terms where $\Omega_{\text{Rabi}} - \omega_j \neq 0$. Note that we assume $\Omega_{\text{Rabi}} \geq 0$ while the ω_j are positive by construction, see Eq. (2.9). Thereby we have the famous Hartmann-Hahn resonance condition generating the effective Hamiltonian

$$\Omega_{\text{Rabi}} = \omega_n \quad \Rightarrow \quad H_{\text{CD,eff}} = \frac{m_s}{2} a_n^\perp (\tilde{\sigma}_0^- I_n^+ + \tilde{\sigma}_0^+ I_n^-) \quad (\text{B.22})$$

where the tilde marks operators in the dressed basis of the NV center, $|\pm\rangle = (|0\rangle \pm |m_s\rangle)/\sqrt{2}$. Here we already assumed that the terms $\sim a_j^\parallel I_j^z$ average out completely, as they are oscillating with Ω_{Rabi} .

For the sensing protocol exploiting Hartmann-Hahn resonance, one continuously drives the NV electron spin for a time T . Between subsequent runs, Ω_{Rabi} is changed. To record a spectrum, one scans the Rabi frequency over a desired interval [23, 322]. By matching the dressed-state energy Ω_{Rabi} to the energies ω_j of the nuclear spins, electron-nuclear flip-flop processes are no longer suppressed by the energy mismatch and change the population of the dressed electron qubit according to $H_{\text{CD,eff}}$, resulting in signals in the spectrum [23, 322].

B.3.5. Variation of the Fourier Coefficients in the Simulations of the Soft Quantum Control

The employed Fourier coefficients depending on the current number of DD periods are shown in Figure B.3.

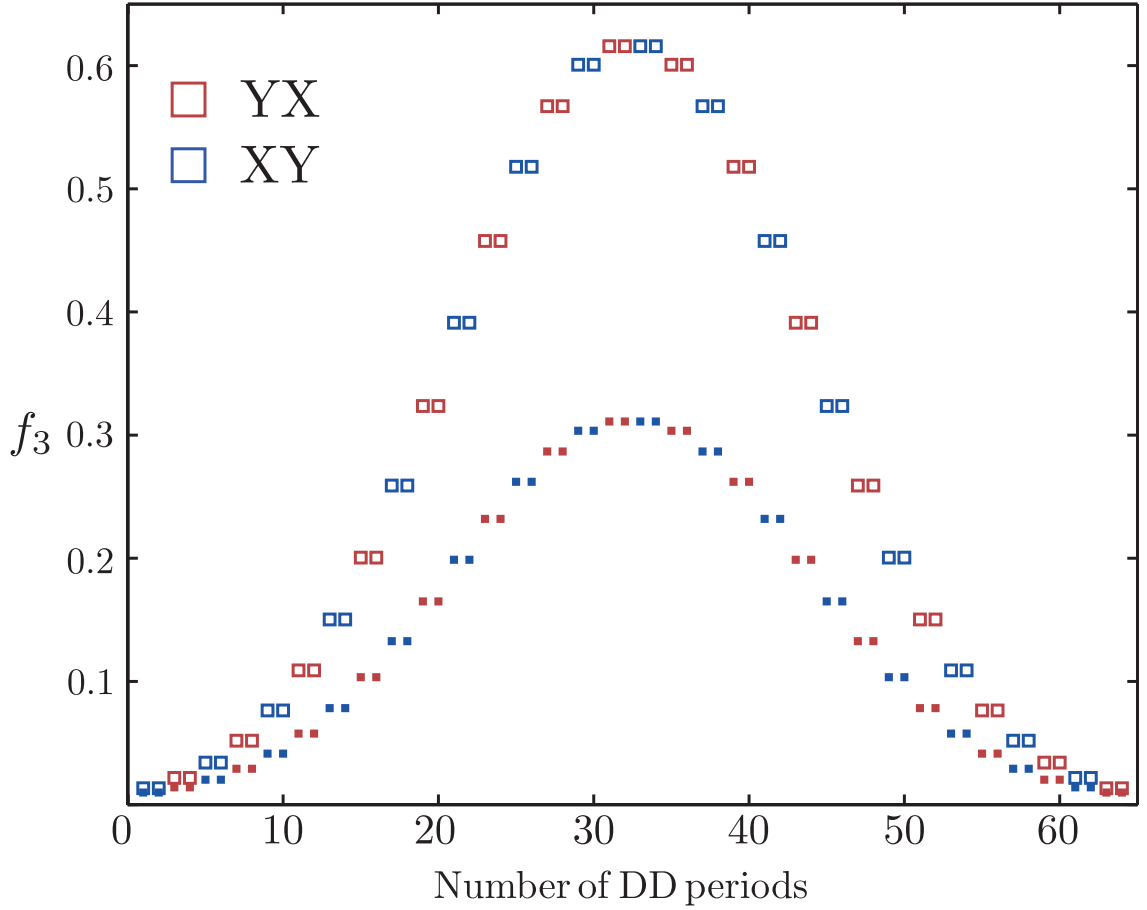


Figure B.3.: **Employed Fourier coefficients for the Gaussian-AXY sequences in Figure 8.4.** Squares with white fill correspond for to the sensing sequence in Figure 8.4 (c), colored squares to gate illustrated in Figure 8.4 (d). A blue square indicates two subsequent composite pulses with phases X and Y, while red squares realize the reversed order. The total sequence realizes 64 periods, i.e. 128 composite pulses.

Curriculum Vitae

Der Lebenslauf wurde aus Datenschutzgründen aus der elektronischen Version entfernt.

Publications

- J. F. Haase, A. Smirne, J. Kołodyński, R. Demkowicz-Dobrzański and S. F. Huelga
Precision Limits in Quantum Metrology with Open Quantum Systems.
Quantum Measurements and Quantum Metrology **5**, 13 (2018)
Preprint: [arXiv:1807.11882](#)
- J. F. Haase, P. J. Vetter, T. Uden, A. Smirne, J. Rosskopf, B. Naydenov, A. Stacey, F. Jelezko, M. B. Plenio and S. F. Huelga
Controllable Non-Markovianity for a Spin Qubit in Diamond.
Phys. Rev. Lett. **121**, 060401 (2018)
Preprint: [arXiv:1802.00819](#)
- J. F. Haase, Z.-Y. Wang, J. Casanova and M. B. Plenio
Soft Quantum Control for Highly Selective Interactions among Joint Quantum Systems.
Phys. Rev. Lett. **121**, 050402 (2018)
Preprint: [arXiv:1708.09611](#)
- J. F. Haase, A. Smirne, J. Kołodyński, R. Demkowicz-Dobrzański and S. F. Huelga
Fundamental limits to frequency estimation: A comprehensive microscopic perspective.
New J. Phys. **20**, 053009 (2018)
Preprint: [arXiv:1710.04673](#)
- J. F. Haase, Z.-Y. Wang, J. Casanova and M. B. Plenio
Pulse-phase control for spectral disambiguation in quantum sensing protocols.
Phys. Rev. A **92**, 032322 (2016)
Preprint: [arXiv:1608.00418](#)
- Z.-Y. Wang, J. F. Haase, J. Casanova and M. B. Plenio
Positioning Nuclear Spins in Interacting Clusters for Quantum Technologies and Bio-imaging.
Phys. Rev. B **93**, 174104 (2016)
Preprint: [arXiv:1510.02811](#)

- J. Casanova, Z.-Y. Wang, J. F. Haase and M. B. Plenio
Robust dynamical decoupling sequences for individual-nuclear-spin addressing.
 Phys. Rev. A **92**, 042304 (2015)
 Preprint: [arXiv:1506.03766](https://arxiv.org/abs/1506.03766)
-

Talks and Conference Participation

- J. F. Haase, A. Smirne, J. Kołodyński, R. Demkowicz-Dobrzański and S. F. Huelga
Quantum metrology in noisy environments. contributed talk, Quantum Optics IX, Gdańsk, Poland, September 17 - 23, 2017
- J. F. Haase, A. Smirne, J. Kołodyński, R. Demkowicz-Dobrzański and S. F. Huelga
Fundamental limits to frequency estimation: A comprehensive microscopic perspective. contributed poster, Second Arctic School on Open Quantum Systems, Utsjoki, Finland, September 10 - 15, 2017
- J. F. Haase, A. Smirne, J. Kołodyński, R. Demkowicz-Dobrzański and S. F. Huelga
Phase-covariant versus non-phase-covariant dynamics in quantum frequency estimation. contributed poster, 636. WE-Heraeus-Seminar: Quantum-Limited Metrology and Sensing, Bad Honnef, Germany, February 06 - 09, 2017
- J. Casanova, Z.-Y. Wang, J. F. Haase and M. B. Plenio *Robust dynamical decoupling sequences for individual-nuclear-spin addressing.* contributed poster, DIADEMS Summer School - Diamond and Spins School in Cargèse, France, April 26 - May 06, 2016
- J. Casanova, Z.-Y. Wang, J. F. Haase and M. B. Plenio *Robust dynamical decoupling sequences for individual-nuclear-spin addressing.* contributed talk, German Physical Society, Spring Meeting 2016, Hannover, Germany, February 03, 2016

Funding

The preparation of this thesis has been supported by an Alexander von Humboldt Professorship, the ERC Synergy grant BioQ and the EU Projects EQUAM, DIADEMS and QUCHIP.

Collaborations

The theoretical work of this thesis has been carried out at the *Institute of Theoretical Physics* (ITP) at the Ulm University under the joint supervision of Prof. Dr. Susana F. Huelga and Prof. Dr. Martin B. Plenio.

The content of the Chapters 4 and 5 arose from a joint work with Dr. Andrea Smirne and Prof. Dr. Susana F. Huelga (both ITP), Dr. Jan Kołodzyński (*ICFO-Institut de Ciències Fotòniques*, Barcelona, Spain) and Prof. Dr. Rafał Demkowicz-Dobrzański (*Faculty of Physics, University of Warsaw*, Poland).

The topics in the Chapters 7 and 8 have been pursued in collaboration with Dr. Zhenyu Wang, Dr. Jorge Casanova and Prof. Dr. Martin B. Plenio (all ITP).

The experimental measurements in Chapter 9 have been performed by Philipp J. Vetter, Thomas Uden, Dr. Boris Naydenov and Prof. Dr. Fedor Jelezko (all *Institute of Quantum Optics*, Ulm University), the diamond sample has been prepared by Alastair Stacey (*Centre for Quantum Computation and Communication Technology*, School of Physics, University of Melbourne, Australia and *Element Six*, United Kingdom), while the theoretical analysis is a joint work with Dr. Andrea Smirne, Joachim Rosskopf, Prof. Dr. Martin B. Plenio and Prof. Dr. Susana F. Huelga (all ITP).

Declaration of Academic Integrity - Erklärung wissenschaftlicher Redlichkeit

I declare that I prepared this doctoral thesis independently and did not use any sources or means other than those indicated by me and, furthermore, I cited the passages where I quoted or referred to works by other people and their contents and I comply with the Statutes of Ulm University on Safeguarding Good Scientific Practice in the applicable version.

Ich versichere hiermit, dass ich die Arbeit selbständig angefertigt habe und keine anderen als die angegebenen Quellen und Hilfsmittel benutzt sowie die wörtlich oder inhaltlich übernommenen Stellen als solche kenntlich gemacht habe und die Satzung der Universität Ulm zur Sicherung guter wissenschaftlicher Praxis in der jeweils gültigen Fassung beachtet habe.

Ulm,

Jan Friedrich Haase